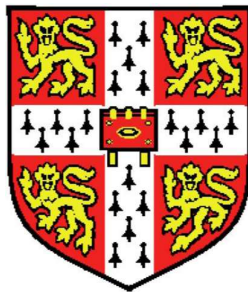


Methods for detailed study of detergent action in
cleaning food soils



Georgina Louise Cuckston

Department of Chemical Engineering and Biotechnology

Churchill College

University of Cambridge

A thesis submitted in December 2019 for the degree of

Doctor of Philosophy

Declaration

This thesis is the result of my own work and includes nothing which is the outcome of work done in collaboration except as declared in the Preface and specified in the text. It is not substantially the same as any that I have submitted, or, is being concurrently submitted for a degree or diploma or other qualification at the University of Cambridge or any other University or similar institution except as declared in the Preface and specified in the text. I further state that no substantial part of my thesis has already been submitted, or, is being concurrently submitted for any such degree, diploma or other qualification at the University of Cambridge or any other University or similar institution except as declared in the Preface and specified in the text. It does not exceed the prescribed word limit for the relevant Degree Committee.

Methods for detailed study of detergent action in cleaning food soils

Georgina Cuckston

Dishwasher detergent formulations contain components which dictate the chemical environment (pH, wettability, solubility) of cleaning solutions. The role of these factors, as well as temperature, in the mechanisms controlling the cleaning of a baked heterogeneous food soil from stainless steel substrates was studied using a combination of fluid dynamic gauging, real-time imaging, millimanipulation, and solution analysis techniques.

The extent of swelling, which is known to affect cleaning, was determined *in situ* using a fluid dynamic gauging (FDG) device developed by Wang *et al.* (2017). A new FDG configuration was developed which enabled measurement of swelling soon after immersion, allowing measurement of initial hydration. These studies were corroborated using a commercial point-light source confocal thickness measurement device. The onset and extent of swelling depended primarily on the solution pH.

At temperatures above 35 °C swelling was followed by the liberation of mobile fat present within the soil. Monitoring of droplet evolution allowed the growth and detachment of the oil droplets to be quantified and modelled. The rate of total carbonaceous material released from the soil was studied in separate tests using both stagnant and flowing solutions. The onset and volume of oil released was chiefly determined by the solution temperature and concentration of surfactant. Oil release was not directly related to deposit strength.

In millimanipulation the force imposed on a blade being passed through the soil layer is measured. The device was modified to allow submersion and flow of cleaning solution across the sample so that the effect of contact time with the reagent(s) could be studied. The force required to remove the soil changed noticeably after a critical soaking time, from an almost constant value to one which decayed with time. The critical soaking time depended on the temperature, pH, and composition of the cleaning solution and in many cases was associated with a transition from cohesive to adhesive breakdown. This transition occurred on similar timescales to the swelling of the soil. Some agents promoted faster adhesive breakdown.

Sinner's circle is classically used to describe the intentions between temperature, formulation, time and mechanical forces in cleaning. The different techniques allowed these to be quantified, particularly in terms of timescales. The cleaning mechanism was broken into two parallel processes: (I) the hydration and swelling of the soil layer after exposure to aqueous solutions followed by the de-wetting and displacement of oils and fats from within the soil structure towards the soil-solution interface, and (II) the ingress of solution at the soil-substrate interface, weakening the adhesive forces attaching the soil to the substrate. Temperature, pH, and surfactant type were demonstrated to act each process to a different extent, influencing the timescales of cleaning.

Preface

The work in this dissertation was conducted at the Department of Chemical Engineering and Biotechnology, University of Cambridge, between January 2016 and December 2019.

It is the original work of the author and includes no work done in collaboration, except where specifically acknowledged in the text. The candidate has not submitted any part of this dissertation elsewhere for a degree or other qualification. This dissertation has 163 figures and tables and is 71,702 words in length.

Georgina Cuckston

Acknowledgements

First, and most of all, I would like to thank Ian Wilson for his expertise, guidance and patience throughout the process of writing this thesis. Without his unfailing support this thesis would not have been possible. He listened to all my queries and patiently translated chemical engineering language into terms a chemist could understand, an effort for which I will always be grateful.

Besides my supervisor I would also like to thank my family, in particular my parents, Tim and Judy Cuckston, who have encouraged me in any endeavour in which I have ever expressed an interest. Without your unwavering love and support I would not have made it to where I am today.

I would like to thank Zayeed Alam, Kevin Blyth, James Goodwin, Michael Groombridge, and Glenn Ward of Procter & Gamble, Newcastle, for their insight and the genuine enthusiasm with which they discussed my results. Thanks go to both the EPSRC and P&G for their financial support in making this project possible as well as to the IChemE, Churchill College, the Cambridge Philosophical Society, and the UK-China Joint Research Newton Fund for their financial support for attending conferences and working abroad. I also thank Professor Dong Chen and Dr Ruben Mercarde-Prieto from Soochow University, Suzhou, for their support during my stay as a visiting student.

I would like to extend my sincere gratitude to the exceptional people in the Department of Chemical Engineering and Biotechnology, in particular to Andy Hubbard in the mechanical workshop and Jheng-Han Tsai for all their efforts in assisting me with the development of the SiDG rig. I also thank my advisor Dr Sarah Rough for her guidance during my NOTAF.

Throughout the project I was fortunate enough to supervise Sudhir Balaji, Jamie Davidson, Pawat Silawattakun, and Cheyanne Xie in their MEng research projects as well as Nathan Ravoisin in his MPhil research project. I thank them all for their enthusiasm, for being easy to work with and, in Nathan's case, for the input to my work.

I would like to thank all the old guard of the M1 office, particularly Jenni Holian, Romilde Kotzé and Michael Sargent for welcoming me into the group and for all the board game nights. Lastly I thank the people of the shiny new 3.17 office, chiefly Melissa Chee for her friendship throughout my time in this department, and to all of P⁴G who provided me with relaxing company alongside endless cups of tea.

Abstract

Dishwasher detergent formulations contain components which dictate the chemical environment (pH, wettability, solubility) of cleaning solutions. The role of these factors, as well as temperature, in the mechanisms controlling the cleaning of a baked heterogeneous food soil from stainless steel substrates was studied using a combination of fluid dynamic gauging, real-time imaging, millimanipulation, and solution analysis techniques.

The extent of swelling, which is known to affect cleaning, was determined *in situ* using a fluid dynamic gauging (FDG) device developed by Wang *et al.* (2017). A new FDG configuration was developed which enabled measurement of swelling soon after immersion, allowing measurement of initial hydration. These studies were corroborated using a commercial point-light source confocal thickness measurement device. The onset and extent of swelling depended primarily on the solution pH.

At temperatures above 35 °C swelling was followed by the liberation of mobile fat present within the soil. Monitoring of droplet evolution allowed the growth and detachment of the oil droplets to be quantified and modelled. The rate of total carbonaceous material released from the soil was studied in separate tests using both stagnant and flowing solutions. The onset and volume of oil released was chiefly determined by the solution temperature and concentration of surfactant. Oil release was not directly related to deposit strength.

In millimanipulation the force imposed on a blade being passed through the soil layer is measured. The device was modified to allow submersion and flow of cleaning solution across the sample so that the effect of contact time with the reagent(s) could be studied. The force required to remove the soil changed noticeably after a critical soaking time, from an almost constant value to one which decayed with time. The critical soaking time depended on the temperature, pH, and composition of the cleaning solution and in many cases was associated with a transition from cohesive to adhesive breakdown. This transition occurred on similar timescales to the swelling of the soil. Some agents promoted faster adhesive breakdown.

Sinner's circle is classically used to describe the intentions between temperature, formulation, time and mechanical forces in cleaning. The different techniques allowed these to be quantified, particularly in terms of timescales. The cleaning mechanism was broken into two parallel processes: (I) the hydration and swelling of the soil layer after exposure to aqueous solutions followed by the de-wetting and displacement of oils and fats from within the soil structure towards the soil-solution interface, and (II) the ingress of solution at the soil-substrate interface, weakening the adhesive forces attaching the soil to the substrate. Temperature, pH, and surfactant type were demonstrated to act each process to a different extent, influencing the timescales of cleaning.

Contents

Preface	i
Acknowledgments	ii
Abstract	iii
Contents	iv
List of Figures	xi
List of Tables	xix
Acronyms	xxii
Nomenclature	xxiv
1. Introduction	1
1.1 System of interest	3
1.1.1 Surfactants	4
1.1.2 Commercial cleaning formulations	5
1.2 Soil removal modes	6
1.3 Factors effecting cleaning	8
1.4 The automatic dishwasher	10
1.5 Scope of the dissertation	11
1.5.1 Conditions explored	12
1.5.2 Structure of the thesis	12
2. Background and literature review	14
2.1. Soils and Substrates	14
2.1.1 Soil types	14
2.1.1.1 Fats, oils and greases	14
2.1.1.2 Carbohydrates	15
2.1.1.3 Proteins	16
2.1.1.4 Fibres	17
2.1.1.5 Salts	18
2.1.2 Baking and drying	19
2.1.3 Commonly studied substrates	21
2.2. The removal of soils from substrates	23
2.2.1 Cleaning of single component soils	23
2.2.2 Cleaning of complex soils	24
2.2.3 Chemical cleaning agents	26
2.2.4 Formulating detergent systems	27

2.3. Cleaning techniques.....	28
2.3.1 Quantification of cleaning	28
2.3.2 Residue testing	29
2.4 Properties of interest.....	32
2.4.1 Visualisation of the soils and surfactants	32
2.4.2 Soil layer thickness over time	32
2.4.2.1 Comparison of non-contact displacement measurement techniques.....	33
2.4.2.1.1 Fluid dynamic gauging.....	33
2.4.2.1.2 The eddy current principle	33
2.4.2.1.3 The capacitive principle.....	34
2.4.2.1.4 The laser triangulation principle	34
2.4.2.2 Technique comparison	35
2.4.3 Measurements of adhesion strength	37
2.4.4 Solution composition over time	38
2.5 Project Objectives	39
3. Soil materials and preparation methods.....	40
3.1 Soils	40
3.2 Substrates	40
3.3 Simple soil layer preparation	41
3.3.1 Repeatability testing	42
3.4 Complex model soil.....	42
3.4.1 Soil drying	44
3.4.2 Soil characterisation	45
3.4.3 Soil Cracking.....	46
3.4.4 Impact of temperature on soil viscosity	47
3.5 Cleaning solutions	47
4. Microscale imaging	49
4.1 Experimental set-up.....	51
4.1.1 Choice of fluorophore in solution.....	51
4.1.2 Choice of fluorophore within the soil.....	52
4.1.3 CFM set-up.....	52
4.1.3.1 Substrate/solution chamber.....	53
4.1.3.2 Calibration and set-up	54
4.2 Results and analysis	55
4.2.1 Surfactant tracking	55

4.2.2 Effect of pH	57
4.2.2.1 Diffusion modelling.....	59
4.2.3 Effect of surfactant	61
4.2.3.1 Effect of surfactant concentration and type	64
4.2.4 Preliminary conclusions	64
4.3 Cleaning of complex model soils.....	65
4.4 Conclusions	69
4.5 Timescales of cleaning	70
5. Soil hydration and swelling.....	71
5.1 zFDG	71
5.1.1 Experimental procedure	73
5.1.1.1 Cleaning the device	74
5.1.1.2 Equipment calibration	75
5.1.1.3 Data Processing	76
5.1.2 Results and discussion	77
5.1.2.1 Effect of temperature	77
5.1.2.2 Effect of cracking	78
5.1.2.3 Effect of pH	79
5.1.3 Conclusions from zFDG	80
5.2 Sideways fluid dynamic gauge (SiDG)	81
5.2.1 SiDG description	81
5.2.1.1 Positional referencing.....	83
5.2.1.2 Substrates.....	83
5.2.1.3 Soils.....	83
5.2.1.4 Modelling.....	83
5.2.1.5 Test Protocol.....	84
5.2.2 Results and discussion	84
5.2.2.1 Effect of temperature	85
5.2.2.2 Effect of pH	87
5.2.2.3 Effect of surfactants	88
5.2.3 SiDG Conclusions	91
5.3 Confocal thickness scanning	92
5.3.1 Method	93
5.3.2 Results and discussion	94
5.3.2.1 Impact of orientation.....	96

5.3.2.3 Measurement of δ_o	96
5.3.2.4 Impact of measurement spot size	97
5.3.3 CTS conclusions.....	98
5.4 Chapter conclusions.....	99
5.5 Timescales of cleaning	100
6. Transfer of soil to solution	101
6.1 Oil recovery technique development	102
6.1.1 Experimental set-up.....	102
6.1.1.1 Sample preparation	102
6.1.1.2 Solution preparation	103
6.1.1.3 Static System	104
6.1.1.4 Flow system	104
6.1.1.5 Data processing	108
6.1.1.6 Data labelling.....	110
6.1.2 Static results and discussion	110
6.1.2.1 Impact of temperature	110
6.1.2.2 Impact of surfactants.....	113
6.1.3. Flow testing results and discussion	116
6.1.3.1 Impact of flow rate	116
6.1.3.2. Impact of temperature	118
6.1.3.3 Impact of surfactants.....	119
6.1.3.4 Impact of chelant.....	120
6.1.4 Oil recovery conclusions.....	121
6.1.5 Timescales of cleaning	121
6.2. Image analysis of droplets	122
6.2.1 Experimental set-up	122
6.2.1.1 Test Solutions	123
6.2.1.2 Test soils	124
6.2.1.3 Test Protocol.....	124
6.2.2 Image analysis protocol	124
6.2.2.1 Droplet identification	124
6.2.2.2 Location of the droplets	125
6.2.2.3 Circle Hough Transform.....	127
6.2.2.4 Droplet tracking	128
6.2.2.5 Data filtering	129

6.2.3 Data processing	131
6.2.3.1 Size distribution	131
6.2.3.2 Droplet detachment	132
6.2.3.3 Sphericity of the droplet.....	133
6.2.3.4 Effect of contact angle.....	134
6.2.3.5 Volume of droplets	135
6.2.3.6 Scaled analysis	136
6.2.4 Mathematical modelling.....	137
6.2.4.1 Model I: solution penetration	138
6.2.4.2 Model II: Solution ingress.....	140
6.2.5 Results and Discussion.....	143
6.2.5.1 Impact of temperature	143
6.2.5.2 Impact of pH	146
6.2.5.3 Impact of surfactants on droplet detachment	148
6.2.5.4 Experimental impact of surfactants	150
6.2.6 Overarching observations.....	153
6.3 Conclusions	155
6.4 Timescales of cleaning	155
7. Soil removal forces	157
7.1. Complex Soils	159
7.1.1 Substrate effects.....	159
7.1.2 Effect of contact with simple cleaning solutions for set time	160
7.1.3 Impact of drying.....	164
7.2 Development of a flow system for the MM3	165
7.2.1 Experimental set-up.....	165
7.2.1.1 Flow system test protocol	167
7.2.1.2 Test solutions in flow system	167
7.2.2 Results and Discussion.....	168
7.2.2.1 Effect of solution temperature	168
7.2.2.2 Effect of solution pH.....	169
7.2.2.3 Effect of surfactant	172
7.3 Conclusions	176
7.4 Timescales of cleaning	176

8. Data fusion.....	178
8.1 Techniques	178
8.2 Collation of data.....	178
8.3 Results and analysis	179
8.3.1 Effect of temperature	184
8.3.2 Effect of pH	185
8.3.3 Impact of surfactants.....	187
8.4 Overall cleaning mechanism.....	189
8.5 Conclusions	190
9. Application to commercial formulations.....	192
9.1. Multichambered Automatic Dish Washing Rig.....	192
9.1.1 Test set-up	192
9.1.1.1 Sample preparation	195
9.1.1.2 Solution preparation	196
9.1.1.3 Test protocol.....	196
9.1.1.4 ADW rig cleaning protocol.....	196
9.1.1.5 Test metrics	197
9.1.2 Results and analysis	197
9.1.2.1 Impact of temperature and pH.....	197
9.1.2.2 Impact of surfactants.....	198
9.1.2.3 Falling films	200
9.1.2.4 Impact of chelant.....	202
9.1.2.5 Step increase in pH.....	205
9.1.2.6 Effect of pH jump.....	207
9.1.2.7 Commercial detergent formulations	208
9.1.3 Shear Forces.....	210
9.1.4 Stage 1 conclusions.....	211
9.2 P&G formulations on Cambridge Rigs	212
9.2.1 Commercial formulation testing.....	212
9.2.1.1 Effect of commercial formulation and bleach on CMS on stainless steel	212
9.2.1.2 Effect of MGDA and bleach on stainless steel.....	215
9.2.3 Glass Substrates.....	217
9.2.3.1 Effect of commercial formulation and bleach on glass	217
9.2.3.2 Effect of MGDA and bleach on glass	218
9.2.4 Overview of results	220

9.2.5 Stage 2 conclusions.....	221
9.3. Oil Recovery - Batch System	222
9.3.1 Test set-up	222
9.3.1.1 Substrates.....	222
9.3.1.2 Test solutions.....	222
9.3.1.3 Batch test protocol	223
9.3.1.4 Data processing	223
9.3.2 Results and Discussion.....	225
9.3.2.1 Total carbon testing.....	225
9.3.2.2 Residual material.....	226
9.3.2.2.1 Gravimetric analysis	226
9.3.2.2.2 Image analysis of residual deposit	227
9.3.3 Stage 3 conclusions.....	228
9.4 Applications conclusions.....	229
10. Project conclusions and looking forward	230
10.1 Simple food soils	230
10.2 Complex food soils.....	230
10.2.1 Microscale imaging	231
10.2.2 Soil swelling	231
10.2.3 Solution analysis	231
10.2.4 Millimanipulation.....	232
10.2.5 Data Fusion	233
10.2.6 Application of findings to commercial formulations	233
10.3 Achievements	234
11. References	235
12. Appendix.....	251
12.1 The Lambert Function.....	251
12.2 CTAB oil droplet formation	253

List of Figures

- Figure 1.1: *Types of food product recalls in the UK in 2016.* (Westgate, 2018)
- Figure 1.2: *Number of publications each year since for the period 2000-2020 (not-cumulative). Dashed lines indicate publications with the words 'Fouling' or 'Cleaning' in the title. Solid lines indicate publications with the words 'Fouling + Food' or 'Cleaning + Food' in the title. Search conducted on Web of Science 18/09/2019.*
- Figure 1.3: *A schematic of soil layer submerged in cleaning solution. The orange layer represents the bulk soil, yellow represents mobile components in the soil.*
- Figure 1.4: *a) cationic: hexadecyltrimethylammonium bromide (CTAB), b) anionic Calbiochem® linear alkyl sulfonate (SDBS), Sigma®, c) Non-ionic: 4-(1,1,3,3-tetramethylbutyl)phenyl-polyethylene glycol (TX-100), Sigma®*
- Figure 1.5: *Soil removal modes in cleaning by submersion in solution. Reproduced from Bhagat et al., 2017*
- Figure 1.6: *Sinner's circle, depicting cleaning as a function of (i) time, (ii) temperature, (iii) mechanical action and (iv) chemical reagents.*
- Figure 1.7: *Water consumption per consumer household in 2018. Produced from data from the Office for National Statistics (UK) 2019.*
- Figure 1.8: *Approaches for studying the cleaning of soils on substrates in solutions. a) visual inspection of the interface, b) swelling of the soil, c) solution analysis, d) mechanical removal.*
- Figure 2.1: *Chemical structure of a typical fat molecule with (I) unsaturated, (II) mono-unsaturated, and (III) poly-unsaturated hydrocarbon chains.*
- Figure 2.2: *Chemical structure of a typical (a) sugar dimer; (b) polysaccharide carbohydrate; and (c) the conversion of a linear to a cyclic sugar monomer.*
- Figure 2.3: *(a) Chemical structure of a typical amino acid, (b) primary protein structure made up of a sequence chain of amino acids, (c) quaternary structure of a protein consisting of more than one coiled amino acid chain. Tertiary structures (not shown) are a coiled amino acid chain and made up one unit of the structure shown in (c).*
- Figure 2.4: *Chemical structure of chitin.*
- Figure 3.1: *(a) stainless steel disc (diameter (d) = 50 mm, height (h) = 3 mm) with baked lard soil. Soil thickness (δ) = $310 \pm 4 \mu\text{m}$, $R_q = 2.5 \mu\text{m}$, mass = $0.55 \pm 0.005 \text{ g}$, coverage = $0.28 \pm 0.003 \text{ kg m}^{-2}$. (b) stainless steel plate (50 x 50 mm, $h = 3 \text{ mm}$) with baked CMS $\delta = 300 \pm 5 \mu\text{m}$, $R_q = 270 \mu\text{m}$, mass = $0.49 \pm 0.06 \text{ g}$, coverage = $0.20 \pm 0.03 \text{ kg m}^{-2}$.*
- Figure 3.2: *(a) schematic and (b) photograph of draw-down applicator for the deposition of CMS films. Dimensions in mm.*
- Figure 3.3: *Average dimensionless mass loss of CMS during drying. The black dashed asymptote represents the average mass of the samples measured after 7 days. The inset presents the absolute value of the rate of CMS of dimensionless mass loss. Reproduced with permission from Nathan Ravoisin (2018).*
- Figure 3.4: *DSC thermograms of (a) fresh and (b) fresh, evaporated and burnt CMS. Temperature ramped from -20 to $100 \text{ }^\circ\text{C}$ at 5 K min^{-1} twice, as shown by inset in (a). Colours: Fresh; black – scan 1, grey – scan 2. Evaporated; blue – scan 1, purple – scan 2. Burnt; orange – scan 1, red – scan 2. Inset: temperature profile of DSC test.*

Figure 3.5: Photographs of $\delta = 300 \mu\text{m}$ CMS layer on $50 \times 50 \text{ mm}$ 316 stainless steel plate (a) before drying, and (b) after baking for 7 min at $204 \text{ }^\circ\text{C}$; (c) Binary image of (b) for calculating area of cracked soil; (d) image (b) with gridlines used for calculating crack distribution.

Figure 3.6: Shear viscosity of fat component of CMS (40 vol.% emulsion of fat in water). (a) shear rate dependency at $22 \text{ }^\circ\text{C}$: below 0.1 s^{-1} the gradient is close to -1, associated with yield stress behaviour. (b) apparent viscosity measured at apparent shear rate of 0.1 s^{-1} . Open symbols indicate data with significant normal stress differences, indicating strongly non-Newtonian behaviour.

Figure 3.7: Effect of surfactant (a-c) and chelant (d) concentration on the interfacial tension between deionised water and sunflower oil.

Figure 4.1: Schematic of confocal laser scanning microscope.

Figure 4.2: Nunc Lab-Tek Chamber for CFM studies (dimensions in mm) Blue squares show scanned areas for 8 locations set-up used CMS testing. Letters A – D define chamber identities.

Figure 4.3: Pictographic representation of z-stacking in imaging

Figure 4.4: Data showing the height of the soils with the maximum concentration of surfactant after submersion of (a) unbaked lard and (b) lard baked at $250 \text{ }^\circ\text{C}$ for 2 hours into a solution of 0.5 wt % fluorescent surfactant at pH 9 and $20 \text{ }^\circ\text{C}$. Inset shows cartoon of the soil layer expanding over time. Loci show linear regression fits. h is the height of soil layer scanned.

Figure 4.5: Fluorescence microscopy of baked lard soil surfaces exposed to alkaline surfactant solutions at pH 8, $20 \text{ }^\circ\text{C}$ over 4 hours. Peak A is at the soil-substrate interface, B at the soil-solution interface. Plots obtained for pH 9-13 demonstrated similar behaviour.

Figure 4.6: Evolution of peak A in baked lard (Peak A shown on Figure 4.5). a) pH 8-10 b) pH 11-13. Lines show fit to Equation 4.2., with parameters in Table 4.2. Shading represents one standard deviation of data from an average of 3 samples.

Figure 4.7: Comparison with simple diffusion model (Equation 4.4) for pH 8 surfactant ingress study in baked lard soil. $D_{\text{eff}} = 76.9 \mu\text{m}^2 \text{ s}^{-1}$. Inset: schematic of substrate-soil-solution interface showing the location of ingress.

Figure 4.8: Stills taken during CFM testing of fluorescence distribution in baked lard. a) $t = 0$, b) $t = 5746 \text{ s}$, c) $t = 12067 \text{ s}$. White arrow indicates movement of dye from outside the viewing plane across the viewing window in as a single front over time.

Figure 4.9: Diffusion modelling of surfactant ingress onto baked lard at pH 8. Points: data, Line: fit to Equation 4.5 with $D = 4.47 \times 10^{-7} \text{ m}^2 \text{ s}^{-1}$

Figure 4.10: Fluorescence intensity plots of Nile Red fluorophore in lard baked at $204 \text{ }^\circ\text{C}$ for 2 hours then submerged in a) sample 1, no solution, (dry); (b) sample 3, pH 9 solution, (c) sample 4, pH 9 solution + 1 wt.% SDBS (S) over 4 hours 14 min 10 s. Results for sample 2, pH 7, not shown. Vertical dashed lines show approximate location of substrate-soil interface (d) Evolution of retained intensity for samples 1 - 4. Model based on Equation 4.8.

Figure 4.11: Fluorescence of Nile Red in lard soil layers exposed to surfactant solutions. All solutions at pH 9 except the 'blank'. Concentrations in wt.%.

Figure 4.12: Photograph of a swollen layer of CMS soil immersed in pH 9 SDBS solution.

Figure 4.13: Total emission intensity of Nile Red in selected z-stacks over time. CMS soil layer contacted with pH 9 + 1 wt % SDBS solution at $t = 100 \text{ s}$. Solution was added at z-stack 3. Insets show cartoon representation of peak location for clarity.

- Figure 4.14: Fluorescence intensity of Nile Red probe in CMS in pH 9 solution. Each line is the recorded intensity over time of each layer of the recorded z-stack. H_T shown. H_I removed for clarity.
- Figure 4.15: Points: Evolution of height of location of soil-solution interface. Points: measured H_T from Figure 4.14. Dashed line: Generalised logistic function (Equation 4.9) fit to the data. G' (swelling rate) = $h / t_{swell} \approx 5 \mu\text{m s}^{-1}$.
- Figure 5.1: Schematic of fluid dynamic gauging action. δ is the soil layer thickness; h the clearance between the nozzle and soil layer; h_0 the clearance between the nozzle and substrate; d_t the diameter of the nozzle throat; d_i the inner tube diameter.
- Figure 5.2: Calibration plot of C_d against dimensionless clearance. Experimental conditions: water at 20 °C, $\dot{m} = 0.33 \text{ g s}^{-1}$, $Re_t = 375$. Triangles – suction, squares – ejection. Shaded region denotes optimal measurement range
- Figure 5.3: Schematic of zero discharge fluid dynamic gauging. Notation; SP; syringe pump; SM; stepper motor; PT; pressure transducer; GT; gauging tank; DAQ; data acquisition device; Reproduced from Wang et al. (2017)
- Figure 5.4 Example calibration plot for zFDG in deionised water at room temperature.
- Figure 5.5. Processing of FDG data based upon δ_i . (a) raw data; (b) data corrected with the assumption that $\delta_i = \delta_0$; (c) averaged data, shaded region shows one standard deviation of all repeats. (i) E - ejection, (ii) S - suction.
- Figure 5.6. (a) averaged ejection and suction data for pH 7 cleaning solution at 20 °C. (b) 2 repeats of suction for pH 7 at 50 °C. $\delta_i = 0.3 \text{ mm}$
- Figure 5.7: Representative plates for the dispersion of cracking as tested on the FDG in Figure 5.8.
- Figure 5.8. Impact of cracking on zFDG testing at 50 °C, a) ejection b) suction. Error band is one standard deviation.
- Figure 5.9. Impact of pH on zFDG testing at 50 °C, (a) ejection, (b) suction. Error band shading shows one standard deviation.
- Figure 5.10: (a) ejection and (b) suction plots for two repeats of pH addition after swelling has stabilised (See Figure 5.9). Addition of 10 g L^{-1} of NaOH at $t = 2700 \text{ s}$ to raise solution to pH 12 at 50 °C.
- Figure 5.11. Photograph and (inset) schematic of SiDG apparatus. Salient points: H – liquid reservoir with heat transfer coil; M - sample mount; N – nozzle; P – pressure transducer; X – nozzle positioner; Z – sample positioner. Reproduced from Tsai et al. (2019).
- Figure 5.12: Photograph of dry CMS soil before immersion with break strips at 15 mm intervals along the sample plate. Red dot indicates section at which positional referencing takes place.
- Figure 5.13: Swelling profile of CMS ($\delta_0: 340 \mu\text{m}$) immersed in deionized water (pH = 5.6, 20 °C) with $\dot{m} = 0.33 \text{ g/s}$ measured on the SiDG. Solid blue circles – ejection; open red triangles – suction. Shaded are represents one standard deviation of up to 15 tests.
- Figure 5.14: (a) SiDG data showing effect of temperature on swelling for CMS layers at $\dot{m} = 0.33 \text{ g/s}$, 20 °C, using ejection mode. Error bars indicate the range of repeated tests. Inset: photograph showing release of mobile components during zFDG testing at 50 °C. Lines show fit to Equation 5.8. Parameters in Table 5.2. (b) Effect of temperature on initial thickness and final change in thickness. Solid black squares – change of initial thickness; solid red squares – final change in thickness.

- Figure 5.15: SiDG data showing (a) Effect of pH on swelling of CMS layers. $\dot{m} = 0.33 \text{ g/s}$, $20 \text{ }^\circ\text{C}$, ejection mode. Error bands indicate the range of repeated tests. Solid lines show fit to equation 5.8 (b) Change of initial thickness and final change in thickness among different pH values. Solid blue squares – change of initial thickness; open black triangles – final change in thickness.
- Figure 5.16: Effect of 0.1 wt% surfactant on SiDG swelling behaviour at (a) $20 \text{ }^\circ\text{C}$ and (b) $50 \text{ }^\circ\text{C}$.
- Figure 5.17: SiDG data showing effect of 0.1 wt. % SDBS on swelling behaviour at $20 \text{ }^\circ\text{C}$ and $50 \text{ }^\circ\text{C}$ at (a) pH 7 and (b) pH 9.
- Figure 5.18: Diagram of confocal thickness scanner (CTS). Inset: Photograph of CTS apparatus.
- Figure 5.19: CTS calibration plot for distance measurement offset caused by the addition of liquid to the chamber.
- Figure 5.20: CTS swelling of CMS at $20 \text{ }^\circ\text{C}$ investigating the impact of (a) pH, (b) SDBS, (c) CTAB, (d) TX-100, (e) pH 9, with and without surfactants, (f) pH 12, with and without surfactants. Each test is an average of 3 repeats. Error bands show one standard deviation
- Figure 5.21: Comparison of δ_0 measured by Mitutoyo and CTS. Standards measured are feeler gauges of thickness 0.04, 0.1, 0.15, 0.2 and 0.4 mm. Inset: extended comparison including 0.5 and 0.8 mm.
- Figure 5.22: Comparison of swelling behaviour measured by the CTS and SiDG devices ($\dot{m} = 0.33 \text{ g s}^{-1}$) of CMS immersed in pH = 9 solution (δ_0 around $300 \text{ }\mu\text{m}$), ejection mode. Blue squares – CTS (2 repeats); black squares – SiDG, ejection (3 repeats).
- Figure 6.1: (a) Appearance of oil droplets on a CMS-SS sample submerged in cleaning solution in zFDG testing at $50 \text{ }^\circ\text{C}$. (b) Oil droplet formation on burnt CMS contacted with pH 7 deionised water at $50 \text{ }^\circ\text{C}$.
- Figure 6.2: Schematics of soil sample plates for (a) static and (b) flow testing. Yellow colouring indicates soiled region.
- Figure 6.3: Static method of oil collection. A – 100 ml solution chamber, solution volume: 50 ml. [1] containing soil sample; B – soil on SS substrate; C – thermostated water bath; D – second solution chamber [2].
- Figure 6.4: Schematic of Flow rig for investigating oil release of CMS samples. (A) Temperature controlled solution reservoir, (B) peristaltic pump, (C) sample chamber, (D) solution collection chambers.
- Figure 6.5: Schematic of sample chamber. $Q = 1 - 30 \text{ cm}^3/\text{min}$, $\bar{U} = 0.0167 - 5.76 \text{ mm/s}$. Residence time = 2.5 – 75 min.
- Figure 6.6: Effect of temperature on cumulative total carbon released from $0.67 \pm 0.1 \text{ g}$ burnt CMS soil after submersion in cleaning solution at (a) pH 7 and (b) pH 10 in static tests. Lines: Experimental fits to Equation 6.12. Associated kinetic parameters given in Table 6.7.
- Figure 6.7: Kinetic parameters obtained from Figure 6.6 (b), pH 10.
- Figure 6.8: Effect of pH on total carbon release at (a) $22 \text{ }^\circ\text{C}$ and (b) $50 \text{ }^\circ\text{C}$ in static tests. Lines: Experimental fits to Equation 6.12. Associated kinetic parameters given in Table 6.8.

Figure 6.9: Effect of additives on cumulative total carbon release at 22 °C and 50 °C. SDBS (S), MGDA (M), CTAB (C), Bleach (B). Static test conditions. Note different y-axis scales. Lines: Experimental fits to Equation 6.12. Associated kinetic parameters given in Table 6.9. R = Reference. Data for SDBS and MGDA have larger error boundaries due to tests occurring at start of method development.

Figure 6.10: Impact of flow rate at pH 10 and (a) 22 °C and (b) 50 °C.

Figure 6.11: Percentage of total oil released that remained in the flow chamber at the end of the 120 minute test. Inset: measured residual carbon (black) as a proportion of total organic carbon (TOC, red + black) released throughout the test.

Figure 6.12: Effect of pH on the cumulative total carbon release at (a) 22 °C and (b) 50 °C in flow mode at 10 ml min⁻¹.

Figure 6.13: Cumulative total carbon release at 22 and 50 °C with (a) 0.1 wt.% SDBS (S), and (b) 0.1 wt.% MGDA (M). Flow apparatus, 10 ml min⁻¹.

Figure 6.14: (a) Experimental set-up for droplet image analysis. H – heating coil, S – stand, L – light ring, C – camera. (b) side view of soiled plate with after droplets formed on the surface.

Figure 6.15: (a) Images acquired at (i) t = 0 min, start of test, (ii) t = 5 min, after swelling but before oil evolution and, (iii) t = 60 min, end of test. (b) (i) CMS imaging plate submerged in pH 7 water at 40 °C. Dashed circle shows region analysed. (ii) CMS on glass slide viewed from beneath showing crack closure and transfer of oil into cracks. (c) Example of droplet growth over time intervals. Test 25: pH 7, 40 °C.

Figure 6.16: Diagram of the Hough Transformation Principle: step 1

Figure 6.17: Types of oil droplet evolution; (a) variations in equilibrium droplet size, (b) growth and detachment and, (c) growth, detachment and regrowth.

Figure 6.18: Histograms of droplet growth on 707 mm² CMS after submersion in pH 7 water at 50 °C. Inset: Evolution of the total number of droplets on the CMS surface. Larger version available in Figure 6.21 (b).

Figure 6.19: Schematics of oil droplet on CMS surface submersed in solution. r_c is the radius of the contact line of the spherical cap on the CMS, R is the droplet radius, γ_{ow} , γ_{so} , γ_{wo} are the oil-water, oil-soil and water-oil interfacial tensions respectively. (a) side view, (b) plan view. Contact angle defined in the denser phase.

Figure 6.20: Effect of contact angle on validity of spherical modelling assumption. Blue line: Equation 6.30.

Figure 6.21: Evolution of (a) total volume and (b) number of droplets on 707 mm² of CMS surface after submersion in pH 7 water at 50 °C.

Figure 6.22 (a) Evolution of scaled droplet diameter d_j^* all droplets, t_{adj} . (b) average scaled droplet diameter data. Shaded region shows one standard deviation. Smooth red line shows the fit to Equation 6.33, parameters reported in Table 6.13.

Figure 6.23 (a) Schematic cartoon representations of a penetration displacement mechanism, (b) water ingress mechanism.

Figure 6.24: Fits of models I and II to droplet formation data for CMS submerged in pH 7 water at 50 °C

Figure 6.25: Schematic of the solution ingress model.

Figure 6.26: (a) Evolution of averaged scaled diameter. (b) Total volume of the droplets. (c) Histograms of droplets formed on CMS after submersion in pH 7 water at (i) 35 °C and (ii) 50 °C. Inset: total number of droplets by time, (d) Model fits of CMS submerged in pH 7 water at (i) 35 °C, t_p here is 40 minutes and (ii) 40 °C, with t_p set to 27 minutes. Model fit to 45 °C not shown. Shaded regions show one standard deviation of three repeats. Model parameters for fits to equation 6.44 and equation 6.56 are recorded in Table 6.13.

Figure 6.27: (a) Effect of pH on evolution of averaged scaled diameter. (b) Total volume of the droplets. (c) Histograms of droplets formed on CMS after submersion at 50 °C in (i) pH 7 water and (ii) pH 9, inset: total number of droplets by time. (d) Model fits of CMS submerged at 50 °C in (i) pH 8 solution, with t_p set to 22 minutes and (ii) pH 9, $t_p = 23$ minutes. Shaded regions show one standard deviation of three repeats. Model parameters for fits to equation 6.44 and equation 6.56 are recorded in Table 6.13.

Figure 6.28: Effect of surfactant on droplet evolution (a) averaged scaled diameter. (b) Total volume of the droplets formed over the test time. (c) Histograms of droplets formed on CMS after submersion in at 50 °C in (i) pH 7 water and (ii) 0.1% SDBS, inset: total number of droplets by time. (d) Model fits of CMS submerging at 50 °C in (i) 0.01% SDBS solution, with t_p set to 16 minutes and (ii) 0.01 TX-100, $t_p = 20$ minutes. Shaded regions show one standard deviation of three repeats. Model parameters for fits to equation 6.44 and equation 6.56 are recorded in Table 6.13.

Figure 7.1: Schematic of millimanipulation deformation testing. A flat blade of thickness L is pulled at velocity, V , through a soil sample of initial thickness, δ , at clearance, c , leaving a residual layer of notional thickness c . The blade displacement, relative to the point of first contact is x . Region (I) denotes material ahead of the blade (boundary, dashed, not known a priori); (II) displaced material collected in front of the blade; and (III) material beneath the blade. Reproduced from Ali (2015).

Figure 7.2: (a) Side view of the millimanipulation device with flow chamber fitted. Labels: A, Perspex viewing wall, outlined in red; B, stainless steel blade; C, force transducer; D, counterweight; E, sample mounting station; I, solution inlet; O, solution outlet. Dashed arrow indicates direction of sample motion. (b) Schematic of the MM III, taken from Magens et al. (2017). Components not shown: axis controllers and force transducer amplifier. Modifications to allow study of immersed systems not shown. Copyright permission obtained for MM3 drawing.

Figure 7.3: Effect of substrate on removal force of dry CMS baked at 204 °C for 7 minutes. Shaded region is standard deviation between 3 repeat samples for (a) stainless steel, (b) glass. (c, d) show individual samples of soiled glazed ceramic. Red dashed lines (L) show point of failure of the MM3 test on the soiled glazed ceramic samples.

Figure 7.4: Effect of contact with cleaning solution on residual soil on substrate. (a) schematic of testing regions; (b) photograph of plate after testing with (conditions for B: 5 minutes soaking in 1 wt.% SDBS solution at room temperature). All dimension in mm. Blade clearance: 50 μm .

Figure 7.5: Side-on view of the removal of an example of (a) dry soil and (b) soil immersed in surfactant solution. Identical CMS with differences in lighting conditions due to submersion in solution causing apparent colour differences.

- Figure 7.6: F_w profiles (a) before (region A in Figure 7.4) and (b) after soaking in 1 wt.% SDBS solution at pH 10 at room temperature (region B in Figure 7.4). The transducer range sets a limit on F_w of 430 N m^{-1} causing the truncation in (a). Legend denotes start time of the test. $V = 0.1 \text{ mm s}^{-1}$
- Figure 7.7: Effect of soaking at pH 10 at room temperature with (solid circles) and without 1 wt.% SDBS (open circles). Insert: full data containing 60 min data points. Error bars show time scale of averaged data points.
- Figure 7.8: Effect of air drying at room temperature after soaking for 30 minutes in 1 wt.% SDBS solution at pH 7. (a) Representative plots of CMS plates dried in air for 1, 15, 30, 60, 120 and 180 minutes. (b) Average force of removal per unit blade width. Dashed line is a dry reference sample. The line shows a generalised logistic function fitted to the data. Error bars show standard deviation of the F_w within each sample.
- Figure 7.9: (a) schematic and (b) photograph of flow system for MM3. A – heater-circulator water bath, B – solution reservoir, C – peristaltic pump, D – sample chamber, E – Drainage system. Labels on photo correspond to items in schematic.
- Figure 7.10: Conductivity of solution leaving test chamber before and after addition of NaOH solution to the reservoir at $t = 10 \text{ min}$. Data from three repeats. The grey area indicates the section plotted in the inset. Solution flow rate 100 mL min^{-1} .
- Figure 7.11: Effect of temperature on removal force following contact with pH 7 solution at $t = 0$ at (a) $20 \text{ }^\circ\text{C}$; (b) $50 \text{ }^\circ\text{C}$. Dashed vertical lines mark initial and final regions subject to edge effects, repeated in subsequent plots. Vertical dot-dashed lines speculate on location of B/C transition observed at time t_c : photograph insets show the plate after testing. Solid line in (b) shows fit to exponential decay $F_w = 920 \exp[-t'/125]$.
- Figure 7.12: Effect of pH on removal profiles at $20 \text{ }^\circ\text{C}$. Solid loci show linear regression to data in the range $50 < t < 350 \text{ s}$. Vertical dashed lines mark initial and final regions subject to edge effects.
- Figure 7.13: Effect of pH on removal profiles at $50 \text{ }^\circ\text{C}$. (a) pH 9, (b) pH 12: pH 7 data given in Figure 7.11 (b). Vertical dashed lines mark region A and D (edge effects). Vertical dot-dashed lines speculate on location of B/C transition observed at pH 7 at 220 s. Photographs show substrate after testing.
- Figure 7.14: Effect of surfactant on removal force at $20 \text{ }^\circ\text{C}$. Soil is contacted with pH 9 solution at $t = 0$. Lines show linear regression to data in the range $50 < t < 350 \text{ s}$. Vertical dashed lines mark initial and final regions subject to edge effects.
- Figure 7.15: Effect of 1 wt.% surfactant on removal profiles at pH 9 and $50 \text{ }^\circ\text{C}$. (a) CTAB, (b) TX-100, (c) SDBS solution. Grey symbols show profile obtained without surfactant common to each plot. Vertical dashed lines mark initial and final regions subject to edge effects. Vertical dot-dashed lines speculate on location of B/C transition. Solid lines show fit of data in stage C to a simple exponential decay.
- Figure 8.1: Data fusion plot for CMS submerged in deionised water at $50 \text{ }^\circ\text{C}$. Data plotted as scaled parameters on the y-axis for millimanipulation (MM3), fluid dynamic gauging (SiDG), oil recovery via solution analysis (Oil R_B), and image analysis of droplet on the CMS surface (Oil M).
- Figure 8.2: Schematics of stages in cleaning of CMS. (a) bulk soil, (b) within a pore
- Figure 8.3: Effect of temperature. Deionised water at pH 7 and (a) $20 \text{ }^\circ\text{C}$ and (b) $50 \text{ }^\circ\text{C}$.

- Figure 8.4: *Effect of pH. Deionised water at 50 °C at (a) pH 7 and (b) pH 9.*
- Figure 8.5: *Effect of surfactants. Deionised water at 50 °C with (a) no surfactant, (b) pH 7 + 0.1% SDBS (MM3, Oil R and SiDG) and pH 7 + 0.01 % SDBS (Oil M), (c) pH 7 + 0.1% CTAB (MM3, Oil R and SiDG) and (d) pH 7 + 0.1% TX-100 (MM3, Oil R_B and SiDG) and pH 7 + 0.01 % TX-100 (Oil M). * denotes samples at 0.01 wt.% surfactant.*
- Figure 9.1: *Schematic of the ADW Rig. a) Front View b) Side view inside a chamber. Labels: A; Sample mount angle adjuster; C; Camera; CS; circulation system; D; drain; H; heating block; J; water jet; S; cleaning solution; SM; sample mount SS; plate with soil sample; T; temperature sensor; VW; viewing window. Water is circulated from the reservoir, through the circulation system and out through the jet at a set flow rate. The jet reciprocates at a set frequency across the top of the sample plate to wet the entire surface.*
- Figure 9.2 (a) *stainless steel stencil for generating uniform soil dots (b) photograph of CMS sample plate.*
- Figure 9.3: *ADW data showing impact of temperature and pH. (a) average mass loss as a percentage of total sample mass over 120 min test with 3-4 samples per point. Error bars indicate sample standard deviation, (b) Final average dot loss over 120 min test with 3-4 samples per point. Error bars indicate sample standard deviation.*
- Figure 9.4: *Impact of surfactants on cleaning of CMS as tested in ADW rig at 50 °C. a) Average mass loss as a percentage of total sample mass, b) average final dot loss after 120 min. Error bars are sample standard deviation. 3-4 sample per test.*
- Figure 9.5: *Photographs of film flow over stainless steel plate soiled with CMS, contacted with (a): DI water: inadequate coverage. (b): 0.1 % SDBS in water: full film coverage. Both pictures taken after one cycle of the water jet. T = 50 °C.*
- Figure 9.6: *CMS soiled substrate after 120 minutes contact with pH 11 cleaning solution.*
- Figure 9.7: (a) *Average dot loss over time for solutions of 0.1 % MGDA plus 0.1 % surfactant at 50 °C and (i) pH 7 and (ii) pH 10. (b) Normalised average dot loss against time plotted in the form of Equation 9.1. (i) pH 7 and (ii) pH 10. Total number of dots = 80. Error bars are sample standard deviation of 3-4 samples. Trendlines are linear regression fits.*
- Figure 9.8: *Photographs of a) top two rows of soil dots over time in the ADW rig. LHS 0.1 wt.% SDBS RHS 0.1 wt.% SDBS + 0.1 wt.% MGDA. b) side view photos showing wet soil curling away from the surface in 0.1 wt.% MGDA + 0.1 wt.% SDBS solution.*
- Figure 9.9: (a) *Effect of step increase in pH from 7 to 10 at set time intervals. Data plotted as (i) time since start of test and (ii) time after addition of alkali. (b) Kinetic plots of normalised average dot loss plotted in the form of Equation 9.1 for (i) time since start of test and (ii) time after addition of alkali. Error bars indicate sample standard deviation of 3-4 samples. Arrows indicate dosage time. Lines show fit to Equation 9.1. Parameters in Table 9.4.*
- Figure 9.10: *Simplified cleaning behaviour timeline*
- Figure 9.11: *Average cleaning of CMS dots with commercial detergents on the ADW rig, plotted in the form of Equation 9.1 with (a) n = 1 and (b) n = 0.5. Solid trendlines show linear fits. Dashed trendline shows fit to initial data. Parameters tabulated in Table 9.5. 4 repeats per solution. 80 soil dots per plate. T = 50 °C, pH 10.4*

Figure 9.12: (a) MM3 testing showing the effect of temperature on average removal force of CMS from stainless steel following contact with 1 % CCF1 solution at $t = 0$ and (i) 0 % bleach, 22 °C (ii) 10 % bleach, 22 °C (iii) 0 % bleach, 50 °C (iv) 10 % bleach, 50 °C. Dashed lines mark initial and final regions subject to soil edge effects from soil pinning at the edge of the plate. Data outside these lines are discounted, repeated in subsequent plots. Dot-dashed lines mark the transition in decay behaviour at t_c . Solid red line in (i, ii, iv) shows fit to linear decay, red line in (iii) shows fit to exponential decay. Shaded grey area region is range of 2 repeat samples. Parameters reported in Table 9.6. (b) SiDG testing at 20 °C showing the effect of effect of (i) CCF1 with and without bleach (ii) CCF1, without MGDA, with and without bleach, on soil swelling using suction mode. B – blister.

Figure 9.13 : (a) MM3 testing showing the effect of temperature on average removal force of CMS from stainless steel following contact with 0.1 wt% MGDA solution at ($t = 0$) and (i) 0 % bleach, 22 °C; (ii) 10 % bleach, 22 °C (iii) 0 % bleach, 50 °C (iv) 10 % bleach, 50 °C. Dot-dashed lines mark the transition in decay behaviour at t_c . Solid red line in (i, ii, iv) shows fit to linear decay, red line in (iii) shows fit to exponential decay. Shaded grey area region is range of 2 repeat samples. Parameters reported in Table 9.6. (b) SiDG testing showing the effect of (i) MGDA and (ii) bleach, on soil swelling using suction mode. Inset in (b, ii) photograph of CMS soil after testing with bleach showing discolouration.

Figure 9.14: MM3 tests showing the effect of temperature on average removal force of CMS from glass following contact with 1 % CCF1 solution at $t = 0$ at (i) 0 % bleach, 22 °C (ii) 10 % bleach, 22 °C (iii) 0 % bleach, 50 °C (iv) 10 % bleach, 50 °C. Dot-dashed lines mark the transition in decay behaviour at t_c . Solid red line in (i-iii) shows fit to linear decay, red line in (iv) shows fit to exponential decay. Shaded grey area region is the range of 2 repeat samples. Parameters reported in Table 9.6.

Figure 9.15 : Effect of temperature on average removal force of CMS from glass following contact with 0.1 wt% MGDA solution at $t = 0$ at (i) 0 % bleach, 22 °C (ii) 10 % bleach, 22 °C (iii) 0 % bleach, 50 °C (iv) 10 % bleach, 50 °C. Dot-dashed lines mark the transition in decay behaviour at t_c . Solid red line in (i-iii) shows fit to linear decay, red line in (iv) shows fit to exponential decay. Shaded grey area region is the range of 2 repeat samples. Parameters reported in Table 9.6.

Figure 9.16: Schematic of batch rig for investigating oil release of CMS samples. Solutions are stirred by a magnetic stirrer bar (SB) at 300 rpm.

Figure 9.17: Recovered organic carbon analysis of CMS submerged in cleaning solutions for 120 min. Horizontal dashed line shows amount of oil/fat present in the deposit. Batch configuration. Lines for pH 7 and pH 9 are fits to Equation 6.12.

Figure 9.18: Gravimetric analysis of soil samples after 2 hours submersion in cleaning solutions and drying overnight in a desiccator. Masses presented as a percentage of the initial burnt soil mass. Error bars are of 4 repeats per sample. CCF1: commercial formulation 1, CCF2: commercial formulation 2.

Figure 9.19: Colour enhanced photographs of sample plates after 2 hours immersion. Each plate is 50 x 50 mm.

Figure 12.1: Profiles of r^* computed from Equation 12.7 using (a): W_0 , and (b): W_{-1} .

Figure 12.2: Example of droplet formation on CMS submerged in (a) 0.01% CTAB solution and (b) pH 7, water at 50 °C.

List of Tables

- Table 1.1: *Types of surfactant and their most common uses*
- Table 1.2: *Evolution of motor consumption in automatic dishwashers, 1950-1994 data from Rosa et al. 2012. 1994-current: Energy Star Ratings Requirements (2019)*
- Table 2.1: *Substrates employed in fouling and cleaning studies relevant to the cleaning of food-based soils.*
- Table 2.2: *Summary of cleaning studies relevant to the cleaning of food based soils*
- Table 2.3: *Summary of residue tests for determining cleanliness of substrate.*
- Table 2.4: *Summary of benefits and limitation of commercially available non-contact sensing techniques*
- Table 2.5: *Investigating of soil deposits by micro- and milli-manipulation. Reproduced and updated from Ali, 2015.*
- Table 3.1: *Dimension and surface characteristics of substrates used in tests*
- Table 3.2: *Repeatability for 10 discs of lard soil layers. $T = 250\text{ }^{\circ}\text{C}$, baking time = 2.5 h, initial mass: 0.81 g. Adhesion measured by millimanipulation testing, discussed in Chapter 7.*
- Table 3.3: *complex model soil composition*
- Table 3.4 *Summary of component properties, reproduced from Ali (2015(a))*
- Table 4.1: *Method parameters for CFM testing.*
- Table 4.2: *Kinetic parameters of Figure 4.6 (a) pH 8 – 10 and (b) 11 – 13.*
- Table 5.1: *Percentage of SiDG tests that successfully yielded swelling data. Tests in which the material sloughed off the substrate were considered unsuccessful.*
- Table 5.2 *Kinetic parameters from data sets in Figures 5.14 – 5.17. Data fitted to Equation 5.8, 5.9.*
- Table 6.1 *Soil sample preparation masses for 60 CMS soil plates.*
- Table 6.2: *Reynolds numbers associated with test flow velocities*
- Table 6.3: *Length of entrance regions associated with test flow velocities*
- Table 6.4: *Average wall shear stresses associated with test flow velocities*
- Table 6.5: *Local wall shear stresses associated with test flow velocities at a) x_1 and b) x_2 (Figure 6.5)*
- Table 6.6: *Drag force over the soil associated with test flow velocities*
- Table 6.7: *Kinetic parameters from both data sets in Figure 6.6.*
- Table 6.8 *Kinetic parameters from data sets in Figure 6.8. Data fitted to Equation 6.12 and Equation 6.15*
- Table 6.9: *Kinetic parameters from both data sets in Figure 6.9. Data fitted to Equation 6.12.*
- Table 6.10: *Conditions investigated using droplet imaging.*
- Table 6.11: *Bond number estimations for range of potential R_1 values in water, $\theta = 53^{\circ}$*
- Table 6.12: *(a) Bond number estimations for droplets sized $0.5\text{ mm} < R_1 < 1.5\text{ mm}$ in surfactant solutions (b) Estimations of the critical radius for droplet detachment from CMS submerged in an aqueous cleaning solution at $50\text{ }^{\circ}\text{C}$. $d_{crit} = 2R_{crit}$.*

Table 6.13: *Table of parameters for image analysis of droplets study.*

Table 7.1: *Summary of rate of change of adhesion forces over 500 s testing. Uncertainty parameters based on one standard deviation.*

Table 8.1: *Summary of kinetic constants and timescales obtained from the different measurement techniques.*

Table 9.1: *Settings used in ADW rig*

Table 9.2: *Soil sample preparation masses for 152 CMS plates.*

Table 9.3: *Kinetic parameters of data in Figure 9.5 fitted to Equation 9.1 for solutions of 0.1 wt.% MGDA with 0.1 wt.% surfactant.*

Table 9.4: *Kinetic parameters of data in Figure 9.7 calculated using Equation 9.1 for pH 7 solutions doped up to pH 10 at set time intervals.*

Table 9.5: *Kinetic parameters obtained by fitting Equation 9.1 to data generated in Figure 9.9 for commercial cleaning detergents. k' denotes $n = 1$, k denotes $n = 0.5$.*

Table 9.6: *Summary of rate of change of MM3 forces over 500 s testing in Figures 9.12 - 9.15. Uncertainty parameters were based on one standard deviation.*

Other

Flow Chart 6.1: *Data processing chart for static and flowing systems described in Figure 6.3 and 6.4.*

Flow chart 9.1: *Data processing chart for batch systems described in Figure 9.16*

Acronyms

ACE	Advanced chemical engineering
ADW	Automatic dishwashing rig
AFM	Atomic force microscopy
ATP	Adenosine triphosphate
BHT	Butylated hydroxytoluene
BODIPY	4,4-difluoro-4-bora-3a,4a-diaza-s-indacene
CARS	Coherent anti-stokes resonance scattering
CCF	Commercial cleaning formulation
CFM	Confocal fluorescence microscopy
CHT	Circular Hough transform
CIP	Clean in place
CLSM	Confocal laser scanning microscope
CMC	Critical micelle concentration
CMS	Complex model soil
CPU	Central processing unit
CS	Circulation system
CTAB	Cetyl trimethylammonium bromide
CTS	Confocal thickness scanner
DAQ	Data acquisition device
DI	Deionised water
DOE	Design of experiments
DLC	Diamond-like carbon
DSA	Drop shape analyser
DSC	Differential scanning calorimetry
EDX	Energy dispersive x-ray
FDG	Fluid dynamic gauging
GBP	British pound sterling
GFP	Green fluorescent protein
GT	Gauging tank
HTST	High temperature short time
IEP	Isoelectric point
IV	Iodine value
LAS	Linear alky lsulfonate
LED	Light emitting diode
MALDI MS	Matrix assisted laser desorption mass spectrometry
MGDA	Trisodium dicarboxymethyl alaninate
MM3	Millimanipulation version 3
Ni-P-PTFE	Nickel-phosphate-polytetrafluoroethylene

NMR	Nuclear magnetic resonance
P ⁴ G	Polymer, pastes, particles and processing group
PC	Personal computer
PEG	Poly ethylene glycol
PEPT	Positron emission particle tracking
PT	Pressure transducer
PTFE	Polytetrafluoroethylene
P&G	Procter & Gamble®
RAM	Random access memory
ROI	Region of interest
SDBS	Sodium dodecylbenzene sulfonate
SEM	Scanning electron microscope
sFDG	Scanning fluid dynamic gauge
SiDG	Sideways fluid dynamic gauging
SP	Syringe pump
SM	Stepper motor or sample mount
SS	Stainless steel
STDEV	Standard deviation
TCTFPS	Trichloro(3,3,3-trifluoropropyl)silane
TM	Trademark
TOC	Total organic carbon
TX-100	Octyl phenol ethoxylate
UHT	Ultra high temperature
USB	Universal serial bus
USD	United states dollar
UV-A	Ultra violet light
zFDG	Zero discharge fluid dynamic gauging
3D	Three dimensional

Nomenclature

Roman

A	Area of the square duct of dimensions width a and depth b	m^2
a	Average distance between two droplets at steady-state or the maximum radial distance that the mobile component travels.	m
Bo	Bond number	-
C	Concentration	$g L^{-1}$
C_d	Discharge coefficient	-
C_f	Fanning friction factor	-
c	The penetration rate constant or blade scrape clearance from substrate	$-/m$
c_n	Constants	-
C_0	Initial concentration	$g L^{-1}$
D	Diffusion coefficient or dot diameter	- or m
Da	Daltons	Da
D_h	Hydraulic diameter	m
DF_t	Dilution factor of the TOC sample at time t_s	-
DI	Deionised water	-
d	Diameter	m
d^*	Scaled droplet diameter	-
d_{crit}	Critical diameter for droplet detachment	m
d_i	Nozzle lip width	m
d_{max}	Maximum diameter	m
d_{pore}	Diameter of the pore	m
d_t	Nozzle throat diameter	m
E	Activation energy	J
e	Exponential term	-
F	Force	N
F_B	Buoyancy forces	N
F_{SF}	Surface tension forces	N
F_D	Drag force	N
F_w	Force per unit width	$N m^{-1}$
$\langle F_w \rangle$	Average force per unit width between samples	$N m^{-1}$
$\langle F_w, 500s \rangle$	Average force per unit width after 500 s	$N m^{-1}$
$\overline{F_w}$	Average force per unit width within one sample	$N m^{-1}$
f	Moody friction factor or total forces on the MM3	- or Nm^{-1}
$f_{adhesive}$	Adhesive forces	$N m^{-1}$
f_I	Forces required to deform material in a soil layer	$N m^{-1}$
f_{II}	Forces required to displace the deformed material	$N m^{-1}$
f_{III}	Forces required to overcome the shear resistance imposed on the bottom edge of the blade	$N m^{-1}$

f_{FE}	The maximum fraction of fat equivalent	mg g^{-1}
G	Growth rate	s^{-1}
g	Acceleration due to gravity	m s^{-2}
H_i	Initial layer height	m
H_T	Height at top of blister	m
h	Height	m
$h_{(max)}$	Height of layer with maximum intensity	m
h_0	Nozzle clearance from hard surface	m
I_i	Intensity at layer, i	-
I_t	Intensity at time, t	-
$I_{R(z,t)}$	Relative intensity at location z at time t	-
$I_{R,A}$	Relative intensity in peak A at time, t	-
$\Delta I_{R,A}(\infty)$	The change in intensity at time $t = \infty$	-
k_I	Linear rate constant of oil recovery data	$\text{mg g}^{-1} \text{s}^{-1}$
k_{ADW}	Rate constant of ADW data with $n=0.5$	s^{-1}
k'_{ADW}	Rate constant of ADW data with $n=1$	s^{-1}
k_{CFM}	First order rate constant of CFM data	s^{-1}
$k_{droplet}$	First order rate constant of image analysis data	s^{-1}
k_{TOC}	First order rate constant of oil recovery data	s^{-1}
k_{SiDG}	First order rate constant of SiDG data	s^{-1}
k_{zFDG}	First order rate constant of zFDG data	s^{-1}
k'_{MM3}	Linear rate constant of MM3 data	$\text{N m}^{-1} \text{s}^{-1}$
L	Blade thickness or width of falling film	m
L_e	Length of the entrance region of a duct or pipe	m
L_c	Capillary length	-
l	Length	m
M	Molar	mol L^{-1}
M_d	Mass of dot	g
M_w	Rate of flow of momentum per unit width	kg s^{-2}
m	Mass	g
m^*	Dimensionless mass	-
\dot{m}	Mass flow rate	kg s^{-1}
N	Number of dots	-
N_0	Number of dots at $t=0$	-
N_c	Number of cracks per mm	-
N_z	Layer number in the z -direction	-
$N_{z, max}$	Layer number in the z -direction with maximum fluorescence intensity	-
n	Number	-
P	Pressure or the wetted perimeter of a square duct	Pa or m^2
ΔP_{12}	Pressure drop	Pa

ΔP_c	Suction induced capillary pressure difference	Pa
Q	Volumetric flow rate	$\text{m}^3 \text{s}^{-1}$
R	Droplet radius	m
R_1	Radius of a droplet with a Bond number of 1	m
R^2	Coefficient of determination	-
R_{crit}	Critical radius of droplet detachment	m
Re_t	Reynolds number evaluated at the nozzle throat	-
Re_{cr}	Critical Reynolds number in a square duct	-
Re_{D_h}	Reynolds number in a square duct	-
R_g	Gas constant	$\text{J mol}^{-1} \text{K}^{-1}$
R_q	Roughness quotient	m
R_z	Roughness parameter	m
R	Radius	m
r^*	Scaled radius defined as r/a	m
r_c	Radius of contact line	m
r_i	The inner radius of the SiDG nozzle	m
r_o	The outer radius of the SiDG	m
T	Temperature	$^{\circ}\text{C}$
t	Time	s
t_1^*	Scaled time defined as (t_{adj}/t_p)	-
t_2^*	Scaled time defined as $(\frac{4\Delta P_c}{\alpha a^2} t_{Adj})$	-
t_{adj}	Adjusted time defined as $(t - t_{onset})$	s
t_{asym}	Time at which data reaches an asymptote	s
t_b	Baking time	s
t_c	Transition time on MM3	s
t_d	Time delay	s
t_D	Decay time	s
t_{dry}	Drying time	s
t_i	Induction time	s
$t_{immersion}$	Immersion time	s
t_{onset}	Onset time	s
$\langle t_{onset} \rangle$	Average onset time	s
t_p	Penetration time	s
t_s	Time at which a sample was taken	s
t_{soak}	Soaking time	s
t_{swell}	Swelling time	s
t_{max}	Time of maximum intensity	s
t_0	Start time of test / time of sample submersion	s
TOC	Cumulative total organic carbon released at time, t	mg g^{-1}

$TOC_{initial}$	Background organic carbon level present in the cleaning solution	$mg\ g^{-1}$
TOC_{max}	Cumulative total organic carbon released by the end of the test	$mg\ g^{-1}$
\bar{U}	Average flow velocity	$m\ s^{-1}$
u_m	Superficial velocity	$m\ s^{-1}$
V	Volume	m^3
V_B	Blade velocity	$m\ s^{-1}$
V^*	Scaled droplet volume	-
$V_{chamber}$	Volume of chamber	m^3
V_D	Droplet volume	L
V_{max}	Maximum volume	L
$V_{substrate}$	Velocity of the substrate	$m\ s^{-1}$
V_{total}	Total volume	L
V_S	The sample volume	L
V_t	The test volume at time t_s	L
$V_{s,t}$	The sample volume collected for a given time interval, t .	L
W^{-1}	Lambert W	-
We	Weber number	-
$wt.$	Weight	kg
w	Blade width	m
X_{dry}	Displacement through a dry sample	m
X_{wet}	Displacement through a wet sample	m
x	Distance travelled within a material, displacement	m
x_0	The TOC measurement in a sample at time, t_0	$mg\ g^{-1}$
x_t	The TOC measurement in a sample at time, t_s	$mg\ g^{-1}$
z	Location in the z-plane	-
z_{max}	Z-plane of maximum intensity	

Greek

α	A lumped constant ($180 \frac{(1-\varepsilon)^2}{E^3} \frac{\mu}{d_{pore}^2}$)	$Pa\ m^{-1}$
$\dot{\gamma}$	Linear shear rate	s^{-1}
γ_{ow}	Interfacial tension between oil and water	$mN\ m^{-1}$
γ_{os}	Interfacial tension between oil and soil	$mN\ m^{-1}$
γ_{ws}	Interfacial tension between water and soil	$mN\ m^{-1}$
δ	Layer thickness	m
δ_0	Absolute initial layer thickness	m
δ_i	Initial measured layer thickness	m
δ_{water}	Water layer thickness	m
δ_{max}	Maximum layer thickness	m
δ_{final}	Final measured layer thickness	m

δ_E	Layer thickness measured by ejection mode	m
δ_S	Layer thickness measured by suction mode	m
$\Delta\delta$	Absolute change in layer thickness	m
$\Delta\delta_i$	Change in layer thickness between first and current measurement	m
$\Delta\delta_{final}$	Final change in layer thickness at the end of the test	m
$\Delta\delta_{max}$	Maximum change in layer thickness	m
$\langle\delta\rangle$	Average layer thickness	m
ε	Porosity of the sample	-
θ	Contact angle, defined in the more dense fluid	°
λ	Wavelength	m
μ	Viscosity	Pa s
π	The mathematical constant, pi	-
ρ	Density	kg m ⁻³
$\Delta\rho$	Density difference	kg m ⁻³
ρ_s	Density of cleaning solution	kg m ⁻³
τ_{dot}	Shear stress acting on the soil dot	N m ⁻²
τ_w	Wall shear stress	N m ⁻²
$\bar{\tau}_w$	Average wall shear stress	N m ⁻²
$\bar{\tau}_w^*$	Dimensionless average wall shear stress	-
τ_{CFM}	Half-life of CFM data	s
$\tau_{droplet}$	Half-life of image analysis data	s
τ_{TOC}	Half-life of oil recovery data	s
τ_{SiDG}	Half-life of SiDG data	s
τ_{zFDG}	Half-life of zFDG data	s
φ_{oil}	Volume fraction of mobile fat within CMS	-

1. Introduction

Cleaning is one of the most critical stages in quality control for any processing or manufacturing plant, irrespective of product type. The formation of fouling layers on the surface of processing equipment can have significant, negative impact on its operating efficiency. The total fouling related costs for industrialized nations in major refining units were estimated to exceed \$4.4 billion USD annually in 2003 (Master *et al.*, 2003). The build-up of fouling layers on industrial heat-exchangers has been ascribed to cost approximately 0.25 % of GDP for industrialised nations through loss of production via reduced transfer efficiency and increased down-time (scheduled or unscheduled) to remove these layers (Müller-Steinhagen *et al.*, 2005).

Improper cleaning practices increase the risk of contamination, especially in multi-product production lines. In 2009 viral contamination of a bioreactor used in the manufacture of a drug produced by Genzyme® forced the halt of its production for five months, costing the company an estimated \$300 million in lost revenue, in addition to \$175m in fines from the US Food and Drug Administration (DePalma, 2010).

Fouling and cleaning is ubiquitous in the food sector, from the domestic kitchen to large scale manufacturing plants. All food produced or manufactured in the UK since 2001 must adhere to standards outlined by the Food Standards Agency or face a costly product recall and, in extreme cases, closure of the production plant. Insufficient cleaning practices leading to biological or foreign matter contamination accounted for over 60 % of all product recalls in the UK in 2016, costing an average of £30,000 per recall (Figure 1.1).

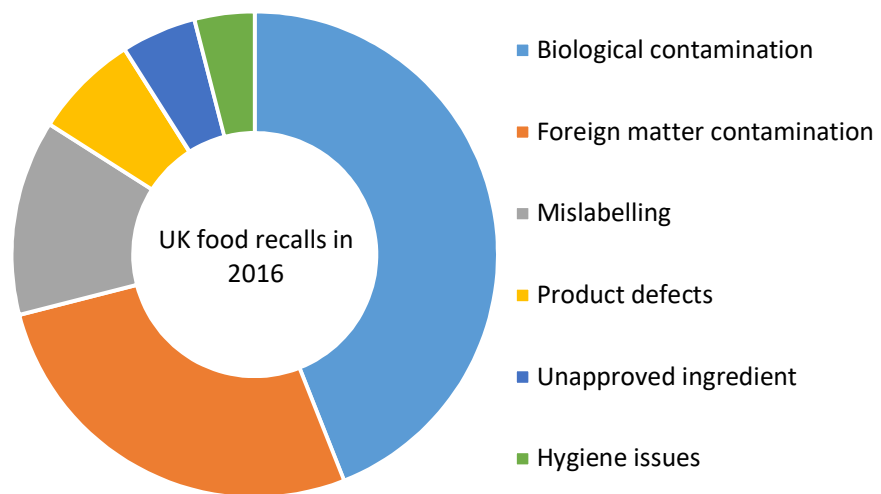


Figure 1.1: Types of food product recalls in the UK in 2016. (Westgate, 2018)

Significant research into the cleaning of fouling deposits has been conducted for over the past century however in recent times this has increased (Figure 1.2). A Web of Science survey of articles published between 2000 and 2020 showed that of the 12,749 containing the word ‘fouling’ in the title, abstract or author-specific key words, 386 related to food soils. Similarly of the 52,697 containing the word ‘cleaning’, 2662 related to the cleaning of food soils. This gives a proportion of interest in the cleaning of food soils as 3.0 % and 4.7 % of the fouling and cleaning sectors, respectively. It can be seen from Figure 1.2, with its primary and secondary axis plotted on a 1:20 scale, that this proportion has remained constant over the time period.

This finding is corroborated by a review conducted by Wilson (2018) for the years 2014-2018 in which he found that 2.7 % and 4.0 % articles published on fouling and cleaning, respectively, related specifically to food soils.

Figure 1.2 shows that the rate of publication has been increasing strongly, further highlighting the increase in interest in this aspect of the manufacturing process.

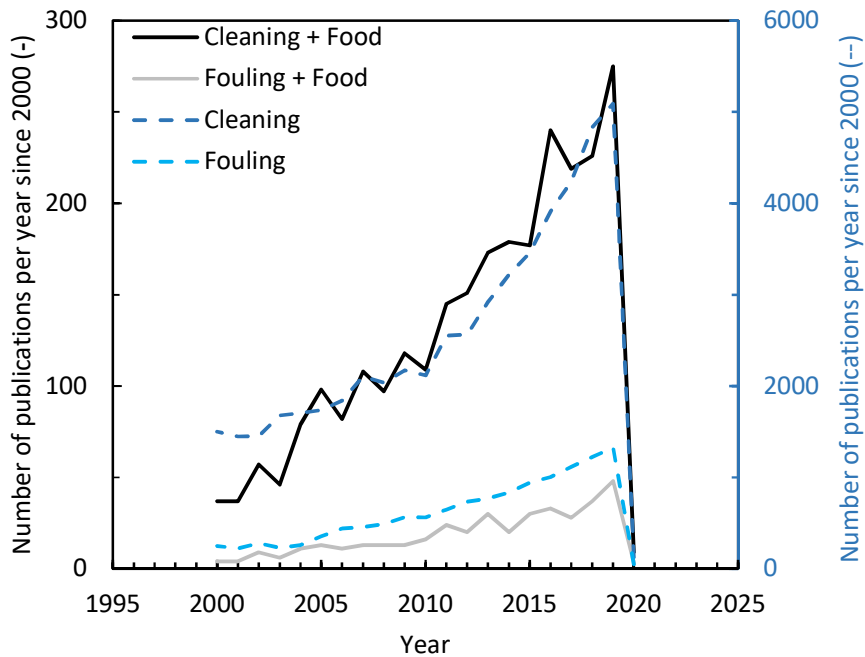


Figure 1.2: Number of publications each year since for the period 2000-2020 (not-cumulative). Dashed lines indicate publications with the words ‘Fouling’ or ‘Cleaning’ in the title. Solid lines indicate publications with the words ‘Fouling + Food’ or ‘Cleaning + Food’ in the title. Search conducted on Web of Science 18/09/2019.

1.1 System of interest

It is important to define the system to be studied in this dissertation. Figure 1.3 introduces key terms used in this work. The *substrate* is the item which provides the surface on which a material is deposited or adheres, for example a stainless steel pipe in a manufacturing line. The *soil* is an undesired layer of food-based material which adheres to the substrate through a combination of Lifshitz-van der Waals, ionic and electrostatic forces (Moeller and Nirschl, 2017). Lifshitz-van der Waals tend to dominate (Kumar *et al.*, 2013) in dry conditions but when immersed in aqueous solution, electrostatic forces, influenced by factors such as pH and electrolyte concentration, play a larger role (Israelachvili, 2011).

The removal of the soil from the substrate is assisted by the use of an aqueous-based cleaning *solution*. Other cleaning methodologies such as gas-phase (e.g. Venturi-type scrubbers), abrasive cleaning, and cleaning with organic solvents are also available but are not typically used within the food industry due to the increased risk of introducing contaminants that are unsuitable for human consumption.

The cleaning solution may contain detergents. These are amphiphilic surface active agents (surfactants) which lower the energy required to transfer the soil from the substrate into the solution by reducing the soil-liquid interfacial energy (Deshpande *et al.*, 2017). When present in sufficient concentration (i.e. above their critical micelle concentration (CMC)), surfactants form micelles. These are colloidal-sized aggregates which act as a store of surfactants for use in emulsification of the soil into the solution (among other operations).

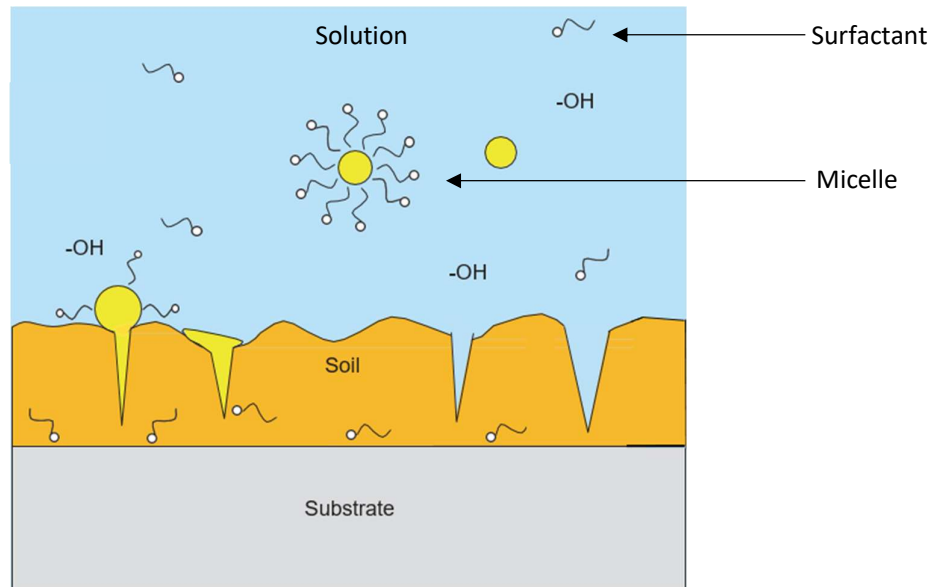


Figure 1.3: A schematic of soil layer submerged in cleaning solution. The orange layer represents the bulk soil, yellow represents mobile components in the soil.

1.1.1 Surfactants

Surfactants have widespread importance in a significant number of applications. They are commonly found in household and personal care products, varying from laundry detergents to shampoo. They also have industrial use in oil recovery and biological systems (Schramm *et al.*, 2003). Ceresana estimated that the global surfactant market in 2016 was worth over \$30 billion dollars, with Acemite determining that production was in the range of 33 million tonnes (Ceresana, 2017; Acemite, 2016).

Surfactants are one of the most versatile molecules used within the chemical cleaning industry. They can act as detergents, wetting agents, emulsifiers, foaming agents, and dispersants (Rosen and Kunjappu, 2012). A surfactant is characterised by its chemical structure. It must contain two different functional groups, with differing affinities to solvents. Typically, this consists of a hydrophobic 'tail', made up of an alkyl chain ($C_8H_{17}-R$ to $C_{22}H_{43}-R$), and a polar 'head' which has a strong affinity to water. Examples of polar groups include sulfates, phosphate esters, and amines (Table 1.1).

Surfactants are typically classified by their polar functional group. A cationic surfactant has a positively charged polar head group; an anionic surfactant a negatively charged group; a non-polar surfactant has no charge; and a zwitterionic has two oppositely charged head groups within the same molecule. The most common synthetic surfactant found in cleaning applications is the anionic linear alkyl sulfonate (LAS). Approximately 3 million tonnes of LAS are produced world-wide each year (Weiss *et al.*, 2012), primarily for use in applications requiring the removal of oily stains and residues, e.g. laundry detergent, engine degreasers, and toothpastes. The choice of surfactant is made based upon the type of soil to be removed, the acceptable toxicity level of the waste stream and the cost of production.

Table 1.1: Types of surfactant and their most common uses

Class	Head Group	Applications	Example
Anionic R-X⁻ M⁺	-CO ₂ ⁻ Na ⁺ -SO ₃ ⁻ Na ⁺ -OPO ₃ ⁻ Na ⁺	Soaps Synthetic detergents Emulsifiers	Sodium dodecyl sulfate, (SDS) CH ₃ (CH ₂) ₁₁ OSO ₃ ⁻ Na ⁺
Cationic R-X⁺ Y⁻	-NMe ₃ ⁺ Cl ⁻ -NMe ₂ ²⁺ 2Cl ⁻	Disinfectants Fabric conditioners	Cetyl trimethylammonium bromide (CTAB) CH ₃ (CH ₂) ₁₅ NMe ₃ ⁺ Br ⁻
Non-ionic	(OCH ₂ CH ₂) _n OH	Detergents, Emulsifiers	Octyl phenol ethoxylate (TX-100) C ₁₄ H ₂₂ O(C ₂ H ₄ O) _{n=9-10}
Zwitterionic	-NMe ₂ ⁺ -(CH ₂) _n -SO ₃ ⁻	Shampoos, Cosmetics	Cocamidopropyl hydroxysultaine C ₂₀ H ₄₂ N ₂ O ₅ S

The choice of surfactants in this investigation was guided by the work of Ali. Ali's work focussed primarily on the cleaning of greasy polymerised food soils such as cooked lard (2015(a)). He

investigated the impact of a range of surfactant types on the cleaning of cross-linked carbon polymer networks via solubility and controlled deformation testing.

The heterogeneous soils to be studied here are complex, consisting of multiple phases and functionalities. Prediction of the most applicable surfactant for this system is impractical without testing. Therefore one of each of the cationic, anionic and non-ionic species studied by Ali (2015(a)) are used in this work in order to maintain continuity across systems (Figure 1.4 (a, b, c)). A zwitterionic surfactant, provided by the project sponsors, was also considered in limited testing, the results of which are not presented owing to commercial confidentiality.

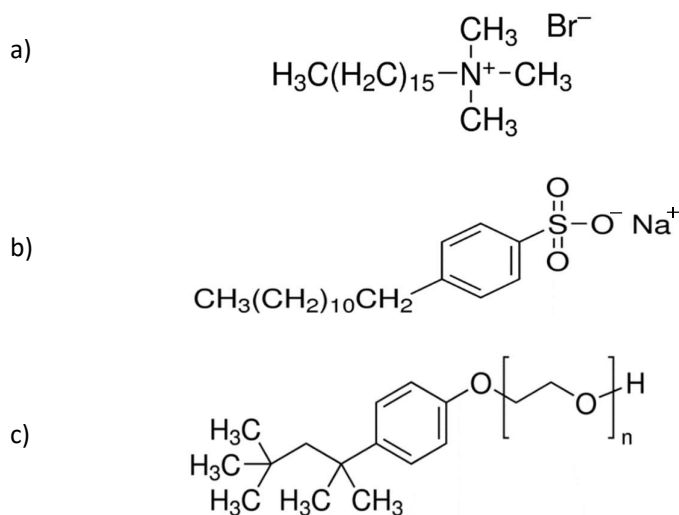


Figure 1.4: a) cationic: hexadecyltrimethylammonium bromide (CTAB), b) anionic Calbiochem® linear alkyl sulfonate (SDBS), Sigma®, c) Non-ionic: 4-(1,1,3,3-tetramethylbutyl)phenyl-polyethylene glycol (TX-100), Sigma®

1.1.2 Commercial cleaning formulations

Whilst surfactants are key to most aqueous cleaning processes, they are often combined with other additives, e.g. alkaline salts for the saponification of greases, forming more complex formulations (Thompson *et al.*, 1997). These additives can include:

Alkaline salts. Sodium hydroxide, and other strongly alkaline salts, have been the primary component in formulations due to its ability to saponify greases effectively and cheaply. These additives generate high pH conditions. In modern products the alkaline content, although present in significant quantities, is restricted due to health concerns (fatal if swallowed).

Enzymes. Proteases and amylases are included to break down proteins and starches present into short chain polymer fragments of amino acids and sugars, respectively.

Phosphates. These bind Ca^{2+} and Mg^{2+} ions present in hard water, preventing surfactant inhibition and limescale formation.

Bleach. Oxygen or chlorine based additives which break down organic soils using radical reactions as well as sterilizing dishware.

Anti-corrosion agents. Sodium silicate ($\text{Na}_{2x}\text{SiO}_{2+x}$) is used to control corrosion by forming a sacrificial layer on metal surfaces.

Other common additives include; anti-foaming agents, chelants, perfumes, anti-caking agents, glaze protectors, starches, gelling agents and sand (as a bulking agent).

As the complexity of the cleaning formulation increases, there is an increase in the risk of product contamination from the cleaning agents themselves. A cleaning protocol is therefore usually a multi-stage process, typically consisting of;

- (i) Pre-clean – this removes excess food waste by mechanical action (fluid flow forces).
- (ii) Main clean - loosen surface waste and grease using a detergent formulation.
- (iii) Rinse - remove loose food waste, grease and detergent.
- (iv) Disinfection - kill any bacteria with disinfectant or heat.
- (v) Final rinse - remove the disinfectant.
- (vi) Drying - remove all moisture.

In a food processing plant factors such as the product composition, processing equipment design, the water supply, and the cleaning regimen influence the type and rate of soil deposition and therefore its removal (Kulkarni *et al.*, 1975). Tailoring cleaning solutions to soil type therefore requires an understanding of the interactions (chemical and physical) involved.

1.2 Soil removal modes

The mechanism via which a soil is removed from the surface is primarily dependent upon the balance between its adhesion to the surface and its internal cohesion. The environment it is immersed in will affect the strength and balance of both the soil adhesion and its cohesion (e.g. its wettability to the surface and/or its solubility in solution).

In this work the cleaning of the soil is first classified as involving adhesive or cohesive removal. In adhesive removal the soil is removed via the breakage of bonds between the soil and the substrate. The internal structure of the soil may remain intact. In cohesive removal the soil is removed piecewise through disruption of its intramolecular bonds until none remains on the surface. Within each of these categories lie multiple mechanisms by which these bonds are disrupted. The four most relevant

mechanisms of cleaning to the removal of food soils by aqueous solutions are shown in Figure 1.5 and described hence:

- (a) **Dissolution:** The soil is soluble in the cleaning solution. The cohesive interactions within the soil are less favourable than those with the solution. This mechanism is favoured by thermodynamic factors such as temperature, pH and solvent nature.
- (b) **Erosion.** The cohesive interactions within the soil are weaker than its adhesion to the substrate. Cleaning occurs via shear forces at the interface removing material. This mechanism can be promoted by agents that weaken the soil.
- (c) **Roll-up:** The cohesion within the soil is strong and the soil is insoluble in the cleaning solution. The soil is deformed by fluid flow and/or buoyancy forces, causing it to leave the substrate. Roll-up can be enhanced by surfactants.
- (d) **Peeling:** The adhesion of the soil to the substrate is weaker than cohesive interactions within the soil. The soil detaches as a coherent layer. This mechanism is promoted by surfactant ingress to the soil -substrate interface.

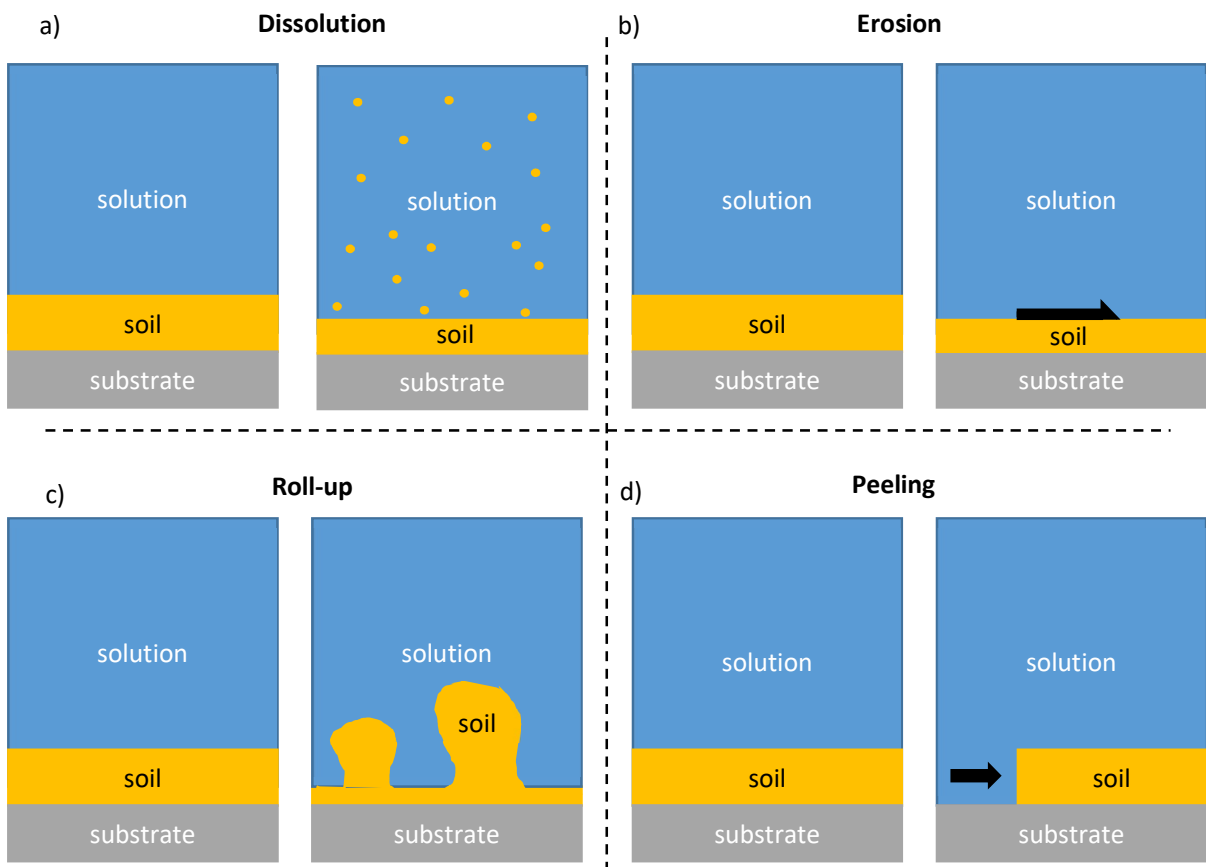


Figure 1.5: Soil removal modes in cleaning by submersion in solution. Reproduced from Bhagat et al., 2017

1.3 Factors effecting cleaning.

The soil-substrate-solution system can be optimised for cleaning through manipulation of its environment. This is summarised by Sinner's Circle (Figure 1.6) (Sinner, 1959). Sinner's concept describes cleaning as being a balance of four major factors;

- (i) the time the soil has spent in contact with the cleaning solution;
- (ii) the temperature of the cleaning solution;
- (iii) the concentration of chemical reagents in the cleaning solution;
- (iv) the mechanical forces applied to the soil.

Each of the first three factors affect how much force is needed to remove the soil from the substrate via manipulation of the cleaning solution. These factors will influence the mechanism by which cleaning will occur. Likewise determining the impact of cleaning agents on the balance of these forces provides insight into the cleaning mechanism(s) and thus informs the development of more effective cleaning regimes (Asteriadou, 2009).

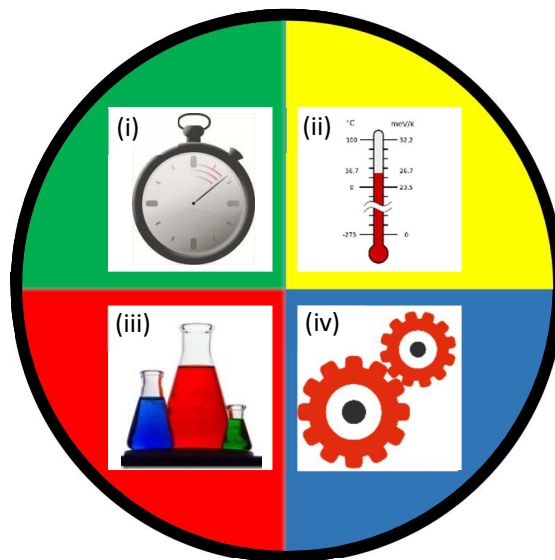


Figure 1.6: Sinner's circle, depicting cleaning as a function of (i) time, (ii) temperature, (iii) mechanical action and (iv) chemical reagents.

An additional challenge to consider in the development of effective cleaning regimes is the volume of fresh water required. For example, in dairy processing, build-up of foulants on pasteurisation and sterilisation heat exchanger surfaces demands such extensive cleaning that for each gallon of milk produced up to five gallons of fresh water is used to clean the processing equipment (Alvarez *et al.*, 2010). This incurs significant expense to the manufacturer as the water must then be treated before

re-use or disposal. The use of high volumes of water for cleaning can also create a strain on local fresh water sources (Innovation Centre for U.S. Dairy, 2012)

A complementary method of reducing waste water streams is through reduction of household water consumption. This includes water consumed by dishwashers, clothes washing machines and bathing facilities.

Contemporary dishwashers are at the forefront of domestic ‘green’ household design with units rated at A+++ (e.g. Gorenje, GV66260UK), (Figure 1.7). Optimisation of the water cycling system has reduced the water use per cycle from 200 L min⁻¹ to under 12.1 L cycle⁻¹ (Rosa *et al.* 2012, Table 1.2).

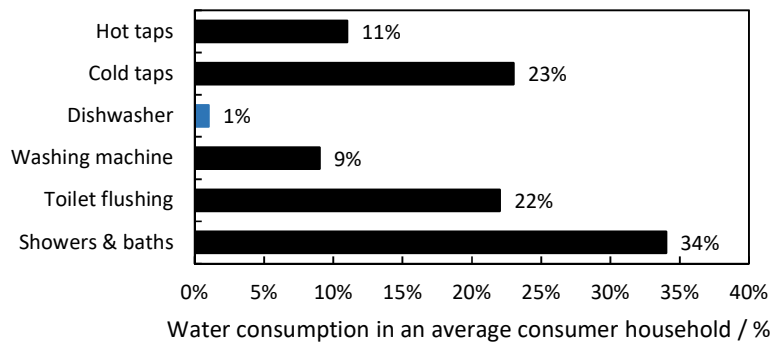


Figure 1.7: Water consumption per consumer household in 2018. Produced from data from the Office for National Statistics (UK) 2019.

Table 1.2: Evolution of motor consumption in automatic dishwashers, 1950-1994 data from Rosa *et al.* 2012. 1994-current: Energy Star Ratings Requirements (2019)

Year	Flow [*L/min][[□] L/cycle]	Power [*W]	Energy per cycle [kWh]
1950	200 *	600/700	-
1980	120 *	110	-
<1994	38 [□]	-	1.27
1994-2016	19 [□]	-	0.64
2016 – current	<12.1 [□]	-	0.38

One method of maintaining performance standards at this low water usage is through advances in cleaning effectiveness through optimisation of the cleaning solution. This led to the development of combinations of cleaning agents in detergent formulations, i.e. a collection of cleaning agents in the form of a powder or a liquid for removing dirt from clothes, dishes, etc. that is added to the dishwasher as a separate product. This detergent enables the dishwasher to clean more quickly and impart dishes with ‘shine’ (Rosen and Kunjappu, 2012; Showell, 2005).

This PhD will focus primarily on automatic dishwashers and the challenges involved in the effort to maintain cleaning performance whilst reducing water and energy use.

1.4 The automatic dishwasher

At the consumer scale, fouling occurs during heat transfer operations including cooking, baking, and frying as well as other techniques used to heat food for safe and enjoyable consumption. The cleaning of fouling deposits from domestic cooking surfaces is of considerable interest to consumers and cleaning product manufacturers (such as Henkel®, Procter and Gamble® and Unilever®) alike. Effective cleaning of dishware both increases the lifetime of the dish and ensures safe hygiene practices, by reducing the risk of food poisoning from the build-up of bacteria on a soiled surface (Pérez-Mohedano *et al.*, 2015).

As dishwashers become more widely available, competition has grown, forcing manufacturers to raise expectations of what the machine can achieve. For example, advertisements boasting of the best 'shine' led to wide-spread use of rinse-aids i.e. chemicals which exploit Marangoni flow phenomena to prevent droplet formation on glassware, reducing the visible 'spotting' caused by lime-scale present in hard water.

The increasing complexity of dishwasher design provides detergent manufacturers with unique challenges when determining the mechanisms by which their systems function. Specific to this thesis, it can be difficult to determine the cause of a failure in the cleaning of food soils.

The work conducted in this project will be conducted on two soils, a relatively simple model soil and a complex multi-component food-based soil.

1. Simple; lard (Sainsbury's Basics®). Lard is mixture of triglycerides of chemical formula $\text{RCO}_2\text{CH}_2\text{CH}(\text{O}_2\text{CR}')\text{CH}_2\text{CO}_2$ where R and R' have formula C_nH_m ($n=12-22$, $m=26-46$). This was the hydrophobic soil studied by Ali (PhD, 2015(a)) and as such allows comparison with prior work.
2. Complex; Complex Model Soil (CMS). This soil was developed in discussion with the project sponsor and is considered to be representative of difficult-to-clean household soils. It is based on a commercial macaroni and cheese mix (Kraft® macaroni and cheese) and contains triglycerides, proteins, starches and sugars, preservatives, colourants and water. The composition and preparation protocol is described in Chapter 3.

1.5 Scope of the dissertation

Sinner's cleaning circle relates how the temperature and chemical composition of a solution, in combination with imposed mechanical forces, can be used to minimise the time taken to clean and/or decontaminate a surface. A combination of techniques is used in this work to monitor how time in contact with a cleaning solution, of fixed temperature and chemistry, affect the mechanical forces required to remove soil from substrate, whilst simultaneously monitoring the change in soil composition and macro-structure. Structural changes linked with more effective cleaning can then be targeted in subsequent experimental designs.

Determination of the behaviour of the surfactants, temperature and pH on two soils and substrates was split into four approaches; (i) monitoring the movement of the soil and surfactant on the microscale; (ii) studying the swelling and mass transport behaviour of the soils in solution; (iii) chemical analysis of the solution over time; and (iv) quantifying the forces required to remove the soil from the substrate. A schematic of the approach is shown in Figure 1.8.

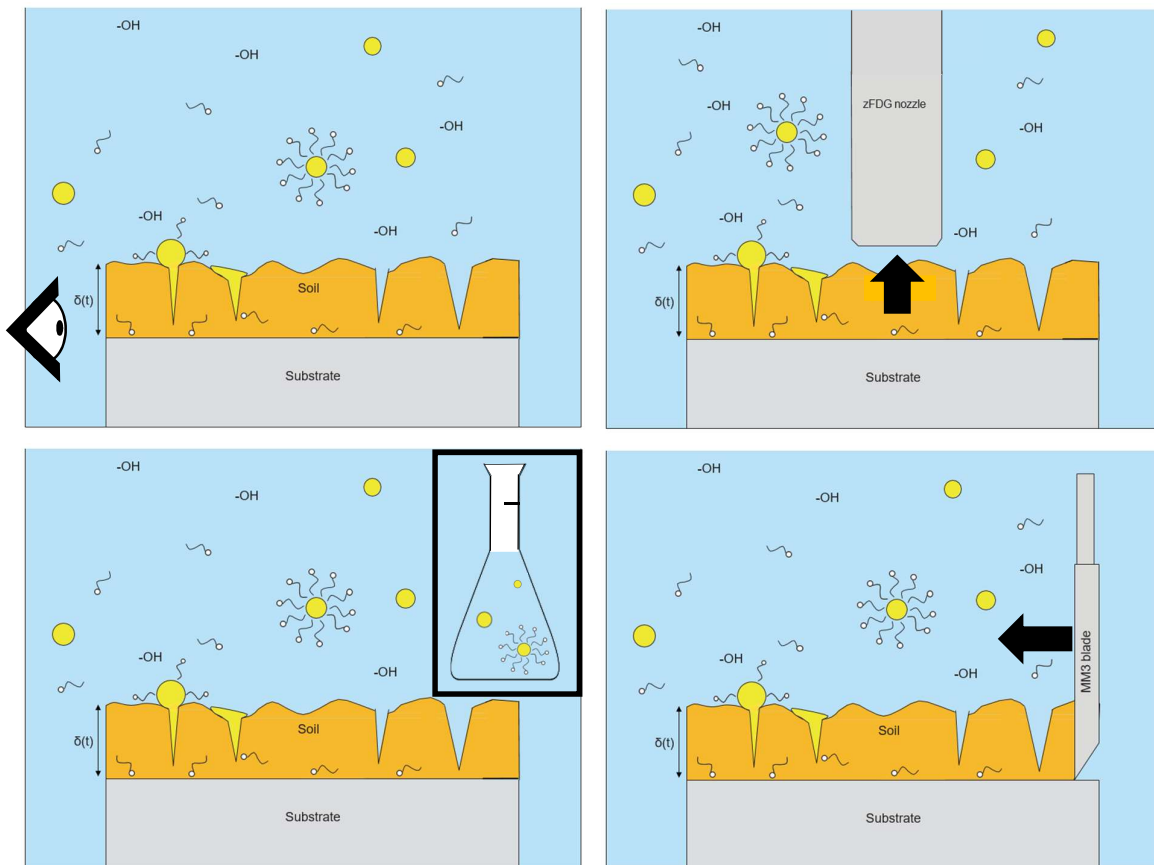


Figure 1.8: Approaches for studying the cleaning of soils on substrates in solutions. a) visual inspection of the interface, b) swelling of the soil, c) solution analysis, d) mechanical removal.

1.5.1 Conditions explored

Five aspects of the cleaning solution were investigated:

1. Temperature – this affects reactions, interactions and transport kinetics. It also impacted the soil viscosity and mobility, including inducing phase changes within the soil.
2. pH – this influences the reactions and interactions between the solution and the soil. It can also change the surface charge of the soil and/or substrate, altering the soil-substrate and substrate-solution interfacial tension.
3. Surfactant type and concentration – the impact of surfactant charge and efficiency on the interfacial forces, such as adhesion strength between the soil and substrate, is explored. Its impact on the capillarity of the soil was also considered.
4. Chelants – these alter the cleaning process via the binding of free ions, such as Ca^{2+} , common to food soils.
5. Bleach – sodium percarbonate was studied to determine the impact of oxidation reactions on cleaning.

1.5.2 Structure of the thesis

This thesis begins by introducing the field of cleaning of food soils and its relevance in both industrial processes and consumer products. Chapter 2 reviews the current knowledge on cleaning of generic food soils and the role of different components within the cleaning solution formulation, e.g. surfactants, on the removal of a model burnt food soil. The chapter concludes with a summary of the quantitative measurement techniques used to monitor the aforementioned cleaning rates and effectiveness.

Chapter 3 describes the substrate and soil materials used throughout this report as well as the method of soil layer generation and cleaning solution formulation.

Chapter 4 is about a 'simple' difficult-to-remove soil, baked lard, following the work of Ali (2015(a)). Confocal laser scanning fluorescence microscopy is used to investigate the mechanisms of surfactant penetration and ingress into a soil layer. It concludes with the introduction of complex model soil layers and their behaviour in cleaning solutions.

Chapter 5 explores the swelling of food soils on submersion in cleaning solutions and introduces modifications of current thickness measurement techniques to access early timescale hydration kinetics of soil swelling. The fluid dynamic gauging technique is also compared with a light based technique for measurement of thickness of submerged layers.

Chapter 6 explores the mechanisms and cleaning rates of heterogeneous soils via analysis of the cleaning solution over time, under both static and flowing solution conditions. Image analysis of the soil layer itself was also conducted and models developed to describe the kinetics of soil loss and mechanisms of cleaning action.

Chapter 7 investigates the impact of different substrates and cleaning solutions on the adhesive and cohesive forces in the soil-substrate system. This chapter also describes the development of a flowing solution system and its integration into the measurement device that allows *in situ* measurement of cleaning action over time.

Chapter 8 brings together the findings from chapters 4 to 7 and discusses the timescales involved in cleaning. The influence of factors such as temperature, pH and surfactancy on the stages of cleaning are discussed.

Chapter 9 demonstrates the applicability of the techniques used throughout the thesis to commercial cleaning formulations. Additional testing equipment provided by the project sponsors was investigated within this chapter to determine if similar phenomena to those described in chapters 4 to 7 were observed.

Chapter 10 concludes the thesis, summarising key developments made in the understanding of cleaning of complex food soils under different cleaning conditions. This chapter concludes by offering some closing thoughts and recommendations for further work in this area.

The author co-supervised two student projects in connection to this work. The first was an MPhil Advanced Chemical Engineering (ACE) masters project conducted by Nathan Ravoisin, in which the image analysis technique and processing code, described in Chapter 6, was developed. The second was a summer student project which investigated the synthesis of novel fluorescent surfactants for studying surfactant transport using the two photon microscope at Soochow University, China. The author spent three months at Soochow in the autumn of 2017 but the equipment developed a fault early in the visit and could not be used.

2. Background and literature review

This chapter describes the current level of knowledge in the scientific literature on the topic of cleaning of domestic food soils. It is organised into three sections; the composition of soils and substrates; the removal of soils from substrates; and techniques used to quantify cleaning rates and effectiveness over time.

2.1. Soils and Substrates

2.1.1 Soil types

In food processing operations, such as domestic cooking, soils originate from the ingredients used in the preparation of the product. Common soils include;

2.1.1.1 Fats, oils and greases

These materials (generic form shown in Figure 2.1 consist of triglycerides of fatty acids of varying chain length and saturation level. The phase behaviour of the triglyceride molecule at room temperature and pressure determines the category in which it is classed; fats take the form of waxy solids, oils are liquid, and greases can consist of either fats or oils that contain high concentrations of free fatty acids, or other solids, after having experienced thermal degradation (Komastu *et al.* 2010).

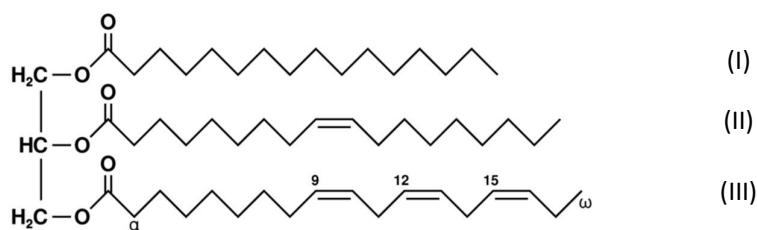


Figure 2.1: Chemical structure of a typical fat molecule with (I) saturated, (II) mono-unsaturated, and (III) poly-unsaturated hydrocarbon chains.

Triglycerides are characterised by their hydrophobicity, typically exhibiting little to no solubility in water (and similar polar solvents) in the absence of strong surfactants. However, the presence of multiple ester groups within close spatial proximity, in combination with only one non-polar hydrocarbon chain, such as in glycerol mono-oleate, impart fat derivatives with the mildly amphiphilic characteristics in non-polar solvents typically found in surfactant chemistry (Biresaw *et al.* 2002).

Triglyceride structures are commonly found in the field of formulation science tailored towards hydrocarbon-based solvents i.e. diesel oil additives (Calhoun and Hewitt, 1958). The chemisorption of triglycerides to stainless steel is advantageous in this case (Tkachuk *et al.* 1989). Triglycerides bind more strongly to metallic surfaces than their methyl ester counterparts due to a phenomenon similar to the chelate effect (Biresaw and Mittal, 2013). The triglycerides undergo chemical breakdown via

oxidation mechanisms under high temperature and/or shear conditions into fatty acids, characterised by the presence of a carboxylic acid functional group (Belinato *et al.* 2011). The more polar carboxylic acid group binds more strongly to the polar steel surface and provides a protective film, preventing corrosion and wear.

The presence of unsaturation in the hydrocarbon chain provides sites for oxidative polymerisation to occur, forming cross-linked polymeric products with increasing viscosity over time. This effect, whilst advantageous in the field of surface lubrication, however proves problematic with food fats in a domestic setting and their removal was studied by Akin Ali, working in the P⁴G group in CEB, on the project preceding this one (Ali, 2015(a)). The formation and cleaning of these fatty polymeric structures is discussed in more detail in Chapter 3.

2.1.1.2 Carbohydrates

Carbohydrates, i.e. starches and sugars, are biomolecules primarily consisting of carbon, hydrogen and oxygen with the chemical formula $C_m(H_2O)_n$, though some deviations from this formula are known (Figure 2.2). For natural carbohydrates, such as those found in food products, $m = n \geq 3$. Carbohydrates are classified based on the number of monomer units, known as monosaccharides, that make up the full structure; monosaccharides (1 unit), disaccharides (2 units), oligosaccharides (3-8 units) and polysaccharides (≥ 9 units) (Flitsch and Ulijh 2003). Each monosaccharide unit has multiple reactive functional groups, allowing combinations to form via glycoside linkages into a variety of linear and branched structures.

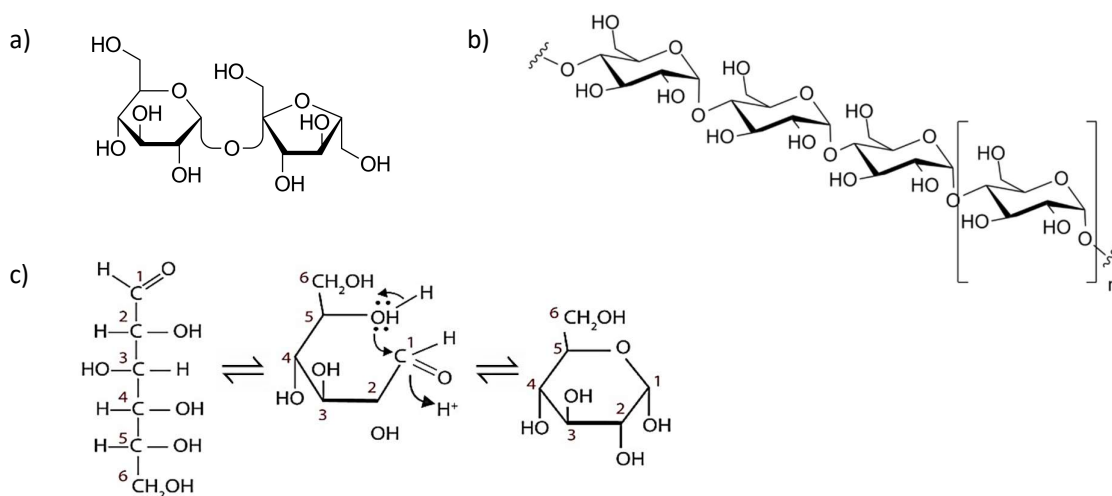


Figure 2.2: Chemical structure of a typical (a) sugar dimer; (b) polysaccharide carbohydrate; and (c) the conversion of a linear to a cyclic sugar monomer.

Low molecular weight fractions of carbohydrates, such as the mono- and di- saccharides, are classed as ‘sugars’ and take the form $C_6H_{12}O_6$ or $C_{12}H_{22}O_{11}$. These are typically depicted in their cyclised ring

form. They exist in equilibrium in aqueous solutions with the straight chain form via a reversible reaction with a hydroxyl group on a different carbon atom (Figure 2.2(c)).

The cyclised form of sugars undergo condensation reactions to form polysaccharides. The most prevalent polysaccharides in food structures serve two functions; energy storage (e.g. starch in plants, glycogen in mammals) or structural integrity (e.g. cellulose) (Ball *et al.*, 2011). The form of interest in this work is the carbohydrate polymer known as starch, commonly found in edible foodstuffs, and its behaviour once cooked (gelatinised) and subsequently contacted with aqueous cleaning solutions.

Many studies have been conducted into the behaviour of the starch bio-polymer in solution. For instance, Capuano (2017) demonstrated that the macrostructure of a specifically synthesised anionic starch polymer depends on the solution pH and ionic strength. As the ionic strength increases the electrical charges on the polymer are shielded. This causes the polymer to take on a globular structure which is more compact. However, in low ionic strength solutions those negatively charged anionic groups repel one another causing the polymer to form a linear structure (Figure 2.2 (c)). These extended polymer chains produce more viscous solutions due to a higher degree of chain entanglement under shear. It would be expected that the macrostructure of a starch molecule will influence its overall cleaning behaviour.

2.1.1.3 Proteins

Proteins are bio-macromolecules consisting of long chains of amino acid monomers (Figure 2.3). These small monomers consist of a central carbon, attached to a carboxylic acid group, an amine, a hydrogen and a side chain (labelled R on Figure 2.3 (a)). It is the chemical nature of the side chain that determines the amino acid/protein type. Although there are over 500 identified natural amino acids, only 22 are found in biological organisms (Berman *et al.* 2000).

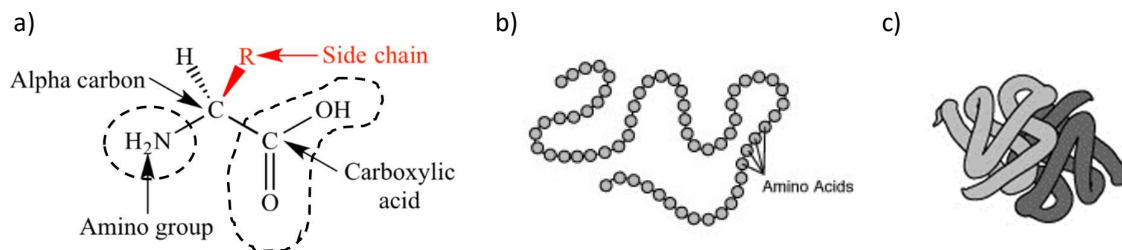


Figure 2.3: (a) Chemical structure of a typical amino acid, (b) primary protein structure made up of a sequence chain of amino acids, (c) quaternary structure of a protein consisting of more than one coiled amino acid chain. Tertiary structures (not shown) are a coiled amino acid chain and made up one unit of the structure shown in (c).

Peptide bonds, formed from a condensation reaction between carboxylic acid and amine groups on neighbouring molecules, connect these monomers into a linear chain polymer with formula masses

between 30 – 3000 kDa. The protein structure increases in complexity from those found in bacteria to those in humans (Jones, 2014). These long chains then combine and fold into sheets or helices to minimise the conformational energy of the spatial arrangement of side chains (Figure 2.3 (c)). These ‘secondary’ structures can then coil further (tertiary structures) and combine with adjacent protein chains (quaternary structures) (Wagner and Musso, 1983).

Proteins have been the subject of significant attention in the cleaning and fouling literature due to their tendency to strongly adhere to a substrate after undergoing thermal denaturation (i.e. loss of their 3D structure and return to a linear chain state with exposed functional groups).

An important example of this is in dairy fouling. Milk is often subjected to heat treatment (either high temperature short time (HTST) or ultra-high temperature (UHT)) in order to ensure it is safe for human consumption. At HTST temperatures (>72 °C) the proteins uncoil and attach to the surfaces of the processing equipment (e.g. a heat exchanger), often entraining other materials such as sugars (lactose). At the higher temperatures of UHT (~95 °C) calcium dominated fouling is encountered (Hagsten, 2016). The build-up of proteinaceous foulants reduces the thermal performance of the heat exchangers and decreases overall effectiveness (and hygiene) of the system (Wilson, 2018).

A commonly observable example of this process occurs when heating milk to create a Béchamel sauce or hot chocolate. A layer of milk ‘scum’ will form at the interface between the liquid and the heating pan. This layer is formed when the proteins within the milk denature and combine with minerals and fat molecules at the surface (fats are hydrophobic and so will typically adsorb and then build up at the solid-solution interface to minimise interactions with the aqueous environment) (Srilakshmi, 2003). Analogues of this process occur in all high temperature preparations of food and as such the cleaning of heat-treated proteins remains a topic of significant interest to those researching the cleaning of heated foodstuffs.

2.1.1.4 Fibres

The term fibre refers to a thread or filament from which a vegetable tissue, mineral substance, or textile is formed (Collins Dictionary, 2019). The most abundant fibre in mammals is collagen, an animal fibre consisting of three polypeptide chains wound around one another to form a fibrous protein (Shoulders and Raines, 2009). Collagen can be a significant factor in food based fouling layers due to its presence in meats and fish which are subjected to long cooking times at high temperatures causing thermal degradation of a fibre into its composite peptides.

In a similar vein, dietary fibres, defined as plant components with more than 10 monomeric units that are not broken down by human digestive enzymes, contribute to fouling (Codex Alimentaris

Commission, 2014; British Nutrition Foundation, 2018). These non-starch polysaccharides, such as cellulose, dextrin, pectin and chitin (Figure 2.4), are found throughout most edible plant structures. Chitin, the world's second most abundant natural polymer with a highly crystalline structure formed from sheets of linear-polysaccharide of β -(1-4)-2-acetamido-2-deoxy-D-glucose, has been shown to surround starch and protein molecules with crystals known as fibrin (Meyers *et al*, 2008). The fibrin then aggregates into randomly orientated networks forming a physical barrier around the starch and protein granules, reducing access for digestive, or targeted cleaning, enzymes (Brennan *et al*. 1996).

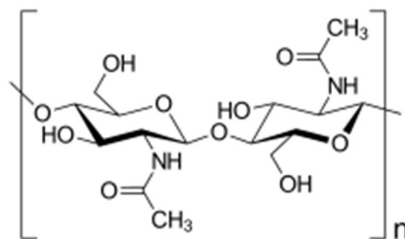


Figure 2.4: Chemical structure of chitin.

The highly ordered structure of dietary fibres leads to low solubility in most solvents, including water. Instead, the polar nature of the fibre strands attract water to form a viscous gelatinous structure. This too can shield components from enzymes designed to break them down into soluble components, and therefore could inhibit cleaning (Gropper *et al*. 2008).

Due to their similar structures, fibres also have been shown to be highly sensitive to solution pH and ionic strength (Capuano, 2017). However, in addition to their ability to alter their macroscale form, it has been shown that, even at low concentrations of fibres such as pectin, mixtures of whey proteins and fibres at pH lower than the isoelectric point of the protein can form gel networks due to strong electrostatic interactions between the anionic polysaccharides and cationic functional groups on the proteins (Zhang *et al*. 2014). These complex structures formed of fibres, proteins, and, following a logical comparison between the functional group similarities of fibres and starches, carbohydrates, are likely to inform upon the complex structure of food foulant layers developed in a domestic kitchen.

2.1.1.5 Salts

Water is commonly classified by the concentration of minerals contained within in it. As water falls to the ground as rain it is naturally soft, i.e. contains almost no minerals. When it comes into contact with the ground it may flow through 'soft' rocks such as limestone or chalk and will dissolve minerals containing calcium or magnesium along the way to a reservoir or collection point. When these minerals are dissolved in water they form salts. Water containing > 180 ppm of dissolved minerals is classified as 'hard'. The prevalence of hard vs soft water depends on the geographic location of the water source. The south east of England is predominantly chalk, limestone and clay and as such has

naturally hard ground water; Scotland is made up of igneous rocks and therefore has naturally soft water (<60 ppm) (Sengupta, 2013).

The water used in the preparation of food soils is rarely deionised before use. In hard water areas multivalent cations such as Ca^{2+} , Mg^{2+} and their accompanying anions CO_3^{2-} , HCO_3^- , form part of the food soiling layer. The presence of these ions can impact the both the soil structure and its response to cleaning solutions. Salts such as calcium phosphate and calcium sulfate exhibit inverse or retrograde solubility; i.e. as the solution temperature increases their solubility decreases. This is what causes the deposition of scale, such as calcium and magnesium carbonate lime-scale, on heat transfer surfaces when they precipitate after their solubility has been exceeded because of increased temperature (Koutsoukos, 2007). Calcium phosphate deposition is routinely observed during high temperature milk processing (Hagsten, 2016).

In sufficiently hard water solutions (>150 ppm) the cations inhibit the ability of the surfactant to form a lather through preferential reaction with the functional head group to form a solid precipitate (commonly known as soap scum) (Borghetty, 1950). An example is sodium stearate surfactant in the presence of Ca^{2+} .



Cambridge water has a total hardness of 297 mg L^{-1} CaCO_3 and is rated at 'hard to very hard (200+ mg L^{-1})' (Cambridge Water Company, 2019).

Table salt (NaCl) and salt based preservatives are commonly used in the preparation of meals and precooked food products, such as when boiling pasta, and will affect the ionic content of the deposit. This affects the cleaning solution and swelling behaviour of the soil undergoing cleaning.

2.1.2 Baking and drying

The properties of the soil to be cleaned are determined both by its composition and its processing history, particularly its thermal history. Thermal transformation is widely used in food processing (e.g. baking, drying, frying ...) and exposure to high temperatures, often in humid environments, promotes evaporation, shrinkage, free radical polymerisation, condensation polymerisation and thermal decomposition. These structural changes encourage closer packing which increases the cohesive forces in most soils (Stanga, 2010).

Soil drying often results in an increase in soil adhesion. Dramatic increases in both the cohesive and adhesive strength of starch soils following water loss were reported in ultrasound cleaning studies by Stanga (2010) and dynamic mechanical analysis measurements by Jonhed *et al.* (2008). Surface energy studies by Otto *et al.* (2016) demonstrated that whilst starch underwent structural changes during

heating to 90 °C for one hour, whey and soy proteins exhibited a significantly larger response. Protein denaturation caused by heating for an hour at temperatures above 55 °C caused internal hydrophobic structures to become exposed, accompanied by a large shift in the measured Lifshitz-van der Waals component of surface energy. Baking surfaces such as stainless steel typically exhibit strong wetting and adhesion to these denatured soils. The additional exposure of internal binding groups such as sulfhydryl allows disulphide bridges to form on drying, forming denser, more cohesive soils on the substrate (Castner and Ratner, 2002).

In some cases the high cohesive strength of the proteinaceous soil overcomes the adhesion to the substrate, causing the soil to curl and detach upon drying. This was evident on surfaces coated to minimise soiling, such as fluorocarbon coatings (Magens *et al.*, 2017).

As the complexity of the soil increases so does the complexity of the reactions occurring on heating. The chemical reactions that occur between reducing sugars, proteins (and subsequently, oxidised lipids) were first studied in depth by Louis-Camille Maillard in 1912 in his studies of biological protein synthesis (Maillard, 1912). Carbonyl groups contained in reducing sugars reacted with amino groups (most commonly the ϵ -amino group of lysine, Martins *et al.*, 2001) on amino acids or proteins to form a complex mixture of small molecules. If continuously exposed to high temperatures these would then undergo extensive 'Maillard' reactions to form a polymeric network of sugars and proteins (and, as discovered by Friedman in 1996, oxidised lipids (Friedman 1996)). This process is described in the baking industry as 'browning'.

Maillard products were subsequently the topic of considerable interest in the food processing industry as the degree to which they occur, and how the resultant polymeric structures, impart a distinctive flavour to the food (Wang *et al.* 2011). Common products that utilise controlled Maillard reactions include: the roasting of coffee beans (Liu and Kitts, 2011); the baking of breads and cakes (Conforti, 2014); and the cooking of meats (Martins *et al.* 2001). In 1953, 41 years after the initial discovery of these reactions, John Hodge published the first attempt to describe the reaction pathway network, starting from glucose sugars to the complex polymeric structures generated as a result of baking (Hodge, 1953). This pathway, with some minor alterations, is the one still used today to identify conditions to produce the desired products. An updated and adapted reaction pathway was produced by Martins *et al.* (2001).

The chemical reactions that occur during baking of foodstuffs are complex and influenced by a range of factors such as the ratio of reducing sugars to amino groups (Martins *et al.*, 2005), the pH and moisture content of the immediate environment (Martins *et al.*, 2005), the temperature of the baking (Benzing-Purdie *et al.*, 1985), and the presence of oxidizable lipids (Karel, 1973). However regardless

of pathway, the final reaction products all fall under the umbrella term of 'melanoidins'. These complex (co-)polymers are characterised by their appearance (solid, brown), their high molecular weight (100-300k+ Daltons, Brudzynski and Miotto, 2011), their structural complexity (high degree of cross-linking between polymer strands often with proteins acting as bridging species, Pellegrino *et al.*, 1999) and their composition (furan-rings, nitrogenous, hydroxyl functionality, Martins *et al.*, 2001).

Attempts to categorize types of melanoidins further have been made over the past century of study but, no one method of classification has been agreed. This is partially due to the fact that the functionality of interest varies between studies, and partially as no full characterization of melanoidin molecular structures has yet been achieved. For the purpose of this thesis the simple division proposed by Nikami (1988) will be used:

- Early fractions – water soluble, low molecular weight molecules, light in colour and formed after short exposure to thermal radiation, and;
- Advanced fractions – water insoluble, high molecular weight molecules, typically darker in colour which require longer periods of exposure to thermal radiation.

Early fractions play a vital role in the eventual binding of the melanoidins to metallic substrates. Johnson *et al.* (1983) demonstrated that some melanoidins demonstrate metal chelating ability, particularly to Zn, Fe and Cu, which they attributed to reductone moieties. Nikami later demonstrated that Amadori rearrangement products (see Martins *et al.*, 2001) can cyclise, resulting in coloured products such as maltol or 4-hydroxy-2,5-dimethyl-1,3-(2H)-furanone which will readily chelate with metal ions, in particular iron (Nikami 1988). Further reactions can then take place subsequent to metallic binding.

The advanced fractions are of particular interest in cleaning as the most common consumer cleaning solvent in the food sector is water. The high molecular weight of the advanced fraction demonstrates stronger adsorption to hydrophobic surfaces than low molecular weight polymers due to van der Waals interactions between the furan/ester/amine groups and polar surfaces (Rabe *et al.*, 2011).

2.1.3 Commonly studied substrates

The choice of surface in the study of fouling and cleaning of food processing is guided by consumer and industrial use. Stainless steel is the standard material of construction in industrial manufacturing due to its high tensile strength, strong corrosion resistance and capacity for steam sterilisation. This is reflected by the common use of stainless-steel cook pots and uncoated baking trays. Stainless steel is therefore the primary substrate material of choice for most academic studies (Table 2.1). For example,

Otto *et al.* (2016) utilised stainless steel substrates when cleaning of modified starch and protein residues.

Table 2.1: *Substrates employed in fouling and cleaning studies relevant to the cleaning of food-based soils.*

Substrate	Fouling studies	Cleaning studies
Stainless steel	Piepiorka-Stepuk <i>et al.</i> , 2016; Truong <i>et al.</i> , 2017; Challa <i>et al.</i> , 2015;	Liu <i>et al.</i> , 2006; Aziz, 2008; Detry, 2010; Ali, 2015(b, c); Michalski <i>et al.</i> , 1999; Cluett, 2001; Hooper <i>et al.</i> , 2006; Akhtar <i>et al.</i> , 2010; Goode <i>et al.</i> , 2010; Moeller, 2017;
Glass	Mercier-Bonin <i>et al.</i> , 2004; Gallardo-Moreno <i>et al.</i> , 2004; Dhadwar <i>et al.</i> , 2003;	Detry, 2010; Jurado-Almdea <i>et al.</i> , 2011; Jurado-Almdea <i>et al.</i> , 2012; Dunstan and Fletcher, 2014; Michalski <i>et al.</i> , 1999; Jensen <i>et al.</i> , 2007; Akhtar <i>et al.</i> , 2010;
PTFE¹	Huang and Goddard, 2015; Barish and Goddard, 2013;	Detry, 2010; Michalski <i>et al.</i> , 1999; Akhtar <i>et al.</i> , 2010; Magens <i>et al.</i> , 2019 (a,b);
DLC²	Boxler <i>et al.</i> 2014;	

¹PTFE – polytetrafluoroethylene

²DLC – diamond like carbon coated steel

A detailed review of the impact of the surface roughness of stainless steel on the adhesion of bacteria and spores to stainless steel surfaces of controlled roughness was conducted by Dürr (2007). He showed that there is a strong correlation between the surface roughness (R_z) and (i) the adhesion strength of soil to substrate ($R^2 = 0.76$) and (ii) the cleanability of the soil ($R^2 = 0.89$). Bobe *et al.* (2007) pointed out that measures of roughness such as R_q provide no information about the ‘structure’ of the roughness elements, *e.g.* spherical vs cylindrical vs conical, which play an important role in adhesion. Quantifying roughness and relating it to adhesion forces continues to be an active topic of investigation, promoted by the advent of nano-fabrication and tailoring of surfaces (LaMarche 2017).

Surface treatment of stainless steel can be used to mitigate or reduce fouling. Zhao *et al.* (2002) published a review of studies conducted on polytetrafluoroethylene-ethylene (PTFE) coatings, showing how it modified both the surface energy (major impact) and roughness (minor impact) of the stainless steel surface. This modification lowered the adhesion strength of model foulant soils (simulated milk) and promoted cleaning over other prominent coating or alloyed surface candidates such as Diamond Like Carbon (DLC), Silica, SiOX, Excalibur® and Xylan® (Beuf *et al.* 2003).

Copper, due to its anti-microbial activity, is commonly used in industrial food and pharmaceutical manufacturing. In this case the benefits provided by the resistance of the surface to bacterial growth must be weighed against ease of cleaning. Copper is susceptible to corrosion damage from both acids and caustic soda, ruling out standard clean-in-place (CIP) protocols (Airey and Verran 2007).

Visualisation techniques are frequently used to monitor the cleaning of food soils. These techniques frequently require that the substrate used is transparent to light to obtain the most accurate results,

particularly when the soil is imaged from the back or underneath. Linderer and Wilbert (1994) used photometric determination to quantify the residual starch on glass substrates in their study of cleaning of cereal starches, investigating why these resist cleaning more strongly than potato or modified starches. Similarly, Joscelyne *et al.* (1994) utilised a glass fouling surface within a flow system in combination with confocal laser microscopy to visualise the transport of foulant materials under turbulent flow regimes.

Stainless steel was chosen as the primary substrate material for this study. Limited testing was also conducted on glass, glazed ceramic and copper substrates.

2.2. The removal of soils from substrates

The primary cleaning mechanism is determined by the composition and structure of both the soil and the substrate to which it is adhered (Fryer and Asteridou, 2009). Emulsification dominates in oil-based soil systems. This often requires long soaking times in surfactant-rich solutions (Dunster and Fletcher, 2014) which are known to promote the detachment and emulsification of mobile soils from the soil-solution interface (Ali, 2015(a)). For more complex soil systems, e.g. involving starches and/or proteins, the cleaning mechanisms are not as well understood. Disruption of intermolecular Lifshitz – van der Waals, ionic and electrostatic forces can be achieved through multiple mechanisms, dependent upon the environment. For starch and protein based soils at low pH, hydration-induced swelling, coupled with chemical or enzymatic breakdown and dispersion, dominates. As the pH increases soil hydrolysis and solubilisation play a more important role.

2.2.1 Cleaning of single component soils

Significant advances have been made in understanding the cleaning mechanisms of single-component food soils over the past 20 years. Systems studied include whey protein isolate gels, milk deposits generated during high temperature pasteurisation and elevated temperature processing, mixtures of commercially available cooking oils, and potato starch. The cleaning mechanism is dictated by the composition and structure of the soil and these listed all differed noticeably.

The baked wheat starches studied by Din and Bird (1996) were cleaned via enzymatic breakdown of the starch polymers into dextrans, oligosaccharides and sugars, each of which are more soluble in water than the parent molecule (Pongsawasdi and Murakami, 2010). Jurado Almeda *et al.* (2015) found that surfactants such as linear alkyl sulphonate (LAS) had little impact on the rate and extent of cleaning of dried starch residues on stainless steel fibres. In the absence of amylases, high pH and long soaking times were required for cleaning regardless of surfactant concentration. Sinner's circle emphasises the effect of temperature on cleaning rates and effectiveness, and heated aqueous solutions (raised from 30 to 60 °C) out-performed all other factors that had significant effect at room temperature.

Many proteins form a gel upon contact with alkali which is steadily eroded by a mechanism which is diffusion limited (Fryer and Asteriadou, 2009; Morison, 2002). Studies have shown that erosion of whey protein deposits can be enhanced by pulsed flows (Christian and Fryer, 2006). However whereas whey proteins swell, losing structural integrity, and erode in flowing alkali, egg proteins swelled but no soil mass loss was observed until a shear force was applied (Perez-Mohedano *et al.*, 2016). Ali *et al.* (2015(a)) found little swelling with burnt oil soils and removal was characterised by a cohesive blistering mechanism, indicating that the soil did not readily interact with the aqueous cleaning solution.

Oils have been found to be the most difficult of all common foodstuffs to clean (Detry *et al.*, 2007; Detry *et al.*, 2009; Palmisano *et al.*, 2011) owing to their inherent hydrophobicity and tendency to wet many substrates preferentially to water. Fat-based soils pose a particular challenge as most consumer detergents employ aqueous solutions. The cleaning agent must therefore be soluble (or can be dispersed) in water, yet preferentially adsorb on to the fatty soil surface, remove the soil from the substrate, and stabilise removed residues in the solution. Highly polymerised lipids such as those found in burnt oil soils have limited solubility in organic solutions and no recorded solubility in water (Ali *et al.* 2015(b)). High pH or long soaking times are often required, in combination with mechanical shear, to remove such soils from the substrate (Dunstan and Fletcher, 2014). Surfactants can promote detachment of mobile components at the soil-substrate interface (Ali *et al.*, 2015 (a,b)). A combination of saponification, mechanical cleaning and surfactant action will be required to clean burnt oil soils. The existing literature does not report a single mechanism as being entirely effective.

2.2.2 Cleaning of complex soils

Model food soils are often used in the study of cleaning mechanisms (see Table 2.2). These soils are chemically and structurally simpler than the real system and are therefore easier to study quantitatively. These simpler systems also support mathematical modelling from first principles. Soils generated from several components are tuneable, allowing the impact of different components on cleaning behaviour to be determined. However, model systems, by design, are simpler in nature than real foodstuffs. The mechanistic behaviour models generated for the model soils may not be directly applicable to complex food-based soils.

The author is currently unaware of any focussed research directed at the cleaning of melanoidins. Research into these compounds has been primarily focussed on identification, classification and control of the final product chemical distribution and not its removal from a substrate.

Other techniques promoting cleaning include the temporary modification of the substrate, such as adjusting the electrostatic charge of a stainless-steel surface (Mauermann *et al.*, 2009) or by the

application of a sacrificial layer between the soil and substrate. This technique, however, is not viable for consumer use (outside of the use of additional media such as aluminium foil on baking trays).

Michalski *et al.* (1999) used a novel adhesive measurement device involving placing a known amount of product at the top of a plate inclined at 10° to the vertical. A gate holding the product was opened and the product flowed down over the plate. The mass remaining on the solid surface after flow has stopped was measured and mathematically related to average adhesion of the soil to substrate. This adhesion was then correlated to the wetting characteristics of the soil. This technique worked well for simple edible oils, however, when complexity was increased even slightly, such as with Vaseline®, the model was no longer fit for use. By 1999, however, the model was refined to include the soil's rheological behaviour, as well as an acid-base interaction parameter, and was now applicable to soils of a significantly more complex nature, such as salad dressing. The impact of PTFE coatings was also explored and, as expected, gave low adhesion between the soil and substrate.

More recently Challa *et al.* (2015) studied the fouling characteristics of model carbohydrate mixtures, including multiphase materials containing corn syrup solids. Their adhesive strength on stainless steel after submersion in water at 75 °C was studied. Here the shorter chain length, multiphase mixture showed reduced fouling over the longer chain length starch polymers. The long chain length materials formed soiling layers with strong adhesion characteristics and resisted cleaning by aqueous clean-in-place (CIP) systems (no NaOH was used in the experiment). Cooked durum wheat starch is present in the soil studied in this thesis and so high adhesion strengths are anticipated.

Table 2.2: Summary of cleaning studies relevant to the cleaning of food based soils

Soil	Type	Substrate	Cleaning agent	Reference
Baked whey protein	simple	stainless steel	water	Liu <i>et al.</i> , 2006
Egg albumen	simple	stainless steel	alkali	Aziz, 2008
Edible oils	simple	stainless steel, glass, PTFE	surfactants	Detry <i>et al.</i> , 2010
Gelatinised maize starch	simple	borosilicate glass	enzymes	Jurado-Almdea <i>et al.</i> , 2011
Unbaked lard	simple	borosilicate glass	ozonation	Jurado-Almdea <i>et al.</i> , 2012
Thermally aged triacylglycerides	simple	glass	surfactants	Dunstan and Fletcher, 2014
Baked lard	simple	stainless steel	surfactants	Ali, 2015 (a)
Model salad dressing	complex	stainless steel, glass, PTFE	mechanical forces	Michalski <i>et al.</i> , 1999
Beer / brewers yeast	complex	stainless steel	alkali, water, acid	Cluett, 2001
Baked tomato paste	complex	stainless steel	water	Hooper <i>et al.</i> , 2006
Mustard	complex	glass	alkali	Jensen <i>et al.</i> , 2007
Turkish delight, caramel, sweetened condensed milk	complex	glass, stainless steel, PTFE	mechanical forces	Akhtar <i>et al.</i> , 2010
Yeast	complex	stainless steel	alkali	Goode <i>et al.</i> , 2010
Mixes of starches, glucose and corn syrup solids	complex	stainless steel	water	Challa <i>et al.</i> , 2015
Wheat dough	complex	stainless steel	mechanical forces	Moeller and Nirschl, 2017
Raw milk	complex	fluorocarbon coated steel	alkali	Magens <i>et al.</i> , 2019 (a)

2.2.3 Chemical cleaning agents

Much research has been conducted on optimisation of chemical cleaning agents for specific soil-substrate systems. This can be categorised into two forms:

1. Mechanistic understanding of the behaviour of chemical additives associated with cleaning or solubilisation of materials.
2. High throughput iterative testing of known materials to determine cleaning formulation effectiveness in real world conditions. This empirical approach often involves design of experiment (DOE) investigations analysed by response surface modelling techniques which explore the relationships between several explanatory variables and one or more response variables.

A combination of these methods is usually required to optimise a formulation for cleaning a particular type of soil. Progress into the mechanistic understanding of cleaning agents can be used to define an effective 'starting' formulation to use in iterative testing or identify key parameters to be investigated.

A brief summary of current mechanistic understanding of cleaning of food soils follows. In addition to surfactants, high pH or long soaking times are often required, in combination with mechanical shear, to remove soils from the substrate (Dunstan and Fletcher, 2014). This is attributed to the base contributing to breakdown of the fatty components via conversion of the triglyceride into a soap-type structure (and glycerol) which renders them water soluble (saponification) (Sparks, 1999). It is likely that a combination of saponification, mechanical cleaning and surfactant action will be required to remove burnt soils as the existing literature does not report a single mechanism being entirely effective. Bourne and Jennings (1963) stated, "The mechanism of detergent action in soil removal has been attributed by different research workers to many factors, including surface tension, interfacial tension, contact angle, surface viscosity, lather, electrostatic properties, solubilisation, adsorption, cryoscopy, wetting, suspending action, emulsification, saponification and lubrication."

2.2.4 Formulating detergent systems

Detry *et al.* (2007) demonstrated a beneficial impact of a commercial detergent mixture containing 5 wt.% LAS-type surfactants along with 5-15% unidentified non-ionic surfactants in cleaning simple systems of oil splashed on a range of substrate materials. They demonstrated that the surfactants, combined with high shear stresses, enhanced the removal of oil from stainless steel substrates in aqueous solutions over pure water. The type, and wettability, of the surfaces investigated determined the efficacy of the surfactant in similar shear environments. On glass the surfactant removed the oil almost immediately upon immersion, however on PTFE there was a 5-10 minute delay before detergent action was observed. The authors attributed this delay to the surfactant's migration to, and alteration of, the oil-substrate interface. This could suggest either an emulsification or a roll-up mechanism as the surfactant acts at the oil-substrate interface to minimise the interfacial tension between the two substances and ultimately to detach the oil into the bulk cleaning solution.

The dominant cleaning mechanism in any given system is ultimately determined by the nature and microstructure of the soil. For example, Ali *et al.* (2015(a)) studied the cleaning of polymerised lard soil layers on stainless steel and reported that solutions of non-ionic TX-100 and anionic LAS at pH 10.4-11 promoted solution ingress and soil detachment at the soil-substrate interface, while the cationic surfactant promoted penetration through the soil layer. These differences illustrate how detergent solutions, like coatings to prevent deposition and fouling, need to be matched to the soil. It is not, however, practical in most applications to formulate a specific detergent formulation for each

individual soil-substrate combination in domestic applications. The consequence of this is that formulations have evolved from simple alkaline surfactant solutions to formulations that take a broad spectrum approach, containing combinations of phosphates, bleaches, surfactants, alkaline salts, enzymes, anti-corrosion agents, anti-foamants, perfumes and, dependent upon the detergent's physical form, gelling agents (liquid tabs), anti-caking agents (granular form), or starches (tablet form).

2.3. Cleaning techniques

2.3.1 Quantification of cleaning

Many studies have been conducted to measure the rate of cleaning of different soil layers in a range of environments. Common factors measured during cleaning testing include; the time taken to clean a soil with water jets of a given size, shape, and geometry (Wilson *et al.* 2014, 2015, Chee *et al.* 2019); the concentration and temperature of a surfactant solution required to remove a soil from a substrate (Dunstan and Fletcher, 2014); and the strength of the mechanical forces required to remove the soil (Wongsirichot, 2014). More unconventional cleaning methods have also been tested, such as ozonolysis (Jurado-Alameda *et al.* 2012), and the use of supersaturated solutions of water at high temperatures and pressures (150 °C, 5 bara, Kim and Kweon, 2009). These techniques, whilst they may provide insight into the mechanism of action of surfactants and soil behaviour during the cleaning process, are impractical for consumer use.

Methods of quantifying the cleaning effectiveness have included measurement of mass loss (Dunstan and Fletcher, 2014), measurement of the amount of solution, energy or time consumed before a visibly clean surface appears (Köhler *et al.* 2015); loss of film thickness via monitoring by, for example surface plasmonic resonance (Onaizi *et al.* 2009); and monitoring luminescence (Wilson *et al.* 2014).

Studies conducted by Ali (2015(a)) show that the cleaning of lipid-based fresh and burnt soils is the result of several complex interactions between the cleaning solution, the soil and the substrate. Subtle changes in factors such as substrate surface energy, surfactant ionic strength and/or concentration, thickness and hardness of the soil layer, caused significant changes in the forces required to clean the soil as the balance of cleaning mechanisms shifts from emulsification of fresh soils to the peeling of baked soils.

Measurement of the forces required to clean, *i.e.* detach elements of soil from a substrate in a given environment is currently investigated at three length scales: nano-, micro- and macro-scale.

Macroscale testing of cleaning performance is the most widespread approach as it supports empirical investigation and transfer of results to practice. Interpretation of the results in terms of cleaning mechanisms requires associated detailed analysis which is not always feasible. The Bath-Substrate-

Flow system employed by Jurado-Alameda *et al.* (2015) allows the effect of solution formulation to be studied but the flow regime in the cell is complex so the forces involved are not readily quantifiable. Cleaning-in-place systems are widely used to ensure the hygiene of food manufacturing plants, and scaled down systems have been used to investigate these, taking care to replicate or set flow conditions so that the results can be related to the full scale. Flow cells (*e.g.* Bishop, 1997; Detry *et al.* 2007; 2009) have also been used to study the impact of shear forces in cleaning by aqueous solutions.

At the other extreme, nano-scale investigations typically involve measuring the adhesive forces between well-defined elements of a test soil and a surface. Aktar *et al.* (2010) used an AFM cantilever to measure the energy required to remove caramel from stainless steel and recorded values in the range of 0.1 – 0.3 J m⁻². Bobe *et al.* (2007) reported similar values, of 0.21 – 1.3 J m⁻², for removal of yeast particles from stainless steel surfaces. These depended on particle size and distance of the tip from the soil. These techniques can provide valuable insight into the chemical and electrostatic forces active in soil-substrate binding, and in attachment of spores and bacteria (*e.g.* Lelièvre *et al.*, 2002).

Food soils tend to be multicomponent and micro-structured, subject to variations in topology, morphology and electrostatic environments across the substrate. Additional information on interactions is required for such systems and researchers have therefore tended to focus at the micro-scale. Moeller and Nirschl (2017) deposited approximately 1000 particles of starch-based soil onto a stainless-steel surface and measured the centrifugal force required to remove them. This allowed statistical treatment of the results from a test of reasonable duration. They found that the repeatability of the method was highly dependent upon the soil type and structure: the more complex the soil the lower the repeatability.

A number of micro-scale devices have been developed for studying the forces involved in cleaning. These typically involve imposing a known shear force or shear stress on the layer and measuring the resulting deformation, or imposing a deformation *etc.* Fluid dynamic gauging is an example of the former and has been used to monitor the strength (Chew *et al.*, 2004) and swelling characteristics (Gordon *et al.*, 2010) of common food soils when contacted with cleaning solutions.

Swelling is an indicator of cleaning and is dependent upon the chemicals within the solution interacting with the soil layer. The action of active agents within the soil layer may cause a change of the soil's bulk properties due to chemical reactions and the increase in moisture content (and possible associated phase changes). This leads to a weakening of the soil structure and facilitates the cleaning process.

2.3.2 Residue testing

One difficulty encountered in previous studies has been establishing a quantitative measure for when a substrate can be considered 'clean'. Visual methods are not uncommon (Jennings, 1965) but suffer from inconsistency between operators (variability) as well as being dependent on the substrate surface texture. The eye can detect residual material on a shiny surface more easily than on a rough one. The argument for visual inspection as an evaluation technique for consumer targeted studies is based on product performance: ultimately one purpose of the cleaning is to generate visually clean substrates at the end of a cleaning cycle as this is the customers metric. The additional requirement for hygienically clean substrates requires a more targeted analysis, e.g. ATP evaluation (use of adenosine triphosphate bioluminescence to quantify residual bacterial contamination, Poulis *et al.*, 1993). These evaluations should be considered in addition to more quantitative techniques for ranking solution performance.

The wetting behaviour of water on the substrate is a common evaluative measure used by sanitarians to determine cleanliness. Nine techniques, such as the droplet test (evaluating the adhesion of water to unclean surfaces) or the water break test (the degree of formation of rivulets when rinsing water off of a surface) were presented by Armbruster (1962).

The addition of dyes to a substrate has been used to highlight remaining soil patches that are not detectable to the eye. Fluorescent tagging (Domingo 1950) can be tuned to detect specific soil types. The squeegee-floodlight test (Abele 1965) can be used to disclose previously invisible protein films by wiping the surface with a squeegee then exposing the film to a high strength floodlight, causing the film to dry and crack into a visible form. The addition of salt (Armbruster, 1962), dyed talc (Armbruster, 1960) or chlorine (Maxcy, 1966) followed by chemical detection methods such as fluorescent microscopy or matrix-assisted laser desorption/ionisation mass spectrometry (MALDI MS) have also been shown to be effective in quantitative evaluation of soil residues. The riboflavin test is commonly used to determine the effectiveness of rinsing steps. The substrate to be cleaned is sprayed with a solution of riboflavin that glows yellow under a UV-A light. The proposed rinsing steps are then completed and the substrate re-inspected to ensure the riboflavin has been completely removed. Any residue showing under the UV-A light indicates areas where the rinsing process is inadequate (VDMA Information sheet, 2007).

Other techniques for monitoring the soil layer removal include light-transmittance variation (Gilcreas, 1941; Jensen, 1946; Leenerts, 1956), microbial doping and detection (Beck, 1962; Holland, 1953), radiological methods (Cucci, 1954; Seiberling, 1956) and calcium residue analysis (Heinz, 1967). Table 2.3 presents a comprehensive listing.

A key consideration in choosing an appropriate residue test for quantifying cleaning effectiveness is whether the analysis can be performed at the site of the contamination. The choice is often a consideration between the specificity of the data obtained about the chemical composition of the soil and the ease of its testing. Techniques such as MALDI-MS and SEM-EDX can detect ppm levels of contamination on a surface and characterise its elemental make-up but lack portability.

Table 2.3: Summary of residue tests for determining cleanliness of substrate.

Residue test	Performed in situ?	Requires specialist equipment	Specificity of soils detected	Reference
Fluorescent tagging	✓	✗	Specific to target molecule	Veran <i>et al.</i> , 2001; Armbruster, 1960, 1962
Molecular Assays	✓	✗	Specific to assay	Hammond, 1996
Riboflavin	✓	✗	n/a ¹	VDMA, 2007
Squeegee floodlight test	✓	✗	Organic material	Abele, 1965
Water break test	✓	✗	Non-specific	Armbruster, 1962
Calcium residue analysis	✓	✓	Calcium (typically used with milk)	Heinz, 1967
Ellipsometry	✓	✓	Non-specific	Karlsson and Tragardh (1999)
Iodine detection of starch	✓	✓	Starches	Griffith <i>et al.</i> 1997
Microbial doping	✓	✓	Biological contaminants	Beck, 1962; Holland 1953
Droplet test	✗	✗	Non-specific	Armbruster, 1962
Atomic force microscopy	✗	✓	All	Bowen <i>et al.</i> , 2001
Blotting and biocultivation	✗	✓	Biological contaminants	Eginton <i>et al.</i> , 1995
Impedimetry	✗	✓	Biological contaminants	Wawerla <i>et al.</i> 1999
Confocal laser scanning microscopy	✗	✓	Non-specific unless tagged	Percival <i>et al.</i> , 2001
Electrophoresis of protein residues	✗	✓	Proteins	Wildbrett and Sauer, 1989
Light transmission variation	✗	✓	Non-specific	Gilcreas 1941; Jensen 1946; Leenerts, 1956
MALDI MS	✗	✓	Organic material	Maxcy 1966
Radiological methods	✗	✓	n/a ¹	Cucci, 1954; Seiberling, 1956;
Scanning electron microscopy energy dispersive X-Ray analysis (SEM-EDX)	✗	✓	Elemental analysis – non-specific to molecular structure	Bouman <i>et al.</i> , 1982
X-ray photoelectron spectroscopy	✗	✓	Oxygen, carbon, nitrogen, trace other elements	Verran <i>et al.</i> , 2002

1. These techniques study the cleanliness of the surfaces only in terms of a material applied as part of the test, not for a residue of a soil. They are used to indicate the effective coverage of a test cleaning protocol.

2.4 Properties of interest

Four main properties were identified by the author for investigating the cleaning mechanisms of surfactants on food soils: (i) visual changes in the soils and surfactants, (ii) soil layer thickness over time, (iii) adhesion strength of soil to substrate, and (iv) soil displacement.

2.4.1 Visualisation of the soils and surfactants

The most common technique for visualising changes in soil structure, as well as movement of cleaning additives in solution, is confocal laser-scanning microscope (CLSM). CLSM was developed in 1957 by Marvin Minsky. However, it wasn't until the late 1980's that it entered mainstream biological research. The CLSM has continued to evolve over the following decades. It is now commonplace and is the basis of newer technologies such as CARS multiphoton microscopy and various super-resolution techniques.

The confocal principle is based upon the collection of reflected or emitted light from a single desired plane within a sample. A laser beam is projected toward a target object. On the way it passes through an objective lens which focusses it to a diffraction limited spot (also known as an airy disk). Any light that is reflected, or fluorescence emitted, is then collected back through the objective lens towards a detector. Immediately prior to the detector a pinhole aperture is installed which blocks all light except that of the target plane being scanned (Cox, 2002). By blocking all out-of-plane light confocal studies show marked decrease in background information, leading to sharper images and improvements in both axial and lateral resolution; axial through precise adjustments of the pinhole aperture and lateral through the minimisation of background emissions. Often successive planes will be scanned to generate a three dimensional image of the target object (Fellers and Davidson, 2019). The confocal principle is often used in biological fluorescence microscopy for imaging cell structures, and is discussed in more detail in Chapter 4.

2.4.2 Soil layer thickness over time

The measurement of soil thickness over time has long been a topic of interest for a wide variety of applications. These applications include paint layering, both for application purposes and for art restoration, and thin film deposit quality certification such as that conducted by Zhongye *et al.* (2018) on the deposition of thin films for coated optical devices.

A comprehensive analysis of thin film thickness devices up to 1985 by Piegari and Masetti, (1985) provides a comprehensive overview of traditional techniques such as stylus profilometry; interferometry; ellipsometry; spectrophotometry; and X-ray microanalysis. This study was updated to near-present day by Lindner *et al.* (2018) who compared the precision, accuracy and scale of more

modern thin film thickness measurement techniques, such as quartz crystal microbalance testing, atomic force microscopy and electrical resistance calibrated measurements, from the perspective of monitoring the *in situ* deposition of physical-vapour-deposited aluminium coatings in packaging applications.

For the purposes of this thesis the measurement technique is primarily required to be non-contact, non-destructive, and able to monitor changes in thickness over time at the length scale of tens of microns.

2.4.2.1 Comparison of non-contact displacement measurement techniques

2.4.2.1.1 Fluid dynamic gauging

The fluid dynamic gauging (FDG) principle was developed by Tuladhar *et al.* (2000) at the University of Cambridge for the measurement of the thickness of soft material deposits *in situ* and in real time. This technique has since been developed to study the strength of biofilms, such as algal films (Augustin *et al.*, 2012) as well as the growth of bacterial films in industrial applications (Peck *et al.*, 2015).

Fluid dynamic gauging was based on the principles of pneumatic gauging (Macleod *et al.*, 1962) but employed liquid flow to make its measurements. Here a nozzle is located a known distance from a substrate that is submerged in a solution with known flow properties. A pressure drop is then imposed across the nozzle. This caused liquid to flow from the surrounding environment into the nozzle at a measureable mass flow rate, which was shown by Tuladhar *et al.* (2000) to be a function of the clearance between the nozzle and the nearest surface. Alternatively, the mass flow rate of the solution can be set and the pressure drop generated by the flow of the solution measured. In this form the solution can either flow out of the nozzle towards the substrate, or into the nozzle, which could potentially lift the substrate from the surface. The technique operates at low mass flow rates (<10 ml min⁻¹) and so the mechanical impact of the flow can be controlled. The choice of measurement mode and flow rate is therefore subject to the target layer's physical and adhesive properties.

FDG has significant advantages over light-based techniques for this work as it can provide *in situ* measurement of changes in the layer thickness, either by swelling or erosion, in opaque solutions. It has a large spot size (diameter \approx 2 mm), a resolution limit of 10 μ m and low portability.

The development and use of this technique is presented in Chapter 5. Four alternative non-contact displacement sensing techniques are discussed below.

2.4.2.1.2 The eddy current principle

The eddy current principle used in inductive measurement sensors is based on the work of Heinrich Lenz, who stated in 1834 that 'the direction of induced current flow in an object will be such that its

magnetic field will oppose the change of magnetic flux that caused the current flow' (Lenz, 1834), and Leon Foucault, who discovered eddy currents in 1855. David Hughes first used eddy currents for non-destructive testing in 1879 when he utilised the fact that the strength of the eddy current imposed on an object is sensitive to its material properties. He thus devised a method of sorting metallurgical objects which was later adapted into modern hand-held metal detectors (Rao, 2006).

Eddy currents are used in a wide range of modern technologies (e.g. braking of electromagnetic trains, metal detection, and detection of counterfeit coins). A coil is supplied with an alternating current causing a magnetic field to form around it. An electrically conductive object in close proximity to the coil will disrupt the field and experience an eddy current. The size and strength of the eddy currents are dependent on the bulk properties of the object (e.g. composition, macrostructure, morphology). The currents then form an electric field (as described by Faraday's Law of Induction). This electric field dissipates within the object as heat. For displacement techniques a controller is used to calculate the change in energy transferred from the sensor coil to the target material which is then converted into a displacement measurement. As the technique is highly sensitive to the material properties of the sample full calibration is required for each new sample type.

2.4.2.1.3 The capacitive principle

Electrical capacitance describes how two electrically conductive objects separated by a gap respond to an applied voltage difference. When the voltage is applied an electric field is generated between the two objects, causing charges to collect on each object. Alternating the current causes the charges on each object to reverse their positions. This creates a current that is detected by a sensor and is proportional to the gap between the two objects (Regtien, 2012).

Non-contact capacitive sensors operate by measuring the changes in the voltage present on a sensor plate placed in proximity to a target plate. An alternating current of known and constant frequency is fed to the sensor capacitor plate. The amplitude of the resultant voltage is then proportional to the distance between the sensor plate and the target and is monitored over time.

2.4.2.1.4 The laser triangulation principle

Laser triangulation is based upon simple light reflection principles. A laser beam is projected at an angle towards a target object. The light is reflected off the object at an angle equal to that of the angle of incidence in the opposite direction to the normal. This light then travels towards an adjacent collection lens which focusses it on a linear array camera. The position of the reflected spot of light on the camera is dependent upon the distance to the target i.e. if the target is near, the reflected light spot will be nearer the emitter than if they target were further away. The measurements are typically

processed digitally in an integral controller and then converted into a scaled output which can be compared to a reference profile (Poredoš *et al.* 2015).

This technique is used in high resolution scanning such as those conducted on electronic control units but can be adapted using time-of-flight analysis for use in motor vehicles for proximity warning systems or in architecture for 3D-scanning of buildings and statues. A clear optical flight path is required for accurate measurement and it is sensitive to refraction, scattering /dissipation of the light and light absorptive materials.

2.4.2.2 Technique comparison

A comparative analysis of the advantages and drawbacks of each of these measurement principles is given in Table 2.4. Two techniques were chosen for this work: fluid dynamic gauging and confocal profilometry. The smaller spot size of confocal devices (9 μm) and higher resolution enables this technique to accurately monitor the swelling of soils. It is, however, unsuitable for use with opaque cleaning solutions, such as some commercial dishwashing solutions. It is also sensitive to changes in solution volume and so cannot be used at high temperatures or low pressures. For such systems, as well as for bulk profile measurements, the fluid dynamic gauge is better suited.

Table 2.4: Summary of benefits and limitation of commercially available non-contact sensing techniques

Technique	Advantages	Disadvantages
Fluid dynamic gauging	<ul style="list-style-type: none"> • Can be used submerged in aqueous solutions • Can be used with opaque systems • Insensitive to conductivity, impurities, temperature, and light-based properties of the target • High resolution (μm scale) 	<ul style="list-style-type: none"> • Large spot size (2 mm) • Requires the target surface to be stable to shear • Sensitive to surface topography and bulk porosity • Requires that the material to be analysed be submerged in liquid
Eddy currents	<ul style="list-style-type: none"> • Can be used on all electrically conductive metals • The size of the sensor is small • Can function over a large temperature range • Immune to non-conductive impurities (such as dirt or dust), humidity, pressure, and dielectric materials in the measurement gap • Only minor preparation of the surface is required 	<ul style="list-style-type: none"> • Requires that material to be analysed is electrically conductive (soil layers typically are not). • Calibration is required for each target material. • Sensitive to minor deformations or cracks (can be an advantage, depending on application) • AC input energy is dissipated as heat within the test sample – may cause deformation for very thin or heat sensitive samples or coatings.
Capacitive	<ul style="list-style-type: none"> • High resolution (nm scale) • High temperature stability • Insensitive to conductivity of target, i.e. can measure insulators 	<ul style="list-style-type: none"> • Sensitive to changes in the dielectric sensor gap • Requires completely clean and dry conditions: any oil or moisture in the gap affects the measurement.
Laser triangulation	<ul style="list-style-type: none"> • Small beam spot size • Long measurement ranges possible (accuracy is inversely proportional to measurement range) • Sensor operates independent of target material 	<ul style="list-style-type: none"> • Requires clean conditions to operate effectively • Specific sensor calibration required for direct reflecting targets. • Large sensor 'target' required dependent upon angle of reflection. • Sensitive to refraction of light beam in submerged environments. • Safety concerns with the use of high powered laser for high resolution testing.
Confocal	<ul style="list-style-type: none"> • Small beam spot size • High resolution in the axial plane • High specificity to target (when used with fluorophores) • Only minor preparation of the surface is required • The size of the sensor can be small 	<ul style="list-style-type: none"> • Slow technique for 3D structures • Only suitable for small areas at short range • Often used in conjunction with expensive fluorophores • Requires precise positioning of the pinhole aperture

2.4.3 Measurements of adhesion strength

The ability to study the strength of adhesion a soil to a substrate *in situ* and in real time is essential to understand the mechanisms of cleaning in house-hold applications. Current methods of measuring the adhesion strength of soft solid food soils are often unreliable as many foodstuffs feature multiple phases with differing hydrophobicity and wetting characteristics. Ideal monitoring systems would allow for the adhesion strength of the soil to be recorded *in-situ*, with the relevant food soil, on the relevant substrate, under conditions which reflect those of the cleaning environment.

Two primary methodologies of studying adhesion strengths are (I) controlled stress (e.g. plynometers (Zorita *et al.*, 2010) or centrifugation (Rennie *et al.*, 1998), and (II) controlled strain. The response of the soils are then monitored, via force or pressure transducers, visual inspection of the residual material, or gravimetrically.

The use of controlled deformation (effectively controlled strain) devices in the field of fouling and cleaning was pioneered by groups at Birmingham (Liu *et al.*, 2002) who adapted a micromanipulation device developed for studying yeast cells to study the removal of biofilms and soil layers. Liu *et al.* (2006) identified and quantified different failure modes between soil types: baked tomato paste removal was dominated by its cohesive strength, exhibited by its detachment in chunks even after soaking in an external bath, while pure protein deposits exhibited predominately adhesive failure (*i.e.* detachment at the soil-substrate interface)(Table 2.5).

Micromanipulation tends to work at length scales of 10s of microns, and the heterogeneity of food deposits prompted workers such as Ashokkumar and Adler-Nissen (2011) and Ali *et al.* (2015(c)) to develop millimanipulation devices which could be used to study composite deposits, as well as hard layers which techniques such as fluid dynamic gauging could not deform. Those workers considered dry deposit layers: in this thesis, the device reported by Magens *et al.* (2017) was adapted to allow immersion of the sample in solution for controlled lengths of time, at temperatures ranging from 20 °C to 50 °C, thereby mimicking the chemical environment in an automatic dishwasher.

Table 2.5: Investigating of soil deposits by micro- and milli-manipulation. Reproduced and updated from Ali, 2015(a).

Soil	Substrate	Soil thickness / mm	Apparent cohesive strength / J m ⁻²	Apparent adhesive strength / J m ⁻²	Failure mode	Source
Baked tomato paste	316 SS	0.7 – 1.7	> 4	1 – 14	Cohesive	Liu et al., 2002
Baked whey protein	316 SS	1.5 – 2.8	0 – 10	0 – 10	Unknown	Liu et al., 2006
Dried bread dough	316 SS	2.0	5 – 80	5 – 60	Mix	Liu et al., 2006(a)
Tomato paste	Ni-P-PTFE	1.2 – 3.6	2 – 15	0.7 – 2.1	Adhesive	Liu et al., 2006(b)
Corn oil	316 SS	3.2 – 3.7	< 4	< 4	Adhesive	Liu et al., 2006(a)
Baked ovalbumin	316 SS	2.2	1.5 – 4	0.5 – 3	Adhesive	Liu et al., 2007
Turkish delight	316 SS glass and TCTFPS	0.7	1 – 3.5	1 – 3.5	Cohesive	Akhtar et al. 2010
Caramel deposit	316 SS glass and TCTFPS	0.7	4 – 16	4 – 16	Adhesive	Akhtar et al. 2010
Baked lard	316 SS	0 – 1	-	-	Adhesive	Ali et al., 2015(a)
Cake	304 SS, and PTFE analogues	10	0 – 7	0 – 7	Cohesive	Magens et al., 2017
Toothpaste	Float glass	0.1 - 0.7	-	0 – 6	Adhesive	Yang et al., 2019
Egg Yolk	304 SS	0.27-0.28	0.2-0.9	0.2-0.9	Mix	Heibig et al., 2019

SS: Stainless steel, Ni-P-PTFE: nickel-phosphate-polytetrafluoroethylene, TCTFPS: trichloro(3,3,3-trifluoropropyl)silane

2.4.4 Displacement of soil into solution

The burnt complex model soil studied here comprises a porous matrix initially saturated with viscous fats and oils. When it swells in water there are similarities to the oil-wet bedrock systems encountered in enhanced oil recovery (EOR) studies. In order to enhance the recovery of petroleum from a reservoir, a technique known as surfactant-based chemical flooding is utilised. Here an aqueous solution containing a low concentration of surfactant is injected into the bedrock with the purpose of decreasing the interfacial tension between the flooding water and residual oil, increasing oil recovery (Cheraghian and Hendraningrat, 2016). The flow of the displaced oil was demonstrated on a microscopic scale by Jamaloei, and Kharrat (2010) to be affected by the wettability of the reservoir rock. Jadhunandan and Morrow (1995) showed that with an oil-wetted porous medium there is a

resistance to imbibition of water leading to high residual oil saturation and an unfavourable mobility ratio i.e. the oil is less mobile than the water leading to a lower recovery rate. Babadagli (2003) investigated the relationship between the spontaneous imbibition of surfactant solutions into different rock types and the recovery rate and showed that both a change in wettability and the lowering of interfacial tension were required to optimise oil recovery.

Visualisation of the mechanisms of surfactant-based flooding processes has been studied in EOR for over 70 years. Early studies (James, 1958) used photographic and cinematographic imaging of two phase liquids interacting in a sand matrix, capturing changes in the oil-water emulsification profiles as well as cataloguing film-formation phenomena. Williams and Dawe (1988) later employed photographic techniques to capture pore-to-pore transfer of the wetting phase at $IFT < 0.1 \text{ mN}^{-1}$. They also proposed a mechanism of gravity-induced instability of the resultant oil-water emulsion. A model matrix consisting of lightly sintered glass beads was used by Hornof and Morrow (1987) in a top-mounted photographic rig to study the displacement of isoctane by aqueous surfactant solutions. When the IFT was lowered, the thin interfaces became 'fuzzy' and they reported noticeable buoyancy effects, i.e. "distinct gravity override by the aqueous phase".

These studies suggest that knowledge of the oil-water interfacial tension and soil wettability are key to understanding the mechanisms involved in the removal of fats and oils from the food soil studied in this work. A significant difference between EOR studies and the soils studied here is that the former do not exhibit swelling, which is expected to convert voids into expanded voids containing oils and fats as isolated droplets surrounded by water solution.

2.5 Project Objectives

The primary objective of this thesis is to develop a mechanistic understanding of the cleaning of complex food soils, specifically heterogeneous (starch, protein and fat) food soils that have been exposed to sufficiently high temperatures such that they have undergone chemical changes. The aims are to;

1. Determine the impact of additional complexity of soil composition on current understanding of the cleaning of model soil systems.
2. Identify the sequence of events that occur in the staged cleaning of the baked complex soils.
3. Utilise and extend currently available techniques to monitor the impact and effectiveness of cleaning agents in a range of conditions.

3. Soil materials and preparation methods

Fryer and Asteriadou (2009) generated a cleaning map detailing the types of cleaning solution which are most effective at cleaning different soil groups. Examples of soil groups are: low viscosity fluids, e.g. milk; high viscosity fluids, e.g. toothpaste; and cohesive solids, i.e. soils which create an immobile fouling deposit, i.e. lime-scale or protein gels. Burnt soil layers tend to be cohesive soils.

3.1 Soils

The range of cohesive soils that could be studied is wide-ranging and determining mechanistic behaviour of surfactant solution interaction on every possible combination of soils is beyond the limit of a single PhD. Ideally, pure component soils would be studied and combined with one another to create model soils. These soils would be chemically and structurally simpler than real systems and therefore easier to study quantitatively and to model from first principles. Soils made from several components would be tuneable, allowing the impact of component concentrations on surfactant solution cleaning behaviour to be determined. However, model systems, by design, are significantly simpler in nature than real foodstuffs. The mechanistic behaviour models generated for the model soils may not be applicable to complex food-based soils. The work conducted in this project will be conducted on two soils, a notionally simple soil (Figure 3.1 (a)) and a complex food-based soil (Figure 3.1 (b)) as described in Chapter 2.

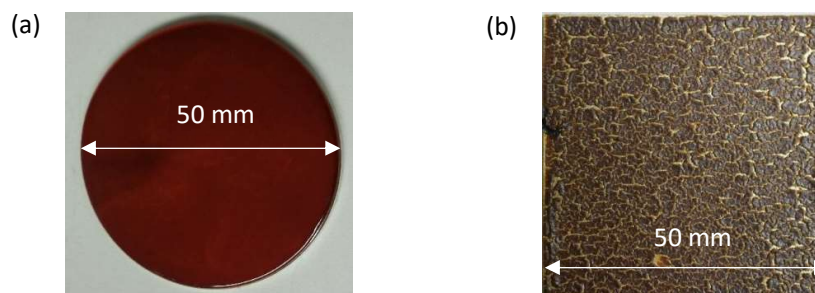


Figure 3.1: (a) stainless steel disc (diameter (d) = 50 mm, height (h) = 3 mm) with baked lard soil. Soil thickness (δ) = $310 \pm 4 \mu\text{m}$, $R_q = 2.5 \mu\text{m}$, mass = $0.55 \pm 0.005 \text{ g}$, coverage = $0.28 \pm 0.003 \text{ kg m}^{-2}$. (b) stainless steel plate (50 x 50 mm, $h = 3 \text{ mm}$) with baked CMS $\delta = 300 \pm 5 \mu\text{m}$, $R_q = 270 \mu\text{m}$, mass = $0.49 \pm 0.06 \text{ g}$, coverage = $0.20 \pm 0.03 \text{ kg m}^{-2}$.

3.2 Substrates

The majority of tests conducted in this work employed 316 stainless steel substrates (Table 3.1). Comparative testing on glass, copper and ceramic plates was conducted in some cases in order to investigate the impact of changes in surface chemistry and energy on the adhesion characteristics of CMS. Chambered borosilicate glass slides (Lab-Tek, 4 well plates) were used to investigate the movement of cleaning agents using microscopy techniques.

Table 3.1: Dimension and surface characteristics of substrates used in tests

Material	Test	Surface dimension	δ	R_q /μm	surface energy /J m^{-2}	Source	
<i>Stainless steel</i>	Disc	MM3	50	2.91 ± 0.007	1.6	0.7 – 1.1	Mill Stainless
	Plate	MM3	50 x 50	1.89 ± 0.009	1.6	0.7 – 1.1	Mill Stainless
	Plate	SiDG	25 x 100	0.62 ± 0.02	2.1	0.7 – 1.1	Mill Stainless
	Plate	P&G	98 x 98	4	2.69	0.7 – 1.1	SlickSteel
<i>Glass</i>	Plate	CFM	75.7 x 25.9	1 ± 0.04		0.25 - 0.5	Lab-Tek
	Plate	MM3	50 x 50			0.25 - 0.5	Lab-Tek
<i>Copper</i>	Plate	MM3	50 x 50	3.25 ± 0.32	-	1.65	Goodfellow
<i>Ceramic</i>	Plate	MM3	50 x 50	2 ± 0.013	1.3	0.039-0.047	Król <i>et al.</i> (2006), RS-online

Prior to applying the soil the substrates were cleaned by sonication for 10 minutes at room temperature in aqueous 1 M NaOH, dishwashing solution (Fairy Liquid™ in reverse osmosis water, < 5 g L⁻¹) then acetone, scrubbing with a soft cloth following each sonication step. Cleaning was repeated if any residual soil was visible. After each test any remaining soil was removed using a plastic spatula and the plate left to soak in 1 M NaOH/soap solution overnight and rinsed with deionised water before undergoing the procedure outlined above.

3.3 Simple soil layer preparation

Lard soil preparation required pre-heating the lard to 50 °C in a Pyrex beaker with stirring until completely homogenous. 0.9 ml of the liquid lard was distributed evenly via syringe injection onto a pre-weighed (3 d.p. Precisa, XB10200G) stainless steel disc (2.91 mm ± 0.007 mm, SS-316, R_q : 1.6 μm , surface energy: 0.7 – 1.1 J m⁻²) pre-heated to 40 °C. When in liquid form the surface tension of the lard was sufficient to ensure even distribution over the bulk of the surface, with some pinning at the edges of the disc. The soil was then left to cool in air for 30 minutes (20 °C, 48 % humidity) and weighed, before being baked in air in a conventional oven (Carbolite®, LHT6/60) at set temperature (up to 250 °C) for a set amount of time (up to 5 h). Baked samples were left standing in ambient air to cool to room temperature before testing. Baked soils were visually inspected for deformation, weighed and the thickness measured using digital vernier callipers. The soil thickness, δ , was typically $310 \pm 4 \mu\text{m}$, roughness $R_q = 2.5 \mu\text{m}$ and layer mass approximately $0.55 \pm 0.005 \text{ g}$, giving an initial coverage on a 50 mm disc of $0.28 \pm 0.003 \text{ kg m}^{-2}$.

3.3.1 Repeatability testing

Experimental variation is inherent in the process of depositing, baking and subsequently removing the soil layers from the stainless steel discs. To establish the variability between samples and the subsequent impact on adhesion testing, a repeatability study was conducted.

The deposition of the layer was measured via two metrics: (i) its thickness when baked, measured at 4 equidistant points on the disc; and (ii) the pre- and post- baking weights of the soil, which were used to determine its coverage and apparent density. The results are summarised in Table 3.2.

Table 3.2: Repeatability for 10 discs of lard soil layers. $T = 250\text{ }^{\circ}\text{C}$, baking time = 2.5 h, initial mass: 0.81 g. Adhesion measured by millimanipulation testing, discussed in Chapter 7.

Sample	δ				$\langle\delta\rangle$	Coverage	Apparent ρ	Adhesion	Adhesion
	/ mm (Position)								
Repeat	(1)	(2)	(3)	(4)					
1	0.29	0.32	0.32	0.29	0.31	0.28	903	3.60	146
2	0.33	0.30	0.30	0.33	0.32	0.27	858	3.37	136
3	0.28	0.32	0.28	0.29	0.29	0.29	994	2.50	101
4	0.29	0.32	0.27	0.27	0.29	0.29	993	2.74	111
5	0.33	0.29	0.30	0.32	0.31	0.27	872	3.01	122
6	0.37	0.30	0.30	0.28	0.31	0.28	881	3.73	151
7	0.27	0.31	0.38	0.30	0.32	0.27	842	3.28	133
8	0.30	0.31	0.29	0.30	0.30	0.29	952	3.27	132
9	0.29	0.33	0.32	0.37	0.33	0.28	856	3.48	141
10	0.27	0.30	0.31	0.32	0.30	0.28	935	4.02	163
Average					0.31	0.28	887	3.47	141
Std Error					0.004	0.003	13.9	0.11	4.51

The variation in δ was ± 0.004 mm for $0.28\text{ mm} < \delta < 0.34\text{ mm}$. There was no correlation between $\langle\delta\rangle$ and adhesion strength over this range. Small variations in layer thickness across a sample are therefore acceptable during adhesion strength testing, with an error band of 4.5 N m^{-1} .

The weight of the sample deposited was also recorded both before and after baking. Approximately 0.81-0.82 g lard was added to each disc prior to baking. The average mass loss during baking was 33%. The composition of lost material was not investigated; it will likely include water and low molecular mass (more volatile) hydrocarbons. No significant density change was recorded (lard: $866 \pm 9\text{ kg m}^{-3}$, baked lard: $842 - 994\text{ kg m}^{-3}$), indicating that the material lost on baking has similar density to the bulk lard.

3.4 Complex model soil

A model burnt soil deposit was generated containing fats, carbohydrates and proteins as detailed in Table 3.3. This formulation was provided by Procter and Gamble® to mimic consumer products known

to pose difficulty in automatic dishwashers. The soil was applied as a slurry to stainless steel substrates, dried and baked.

Slurry preparation consisted of boiling the pasta in deionised water for 7 minutes before draining the liquid off and adding the solids to the fat emulsion (pre-heated to 50 °C), milk, cheese powder and salt. The mixture was then blended for 1.5 minutes at maximum speed on a household food processor (Cookworks, HA-3213) until it appeared homogeneous to the eye. An excess of the slurry was placed on the sample plate and a wiping blade device (Figure 3.2) similar to that reported by Glover *et al.* (2016) was used to generate a smooth layer of initial thickness δ . The gap between the blade and the substrate is set by a pair of micrometers with a precision of $\pm 10 \mu\text{m}$: the dried layer was rougher than this owing to the inherent heterogeneity of the slurry. δ was typically 500 μm and the layer mass approximately 1.8 g, giving an initial coverage on 50 × 50 mm test plates of 0.72 kg m⁻².

The sample was then left to dry in air (20°C, 48 % humidity) for 24 hours before being baked in air in a conventional oven at 204 °C for 7 minutes. The high water content of the mixture as well as breakdown of carbohydrate into carbon dioxide and water results in a high evaporation rate during baking. For an initial charge of 1.49 g CMS mix, 0.49 g remained after baking for 7 minutes, representing 67 wt.% loss and a soil coverage of approx. 200 g m⁻². This resulted in an inhomogeneous soil. Baked samples were left standing in ambient air to cool to room temperature before testing.

Table 3.3: *complex model soil composition*

Component	mass fraction wet basis	nature	Supplier/source
<i>fat</i>	0.18	mixture of saturated and unsaturated fats	margarine blend 'I can't believe it's not butter™', whole milk
<i>protein</i>	0.057	milk protein	whole milk, Kraft cheese powder pasta (cooked)
<i>carbohydrate</i>	0.240	durum wheat starch	pasta (cooked)
<i>salt</i>	0.003	NaCl, dissolved	Kraft cheese powder
<i>water</i>	0.52	deionised water	pasta (cooked), whole milk

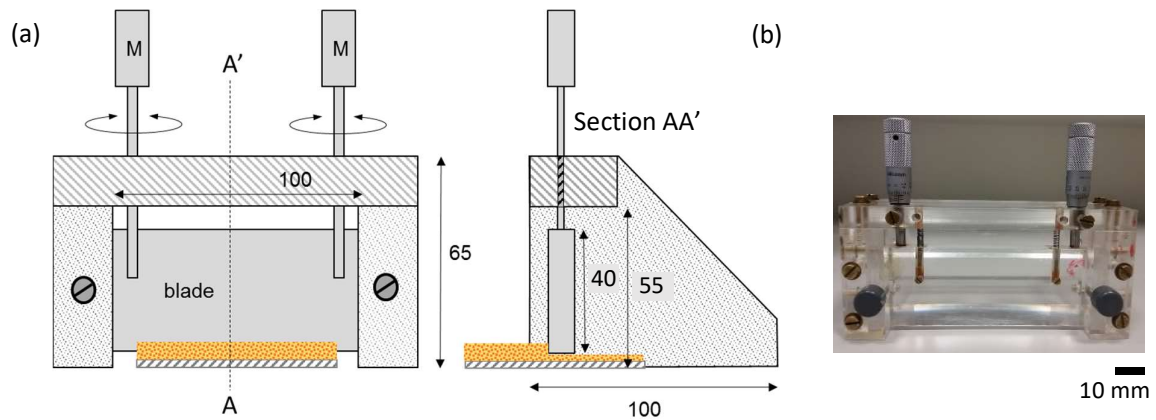


Figure 3.2: (a) schematic and (b) photograph of draw-down applicator for the deposition of CMS films. Dimension in mm.

3.4.1 Soil drying

The soil was dried in air for 24 hours to allow slow evaporation of water. Figure 3.3 shows a linear drying rate for the first 4 hours of $12.3\% \text{ h}^{-1}$. The rate decreases thereafter until it reaches an asymptote at a mass fraction of 0.36. This transition from constant falling rate behaviour is associated with the evaporation of free water followed by an internal diffusion regime. Comparison with Table 3.3 indicates that the mass loss includes the water present in the pasta, milk and margarine.

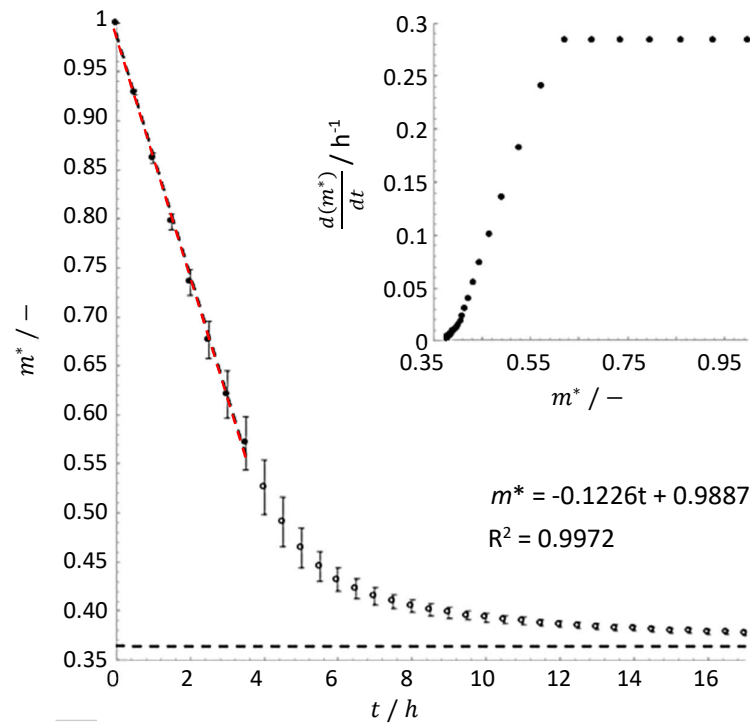


Figure 3.3: Average dimensionless mass loss of CMS during drying. The black dashed asymptote represents the average mass of the samples measured after 7 days. The inset presents the absolute value of the rate of CMS of dimensionless mass loss. Reproduced with permission from Nathan Ravoisin (2018).

3.4.2 Soil characterisation

Differential scanning calorimetry (DSC, Figure 3.4) indicated that the majority of volatiles present in the CMS were lost in the drying stage of sample preparation (Figure 3.4 (a) vs (b)). Figure 3.4 (a) shows the phase change profile for fresh CMS; on the first heat-cool cycle (black) two large peaks appear on heating from -20 to 100 °C which are attributed to the melting (II) and boiling (III) of water. Upon cooling there is a small peak (I) at 18 °C which is attributed to a phase change of the fat components. When passed through another heat-cool cycle (grey), the two peaks associated with the water content are absent and only the fat peak remains.

Figure 3.4 (b) shows the behaviour of evaporated (blue) and burnt (red/orange) CMS upon heating and cooling. The second heat-cool cycle of the fresh CMS (grey) is included for comparison. It can be seen that the evaporated and burnt soils contain little water (no evidence of the peaks denoted II and III). Upon heating a broad peak (IV on Figure 3.4 (b)) was evident in the dried and burnt samples between 20 and 40 °C, associated with the melting of the fat phase. Upon cooling there is a sharper exothermic peak at 18 °C, similar to that in the fresh CMS, which is attributed to the solidification of the fat phase. The second heat-cool cycle showed little variation in the DSC profile, (small differences are evident in the scale of the heat flow) indicating that no significant further change occurred in the material.

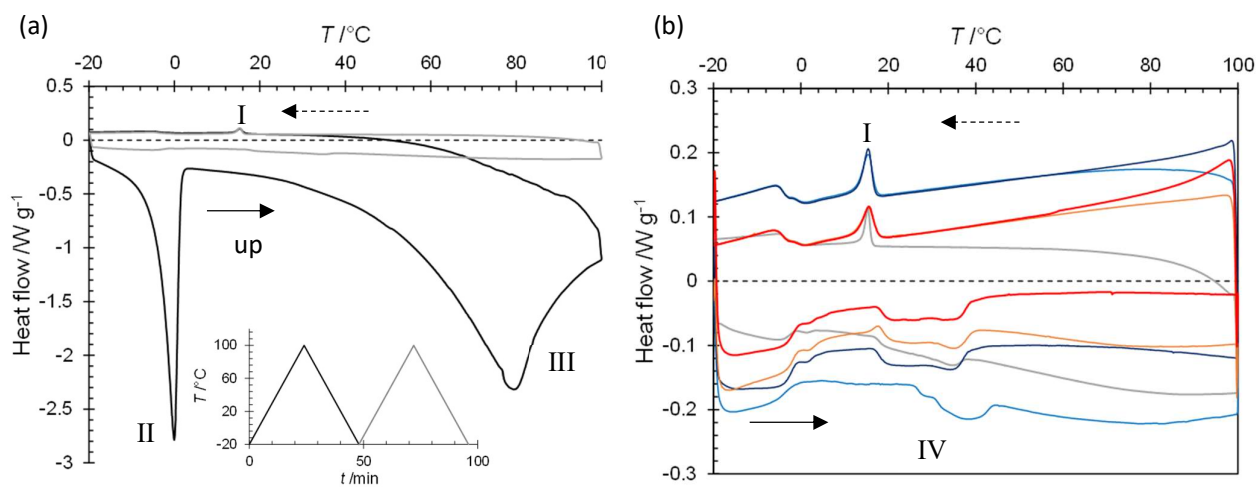


Figure 3.4: DSC thermograms of (a) fresh and (b) fresh, evaporated and burnt CMS. Temperature ramped from -20 to 100 °C at 5 K min⁻¹ twice, as shown by inset in (a). Colours: Fresh; black – scan 1, grey – scan 2. Evaporated; blue – scan 1, purple – scan 2. Burnt; orange – scan 1, red – scan 2. Inset: temperature profile of DSC test.

3.4.3 Soil Cracking

Figure 3.5 shows photographs of the CMS layer before and after baking. 10 wt.% of mass was lost during baking and was accompanied by visible cracking of the layer (Figure 3.5 (b)). It was not possible to generate crack-free layers. Prolonging the drying time, such as allowing the moisture to evaporate overnight before baking, reduced the severity and width of the cracking. Thinner soil layers ($\delta_{\text{initial}} < 200 \mu\text{m}$) exhibited finer scale cracking patterns, as defined both by cracking frequency and width, than thicker ones ($\delta_{\text{initial}} > 500 \mu\text{m}$), which is consistent with the literature on film cracking (Lee and Routh, 2004).

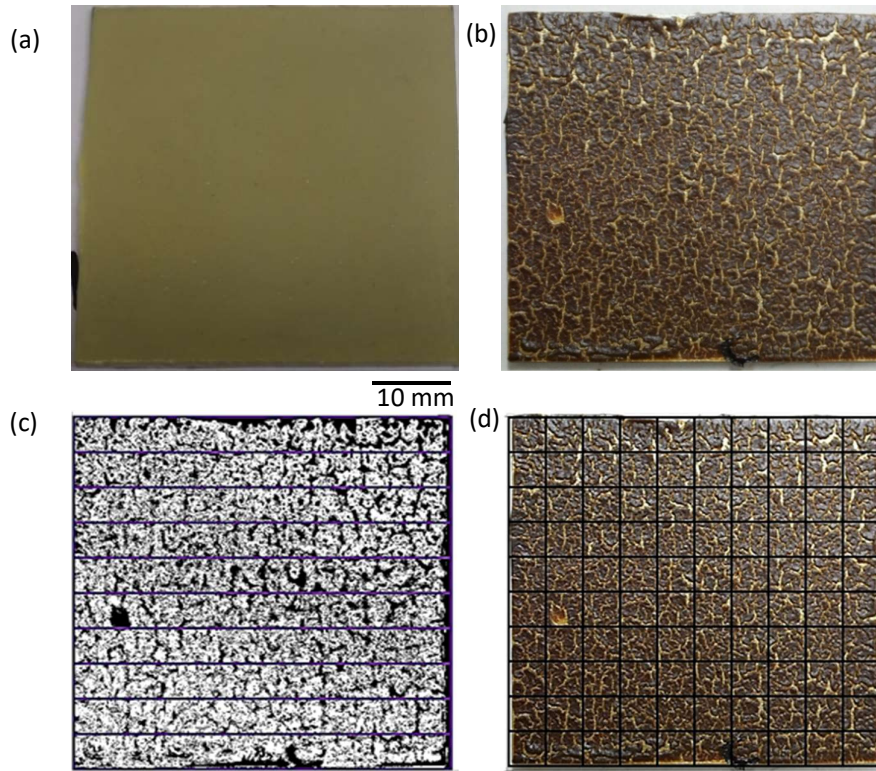


Figure 3.5: Photographs of $\delta = 300 \mu\text{m}$ CMS layer on $50 \times 50 \text{ mm}$ 316 stainless steel plate (a) before drying, and (b) after baking for 7 min at $204 \text{ }^\circ\text{C}$; (c) Binary image of (b) for calculating area of cracked soil; (d) image (b) with gridlines used for calculating crack distribution.

The crack pattern structure was quantified using two methods. The first was based on the fraction of the plate area occupied by cracks. This was calculated by converting a photograph into a binary image in Matlab™ (Figure 3.5 (c)) and dividing the soiled region into ten equal strips. The fraction of cracked area was calculated for each strip, giving an average of 38.8 % with a standard deviation of 5.3 %. The second was to count the number of cracks along 9 equally-spaced gridlines (Figure 3.5 (d)). This gave averages (\pm standard deviation) in the vertical and horizontal directions of 19.0 ± 3.0 and 21.2 ± 2.6 , respectively, corresponding to a crack spacing of approximately 2.5 mm.

3.4.4 Impact of temperature on soil viscosity

The effect of temperature on the fat component was evaluated by studying the rheology of the emulsion used in the formulation over the range 10 – 60 °C, spanning the temperatures employed in the cleaning tests (Figure 3.6). The fat present in the soil contains less water and its rheological behaviour will be affected by changes introduced by baking and components absorbed from other ingredients in the CMS, so these results are interpreted as indicators of the fat behaviour. Samples were tested in a Malvern Kinexus rheometer using a 40 mm diameter, smooth, 4° cone and plate configuration. Shear rate sweeps at 22°C indicated viscoplastic behaviour (Figure 3.6(a)) with a critical stress of approximately 160 Pa and a critical shear rate of around 1 s⁻¹. Measurement of apparent viscosity were therefore made at 0.1 s⁻¹ at intervals of 5 K. The apparent viscosity decreased strongly with temperature until 40 °C, above which it was almost insensitive to temperature and the behaviour was Newtonian. This was interpreted as the temperature at which the fat phase in the soil was expected to become mobile. These observations are consistent with the DSC results.

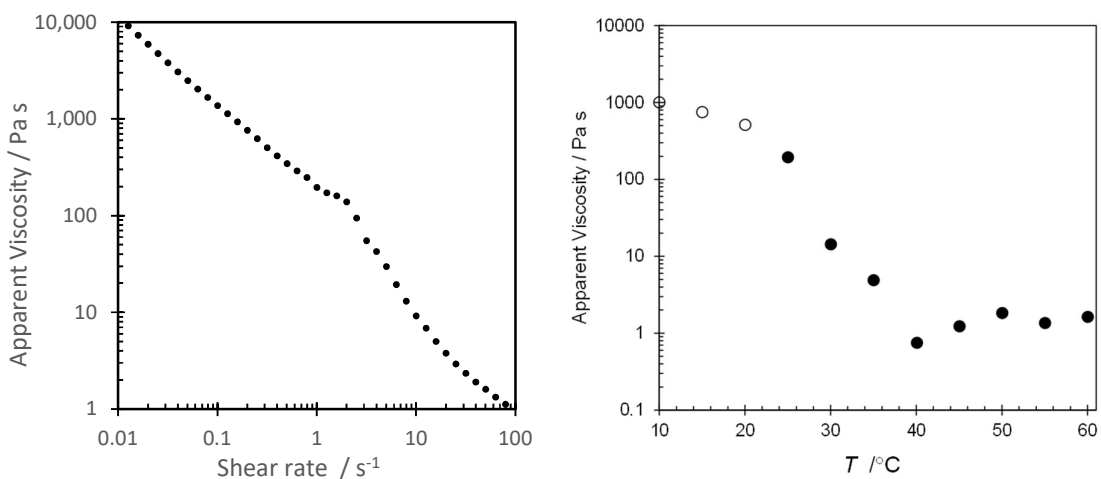


Figure 3.6: *Shear viscosity of fat component of CMS (40 vol.% emulsion of fat in water). (a) shear rate dependency at 22 °C: below 0.1 s⁻¹ the gradient is close to -1, associated with yield stress behaviour. (b) apparent viscosity measured at apparent shear rate of 0.1 s⁻¹. Open symbols indicate data with significant normal stress differences, indicating strongly non-Newtonian behaviour.*

3.5 Cleaning solutions

Three surfactants were chosen for use in this work: CTAB (Figure 1.4 (a)) SDBS (Figure 1.4 (b)), and TX-100 (Figure 1.4 (c)). Table 3.4 contains a summary of the relevant properties of the surfactants and chelant used in this work. The surfactants' critical micelle concentrations (CMCs) were measured using a pendant drop tensiometer (DSA100, KRÜSS GmbH) and were found to be consistent with literature values (Figure 3.7).

Two commercial formulations provided by P&G® were tested to compare with the simple surfactant solutions. These are denoted as CCF1 and CCF2.

Solution preparation protocols were specific to each test method and are therefore reported at each juncture.

Table 3.4: Summary of component properties, reproduced from Ali (2015(a))

Component	Type	CMC / wt.%	Molecular mass	Dissociation	Concentration / wt.%	Source
Water	Solvent	-	18	14.16	-	Heplar <i>et al.</i> (1970)
CTAB	Cationic surfactant	~0.0001	364.45	2.9 - 3.9	0.01, 0.1	Previdello <i>et al.</i> (2006)
SDBS	Anionic surfactant	~0.005	342.4	2.142	0.01, 0.1	Sanz <i>et al.</i> (2003)
TX-100	Non-ionic surfactant	~0.0013	647	-	0.01, 0.1	Ruiz <i>et al.</i> (2001)
MGDA	Chelant	~0.001	271	1.6, 2.5, 10.5	0.1	Trilon M (2018)
NaOH	pH modifier	-	40	-	-	Sigma (2019)

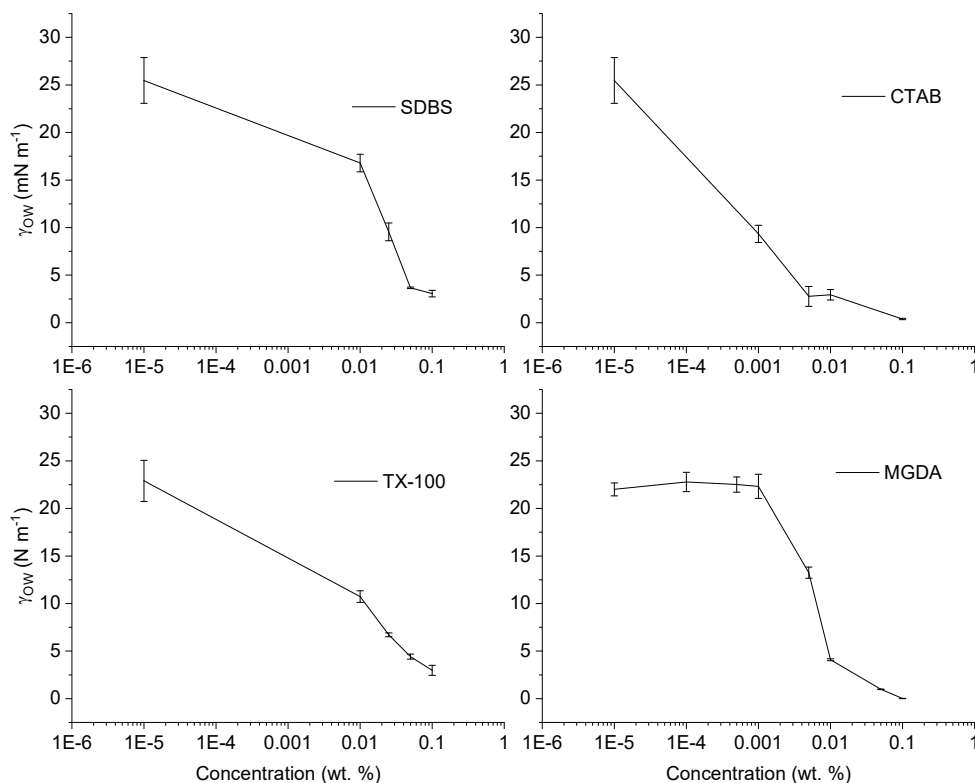


Figure 3.7: Effect of surfactant (a-c) and chelant (d) concentration on the interfacial tension between deionised water and sunflower oil.

4. Microscale imaging

Microscale imaging techniques are commonly used in the study of fouling and cleaning in food processing. Visualisation of the removal of material in-situ has proved vital in progressing scientific understanding of the mechanism of cleaning model soils (e.g. Joscelyne *et al.*, 1994).

One such technique is the confocal laser scanning fluorescence microscope (Figure 4.1). This technique combines high-resolution optical imaging with depth selectivity through the use of a pinhole aperture. Using similar principles to a conventional microscope the CFM utilises a laser beam in place of the conventional lamp. The laser light is focussed on the sample through the use of a series of scanning mirrors which can move the beam quickly and precisely in the X-Y plane. The energy is then focussed on the sample by the objective lens. If the sample is fluorescent the energy is absorbed by the sample and re-emitted at a different wavelength. This emitted light travels back along the same path as the laser light. The light passes through a semi-transparent mirror reflecting it away from the laser and instead towards a photomultiplier amplified detector.

In *confocal* laser scanning microscopy, a pinhole aperture is installed prior to the detector to filter out all light except the central portion, all of which would have originated on the same z-plane. Fluorescence emission from the in-focus plane is imaged through the pinhole onto the detector. The fluorescence intensity for this one spot becomes 1 pixel of the final image. Fluorescence from out-of-focus planes is deflected by the pinhole (Jonkman and Brown, 2015). The focused spot is then scanned back and forth across the specimen to generate an image. This allows depth selectivity to be controlled through the combination of the size of the pinhole and the positioning of either the pinhole relative to the detector or by movement of the sample on an adjustable z-stage.

The use of the aperture minimises the interference from the surroundings, as well as from above and below, creating an improvement in both axial and lateral resolution compared to conventional microscopy. Moreover, when optimised, the z-axis resolution can be up to three times the x- and y-axis resolutions. Optimisation of the resolution requires that the diameter of the aperture is adjusted so that it collects fluorescence from only the central part of the illuminated area, out to where the intensity falls off to about 50 % of its peak value (Hepler and Gunning, 1998). However this optimisation of resolution decreases the intensity of the fluorescence at the detector, requiring either a loss of sensitivity, or an increase in laser intensity which may damage the specimen (Pawley, 1995; Sanderson *et al.* 1995).

One of the main drawbacks of the CFM is speed. It takes approximately 1 second to collect a 1024×1024 pixel image with a $1 \mu\text{s}$ pixel dwell time. Typically four sequential fluorophore channels are used to improve the signal to noise ratio. If 20 planes of focus are scanned to capture a 3D volume, then each 3D data set can take several minutes. As a consequence of this the choice of magnification lens is critical; high magnification lenses ($\sim x40$) can be used to construct a small region of an image but to image larger regions lower magnification lenses ($< x20$) are required (Papp *et al.*, 2003).

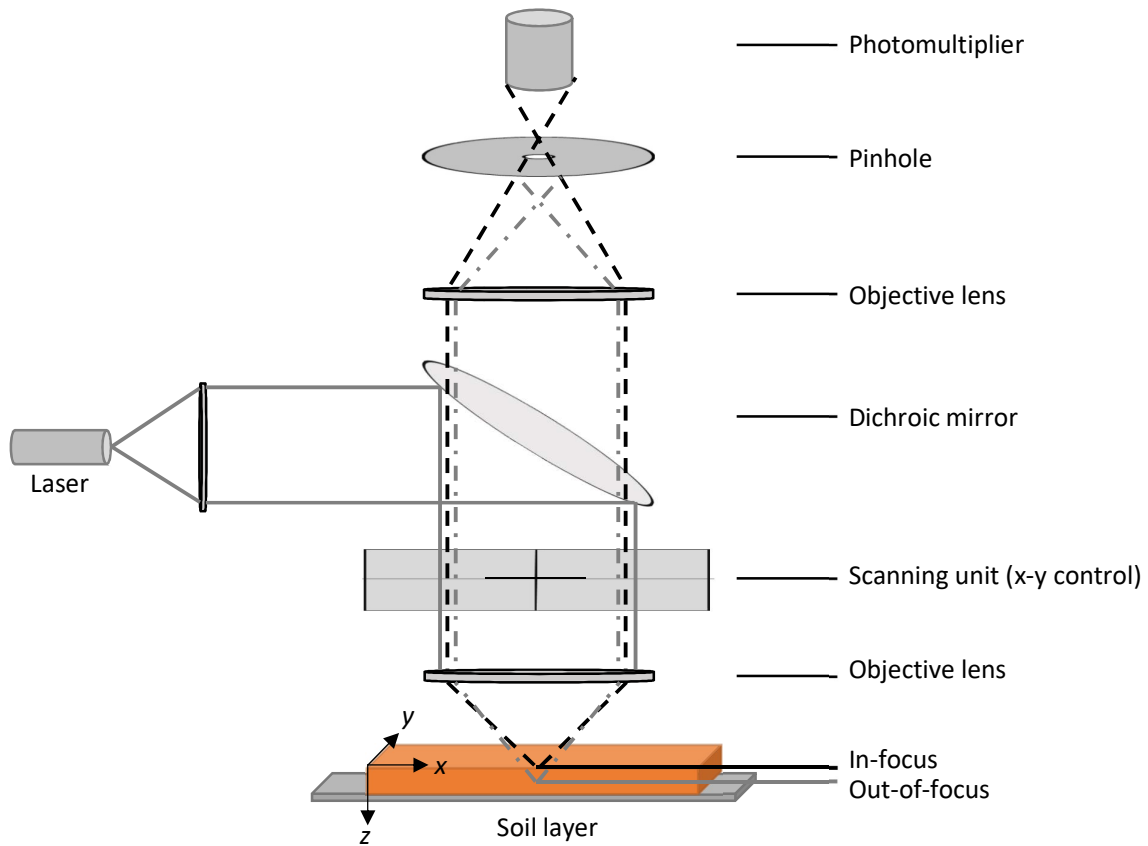


Figure 4.1: Schematic of confocal laser scanning microscope.

A secondary concern is photobleaching (Tsein and Waggoner, 1995). This is the photochemical alteration of a dye, or in this case fluorophore, such that it is no longer fluorescent. Photobleaching is typically caused by reaction between the fluorophore and surrounding molecules whilst in its excited state, causing it to change from a singlet state to a triplet state. This is especially problematic in time-lapse microscopy as the fluorophores are destroyed by the light necessary to stimulate them to fluoresce (Ghauharali, 2001). As different fluorophores have different photobleaching resistance, this is an important factor in their selection for time-lapse microscopy.

4.1 Experimental set-up

In these tests the fluorescent species are introduced to the system, either within the soil itself or dissolved in the cleaning solution. Fluorescence in the solution enables visualisation of the movement of surfactants as the cleaning solution penetrates (permeates through the soil at the soil-solution interface) or ingresses (permeates beneath the soil at the soil-substrate interface) into the soil layer.

One drawback of this technique is that it relies on the assumption that the fluorescent molecule behaves similarly to the cleaning agents within the solution. Specifically designed fluorescently tagged surfactants are available commercially to mitigate this problem. However, the tags are by nature bulky relative to a standard surfactant. In addition to this the manufacturing difficulty involved in the generation of ultra-pure small tagged molecules causes these surfactants to be too expensive at the concentrations required for cleaning (Dong *et al.*, 2007).

4.1.1 Choice of fluorophore in solution

The fluorophore selected should be both excitable and detectable with the available instrumentation. It should be bright, possessing a high molar absorption coefficient at the desired excitation wavelength, with a high fluorescence quantum yield. Additionally it should be soluble in the relevant solvent, and be sufficiently stable under relevant conditions (Resch-Genger *et al.*, 2008). Organic dyes are able to meet most of these criteria and are commonly used for biological applications including calcium imaging (Yazawa *et al.* 2011) and focal adhesion dynamics (Digman *et al.* 2008).

Fluorescence in small, synthetic organic compounds is caused by the delocalisation of electrons across a conjugated system (e.g. combined aromatic groups or planar molecules with several π bonds) which form energy bands across which electrons can move (PerkinElmer, 2000). Their optical properties are determined by the size of these electronic band gaps. The main advantage over other types of fluorescent molecules (e.g. natural proteins such as GFP, (Prendergast, 1978) is that the manufacturing requirements of these synthetic compounds are well understood. This allows for relatively simple alteration of the molecular 'backbone' to produce a range of different dyes with tuneable binding properties to other substrates and surfaces.

One of the most prevalent fluorophores in fluorescent microscopy is fluorescein. This molecule has been used as a scaffold for cheap, targeted fluorescent tagging for over a century (Lavis, 2017). Fluorescein isothiocyanate is often used due to its reactivity towards amine and sulphydryl groups found on all protein structures. Many variants have been manufactured for use over the past century (see Lavis, 2017 for a full list), one being dialkyl esters of fluorescein (e.g. fluorescein dilaurate). These were developed to increase solubility in organic media in order to probe lipases (Kramer and Guilbault,

1963) and have become the fluorescent tag of choice in studies involving the pancreas due their easy manufacture, low toxicity and long fluorescent lifetime (full review available at Robertson *et al.*, 2013).

Due to its widespread use fluorescein dilaurate is well characterised. It also contains features typical to that of a surfactant; a large hydrophilic head group attached to, in this case two, long hydrophobic hydrocarbon chains. Its solubility in water, though limited, is sufficient for imaging at the concentrations used here (0.1 wt.%, Sigma Aldrich, 2016).

The specificity of the surfactant in these tests is not required to be as refined as that in biological testing. As the target to be probed is a near-homogenous, hydrophobic medium (lard) with bulk properties, fluorescein dilaurate (97 % purity) was considered a suitable fluorescent surfactant molecule for all testing conducted here.

4.1.2 Choice of fluorophore within the soil

The movement of lipid droplets within cells is a current area of intensive research. In the 1900s J. Lorrian Smith developed Nile Blue, a histological stain which interacts with cell nuclei, dyeing them blue (Smith, 1908). This invention was used extensively until Cleine and Dixon (1985) synthesised a variant now known as Nile Red. Nile Red is the oxidative product of Nile Blue and has the key characteristic that it is a hydrophobic and metachromatic dye, varying its emission wavelength from deep red to yellow gold dependant on the exact nature of its environment. Nile Red is highly hydrophobic, exhibiting low levels of fluorescence in water and other polar solvents but undergoes fluorescence enhancement in non-polar environments, making it an ideal candidate to determine when the soil is being solubilised (Greenspan and Fowler, 1985).

Another fluorescent dye commonly used to target lipids is BODIPY 505/515 (Cooper *et al.*, 2010). Both molecules offer rapid and relatively inexpensive doping of hydrophobic media, however in this study Nile Red was chosen due its peak excitation (λ_{ex}) and emission (λ_{em}) wavelengths (552 nm and 636 nm, respectively) being within the range of the available equipment.

A subproject, involving the synthesis of modified BODIPY molecules to increase their surfactant characteristics, was conducted in a summer student project conducted by Amir Akbari. These were intended for use with a two photon CARS microscope, at the Department of Chemical and Environmental Engineering, Soochow University (Suzhou, China). It proved impossible to do the testing during my visit there in September – December 2017 due to breakdown of the microscope.

4.1.3 CFM set-up

Tests used a Leica TCS SP5 inverted laser scanning confocal microscope fitted with four fluorescent detectors (one UV 364 nm, one Argon 488 nm, one HeNe 543 nm, and a HeNe 633 nm) as well as a

standard transmission detector. The key parameter for relative intensity testing is the gain (detector sensitivity) of the CFM. This must be kept constant throughout an individual experiment but may vary between different sets of experiments. The relevant parameters used are listed in Table 4.1.

Table 4.1: *Method parameters for CFM testing.*

	Lard		CMS
Fluorophore	Fluorescein DL	Nile red	Nile Red
Layer thickness / mm	0.1	0.1	0.2
Magnification	x20	x20	x20
Detection λ / nm	500-530	600-640	600-640
Aperture	60.6	60.6	60.6
Gain	800 V	700 V	700 V
Locations detected	4	4	8
Step size / μm	4.99	9.99	9.99
Number of steps	61	50	50
Time per step / s	5.5	5.8	11.4
Number of stacks	53	33	29
Time per stack / min	5.6	4.8	9.5
Total time / min	295	158	276
Scan field rotation / $^\circ$	0	0	0
Smart offset / %	0	0	0
Zoom	1	1	1

4.1.3.1 Substrate/solution chamber

Nunc Lab-Tek borosilicate glass 4 chambered coverslips (25 x 57 x 10.8 mm, Nunc Lab-Tek, 155383) (Figure 4.2) with a coverslip thickness of 130 – 170 μm were used in this study. Each coverslip was mounted with a plastic frame dividing it into 4 identical chambers with dimensions 22 x 11 x 10.8 mm giving a chamber volume of 1 ml.

The plastic mounting was unsuitable for exposure to the thermal conditions required to bake the soil samples (204 - 250 $^\circ\text{C}$) and required removal before the coverslip was soiled. The chamber divisions remained intact due to a hardened silicone mounting gel at a height of approximately 1 mm. 0.2 ml of molten lard ($T = 50\text{ }^\circ\text{C}$) was pipetted on to the base of each chamber. The slip was then baked in air in a conventional oven (Carbolite[®] LHT6/60) at 204 $^\circ\text{C}$ for 2 hours. The samples were left standing in ambient air (20 $^\circ\text{C}$, 48 % humidity) to cool to room temperature before the plastic mount was reattached to the coverslip. Silicone sealant gel was applied to the outer edges to minimise leakages. The sample was covered with paper towelling to minimise dust settling onto the soil and left overnight for the sealant to harden.

Multiple locations can be defined on the confocal microscope. 8 areas were chosen on the coverslip, 2 per chamber, and an experiment run on each area in parallel (Figure 4.2).

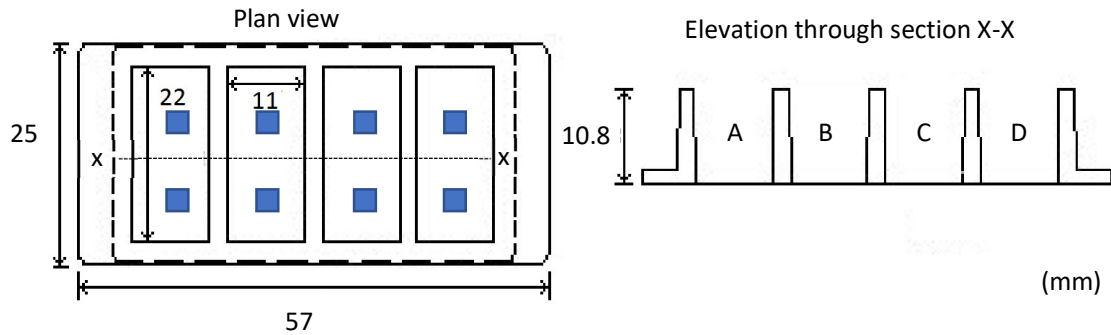


Figure 4.2: *Nunc Lab-Tek Chamber for CFM studies (dimensions in mm) Blue squares show scanned areas for 8 locations set-up used CMS testing. Letters A – D define chamber identities.*

4.1.3.2 Calibration and set-up

The CFM has the ability to focus on, and scan across, a single plane, on multiple planes over a set time period. This technique is henceforth referred to as ‘z-stacking’. A z-plane with $N_z = 0$, is defined at the base of sample and located using transmission microscopy. Multiple Z-planes are then defined at set heights above this plane. Each z-plane is scanned individually using reflectance microscopy, and can then be stacked together to reconstruct a 3D shape (Figure 4.3).

The initial z-plane is then scanned again to start the next Z-stack, with each stack assigned a time point based on the time after submersion of the soil. This allows changes in the thickness of the soil or movement of the surfactant to be monitored nearly simultaneously. This mode was used to monitor both the ingress of surfactant through the layer and the loss of the soil into the solution, dependant on the fluorescent species present in the system. For experiments with Nile Red the measurement start point was set at $50 \mu\text{m}$ below the substrate-soil interface and the z-range set at $500 \mu\text{m}$ split into 50 planes spaced $10 \mu\text{m}$ apart. For fluorescein dilaurate the range was $300 \mu\text{m}$, with 61 planes of height $4.99 \mu\text{m}$.

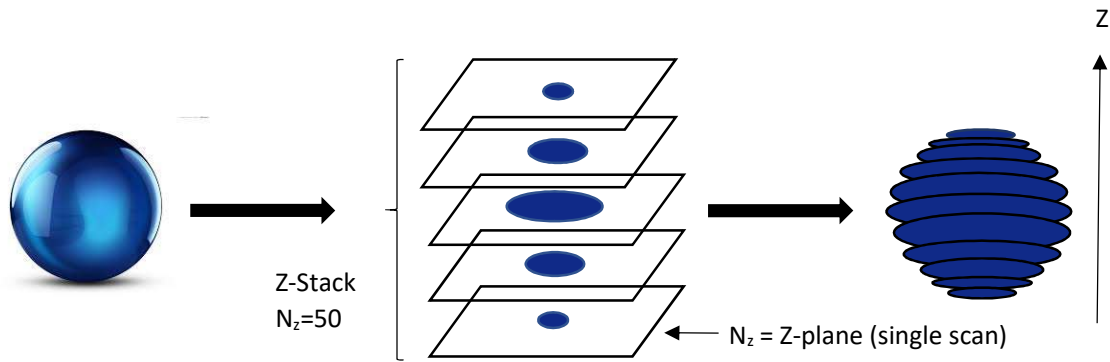


Figure 4.3: Pictographic representation of z-stacking in imaging

Each position (1 – 4 or 1 – 8 on Figure 4.2) produces an averaged intensity of fluorescence (I_i) in that z-plane associated with a time-stamp (t). The data are transposed with an assigned z-stack in MATLAB® and background fluorescence removed via a baseline correction. The total fluorescence of each z-stack is then summed and a percentage of each layer of the z-stack is calculated to give the relative intensity of that z-stack at that time ($I_{R(z,t)}$).

$$I_{R(z,t)}(t) = \frac{I_i(z,t)}{\sum_{i=0}^{i=50} I_i(z,t)} \quad \text{Equation 4.1}$$

The relative intensities of the layers over time are then plotted. The results presented here employ the same z-stack set for each area in a given experiment. The equipment cycles through defined areas 1 – 4 (or 1 – 8), running a z-stack on each before moving to the next location. A full cycle takes approximately 5 minutes (for 4 locations, 10 for 8 locations).

A single z-stack is run on each of the cell positions before 1 ml of surfactant solution is added. The experiment is then set to complete 30 – 50 cycles at each position for a test duration of 2 – 5 hours.

4.2 Results and analysis

The mechanism involved in surfactant based cleaning of hydrophobic soils was shown by Ali (2015(a)) to be dependent upon the level of baking, the soil composition (ratio of hydrophilic to hydrophobic material) as well as the surfactant used. Testing was conducted on the CFM to determine whether the interaction between surfactants and lard soils on the microscale could be resolved. All samples were baked unless stated otherwise.

4.2.1 Surfactant tracking

Initial experiments involved monitoring the movement of fluorescein dilaurate into baked lard layers (Figure 4.4). It is known from previous work (Ali, 2015(a)) that detergents used to clean unbaked fatty soils are not guaranteed to be effective on their baked equivalents. CFM was used to determine if the same mechanism of cleaning applies to both.

The layer at which the surfactant was at its highest concentration was assumed to correspond to the initial position of the soil-solution interface. This was expected as the surfactant had greater affinity for non-polar materials than the aqueous solution. Monitoring the location of the region of highest fluorescence ($N_z = N_{z, (max)}$) was considered to be associated with tracking the movement of the surfactant. This allowed determination of how far the surfactant had penetrated into the soil or alternatively, how much the soil has expanded, in the cases where swelling occurs.

Fresh lard was investigated as a benchmark. Figure 4.4 (a) shows a steady increase in height of the layer emitting maximum fluorescence, i.e. the unbaked fatty soil expands on contact with alkaline surfactant solution. The stepwise nature of the data originate from the discrete z-planes described in the experimental set-up. Absolute values for intensity are arbitrary in this case as they are related to the gain that is set on the microscope in relation to the fluorescence concentration in the $750 \times 750 \mu\text{m}$ area examined. The rate of expansion, or swelling, of the soil is approximately $+0.28 \mu\text{m min}^{-1}$.

Figure 4.4 (b) shows a steady decrease in $N_{z,(max)}$ over time at a linear rate of approximately $0.66 \mu\text{m min}^{-1}$ (twice that of the unbaked soil movement). It is unclear from this experiment whether the fluorescence front is moving due to penetration of the surfactant into the soil layer or due to the removal of the topmost soil. Subsequent experiments were conducted to determine this via fluorescent tagging of the soil layer.

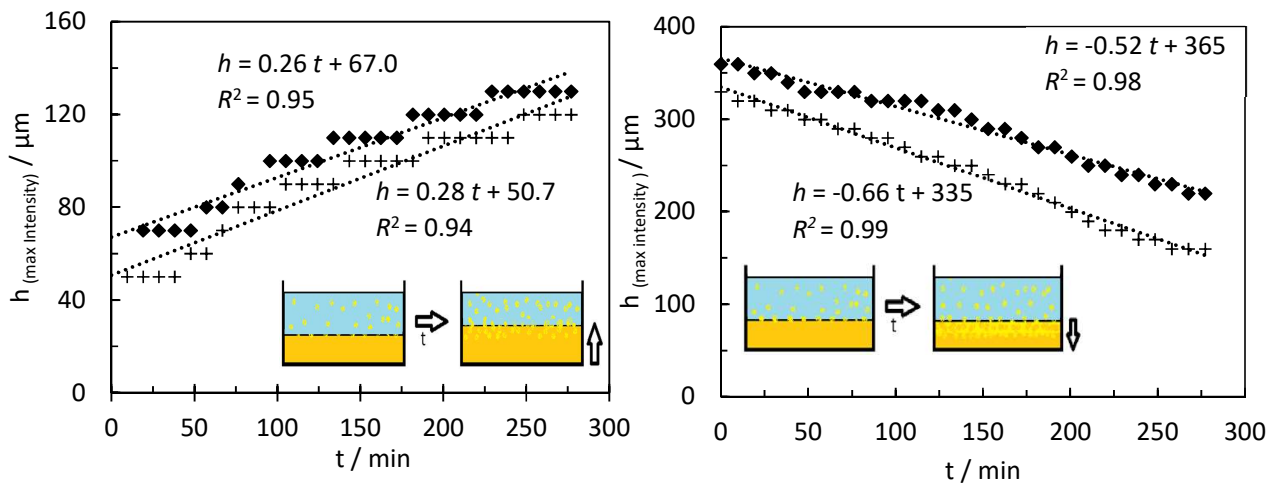


Figure 4.4: Data showing the height of the soils with the maximum concentration of surfactant after submersion of (a) unbaked lard and (b) lard baked at 250°C for 2 hours into a solution of 0.5 wt % fluorescent surfactant at pH 9 and 20°C . Inset shows cartoon of the soil layer expanding over time. Loci show linear regression fits. h is the height of soil layer scanned.

4.2.2 Effect of pH

Figure 4.5 shows that in baked samples a new peak at the soil-substrate interface, coinciding with the movement of fluorescence intensity at the soil-solution interface. This peak is due to the ingress of fluorescent surfactant beneath the soil layer at the interface of the glass and soil over time. The peak, labelled A, forming at $N_z \approx 10 - 15$, corresponding to the interface between the substrate and the soil. A second peak labelled 'B', located at the soil-solution interface ($N_z \approx 15 - 35$), decreases in intensity over time. The decay at $N_z > N_{z,B}$ arises from the unevenness of the surface (the intensity is averaged over an area of 0.56 mm^2) and a concentration gradient in the solution.

Peak A indicates an accumulation of material at the interface. This implies that the surfactant channels through or displaces the soil to form a layer between it and the glass substrate. The appearance of this peak suggests that the adhesion between the soil and the glass surface is more susceptible to the alkaline pH, in combination with the surfactant, than the cohesive bonds within the baked lard soil layer.

It is of note that the first data point is obtained 8 minutes after submersion, with each subsequent data point 8 minutes apart. Any hydration of the soil would occur within these first 8 minutes and therefore will not be visible in the test data. Burnt lard is however a highly hydrophobic soil (Ali, 2015(a)) and therefore hydration is expected to be limited.

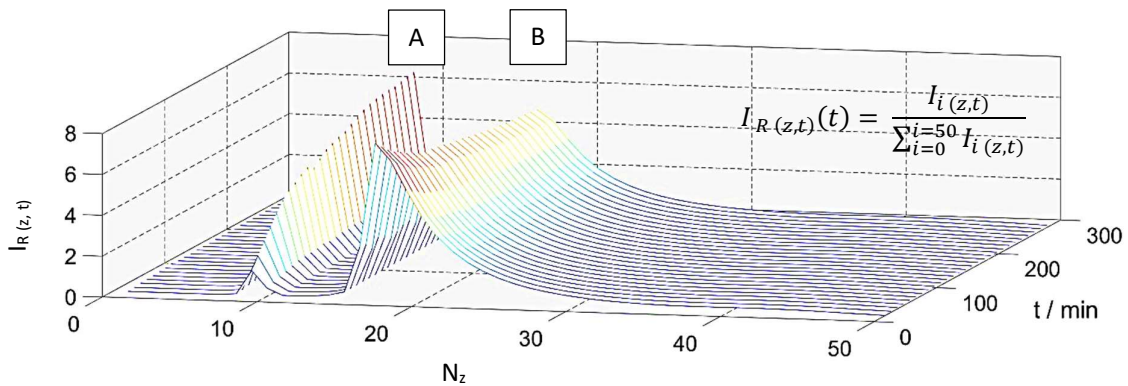


Figure 4.5: Fluorescence microscopy of baked lard soil surfaces exposed to alkaline surfactant solutions at pH 8, 20 °C over 4 hours. Peak A is at the soil-substrate interface, B at the soil-solution interface. Plots obtained for pH 9-13 demonstrated similar behaviour.

Experiments run at pH 9-13 on baked samples showed similar ingress behaviour (Figure 4.6). The increase of the new peak was plotted for each position, presented as the relative intensity, I_R (Equation 4.1), due to variability in the total fluorescence intensity recorded. This is due to diffusion of the surfactant into/out of the small area monitored in the confocal microscope. All pHs demonstrated

similar histories; a sharp increase in surfactant concentration beneath the soil followed by reduction in the rate of increase.

The ingress can be modelled using a simple exponential decay function (Equation 4.2);

$$(I_{R,A} - I_{R,A=0}) = \Delta I_{R,A(\infty)} \left(1 - e^{-\frac{(t-t_0)}{\tau_{CFM}}} \right) \quad \text{Equation 4.2}$$

where $I_{R,A}$ is the relative fluorescence intensity in peak A at time t , $I_{R,A=0}$ is the background fluorescence intensity, $\Delta I_{R,A(\infty)}$ is the change in intensity at time $t = \infty$, t is time, t_0 is the time at which immersion occurs, and τ_{CFM} is the half-life which yields a first order rate constant, k_{CFM} , via

$$k_{CFM} = \frac{1}{\tau_{CFM}} \quad \text{Equation 4.3}$$

The rate of ingress was similar for $8 \leq \text{pH} \leq 10$, with rate constants $k_{CFM} = 0.12 - 0.17 \times 10^{-3} \text{ s}^{-1}$ and similar asymptotic values ($I_{R,A(\infty)} \sim 6.7 - 7.4$) (Figure 4.6 (a)). At higher pH the initial rate of ingress decreased with increasing pH though its magnitude after 300 s remained constant (Figure 4.6 (b)). The time taken to reach an asymptote in intensity increased with increasing pH, with pH 13 appearing linear during the 300 min test period. It is likely that the asymptote indicates the saturation point in each case which is dependent upon available space at the soil-substrate interface. As pH increases, so does the soil swelling (see Ali, 2015(b) and discussed in Chapter 5): this could decrease the voidage at the soil-substrate interface as the soil swells into the gaps, decreasing the rate of ingress.

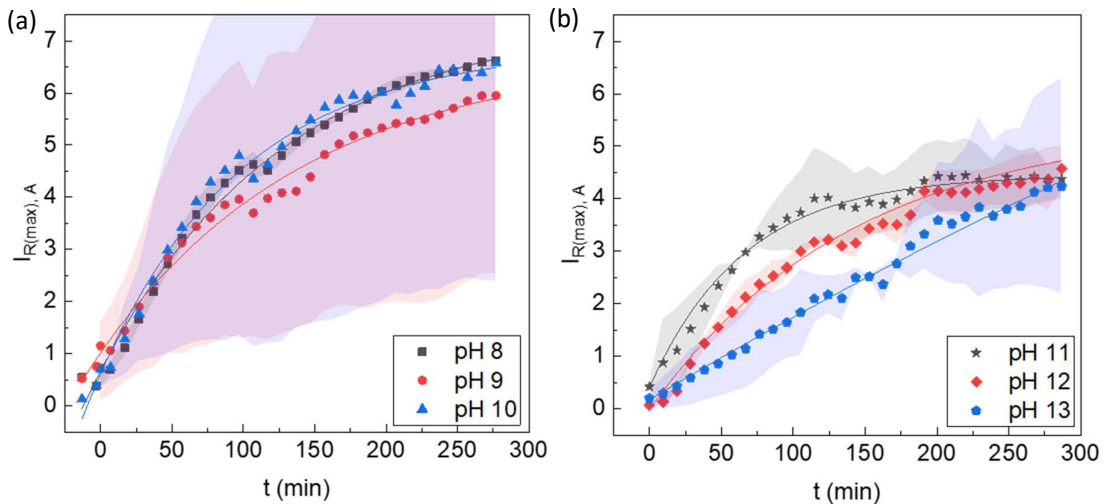


Figure 4.6: Evolution of peak A in baked lard (Peak A shown on Figure 4.5). a) pH 8-10 b) pH 11-13. Lines show fit to Equation 4.2., with parameters in Table 4.2. Shading represents one standard deviation of data from an average of 3 samples.

The profiles at pH 14 were very different: the binary peak structure was swamped by a uniformly high baseline. No further studies were conducted at pH 14.

At pH 8 – 10 the rate of ingress of the surfactant solution was slow compared to that desired in a dishwashing cycle. In these tests the soil was submerged in surfactant solution and solution penetration only occurred fully after 270 minutes, which is longer than a typical dishwashing cycle. In a dishwasher the soil is unlikely to experience constant contact with the cleaning solution, and therefore this timescale is likely extended, dependent upon the level of surface wetting. Increasing the pH to 11 gave a higher rate constant ($k_{CFM} = 0.25 \times 10^{-3} \text{ s}^{-1}$ vs $0.13 - 0.17 \times 10^{-3} \text{ s}^{-1}$ at pH 8 – 10). This pH is not practical for consumer applications due to safety concerns. Beyond pH 11 the rate constant of ingress rapidly decreases. This decrease may be a function of enhanced soil swelling promoting a change in cleaning mechanism, from surfactant ingress at the soil-substrate interface to soil breakdown or saponification.

Table 4.2: Kinetic parameters of Figure 4.6 (a) pH 8 – 10 and (b) 11 – 13.

(a)

pH	k_{CFM} $\times 10^{-3} / \text{s}^{-1}$	t_{asym} / s
8	0.13	> 16,000
9	0.12	> 16,000
10	0.17	> 16,000

(b)

pH	k_{CFM} $\times 10^{-3} / \text{s}^{-1}$	t_{asym} / s
11	0.25	11,400
12	0.12	15,000
13	0.014	> 16,000

This work shows that when cleaning lard soils from glass with alkaline water, a pH of 11 should be used to promote the ingress of solution to the soil-substrate interface. Further work is required to investigate the impact of changing the surface energy and composition on solution ingress behaviour.

4.2.2.1 Diffusion modelling

The evolution of intensity of peak A is suggestive of a diffusion-controlled process. The simplest form of diffusion model for this case is that of a semi-infinite slab, which for the dilute case can be described by (Crank, 1975);

$$\frac{I}{I_0} = \text{erf} \frac{x}{\sqrt{4Dt}} \quad \text{Equation 4.4}$$

where I is the local intensity ($I(x,t)$), x is the distance into the material, t is time and D is the diffusion coefficient. The error function is linear for argument values up to 0.5, i.e. $I/I_0 \propto t^{0.5}$. The plot of I_A/I_0 against $t^{0.5}$ in Figure 4.7 shows quasi-linear behaviour for pH 8: pH 9-13 data sets gave similar results.

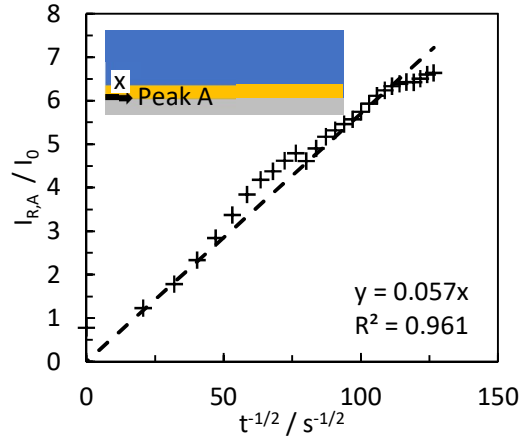


Figure 4.7: Comparison with simple diffusion model (Equation 4.4) for pH 8 surfactant ingress study in baked lard soil. $D_{eff} = 76.9 \mu\text{m}^2 \text{s}^{-1}$. Inset: schematic of substrate-soil-solution interface showing the location of ingress.

One shortcoming of the above model is that the $I_{R,A}$ values reported are normalised and the absolute values are needed for modelling. Moreover, the monitored location is not at the edge of the cell, and the spatial distribution needs to be considered: the contribution from different values of x or y within the field of view needs to be calculated. For a finite 1-D slab of thickness $2l$, the local concentration, C , is given by (Crank, 1975);

$$\frac{C}{C_0} = \frac{4}{\pi} \sum_{n=0}^{n=\infty} \frac{1}{2n+1} e^{-\frac{D(2n+1)^2 \pi^2 t}{l^2}} \sin \frac{(2n+1)\pi x}{l} \quad \text{Equation 4.5}$$

Video analysis of the change of the fluorescence intensity over the $750 \times 750 \mu\text{m}$ spot was conducted. This showed that the increase in fluorescence occurred directionally as the surfactant diffuses into the monitored section and so the approximation shown in Equation 4.5 can be used (Figure 4.8).

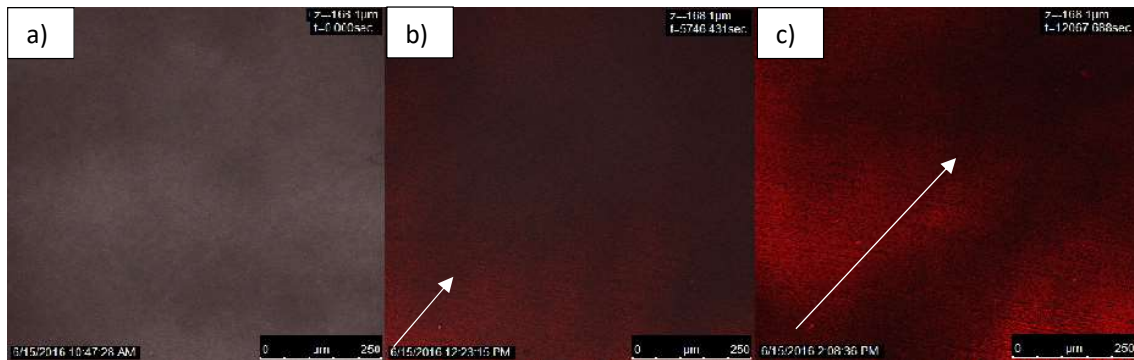


Figure 4.8: Photographic stills taken during CFM testing of fluorescence distribution in baked lard. a) $t = 0$, b) $t = 5746 \text{ s}$, c) $t = 12067 \text{ s}$. White arrow indicates movement of dye from outside the viewing plane across the viewing window in as a single front over time.

Fitting the model to the data in Figure 4.9, and assuming measured intensity is proportional to the fluorophore concentration, gave an estimated diffusion constant of $4.5 \times 10^{-7} \text{m}^2 \text{s}^{-1}$. Values of similar

order were obtained for pH 9 - 13. This is significantly larger than expected for Fickian diffusion in a liquid, where D is of the order of 10^{-9} to $10^{-10} \text{ m}^2 \text{ s}^{-1}$ (Crank, 1975). Penetration of a liquid through a solid is highly dependent on the solid porosity and liquid viscosity. The penetration rate tends to be higher than the rate of simple diffusion, indicating that there is another effect occurring other than simple diffusion of a surfactant through the liquid phase (Javadi *et al.*, 2017). It is possible that the lard soil contains air bubbles throughout which, once a small layer has been 'cleaned' or removed into the solution, allows a 'rush' of solution to fill the void. If this were the case it would be expected that the data would be more step-wise. This would be hard to capture here as images could only be taken at intervals of 5 minutes or longer. Surface tension driven flow, including Marangoni effects, may be responsible (Javadi *et al.*, 2017).

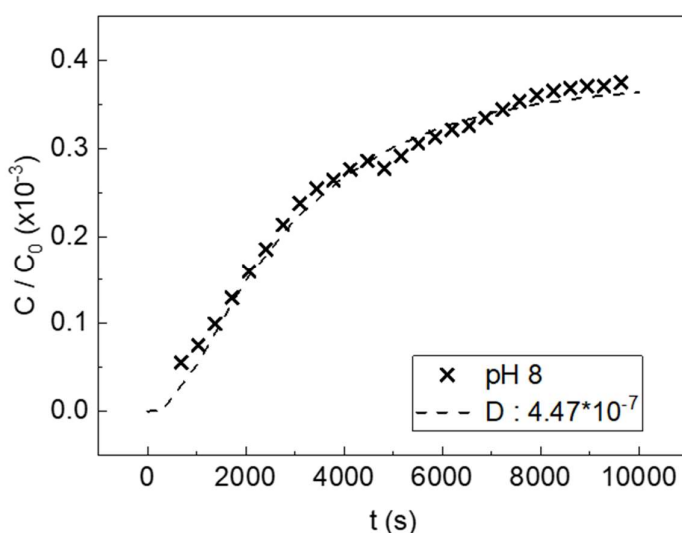


Figure 4.9: Diffusion modelling of surfactant ingress onto baked lard at pH 8. Points: data, Line: fit to Equation 4.5 with $D = 4.47 \cdot 10^{-7} \text{ m}^2 \text{ s}^{-1}$

4.2.3 Effect of surfactant

The soil was made fluorescent by doping 0.2 ml of lard with 1 wt. % Nile Red before baking for 2 hours at 204 °C. The soil was deposited into each chamber to give an initial layer of thickness 100 – 150 μm. Each cell was subject to a different solution environment and the level of fluorescence of the Nile Red (and, it was assumed, the lard soil) was recorded as it dissolved into the solution over a period of 254 min. Four chambers (A – D) were prepared as follows:

- A. No solution added – dry, control
- B. pH 7 aqueous solution added (1 ml, 20°C)
- C. pH 9 NaOH_(aq) solution added (1 ml, 20°C)
- D. pH 9 NaOH_(aq) + 1 wt. % SDBS (1 ml, 20°C)

The test at pH 9 gave a greater overall intensity than dry or pH 7 (Figure 4.10 (a, b, d)). This is either due to deprotonation of the Nile Red molecule in the lard soil by the alkaline solution, causing the probe to emit at greater intensity, or is an artefact resulting from uneven distribution of the Nile Red in the lard soil between the 3 cells. All three samples showed no change in fluorescence intensity over time.

The intensity is recorded as an arbitrary unit dependent on the gain set in the detector. As long as the gain remains constant throughout the experiment the absolute values of the recorded intensity are not the values of most importance: it is the trend in intensity over time that is under investigation.

The fluorescence intensity recorded in each of the 50 z-stacks was summed to give the total z-stack intensity over the cycle and divided by the starting intensity, I_0 , to give the retained intensity, I_t :

$$I_t = \frac{\int_{N=L}^{N=50} I_{(z,t)} dz}{\int I_{(z,0)} dz} = \frac{\sum I_{(z,t)}}{\sum I_{(z,0)}} \quad \text{Equation 4.6}$$

Figure 4.10(d) shows that the retained intensity for chambers A – C showed a slow decrease (from 1.0 to 0.95 for cell 3), which is attributed to slow bleaching of the Nile Red over the course of the experiment.

The pH 9 solution containing 1 wt. % SDBS showed a significant decay in retained intensity over time. This loss of intensity was non-linear and appeared to be progressing towards a plateau, which is interpreted as the amount of soil removed reaching a limit.

One explanation for the asymptotic behaviour is that the solution may have been becoming saturated. The 1 ml of surfactant solution is static over the course of the 254 min test. This would result in a changing concentration difference as the soil was ‘dissolved’. One method of testing this hypothesis would be to remove the saturated solution mid-way through the test and replace it with fresh solution. The physical arrangement of the cells in the microscope make this a difficult task. An alternative method would be to set up a flow cell so that the soil is always in contact with fresh surfactant solution, however this could also introduce forces promoting cleaning through a mechanical mechanism rather than the chemical mechanism under investigation.

A simple model can be constructed which exhibits the trend, assuming that the change in fluorescence is first order in the amount of soil present not in the solution as quantified by I_t . When I_t reaches a value of 0.37 (taken from Figure 4.10 (d)), it is saturated so no further dissolution occurs. This gives

$$\frac{dI_t}{dt} = k'(I_t - I_t^*) \quad \text{Equation 4.7}$$

where k' is a rate constant. Setting $I_t^* = 0.37$ yields

$$I_t - 0.37 = e^{-k't+c} \quad \text{Equation 4.8}$$

Figure 4.10 (d) shows that this model fits the data well, indicating that the loss of material into the solution follows first order kinetics, similar to those observed for the ingress of solution at the soil-substrate interface in Figure 4.6. The rate constant k' was $8.1 \times 10^{-4} \text{ s}^{-1}$, which is larger than that for solution ingress ($k_{CFM} = 1.2 - 2.5 \times 10^{-4} \text{ s}^{-1}$) though of the same order of magnitude. This increase in rate constant can be attributed to the presence of the surfactant enhancing the cleaning of the soil.

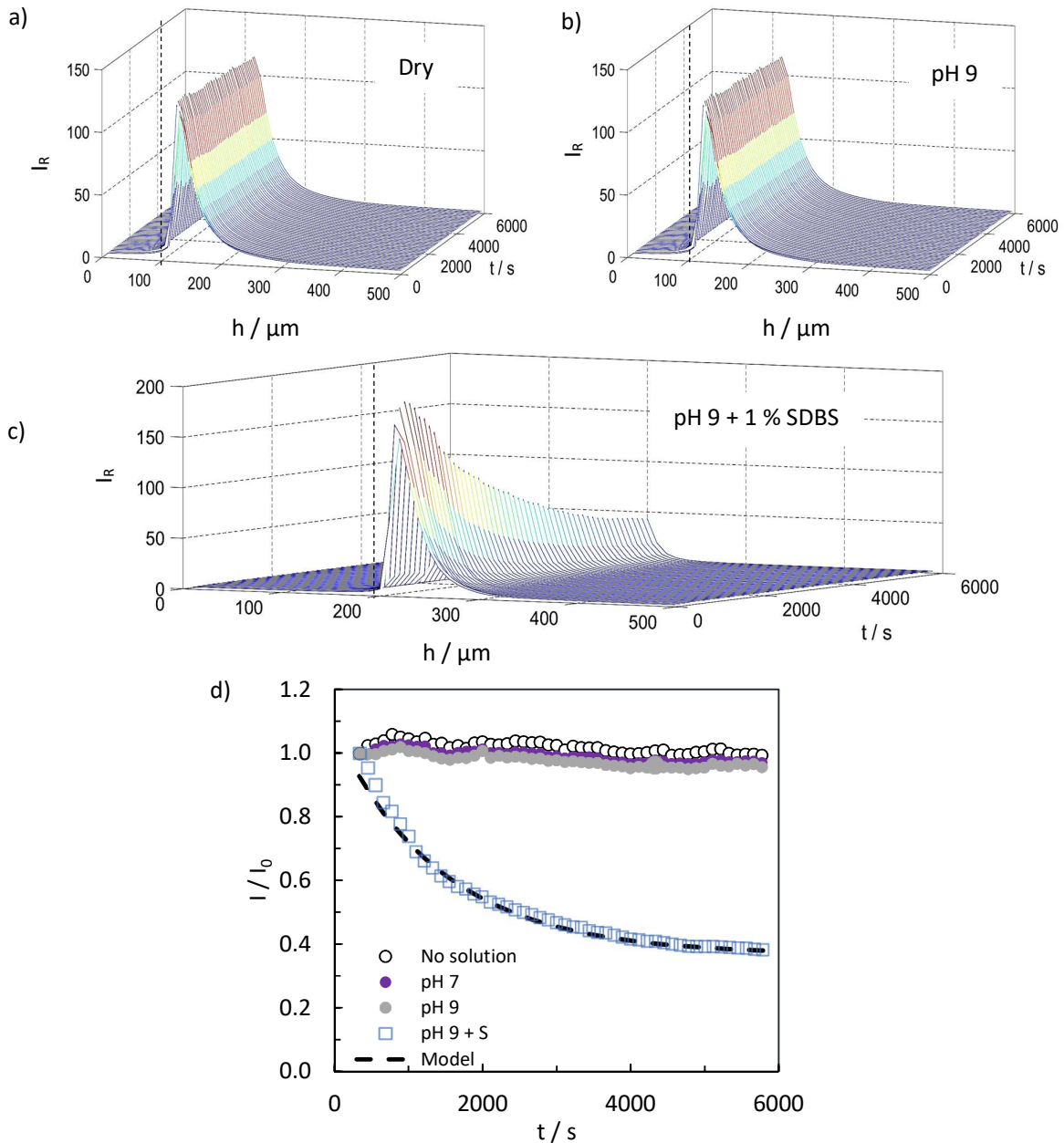


Figure 4.10: Fluorescence intensity plots of Nile Red fluorophore in lard baked at 204 °C for 2 hours then submerged in a) sample 1, no solution, (dry); (b) sample 3, pH 9 solution, (c) sample 4, pH 9 solution + 1 wt.% SDBS (S) over 4 hours 14 min 10 s. Results for sample 2, pH 7, not shown. Vertical dashed lines show approximate location of substrate-soil interface (d) Evolution of retained intensity for samples 1 - 4. Model based on Equation 4.8.

4.2.3.1 Effect of surfactant concentration and type

The impact of increasing the concentration of the surfactant, as well using alternative types (cationic vs anionic), was also investigated using the CLSM method. Figure 4.11 shows that a 0.5 wt. % solution of CTAB, a cationic surfactant, prompted a significant increase in intensity measured in the lard soil for approximately 4500 s. This was followed by a slight decrease in the peak intensity indicating cleaning or solubilisation of the Nile Red doped soil.

Further studies using SDBS showed that halving the concentration (0.5 wt. % compared to previous tests at 1 wt.%, CMC = 0.005 wt.%) gave a shorter period of increased intensity (to 1500 s) followed by a gradual decay. No change in fluorescence intensity was observed in the absence of surfactant. This indicates that surfactant action is responsible for the changes in soil fluorescence intensity. The direction of intensity change is likely related to whether the mechanism of surfactant action is to first penetrate into the soil then solubilise it or to directly solubilise the soil at the surface. The increase in intensity is considered to be due to the experimental set-up only monitoring a small section of the soil. As the soil swells more soil (and therefore more Nile Red) is brought within the frame of view (0.8 mm by 0.8 mm). This leads to an overall increase in fluorescence intensity relative to the initial fluorescence.

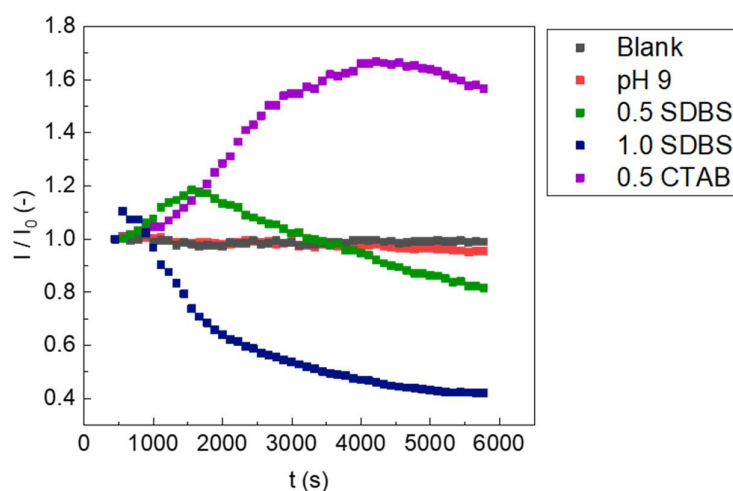


Figure 4.11: Fluorescence of Nile Red in lard soil layers exposed to surfactant solutions. All solutions at pH 9 except the 'blank'. Concentrations in wt.%.

It is assumed that the dye does not dissolve into the water separately from the lard. Visual inspection of the microscope slip after each experiment indicated that the residual soil contained dye.

4.2.4 Preliminary conclusions

Two mechanisms of surfactant behaviour and soil response have been observed with the lard soils. The method of cleaning is dependent on the nature of the soil layer (e.g. baked lard soils vs fresh lard)

and the solution (pH, surfactant concentration). This work demonstrates the importance of identifying the nature of the soil to be cleaned. With fresh lard the surfactant material was shown to act at the surface of the lard, which swelled after exposure to the alkaline surfactant solution. Acidic solutions were not tested. Conversely, with the burnt material, the fluorescent surfactant either penetrated into the soil or remained at the surface whilst the soil was being solubilised. Fluorescein dilaurate is a non-ionic molecule and is expected to have limited cleaning action with burnt hydrophobic materials. This would indicate that the molecule is instead penetrating into the soil layer.

Using Nile Red to investigate the changes in the soil layer over time showed that the presence of surfactants strongly influences the behaviour of the soil. At pH 9, the cationic surfactant tested caused the soil to fluoresce significantly, indicating swelling of soil into the viewing window, while when submerged in the anionic surfactant solution (Figure 4.11) the soil appeared to be solubilised away. At lower concentrations of surfactant the initial increase in intensity of soil dye after exposure to the solution was higher than the initial cleaning intensity changes, indicating that the soil swelled (increasing fluorescence) before the solubilisation outpaced the swelling, and the fluorescence decreased at a steady rate. Choice of surfactant type and concentration is therefore critical for targeting a particular cleaning mechanism in a chosen system.

At this point in the work focus shifted from the lard-based hydrophobic soils used by Ali towards heterogeneous soils, specifically CMS. Further work was planned during a study placement in Soochow University (Suzhou, China) however this was not possible due to equipment failure.

4.3 Cleaning of complex model soils

Preliminary experiments were conducted on CMS samples, both with fluorescent surfactant and with fluorescent soil, however they yielded little useful data for the following reasons:

1. The cheese powder within the CMS mix contains a fluorescent component which interferes with the fluorescent surfactant and dyes.
2. The porosity of the baked CMS is high due to channels generated from the evaporation of the water within the mix (from the milk and pasta) and possibly from the generation of CO₂ in the breakdown of the starch.
3. The soil swelled markedly when exposed to alkaline surfactant solution (Figure 4.12).

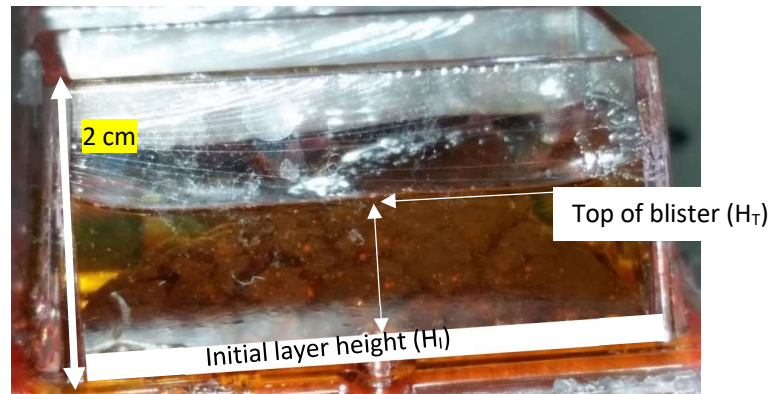


Figure 4.12: Photograph of a swollen layer of CMS soil immersed in pH 9 SDBS solution.

For this reason, the standard protocol could not be used as the thickness of the swollen CMS layer exceeded the 500 μm range of the microscope stage within 10 minutes. In its place a 'wide' stage was used with a range of 2 mm. The CMS soil was also doped with Nile Red to allow the swelling of the layer to be tracked by fluorescence. As only one location was analysed (previously 8) the time to run a stack was decreased to 34 s, increasing the time-dependent resolution of the technique.

Figure 4.13 shows samples of raw data recorded during the experiment. The surfactant was added at 100 s (after stack 2). The appearance of a new peak, H_T , 150 s after the surfactant was added at 100 s represents the blistering of the CMS. Peak H_i corresponds to the residual layer left on the substrate and peak H_T to the top of the swollen CMS layer. The height of the blister, given by the separation of H_i and H_T , increases over time.

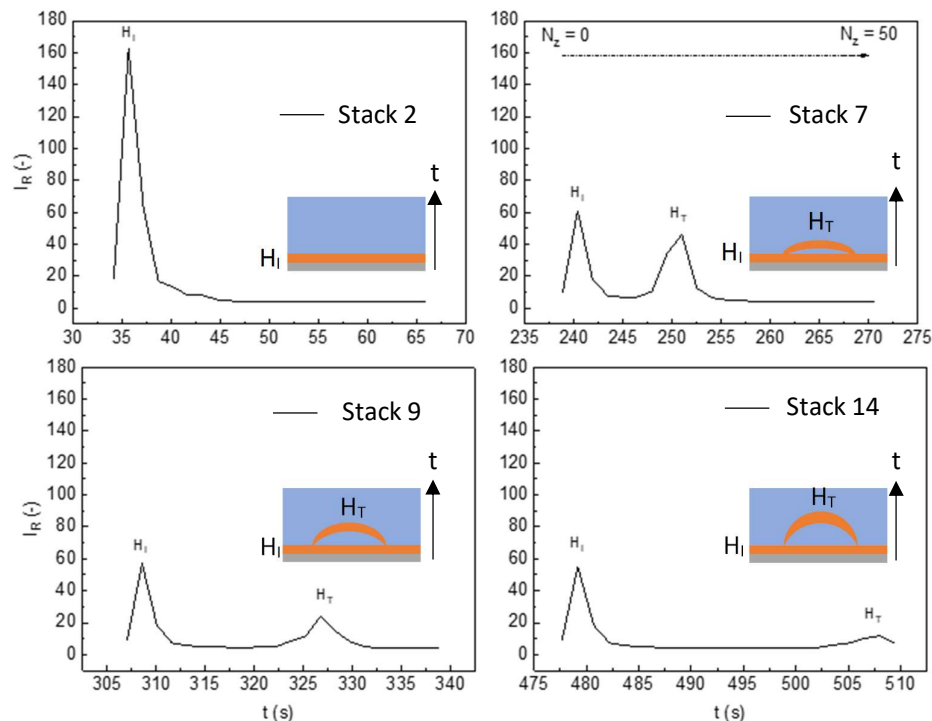


Figure 4.13: Total emission intensity of Nile Red in selected z -stacks over time. CMS soil layer contacted with pH 9 + 1 wt % SDBS solution at $t = 100$ s. Solution was added at z -stack 3. Insets show cartoon representation of peak location for clarity.

The intensity of each z-plane over time is plotted in order to track the upward movement of the top layer of CMS (H_T on Figure 4.13). The longer the CMS was in contact with the solution, the broader the fluorescence peak, indicating that the CMS was no longer swelling, forming the top of the blister shown in Figure 4.12.

Figure 4.14 shows that the expansion of the layer was rapid: it expanded from an initial thickness of 0.2 mm to approximately 2.2 mm after 500 s. It is unclear whether further expansion of the material occurred after this time as the detection limit of the CFM apparatus was reached.

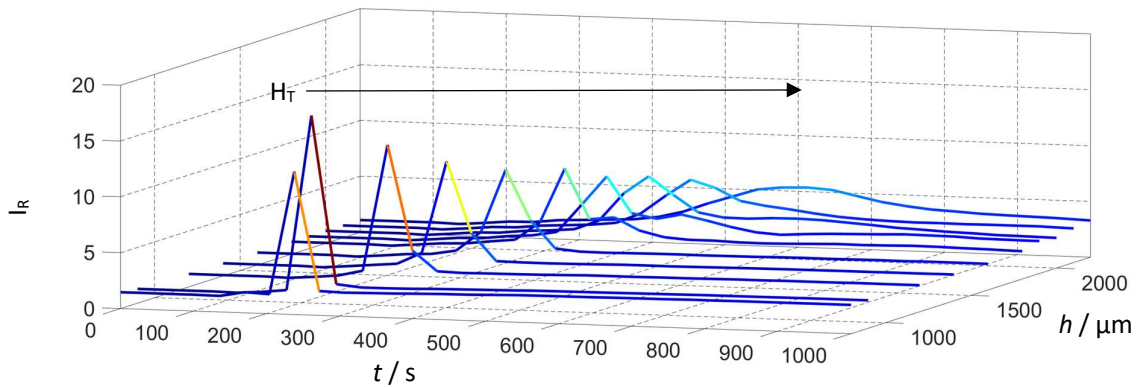


Figure 4.14: Fluorescence intensity of Nile Red probe in CMS in pH 9 solution. Each line is the recorded intensity over time of each layer of the recorded z-stack. H_T shown. H_i removed for clarity.

After swelling the fluorescence intensity within the swollen region drops back down to the baseline value, e.g. the soil at 2500 s in Figure 4.14 no longer fluoresces after at 400 μm . This indicates that the swelling of the soil involves the creation of a void rather than a thinned or expanded soil network, as the latter would still fluoresce in this region after expansion has occurred. The void appears to be filled with solution rather than CMS soil upon swelling.

The location of the soil-solution interface peak is plotted against elapsed time in Figure 4.15. Two data points were excluded from the set as these anomalous results were obtained during the addition of surfactant solution.

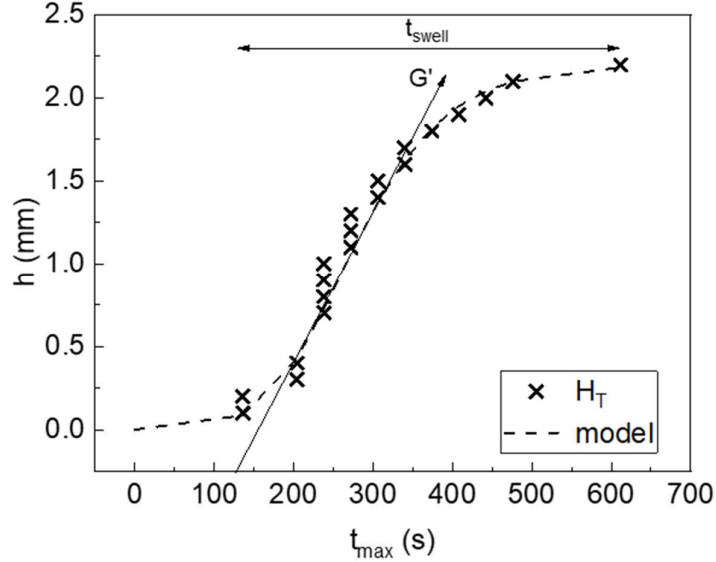


Figure 4.15: Points: Evolution of height of location of soil-solution interface. Points: measured H_T from Figure 4.14. Dashed line: Generalised logistic function (Equation 4.9) fit to the data. G' (swelling rate) = $h / t_{swell} \approx 5 \mu\text{m s}^{-1}$.

The generalised logistic function (or Richards' Curve) was fitted to the data manually. G is representative of the growth rate of the curve in this instance.

$$z(t) = \frac{Z_{max}}{(c_1 + c_2 e^{-G(t-c_3)})^{c_4}} \quad \text{Equation 4.9}$$

The parameters obtained from fitting Equation 4.9 to Figure 4.15 are $G = 0.014 \text{ s}^{-1}$, $Z_{max} = 2200 \mu\text{m}$, $c_1 = 1$, $c_2 = 0.005$, $c_3 = 550 \text{ s}$, and $c_4 = 3.3$. The value of G is related to the swelling rate. Values of G , along with Z_{max} , could be used to compare results from different tests. G' (shown on Figure 4.15) can also be calculated graphically to give a linear swelling rate (assuming symmetry in the curve). For this test G' was found to be approximately $5 \mu\text{m s}^{-1}$ which is considerably faster than that found for the swelling of baked lard ($G'_{lard} \approx 0.005 \mu\text{m s}^{-1}$). This is attributed to the higher porosity in the CMS allowing faster surfactant penetration. There is also more chemical complexity in the CMS layer and so more components to interact with the OH^- ions in the pH 9 solution. A more rigorous model, based upon situationally relevant values, would be preferred to the generalised logistic function used here. The interpretation of constants c_1 - c_4 was not pursued.

The swelling behaviour observed above made the use of the CFM impractical to observe the ingress or penetration of surfactant into a CMS layer, as the resolution required to gather meaningful spatial data, achieved with lard at a z -range of 0.3 mm, is smaller than the z -range required to capture the soil layer during swelling ($\sim 2.5 \text{ mm}$). Alternative techniques, which function at a larger scale, were therefore used to monitor the swelling of CMS after exposure to a range of cleaning conditions (Chapter 5). The mechanism of solution wetting of the layer, either by ingress or penetration

mechanisms, were explored further for CMS in Chapter 6. Other factors, such as the fluorescence interference from the constituents of CMS, along with its high porosity, contributed to the decision that no further studies would be conducted on the CFM at Cambridge.

4.4 Conclusions

There are a number of findings in this chapter that have implications for the cleaning of burnt soil materials. Primarily the chemical nature and complexity of the soil has been shown to have a marked impact on its response to submersion in simple cleaning solutions.

Two techniques for quantifying visual monitoring of the cleaning mechanisms of burnt lard soils were developed. The first focused on the movement of the surfactant in the cleaning solution upon exposure to the soil, utilising the molecule fluorescein dilaurate as a fluorescent surfactant. These studies highlighted that the mechanism of surfactant interaction with the soil can be considered to be dependent upon its baking time (and thus chemical changes that occur in the soil during baking). Unbaked lard showed an increase in the layer height at which the surfactant had concentrated, indicating both that the surfactant had concentrated at the soil-solution interface and that the soil was expanding. For burnt lard, surfactant concentration was observed at a lower height through the soil, indicating either that the surfactant was penetrating into the soil layer or that surfactant remained on the soil-solution interface but that the material was being eroded away by the solution. As burnt lard has been found to be insoluble in aqueous solutions (Ali, 2015(a)) the former explanation is considered more likely. This mode of action was defined as solution penetration.

Above pH 8, a secondary mechanism of solution interaction was observed: solution ingress. In these studies the surfactant moved into the soil at the soil-substrate interface with a rate constant of $k_{CFM} \approx 0.15 \times 10^{-3} \text{ s}^{-1}$. The kinetics of ingress were dependent upon the solution pH with the optimum at pH 11. A simple diffusion model of movement of a species through a 1-D slab of thickness $2L$ based on the work by Crank (1975) was shown to give reasonable fit to the data and a diffusion constant of $D = 4.47 \times 10^{-7} \text{ m}^2 \text{ s}^{-1}$. This is attributed to a wetting driven flow.

The second technique focused on the behaviour of the burnt lard soil upon exposure to a cleaning solution. A fluorescent dopant, Nile Red, was used to monitor changes in the soil layer thickness and concentration. Increasing the pH of the solution was shown to have no impact on the fluorescence intensity of the soil, indicating that no solubilisation of the soil was occurring. This indicates that at increased pH the surfactant ingressed into the soil layer, but did not promote removal.

Addition of surfactants to the cleaning solution caused changes to the soil dye intensity, which was correlated to soil thickness, the nature of which was dependent upon the surfactant type. 1 wt.% CTAB

caused the soil to fluoresce intensely upon submersion, to almost 180 % of its original fluorescence, indicating swelling was occurring. Solubilisation of the layer occurred after ~4000 s. SDBS at 0.5 wt.% caused the soil to fluoresce for ~1500 s before solubilisation occurred, and increasing the concentration to 1 wt.% caused solubilisation of the soil to take place in <500 s. As readings could only be taken every 8 minutes in this set-up, better resolution of the events was not feasible.

Preliminary testing was conducted on the heterogeneous CMS, but it was found to swell rapidly and blister within 500 s of exposure to the solution. The scale of the blistering ($h = 0.2$ mm at $t = 0$ s to $h = 2.2$ mm at $t = 500$ s) meant that the CFM, with a z-axis resolution range of 2 mm in wide frame (low resolution) and 1 mm in standard (higher resolution) modes was unsuitable for studying this system. Chapter 5 describes the use of equipment better suited to monitor this scale of change within the soil.

In summary the CFM was able to distinguish between different cleaning mechanisms involved in cleaning baked soils. In the simple lard-based systems the promotion of each mechanism was shown to be dependent upon surfactant, baking time, pH and soil type.

4.5 Timescales of cleaning

Establishing the timescale of cleaning is important for comparison between different techniques and cleaning monitoring systems. Here the timescale of cleaning was primarily dependent upon the soil type. The simple hydrophobic soil reached final penetration after approximately 16,000 s in pH 7 water with a rate constant $k_{CFM} = 1.3 \times 10^{-4} \text{ s}^{-1}$. The most effective solution tested here, pH 11, had the shortest t_{asym} of 11,400 s and rate constant of $2.5 \times 10^{-4} \text{ s}^{-1}$. Adding surfactant decreased t_{asym} of soil erosion to ~ 6000 s with a cleaning rate constant of $7.7 \times 10^{-4} \text{ s}^{-1}$. For CMS soil layers, however, the soil blistered immediately and reached its maximum within 600 s, a factor of 10 shorter than the hydrophobic lard soil. The various timescales recorded in these investigations are discussed further in Chapter 8.

5. Soil hydration and swelling

Swelling is a key step in the cleaning of complex food soils as it promotes access of cleaning agents into the soil matrix, increasing the rate of reactions involved in cleaning as well as the dissolution of soil components. The presence of water also weakens the deposit, causing it to be easier to remove via hydraulic action. FDG was used to investigate this aspect of cleaning.

5.1 zFDG

Fluid dynamic gauging was developed by Tuladhar *et al.* (2002) at the University of Cambridge to monitor the thickness and strength of deposit layers which deform readily when contacted with a solid probe (i.e. have low elasticity). This non-contact technique has been developed over the past 15 years and is now capable of resolution $<10 \mu\text{m}$ (Tsai *et al.* 2019).

A schematic of the fundamental principles of FDG action is shown in Figure 5.1. A nozzle, of known geometry (nozzle throat diameter, d_t , nozzle lip width, d_l), is located at a set distance, h_0 , from a hard surface. The apparatus is submerged in a solution of known density, ρ , and viscosity, μ , such that no air can be entrained. Liquid is then passed through the nozzle, by ejection or suction, at a set mass flow rate, \dot{m} , causing a pressure drop ΔP_{12} . When all other conditions (d_t , d_l , μ , ρ , Re_t and nozzle geometry) are fixed the magnitude of ΔP_{12} is dependent only upon the measured distance between the nozzle and the closest surface, h , by the relationship

$$C_d = f\left(\frac{h}{d_t}, \frac{d_l}{d_t}, Re_t\right) \quad \text{Equation 1.1}$$

Here C_d is the discharge coefficient (a dimensionless pressure drop) and Re_t the Reynolds number evaluated at the nozzle throat, defined $Re_t = 4\dot{m} / \pi\mu d_t$.

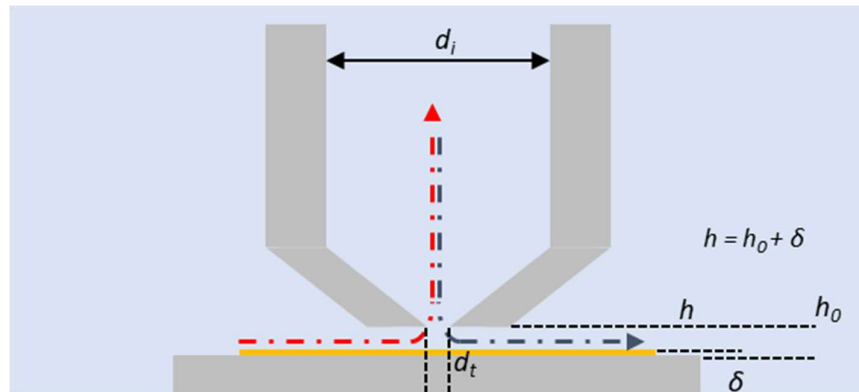


Figure 5.1: Schematic of fluid dynamic gauging action. δ is the soil layer thickness; h the clearance between the nozzle and soil layer; h_0 the clearance between the nozzle and substrate; d_t the diameter of the nozzle throat; d_i the inner tube diameter.

C_d is defined

$$C_d = \frac{\dot{m}}{\frac{\pi}{4} d_t \sqrt{2\rho\Delta P_{12}}} \quad \text{Equation 5.2}$$

Giving the relationship for h and ΔP_{12} in a given nozzle geometry as;

$$\frac{h}{d_t} = f\left(\frac{\Delta P_{12}}{\dot{m}}\right) \quad \text{Equation 5.3}$$

This enables the thickness of the deposit, δ , to be calculated from;

$$\delta = h_0 - h \quad \text{Equation 5.4}$$

where h_0 is measured independently of the FDG functionality. In this work h_0 is determined initially via the use of a feeler gauge (used with the zFDG apparatus). A calibrated mechanical positioner was used for increased accuracy (built into the SiDG apparatus, an FDG iteration developed as part of a collaboration, reported later in this chapter). A representative calibration plot for C_d vs h_0 is shown in Figure 5.2. The relationship is almost linear for $0.07 < h_0/d_t < 0.2$ followed by an approach to an asymptotic value (here, 0.76), at large clearance. For $h_0/d_t < 0.07$ the upper limits of the pressure transducer have been exceeded. The functional window for dynamic gauging under these conditions is taken to be $0.07 < h_0/d_t < 0.27$. A software feedback mechanism similar to that designed by Gordon *et al.* (2010) and utilised by Wang *et al.* (2016) ensures the nozzle clearance remains within this range via automated retraction/advancement of the nozzle should the measured pressure drop fall outside acceptable limits.

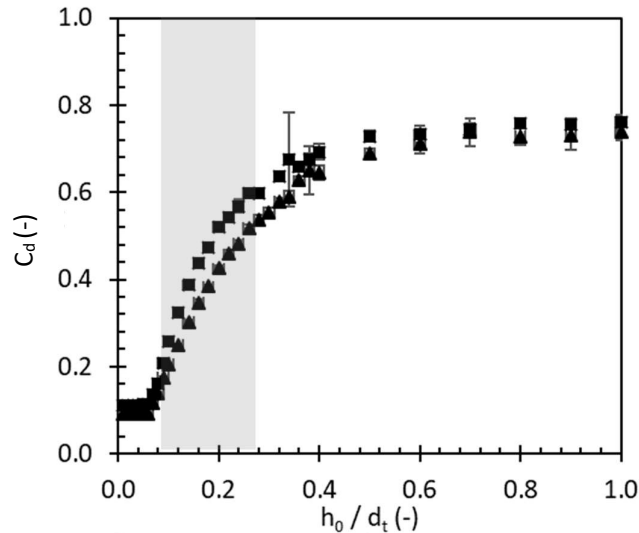


Figure 5.2: Calibration plot of C_d against dimensionless clearance. Experimental conditions: water at 20 °C, $\dot{m} = 0.33 \text{ g s}^{-1}$, $Re_t = 375$. Triangles – suction, squares – ejection. Shaded region denotes optimal measurement range

Initial iterations of the FDG, such as ‘duct-flow’ and ‘quasi-static’ FDGs developed by Tuladhar *et al.* (2002), the ‘annular flow’ FDG developed by Gu *et al.* (2006) to study curved surfaces made measurements at a single point. The ‘scanning’ FDG developed by Gordon *et al.* (2012) monitored multiple points on a single plate. These early versions differ from the current iteration through the fact that they controlled the pressure drop across the nozzle and measured the actual vs expected mass flow rates. Gu *et al.* (2009) subsequently showed that difficulties in controlling small differences in pressure at higher pressures was limiting the available resolution range. Converting from fixed ΔP_{12} to fixed \dot{m} also resolved a limitation highlighted by Tuladhar *et al.* in which C_d under certain conditions exhibited non-linear behaviour with h during duct flow gauging.

Wang *et al.* (2015) followed the work of Salley *et al.* (2012) in using low mass flow rates to study soft biofilms and, developed the next generation of FDG known as the zero discharge fluid dynamic gauging, or zFDG (Figure 5.3). In this operating mode, liquid is ejected from, then sucked back into, the nozzle sequentially, giving a closed fluid system. This reduced the volume of fluid required, allowing a smaller device footprint. It also enables aseptic conditions to be maintained. Initial swelling studies in this chapter were conducted on the zFDG rig developed by Dr Shiyao Wang (2015).

5.1.1 Experimental procedure

The zFDG test rig is similar to that used by Wang (Wang Thesis Chapter 3, 2017) but was adapted by Wang to feature a smaller (cylindrical) liquid reservoir (Wang *et al.*, 2016). Figure 5.3 is a schematic of the apparatus.

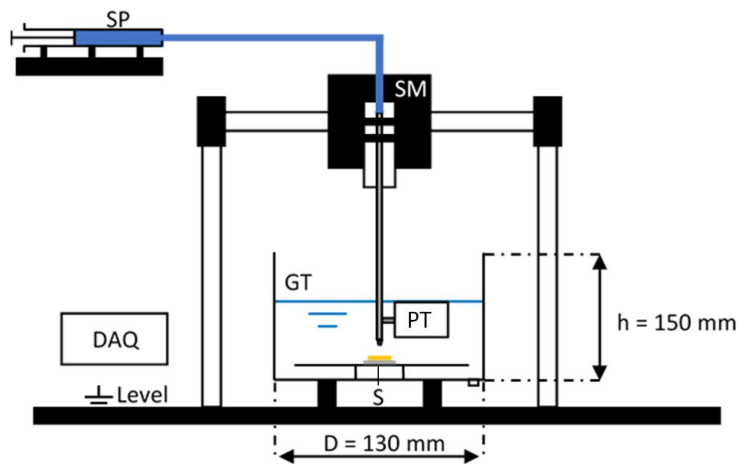


Figure 5.3: Schematic of zero discharge fluid dynamic gauging. Notation; SP; syringe pump; SM; stepper motor; PT; pressure transducer; GT; gauging tank; DAQ; data acquisition device; Reproduced from Wang (2017).

The reservoir is constructed from Perspex® (height 150 mm, diameter 130 mm, operating volume 2 L) allowing the layer to be monitored visually during testing. Liquid is ejected or withdrawn by a

computer-controlled syringe pump (Hamilton® Glass, $d_i = 32.6$ mm syringe; Harvard Apparatus PHD Ultra® Series pump). The accuracy of the flow rate, \dot{m} , was measured as 1 % of the set value.

The nozzle (d_i 0.001 m, d_t 0.0058 m) was constructed from 304 stainless steel and is attached to the end of a long (310 mm) stainless steel tube. The nozzle z-axis movement is controlled by a stepper motor (Zaber Technologies, T-LSR075B). The pressure drop across the nozzle, ΔP_{12} , was measured by a pressure transducer (SensorTechnics HMAP001BU7H5) with an operating limit of approximately 7 kPa. Data collection and processing was performed with a LabVIEW® (National Instruments®) application, which also controlled the nozzle location and syringe pump motion. The LabVIEW code included a pressure difference cut-out to avoid damage to the pressure transducer (Wang, 2017).

At the start of each test the nozzle is located at $h_0 = 50$ mm to give room to place the sample in the sample mount without damaging potentially fragile soils or contaminating the nozzle surface. A timer is started upon first contact of the soil sample with the cleaning solution. The sample is located, avoiding cracks in the soil where possible, and fixed into place with spring loaded clamps, and the nozzle then advanced towards the soil to $h_0 = 0.25$ mm. Liquid is then ejected from the nozzle at a fixed flow rate and the first data point recorded. The stop watch is then stopped. The time delay, t_d , between first soil contact and first thickness measurement, is used as an offset during data processing.

Tests typically involved 200 cycles, each consisting of 4 s ejection, 2 s pause, 4 s suction, 2 s pause, at a mass flow rate of 3.33 g s^{-1} (giving $Re_t = 377$ for $\mu = 0.001122 \text{ Pa}\cdot\text{s}$ and $\rho = 997.3 \text{ kg m}^{-3}$) giving a total test time of approximately 2600 s. The sample was then removed and the zFDG partially dismantled for cleaning.

5.1.1.1 Cleaning the device

Cleaning tests are designed to test the effectiveness of surfactants and chelants within a known environment. To avoid cross-contamination a rigorous cleaning protocol for the zFDG rig was required to ensure that no contaminants remained after testing. The rig was cleaned as follows:

- (i) The nozzle was raised out of the chamber and dismantled for cleaning. The nozzle cap was unscrewed to create a wider aperture for solution flow.
- (ii) The chamber and syringe pump were removed from the rig and all solution was drained.
- (iii) All components were then submerged in warm soapy water and scrubbed clean with a soft sponge, rinsed in tap water, then again in deionised water.
- (iv) Components were then left to dry in ambient air
- (v) Visual inspection, with repeats of stages (iv)-(vi) if required.
- (vi) The equipment was reassembled.

5.1.1.2 Equipment calibration

After each disassembly and cleaning the equipment required recalibration to maintain the desired resolution and reproducibility during testing.

For calibration, the nozzle was located at $h_0 = 0.2$ mm via the use of feeler gauges and operator judgement. The nozzle was then mechanically retracted via use of the z-positioner to $h_0 = 0.3$ mm and gauging commenced. Liquid was alternately ejected then withdrawn at each nozzle location then advanced towards the surface in steps of 0.1 mm, 0.05 mm and 0.02 mm as h_0 decreased. The control software waited for the ΔP_{12} reading to reach steady state at each location, which took ~ 4 s. Any hydrostatic component arising from a difference in liquid levels was accounted for by measuring the pressure drop for the static (no flow) steady state. As the nozzle advanced towards the surface the pressure drop approached the sensor's limit, activating a feedback loop which stopped the motor and acted to withdraw the nozzle.

In the tests presented here the nozzle-surface clearance reached approximately 0.07 mm. Calibration plots (C_d vs h_0/d_t) were then generated (e.g. Figure 5.4). Quadratic equations were fitted to the calibration data and compared to known standards. If within acceptable limits, the fitted equations were subsequently used in the conversion of experimental C_d (calculated from ΔP_{12}), to h/d_t (ultimately yielding δ).

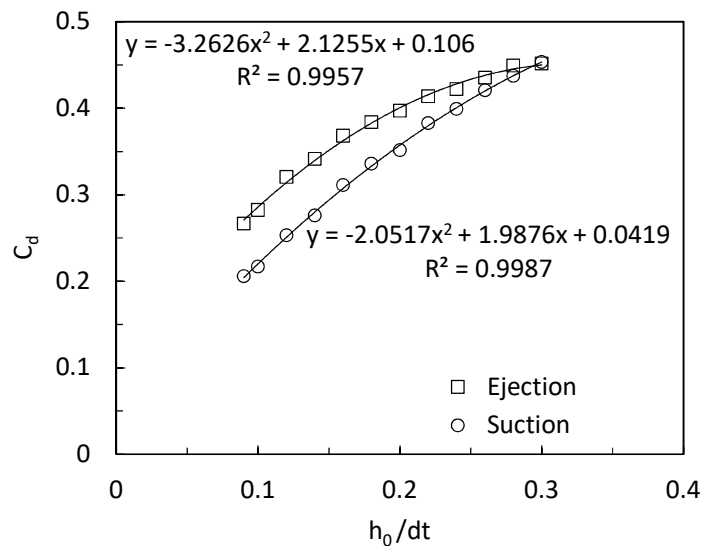


Figure 5.4: Example calibration plot for zFDG in deionised water at room temperature.

5.1.1.3 Data Processing

Pressure drop is measured for each sample during both the ejection and suction modes on the zFDG. The values are compared to the reference data set (Figure 5.4) to estimate δ for each sample (Figure 5.5).

The ejection and suction data are considered separately and plotted as δ_E and δ_S against time after first contact with the cleaning solution (Figure 5.5 (a)). Each test was then normalised relative to their initial positions taken here as the first data point measured by the zFDG, δ_i (Figure 5.5 (b)). δ_i differs from δ_0 , the dry soil thickness, as some hydration or swelling may occur during the time between first contact with the solution and first datum (typically in the order of 60 s). Variations in the thickness of the substrate ($2.91 \text{ mm} \pm 0.007 \text{ mm}$) and initial soil thickness ($0.4 \text{ mm} \pm 0.05 \text{ mm}$) cause uncertainty in δ_0 , preventing it from being used as a viable reference point in these tests. Repeated data sets are averaged to give $\langle \delta - \delta_i \rangle$ with a shaded error band of one standard deviation (Figure 5.5 (c)).

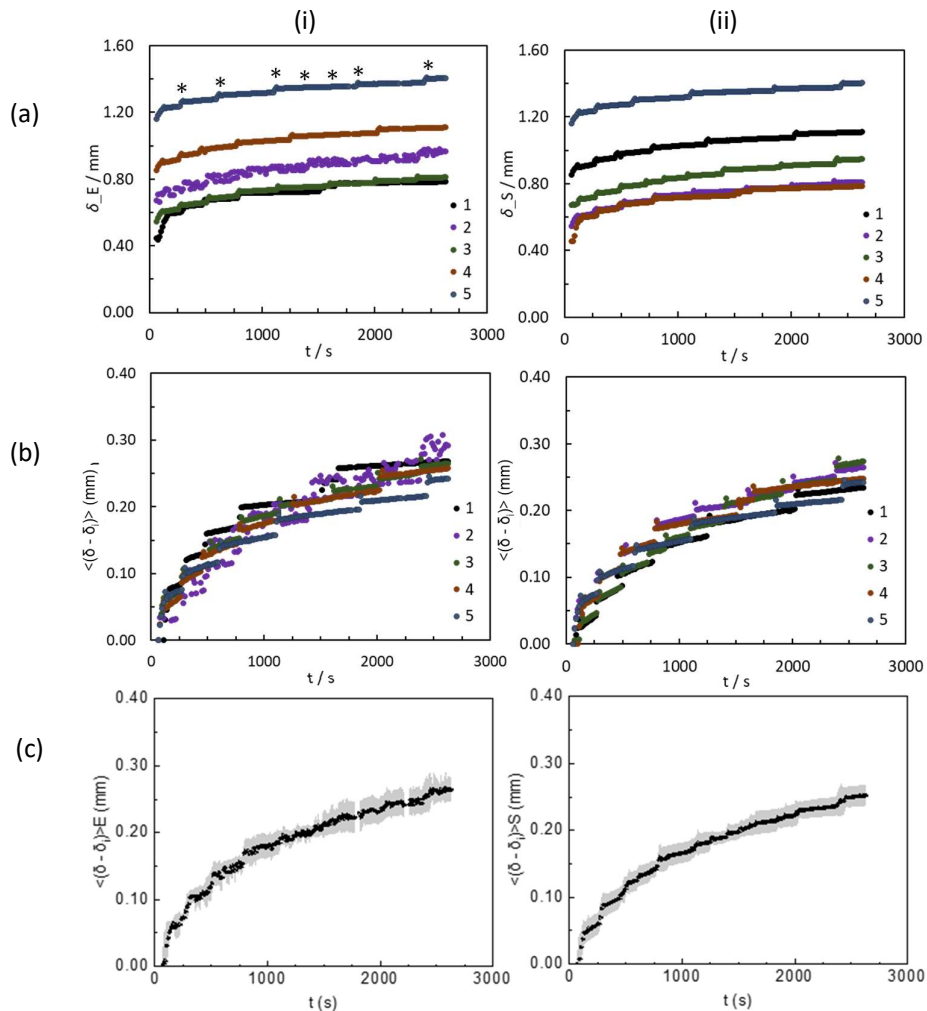


Figure 5.5: Processing of FDG data based upon δ_i . (a) raw data; (b) data corrected with the assumption that $\delta_i = \delta_0$; (c) averaged data, shaded region shows one standard deviation of all repeats. (i) E - ejection, (ii) S - suction.

5.1.2 Results and discussion

5.1.2.1 Effect of temperature

Prior to averaging the data, it is inspected visually. The soil used in these studies is heterogeneous, so components within the soil may behave differently when hydrated or subjected to shear flows. If inconsistencies in the data are noted then similar data are averaged and the remaining tests are reported separately. In some cases the data were discarded where they were not representative of the general soil behaviour.

Figure 5.6 shows that the CMS swelled rapidly upon hydration in an aqueous environment at both 20 °C and 50 °C. At room temperature the soil increases in thickness by over 50 % after 1600 s. Unexpectedly, the rate and magnitude of swelling is greater at lower temperatures. The lower solution viscosity and faster diffusion rates at 50 °C should have aided swelling in this case. The cause of this observation is now considered. Figure 5.6 (b) exhibits rapid swelling at $100 < t < 400$. This swelling likely started immediately upon contact with the solution during the first 100 s required to establish flow before the first data point could be taken. In this case δ_i could be a significant overestimation of δ_o . Extrapolating backwards to $t = 0$ s using an exponential decay model projects that the overestimation is in the order of 0.027 mm, raising δ at t_{final} from 0.101 mm to 0.128 mm, a small change relative to that at room temperature of 0.17 mm.

After 500 s at 50 °C the swelling curves of repeated CMS studies deviate (marked D on Figure 5.6 (b)). As the soil swells it loses structural integrity and softens. Components such as fats and oils present in the soil become more mobile and are released from the soil structure (Chapter 6). In some cases this caused the soil to swell, then relax or erode after a period of time. In this case both samples are identical for 500 s, however beyond D the thickness of ‘Suction 2’ shrinks to ~ 0.05 mm, almost half that of Suction 1 (~ 0.1 mm).

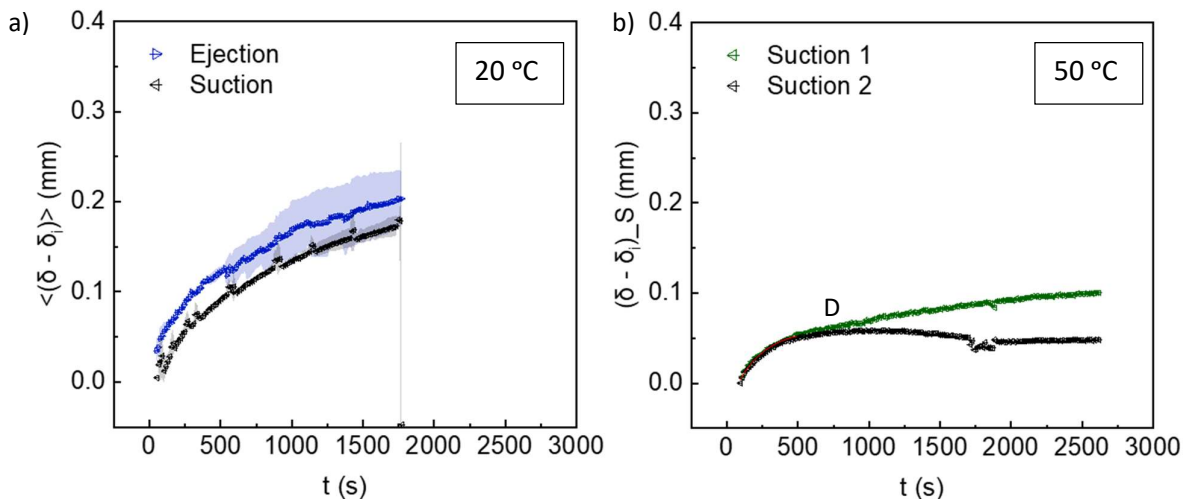


Figure. 5.6: (a) averaged ejection and suction data for pH 7 cleaning solution at 20 °C. (b) 2 repeats of suction for pH 7 at 50 °C. $\delta_i = 0.3$ mm

5.1.2.2 Effect of cracking

Visual inspection of the CMS layers during testing suggested that there may be a link between the soil swelling behaviour and the proximity of cracks in the soil to the gauging nozzle. Samples with differing crack distributions were generated to investigate this feature (Figure 5.7).



Figure 5.7: Representative plates for the dispersion of cracking as tested on the FDG in Figure 5.8.

Figure 5.8 shows that crack distribution influences the CMS behaviour strongly. Finely cracked CMS demonstrated the swelling-relaxation behaviour after 1400 s reported in Figure 5.6. As crack size increased the soil swelled but did not relax, and in the case with the widest cracks the soil swelled until 1300 s at which point a sharp increase in ΔP_{12} was recorded. This is attributable to sections of the CMS detaching from the substrate and becoming lodged on or in the nozzle, disrupting the fluid flow. The CMS with the widest crack distribution is characterised by large islands of coherent soil, up to 13 mm in size. During baking the edges of the soil undergoes a greater extent of Maillard reactions (Benzing-Purdie *et al.* 1985) as they are in direct contact with the heated air. The material on the edge of the island would therefore be harder and more tightly bound to the substrate than the material in the centre (Cuckston *et al.* 2019). As water ingresses into the soil, weakening it, the shear forces imposed by the nozzle are now sufficient to overcome the adhesive forces of the soil to the substrate, causing it to lift off and detach.

This does not occur in the more finely cracked samples as a greater proportion of the soil is proximate to the cracks ($0.36 \text{ cracks mm}^{-1}$ in fine samples vs $0.17 \text{ cracks mm}^{-1}$ in wide) and therefore exposed to the high heat and consequently is bound more tightly. In addition to this effect some zFDG flow may be dissipated through the cracks, decreasing the shear forces imposed on the soil directly. The more cracks, the more dissipation that could occur. Similarly, mobile components within the soil would have greater access to the soil-solution boundary in a highly cracked sample, increasing the rate of their removal.

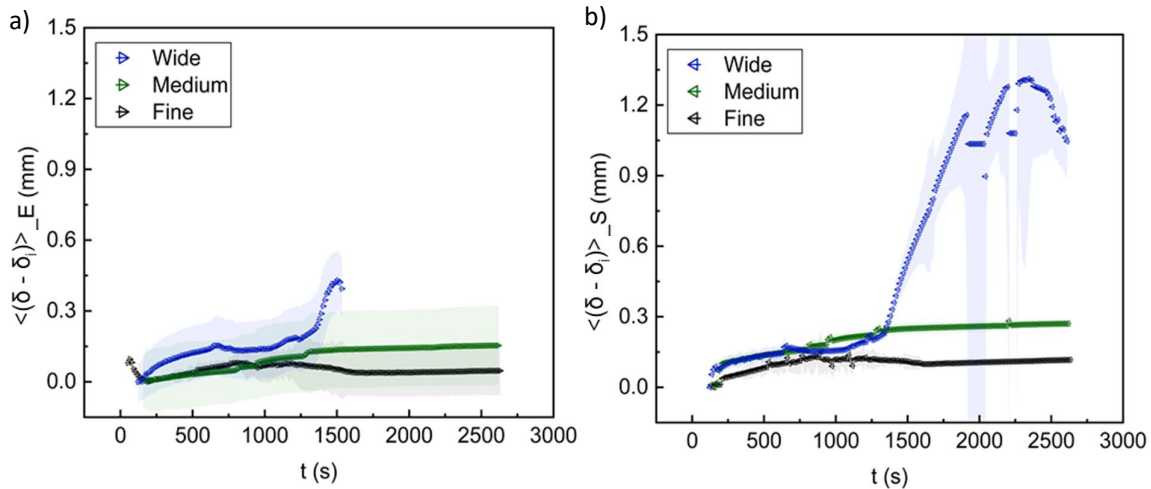


Figure 5.8: Impact of cracking on zFDG testing at 50 °C, a) ejection b) suction. Error band is one standard deviation.

It is for the reasons outlined above that for all subsequent experiments, in swelling and all other forms of testing (e.g. adhesion testing, oil recovery analysis) finely cracked samples were used. It is recommended that any testing using CMS be optimised for minimisation of crack size. This was achieved by creating thin (<0.3 mm) samples and allowing the soil to dry slowly (in air for 18 hours) before baking.

5.1.2.3 Effect of pH

The swelling behaviour of many polymeric materials is sensitive to pH as acid or base can cause chains to become charged and repel each other. Swelling in alkaline conditions is attributed to hydroxyl groups within the proteins and sugars becoming negatively charged and generating intra-network repulsion (Tuladhar *et al.* 2000). Figure 5.9 shows that the pH influences CMS behaviour above pH 9. The maximum height that the soil grew, $\Delta\delta_{i,max}$, increased by 50 % above that observed for pH 7 or 9 ($\Delta\delta_{i,max} \sim 0.2$ mm at pH 7 – 9, ~ 0.3 mm at pH 10, $\delta_0 = 0.47$ mm).

The characteristic time of swelling in this system, $t_{asym, zFDG}$, was not affected by pH. All samples reached their swelling maximum after approximately 500 s. This indicates that the kinetics of swelling are dependent upon a variable other than OH^- concentration. Here it is likely that it is the presence of hydrophobic components within the soil, which slow the ingress of the water (and therefore also the OH^- ions) into the soil matrix. After 500 s the soil is believed to be completely saturated in cleaning solution. This is a relatively slow process; hydration of starch-containing materials is typically a rapid process, on the scale of tens of seconds, and as such this data may also be confounded by the absence of hydration data for $t < 100$ s where pH would be expected to have the strongest impact. At the later stages of swelling the wetting forces are similar and so it is the viscosity of the water which controls the rate.

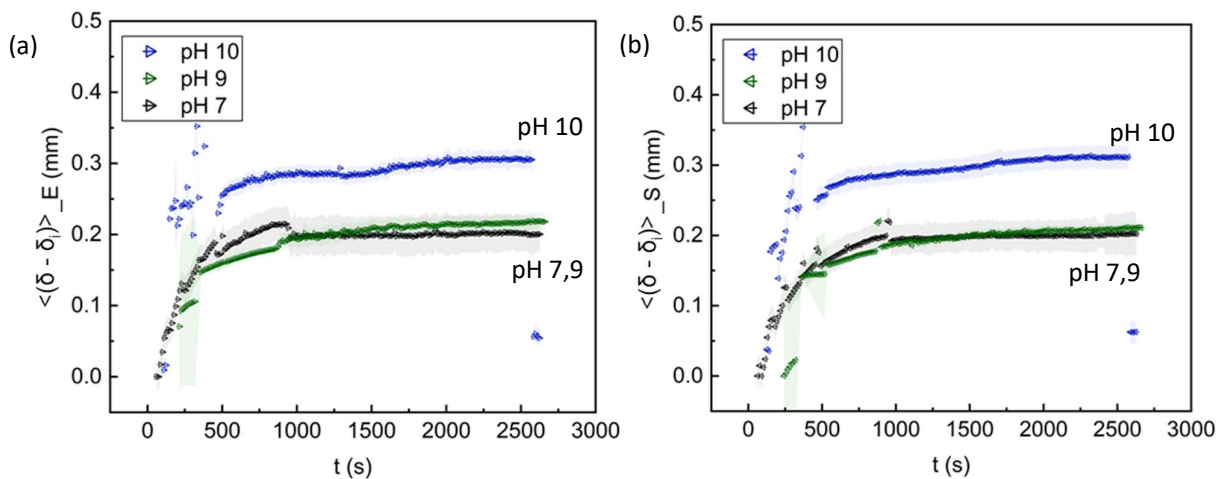


Figure 5.9: Impact of pH on zFDG testing at 50 °C, (a) ejection, (b) suction. Error band shading shows one standard deviation.

In order to separate the action of hydration and OH^- induced swelling CMS samples were first submerged in pH 7 water at 50 °C and allowed to swell for 2700 s. A dose of 10 g L^{-1} NaOH was then introduced to the gauging solution to raise the pH to 12. Figure 5.10 shows that 0.15 mm additional swelling occurs immediately upon contact with the OH^- and proceeds for ~ 600 s. After this time the soil structure weakened to the extent that it could no longer be measured by the zFDG.

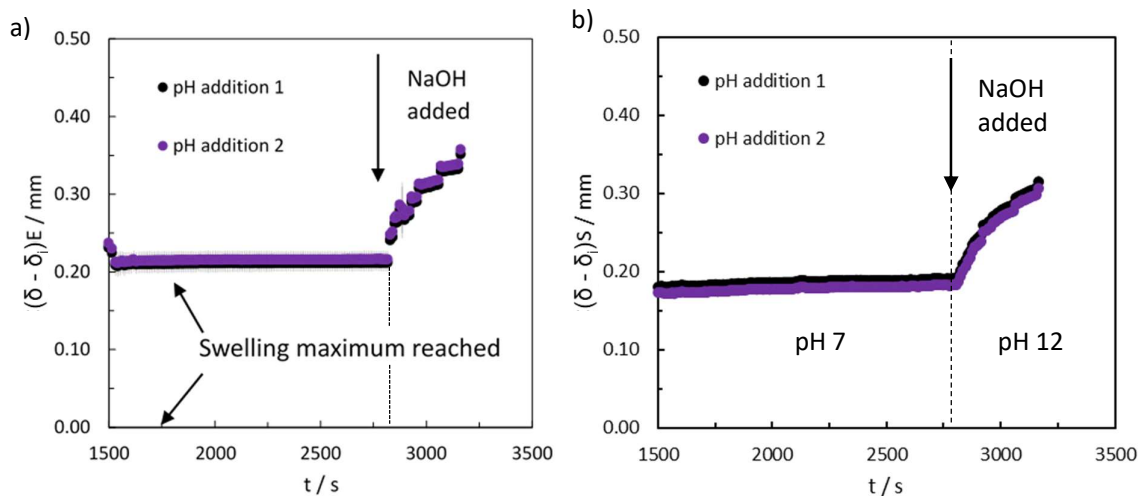


Figure 5.10: (a) ejection and (b) suction plots for two repeats of pH addition after swelling has stabilised (See Figure 5.9). Addition of 10 g L^{-1} of NaOH at $t = 2700$ s to raise solution to pH 12 at 50 °C.

5.1.3 Conclusions from zFDG

Preliminary work conducted on the zFDG indicated that to achieve optimal repeatability the CMS samples should be prepared taking care to minimise the size of the cracks that form during the drying phase. zFDG results on soil layers with a wide crack distribution showed low repeatability due to lower soil adhesion to the surface and disruption of the flow of the water beneath the nozzle. Tests conducted at higher temperature featured lower repeatability in this system due to soil weakening

and erosion, which was not as apparent in tests conducted at 20 °C. Finally the effect of raising the pH from 7 to 10 was explored. Relatively high concentrations of OH⁻ were required (>pH 10) to achieve an observable impact on the soil. This impact took the form of increasing the extent of swelling, whilst not strongly influencing the swelling timescale or kinetics. This was confirmed by switching the pH after the soil was fully hydrated. The slow kinetics of swelling exhibited here could be attributed to the presence of hydrophobic molecules with the soil impeding solution penetration, but could also be due to equipment limitations; swelling measurements are not taken during the first 100 s of submersion. This leads to an unquantified systematic underestimation in $\Delta\delta_t$.

5.2 Sideways fluid dynamic gauge (SiDG)

One inherent difficulty in using zFDG for cleaning is the requirement to measure h_0 at the start of the experiment. The requirement to reference the nozzle against a standard substrate before each measurement set creates a delay of approx. 1 minute between submersion of the test sample and the first measurement. The author worked with PhD student Jheng-han Tsai (Cambridge, P⁴G) to modify the zFDG system to overcome this delay (Tsai *et al.* 2019).

5.2.1 SiDG description

Figure 5.11 is a photograph and schematic of the SiDG device. Its design builds on the zero fluid dynamic gauge developed by Wang. In this version the nozzle (N, 295 mm long, 4 mm i.d. 316 stainless steel tube, 45° convergent nozzle, throat diameter $d_t = 1$ mm, rim width 0.5 mm) is mounted horizontally and enters a Perspex tank (150 × 150 × 150 mm³, 2 L filled volume) containing the gauging liquid.

The nozzle sits approximately 15 mm beneath the solution surface. The gauging tube passes through an O-ring seal in the side wall. The nozzle is moved in the horizontal plane by a linear drive (X, Zaber Technologies T-LSR075B). A heated coil (H) at the base of the tank controls the solution temperature, while inlet and outlet ports allow for adjustments in its composition. As with the zFDG, solution is ejected or withdrawn by a computer controlled syringe pump.

The sample is mounted on a vertical holder (M) which can be raised or lowered into the test solution with a displacement accuracy of 0.45 μm. This positioning allows for locational referencing to be conducted whilst the sample remains out of the test solution. This reduced the time between the sample being wetted and the first gauging measurement to the time taken for the y-positioner (Zaber T-LSR075B) to move the mount down and the syringe pump (Harvard Apparatus PHD Ultra Series; Hamilton glass syringe, internal diameter 23 mm) to initialize. On average this took less than 10 s.

The pressure drop (ΔP_{12}) across the nozzle is measured by a pressure transducer (SensorTechnics HMAP001-BU7H5, range -8 kPa to 9 kPa) connected to a tapping located 50 mm from the nozzle throat. A multifunction DAQ (National Instruments, USB-6210, 16 AI (16-Bit, 250 kS/s)) collects the transducer signal as an analogue input and converts it to a pressure drop using results from separate calibration tests (not shown). A control script written in Python 3.0 by Tsai operates the SiDG, collects, and processes the pressure drop and positioner data. Full details of device construction and operating algorithms are provided in Tsai *et al.* (2019).

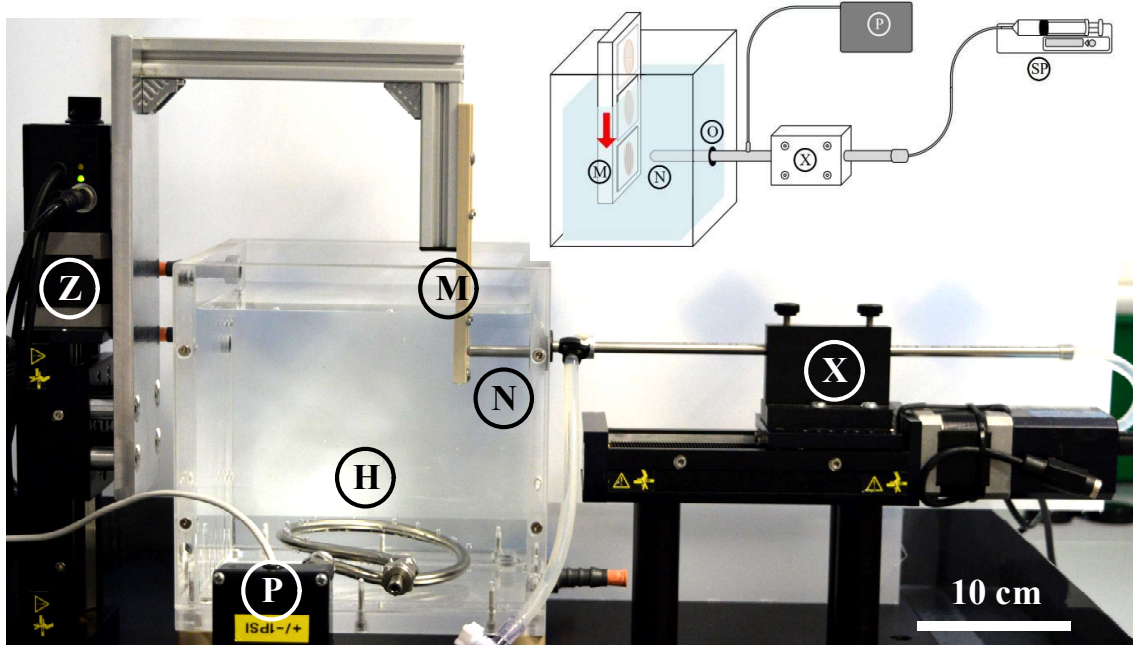


Figure 5.11: Photograph and (inset) schematic of SiDG apparatus. Salient points: H – liquid reservoir with heat transfer coil; M - sample mount; N – nozzle; P – pressure transducer; X – nozzle positioner; Z – sample positioner. Reproduced from Tsai *et al.* (2019).

Only a small section of the soil is submerged on first contact (gauging position + 15 mm above). This allows multiple tests to be achieved on the same sample plate. Typically five tests were conducted per plate. This enables automated repeated testing to be conducted on each sample. It also allows the effect of different cleaning agents on the same sample to be investigated, reducing the impact of variation between samples.

It was discovered that porous samples could wick liquid up into the untested material by capillary action. To ensure that the soil remained dry before testing, break strips (~1 mm wide) were generated at 15 mm intervals along the sample (Figure 5.12).

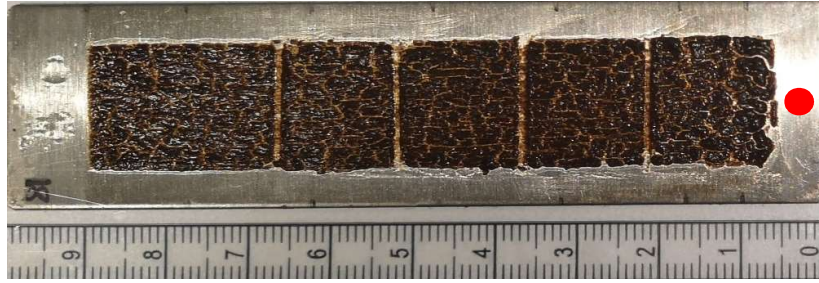


Figure 5.12: Photograph of dry CMS soil before immersion with break strips at 15 mm intervals along the sample plate. Red dot indicates section at which positional referencing takes place.

5.2.1.1 Positional referencing

The location of the substrate surface (h_0) is determined by making measurements on a clean area of the substrate prior to the start of the test (Figure 5.12, red dot). The difference between this value and the measured clearance between the nozzle and the soil-solution interface gives δ . (Figure 5.1). Calibration is then run in a manner similar to that described in the zFDG protocol.

For SiDG testing h_0/d_t was kept between 0.07 and 0.27. This is due to the fact that C_d is almost linear in h/d_t within this range and the signal to noise ratio of the measured pressure is large. The resolution within this measurement range was $\pm 10 \mu\text{m}$.

5.2.1.2 Substrates

The samples used with this device were rectangular 316 SS substrates (25 mm \times 100 mm, thickness 0.7 mm). The substrates were cleaned by the standard protocol described in Chapter 3.

5.2.1.3 Soils

The complex model food soil (CMS) was spread as a slurry on the substrate using the draw-down device to give a wet thickness of 0.4 ± 0.05 mm. The layers were left for at least one day to dry then baked at 204 °C for 7 minutes followed by cooling to room temperature. The layers featured small cracks which penetrated through to the substrate with an average crack spacing of 2.5 mm, and the fraction of area occupied by cracks of 39 %. The thickness of these rough layers was measured using a Mitutoyo digital micrometer. This technique gives an overestimate of the average thickness as the micrometer primarily locates peaks on the layer surface.

5.2.1.4 Modelling

Computational modelling was conducted by Jheng-han Tsai (2019) and is not discussed in detail here. A key outcome of the modelling was the finding that the minimum depth required between the nozzle and the solution-air interface was 15 mm.

A second useful quantity calculated in this work was the average wall shear stress, $\bar{\tau}_w$, imposed on the soil by the SiDG flow directly beneath the nozzle. Zhou *et al.* (2017) reported the result obtained for viscous flow between two parallel discs,

$$\bar{\tau}_w = \frac{1}{r_o^2 - r_i^2} \int_{r_i}^{r_o} 2r\tau_w dr \quad \text{Equation 5.5}$$

$$= \frac{\mu Q}{4\pi(h/2)^2} \frac{2}{r_i + r_o} \quad \text{Equation 5.6}$$

Giving, in dimensionless form,

$$\bar{\tau}_w^* = 4\pi \frac{\mu r_i}{\rho Q} \left(\frac{r_i}{h}\right)^2 \frac{r_i}{r_i + r_o} \quad \text{Equation 5.7}$$

Where r_i is the inner radius of the SiDG nozzle, r_o is the outer radius of the SiDG, Q is the volumetric flow rate, and the reference τ_w is approximated as $1/2 \rho U^2$ at $h/d_t \approx 0.5$ (Tsai *et al.*, 2019).

Shear-induced deformation of the layer was to be avoided when studying swelling or shrinking, so a feedback mode was implemented in the SiDG control programme similar to that in the zFDG. Simulations based upon the wall shear stress at each flow rate allowed for determination of the pressure drop associated with a shear stress limit at a given clearance. This enabled the user to set pressure limits to avoid deformation depending on the soils deformation limits.

5.2.1.5 Test Protocol

The first measurement was taken 6 – 10 s after the sample contacted the solution. 10 measurements were then made at intervals of 2 s, followed by 190 measurements lasting 5 s of flow alternated with 5 s periods in which no liquid flowed.

5.2.2 Results and discussion

The results are presented as the change in thickness, $(\delta - \delta_0)$ (measured thickness – initial dry thickness, $\delta - \delta_0$), against time since immersion in Figure 5.13. This is a key difference from the zFDG measurement protocol where δ_i is the referencing point. The enhanced positional referencing system eliminates the impact of substrate thickness variation as $h_0 = 0$ is set for each individual substrate. The ability to utilise measured δ_0 in place of δ_i allows initial hydration data to be collected.

Figure 5.13 shows that the soil swells rapidly on hydration, and the SiDG unit is able to capture the initial swelling behaviour successfully. In this case t_d was reduced to 12.7 s, a significant improvement over the 60 s required in the zFDG set-up. The error bars on the plot show the variation between up to 15 tests conducted on the 3 samples, achieved by moving the plate down after each test to contact dry deposit with the solution up to 5 times.

The measured $\Delta\delta$ on the SiDG is smaller than that observed for a similar system on the zFDG ($\Delta\delta_{(i)} = 0.11$ mm on the SiDG vs 0.17 mm on the zFDG, Figure 5.6) even though $\delta_0 < \delta_i$. This is because refinement of the CMS soiling protocol during the commissioning of the zFDG gave thinner samples (SiDG $\delta_0 = 0.34$ mm vs 0.47 mm on the zFDG). The thicker samples, with a wider crack distribution, were unsuitable for use on the vertical sample stage of the SiDG. Scaled analysis of the suction mode values shows the two techniques are comparable ($\Delta\delta_{(i)}/\delta_0 = 0.32$ on the SiDG vs 0.36 on the zFDG). All samples used on the SiDG featured similar δ_0 and so scaled analysis was not used throughout.

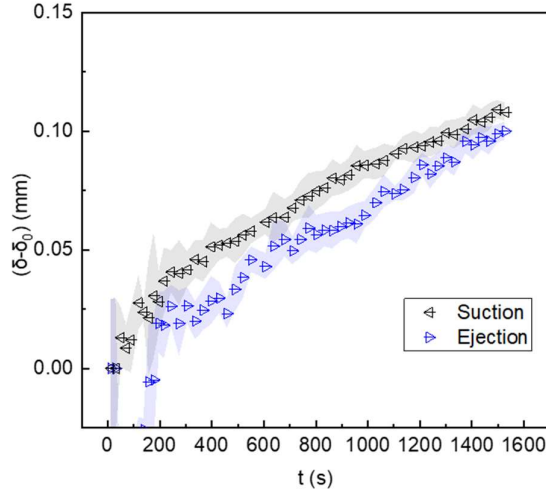


Figure 5.13: Swelling profile of CMS (δ_0 : 340 μm) immersed in deionized water (pH = 5.6, 20 $^{\circ}\text{C}$) with $\dot{m} = 0.33$ g/s measured on the SiDG. Solid blue circles – ejection; open red triangles – suction. Shaded are represents one standard deviation of up to 15 tests.

The thickness measured in suction mode is consistently larger than in ejection mode. This is attributed to the spongy and cracked nature of the soil: as liquid is ejected from the nozzle a compressive force will be imposed on the surface, reducing δ , while during suction a lifting action occurs in any soil with an elastic component, increasing δ . In all subsequent data reported only ejection data are shown. Any aberrations in suction data will be shown and discussed when required. In general the suction data matched the ejection data closely.

5.2.2.1 Effect of temperature

Figure 5.14 (a) shows that in general the swelling profiles show asymptotic behaviour. This can be described by an exponential decay model such as;

$$(\delta - \delta_0) = \Delta\delta_{final} \left(1 - e^{-\frac{(t-t_0)}{\tau_{SiDG}}} \right) \quad \text{Equation 5.8}$$

where δ is the soil thickness at time t , δ_0 is the dry soil thickness, $\Delta\delta_{final}$ is the final change in soil thickness at time, $t = 1600$ s, calculated through estimation of the asymptotic value, t_0 is the time at which immersion occurs, and τ_{SiDG} is the half-life which yields a rate constant, k_{SiDG} (s^{-1}), via

$$k_{SiDG} = \frac{1}{\tau_{SiDG}} \quad \text{Equation 5.9}$$

The δ_{final} and k_{SiDG} values calculated in this testing are reported in Table 5.2.

The quasi-exponential decay behaviour described above was common to the microscopy, swelling, oil recovery, and layer image analysis techniques. The use of an asymptotic exponential decay model such as that in Equation 5.8 enables comparison of first order kinetic rate constants between data sets. This provides a valuable metric to quantify the stages of cleaning of complex soils and is explored in detail in Chapter 8.

Above 20 °C the soil swells with an exponential approach to a maximum. The rate of swelling increased with temperature (k_{SiDG} at pH 7 = $0.91 \times 10^{-3} \text{ s}^{-1}$ at 20 °C, $3.26 \times 10^{-3} \text{ s}^{-1}$ at 50 °C), as expected due to the lower viscosity of the water, faster diffusion and reactions causing swelling. There is a noticeable difference in the final extent of swelling between 20 °C and higher temperatures (δ_{final} = 0.08 mm at 20 °C, 0.18 at 50 °C). At 50 °C similar values were obtained, of about 150 % that at 20 °C. One of the reasons for this difference is that the fat present in the soil is not mobile at 20 °C and this prevents the water contacting all the soil (Wang and Wilson, 2015). The release of fat from the soil layer surface was visible at temperatures above 30 °C (Figure 5.14 (a) inset, explored in Chapter 6).

The results presented in Figure 5.14 (a) differ from those obtained with the zFDG (Figure 5.6). zFDG testing implied that the soil swelled more at 20 °C than 50 °C, with the opposite effect being shown here. It is likely that this difference is a result of the use of δ_i (at $t = \sim 60 \text{ s}$) vs δ_o as the initial referencing point. On the SiDG $\Delta\delta$ during the first 60 s submersion was 0.045 mm at 50 °C and 0.0085 mm at 20 °C. Adjusting the $\Delta\delta_i$ from the zFDG to compensate for this missing swelling time gives a $\Delta\delta_{i,max}$ of 0.16 mm at 20 °C and 0.15 mm at 50 °C. This value is in line with the results obtained on the SiDG at 50 °C however it is larger than the SiDG results at 20 °C. The reason CMS swelled more at 20 °C on the zFDG than on the SiDG is unclear.

The technique for generating the CMS layers was refined during the commissioning of the SiDG technique, allowing for the minimisation, though not elimination, of cracks in the soil surface. Swelling occurs in all directions and a delay will be experienced in measurement of δ if swelling is occurring in the plane of the soil rather than normal to it.

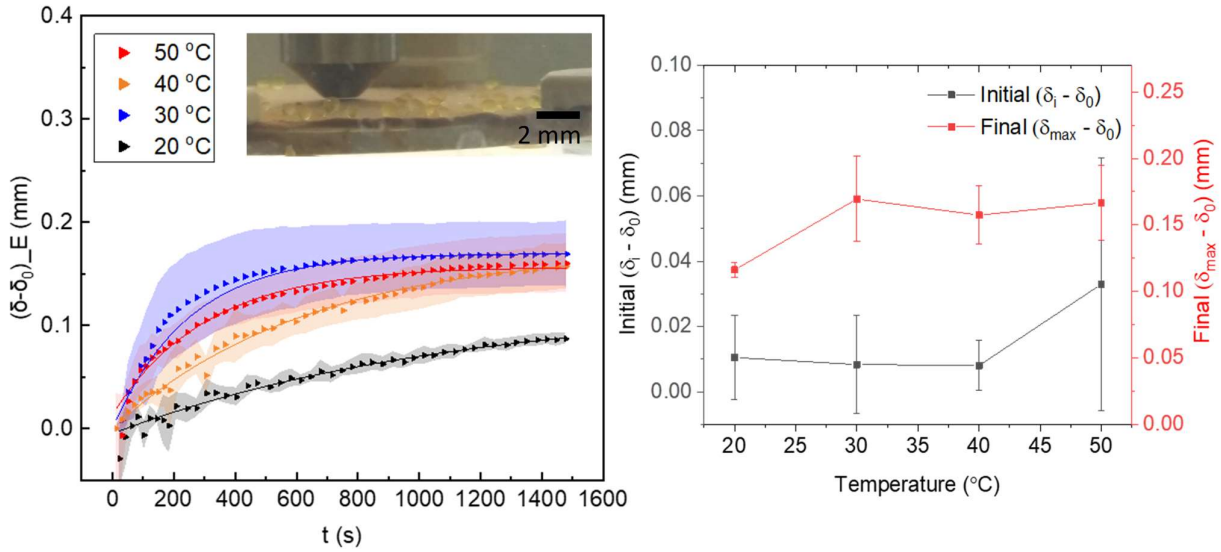


Figure 5.14: (a) SiDG data showing effect of temperature on swelling for CMS layers at $\dot{m} = 0.33 \text{ g/s}$, $20 \text{ }^\circ\text{C}$, using ejection mode. Error bars indicate the range of repeated tests. Inset: photograph showing release of mobile components during zFDG testing at $50 \text{ }^\circ\text{C}$. Lines show fit to Equation 5.8. Parameters in Table 5.2. (b) Effect of temperature on the initial thickness and final change in thickness. Solid black squares – change of initial thickness; solid red squares – final change in thickness.

5.2.2.2 Effect of pH

Figure 5.15 shows that pH has a significant effect on the swelling of CMS at $20 \text{ }^\circ\text{C}$ (δ_{final} at $20 \text{ }^\circ\text{C} = 0.08 \text{ mm}$ at pH 7, 0.32 mm at pH 10). pH dependency was a feature that was not as easily resolved during zFDG testing (Figure 5.9). The interaction between the OH^- ions and CMS that caused swelling is more evident in the SiDG. The plots show rapid changes in thickness on contact with alkali at pH 8 and above, of order 50 to $150 \text{ }\mu\text{m}$ in the first 10 s . Following this initial jump the swelling behaviour at pH 8 and pH 9 is similar, reaching a similar final value, whereas the rate (k_{SiDG} at $20 \text{ }^\circ\text{C} = 0.91 \times 10^{-3} \text{ s}^{-1}$ at pH 7, $1.38 \times 10^{-3} \text{ s}^{-1}$ at pH 10) and final extent at pH 10 are greater: the predicted final extent at pH 10 at $20 \text{ }^\circ\text{C}$ is twice that observed at $50 \text{ }^\circ\text{C}$ and pH 7.

There is an increase in the uncertainty in $(\delta - \delta_0)$, as pH increases. This is because CMS is heterogeneous and at increased pH the layer would often lose its structural integrity. In this system the sample is mounted vertically and occasionally pieces fell off.

A key feature of the SiDG device is the ability to quantify the rapid initial hydration that occurs with CMS. Figure 5.15 (b) shows that $\Delta\delta$ increases linearly with pH. The hydration is then followed by slower swelling in alkaline conditions, which is attributed to hydroxyl groups within the proteins and sugars becoming negatively charged and generating intra-network repulsion. This feature also increases with pH at 1500 s . There is a large variation in initial behavior at pH 8.

The initial change in thickness, $(\delta_i - \delta_0)$, Figure 5.15 (b)), is negative in some cases because the initial thickness of the dry layer was determined by micrometer, which is based on the peak height of the rough surface. This would result in slight overestimation of δ_0 and therefore underestimation of $(\delta_i - \delta_0)$.

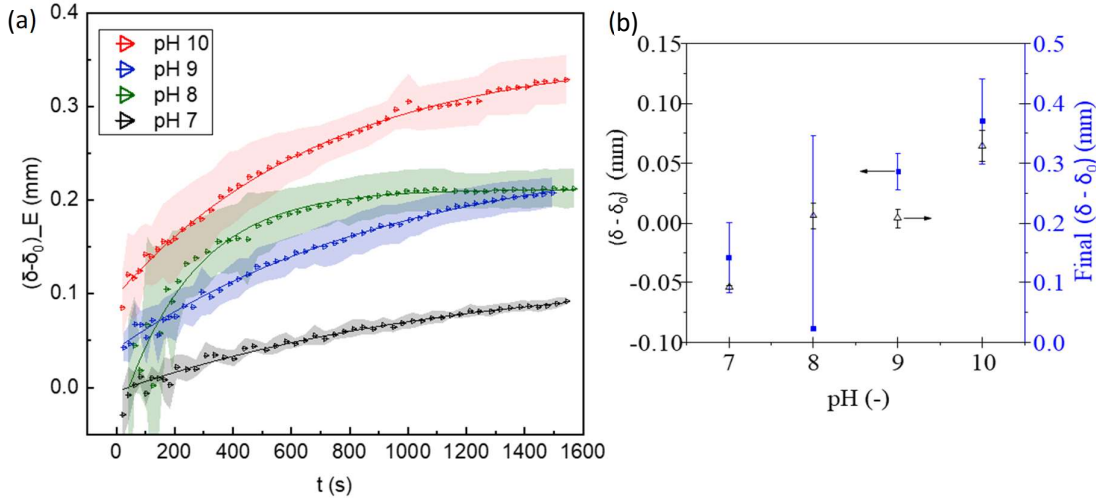


Figure 5.15: SiDG data showing (a) Effect of pH on swelling of CMS layers. $\dot{m} = 0.33 \text{ g/s}$, $20 \text{ }^\circ\text{C}$, ejection mode. Error bands indicate the range of repeated tests. Solid lines show fit to equation 5.8 (b) Change of initial thickness and final change in thickness among different pH values. Solid blue squares – change of initial thickness; open black triangles – final change in thickness.

At $50 \text{ }^\circ\text{C}$ (not shown) the impact of pH was reduced. All samples exhibited swelling similar to that of pH 8 at $20 \text{ }^\circ\text{C}$. Swelling rate constants from fits to Equation 5.8 of $2.7 - 3.4 \times 10^{-3} \text{ s}^{-1}$ were obtained with $\Delta\delta_{max}$ of $\sim 0.16 \text{ mm}$ in all cases. It can be concluded that pH has the most significant impact on CMS when submerged at room temperature. At higher temperature OH^- enhanced swelling either occurs less quickly or its measurement is mitigated by another mechanism such as soil erosion.

5.2.2.3 Effect of surfactants

The effect of 0.1 wt.% surfactant was studied at pH 7 at $20 \text{ }^\circ\text{C}$ and $50 \text{ }^\circ\text{C}$, representing standard dishwasher conditions. Figure 5.16 shows the effect of three surfactants, TX-100 (non-ionic), CTAB (cationic), and SDBS (anionic), on swelling, with the bulk concentration $> \text{CMC}$ in each case (Table 3.4, Chapter 3).

At $20 \text{ }^\circ\text{C}$ all three surfactants promote swelling ($\delta_{final} = 0.08 \text{ mm}$ vs $\sim 0.18 \text{ mm}$ with surfactants), which is attributed to their ability to solubilize the accessible surface fats present, enhancing hydration. Raising the temperature to $50 \text{ }^\circ\text{C}$ had little observable impact for surfactant containing solutions. The rate of swelling is similar in most cases with surfactant at both $20 \text{ }^\circ\text{C}$ and $50 \text{ }^\circ\text{C}$ with rate constant k_{SiDG} approximately $3 \times 10^{-3} \text{ s}^{-1}$. At $50 \text{ }^\circ\text{C}$ the fat is more mobile, so there is little advantage in adding surfactant on swelling behaviour ($\delta_{final} = 0.18 \text{ mm}$ vs $\sim 0.17 \text{ mm}$). TX-100 at $50 \text{ }^\circ\text{C}$ appears to inhibit swelling

to some extent ($\delta_{final} = 0.11$ mm). Non-ionic surfactants are known to be effective at removing oily soils from synthetic fibres (Williams, 2007) at room temperature and so solubilisation of the fats could play a role in the observed inhibition of swelling. This hypothesis will be explored further in Chapter 6.

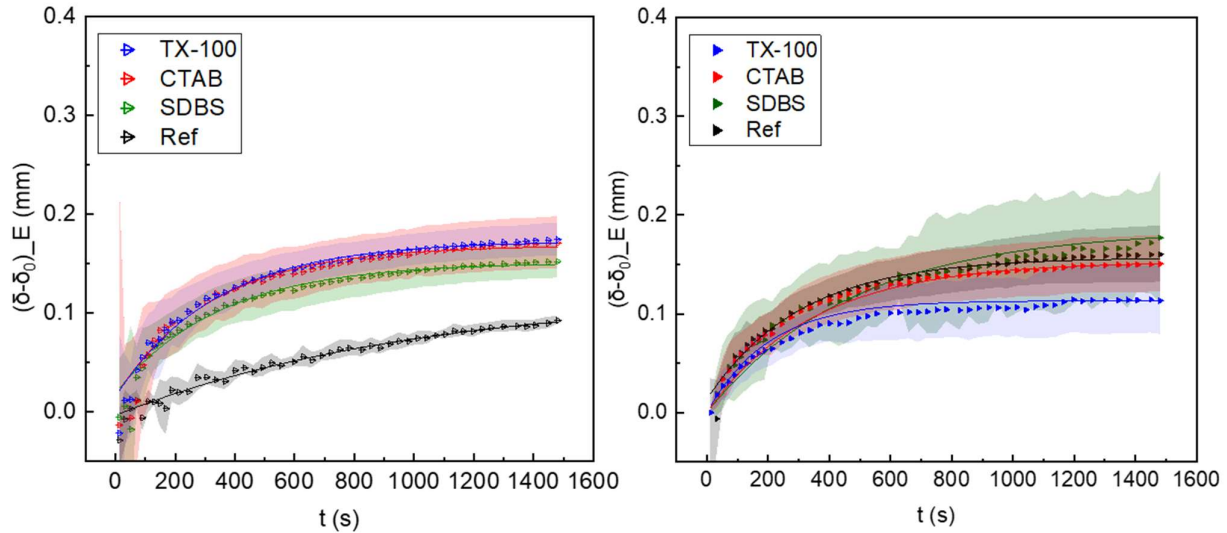


Figure 5.16: Effect of 0.1 wt% surfactant on SiDG swelling behaviour at (a) 20 °C and (b) 50 °C.

One artefact introduced by the vertically mounted sample is the gravity-driven sloughing of the material down the substrate. This sloughing occurred in tests in which the soil’s cohesive strength was lowered by the action of the cleaning solution. Any tests where this occurred were considered ‘unsuccessful’ and the results were not included in the average $\Delta\delta$ calculation (due to loose soil being drawn into the nozzle, disrupting the smooth flow of solution required to measure pressure drop accurately). Table 5.1 shows that TX-100, at both 20 °C and 50 °C, and SDBS at 50 °C exhibited a lower success rate than the reference solutions at these temperatures. SDBS at 50 °C had the lowest success rate of samples tested, with only 27 % of tests successfully completed. Increasing the pH of the cleaning solution also weakened the soil’s cohesive strength and led to an increase in sloughing. This loss in cohesion is explored further via mechanical removal forces testing in Chapter 7.

Table 5.1: Percentage of SiDG tests that successfully yielded swelling data. Tests in which the material sloughed off the substrate were considered unsuccessful.

	Temperature / °C	Reference	0.1 % SDBS	0.1 % TX-100	0.1 % CTAB
pH 7	20	93 %	87 %	67 %	83 %
	50	93 %	27 %	77 %	87 %
pH 9	20	91 %	60 %	-	-
	50	40 %	46 %	-	-

Figure 5.17 shows the impact of the combination of raising the pH with 0.1 wt.% SDBS surfactant. The results demonstrate that in general the high pH (δ_{final} water only = 0.08 mm at pH 7 vs 0.22 mm at pH 9) or use of surfactant (δ_{final} at pH 7, 20 °C = 0.08 mm vs 0.13 mm with SDBS) enhanced swelling and therefore would be expected to promote cleaning. Figure 5.17 (b) shows that the two factors are synergistic, with the most swelling observed with pH 9 and 0.1 wt. % SDBS at 20 °C (δ_{final} = 0.13 mm at pH 7 vs 0.27 mm at pH 9).

This synergism can be rationalised mechanistically thus: At 20 °C the SDBS is believed to function to solubilise the solid fatty component from within the soil layer, and at 50 °C the soil is actively being broken down (Table 5.1). pH alone at 20 °C serves to increase the overall amount of swelling (δ_{final} = 0.08 mm at pH 7, 0.22 mm at pH 9). The pH and SDBS can therefore reinforce each-others action; the SDBS promotes solubilisation of the fats, increasing access of the hydroxyl ions to promote swelling.

At 50 °C most solutions gave similar swelling rate constants and final swelling thicknesses ($k_{SIDG} \approx 3 \times 10^{-3} \text{ s}^{-1}$, $\delta_{final} \approx 0.18 \text{ mm}$). The exception to this is the long term data for pH 9 + 0.1 wt. % SDBS, which after 800 s exhibited an unstable profile, deviating from the exponential decay model. The reliability of experimental measurements at with 0.1 % SDBS at 50 °C is low (Table 5.1) due to material sloughing. The unstable profile described above is likely due to sloughing occurring once the soil reaches a critical point of SDBS solution uptake in the softer soil at 50 °C.

Most cleaning-in-place testing conducted in the food industry is conducted between 50 and 95 °C with the lower range usually encountered with liquid tankers, filling machines and circulation pipes (Gilbert, 1994) and the highest temperatures reserved for sterilisation units (Lelievre *et al.*, 2001). These results demonstrate that whilst raising the temperature of a cleaning solution can have a beneficial impact on the cleaning of soils, it may not be the optimal condition in the initial stages of a clean-in-place system for complex food soils that swell in the presence of OH⁻. Further testing is recommended to determine if a staged temperature profile could enhance the overall cleaning rate of CMS through enhancing hydration and swelling on its first contact with the solution.

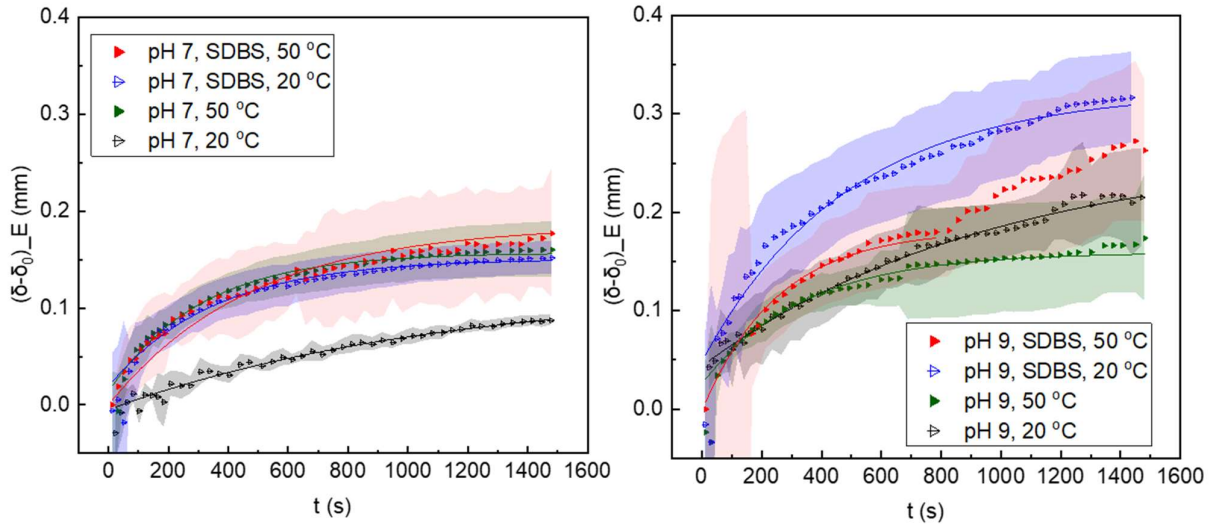


Figure 5.17: *SiDG* data showing effect of 0.1 wt. % SDBS on swelling behaviour at 20 °C and 50 °C at (a) pH 7 and (b) pH 9.

Table 5.2 Kinetic parameters from data sets in Figures 5.14 – 5.17. Data fitted to Equation 5.8, 5.9.

pH	T / °C	$k_{SiDG} (x10^{-3}) / s^{-1}$	δ_{final} / mm
7	20	0.91	0.08
	30	4.03	0.17
	40	1.58	0.18
	50	3.3	0.18
8	20	4	0.25
	50	3.4	0.16
9	20	1.02	0.22
	50	2.7	0.15
10	20	1.38	0.32
	50	-	-

pH	T / °C	Surfactant	$k_{SiDG} (x10^{-3}) / s^{-1}$	δ_{final} / mm
7	20	SDBS	2.87	0.13
		CTAB	3.10	0.15
		TX100	2.99	0.16
	50	SDBS	2.09	0.19
9	20	CTAB	2.87	0.15
		TX100	4.95	0.11
	50	SDBS	3.97	0.18

5.2.3 SiDG Conclusions

Promoting swelling is known to enhance cleaning behaviour but is not the sole mechanism involved in cleaning. Other mechanisms are involved in breaking the swollen soil down and detaching it from the substrate. These results demonstrate the ability of the SiDG device to capture initial behaviour and forms a key part of developing an understanding of the mechanisms at action during cleaning. There is some scatter shown in the plots shown in this chapter resulting from soil inhomogeneity, so numerical values should be treated with caution, but the trends in the data are evident.

Hydration induced swelling was demonstrated to occur within 60 s of submersion, followed by slower chemically induced swelling for an average of a further 450 s. The higher the pH, the longer timescale at which swelling took place ($t_{asym} = 600$ s at pH 7 and 8 vs > 1500 s at pH 9 and 10).

The anionic surfactant SDBS at pH 9, 20 °C had the largest impact on the swelling of any system tested. This impact was apparent in both the swelling maximum and timescale at pH 9, though little impact was noted at pH 7. At 50 °C SDBS caused the soil to slough on the plate and few reliable readings were taken. TX-100, the non-ionic surfactant, inhibited swelling at 50 °C and caused the soil to slough on the sample plate, likely due to cohesive breakdown of the soil. CTAB did not show any significant impact on swelling rates or extents at 50 °C but did enhance the swelling of CMS at 20 °C.

This information is combined with measurements of soil strength (Chapter 7), and solution composition during cleaning (Chapter 6), to identify the key steps and timescales involved in removal of these soil layers.

5.3 Confocal thickness scanning

A confocal LED thickness sensor (Micro-Epsilon IFC2461 controller paired with an IFS2405 sensor) was also investigated for use as an alternative method to measure swelling. The sensor was used as a non-contact high frequency measurement technique. The principle of scanning sensing is as follows: polychromatic white light is split into monochromatic wavelengths using a series of lenses within the sensor (Figure 5.18). Each generated wavelength has a unique focal plane in the region 20-23 mm below the sensor. A spectral shift in the reflected light denotes an interface at the focal plane associated with that wavelength. Peak resolution is 36 nm and the measurement range is 3 mm. Due to the light-based detection mechanism, changes in refractive index are required for the interface to be detected. A significant drawback of light based techniques is that, unlike FDG, they cannot function in opaque solutions. The consequence of this is that impact of commercial formulations, which are often cloudy, cannot be measured. Similarly, raised temperature testing, e.g. at 50 °C, is difficult as solution evaporating from the test chamber can condense on the sensor lens, causing light scattering and obscuring the results.

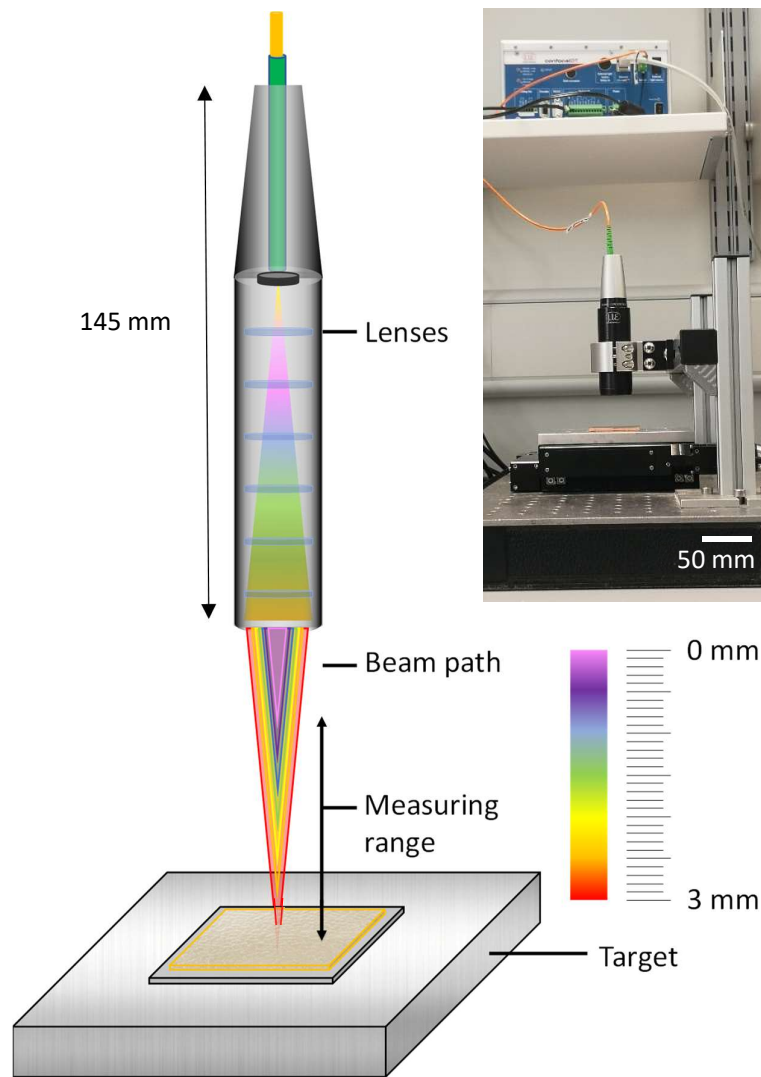


Figure 5.18: *Diagram of confocal thickness scanner (CTS). Inset: Photograph of CTS apparatus.*

5.3.1 Method

The CTS can measure layers in both dry and wet states. The confocal light can pass through a water layer and reflect off the layer-liquid interface as well as the air-liquid interface. The interfaces have to be several millimetres apart for their separation to be measured accurately. The CTS device had a noticeably smaller measurement area than the SiDG: the beam footprint was $9\ \mu\text{m}$ in diameter, whereas the SiDG footprint was 2 mm in diameter.

A $50 \times 50\ \text{mm}$ stainless steel substrate soiled with a $0.36 \pm 0.04\ \text{mm}$ layer of CMS sample was placed in a 95 mm diameter borosilicate evaporating basin (SIMAX, CNN011) and positioned within the focal window of the CTS. Data are collected as 'distance from sensor / mm'. Initial dry thickness values are taken as δ_0 .

The dry sample was gauged at 100 Hz for 30 s. 55 ml of aqueous cleaning solution was added to the dish, causing a systematic change in the measured soil height due to a change in refractive index (RI) of the bulk medium. The solution-air interface was kept outside the CTS focus window. A calibration of δ_{water} between sensor and soil is used to compensate for this change in RI over the test duration (Figure 5.19). Data were collected for 1000 s. The thickness measured over time is denoted as δ . Three samples were run at each condition and averaged, with final results plotted as $\langle \delta - \delta_0 \rangle$. All tests were conducted at 20 °C to minimise the loss of water due to evaporation and condensation on the detector. The solutions were weighed before and after testing so compensations for water loss on CTS offset could be made, assuming a constant evaporation rate.

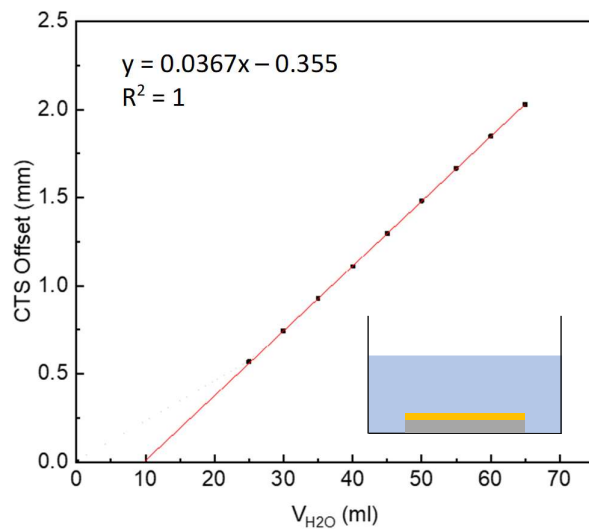


Figure 5.19: CTS calibration plot for distance measurement offset caused by the addition of liquid to the chamber.

5.3.2 Results and discussion

The swelling profiles in Figure 5.20 are markedly different than those obtained with the zFDG and SiDG. They show rapid swelling/hydration after addition of solution for about 30 s, followed by a slow steady increase thereafter. The reasons for this deviation are discussed later in this section.

Figure 5.20 (a) shows that, as expected, increasing the pH of the solution enhances swelling with δ_{final} increasing from 0.14 to 0.2 mm from pH 7 to pH 9. Unlike the SiDG tests no improvement was noted above pH 9. There is a small bump between 10 – 200 s for the sample submerged in pH 12 (Figure 5.20 (a)) associated with a blister forming and breaking before relaxing back to a stable soil level.

The addition of surfactant at pH 7 showed universal improvement over the no-surfactant case (Figure 5.20 (b-d)). However, the magnitude of increase was independent of concentration between 0.1 and 1.0 wt.% , except with CTAB. All solutions increased the final swelling magnitude from 0.14 mm to approximately 0.2 mm, similar to the impact of increasing the pH to 9. It is possible that there is a

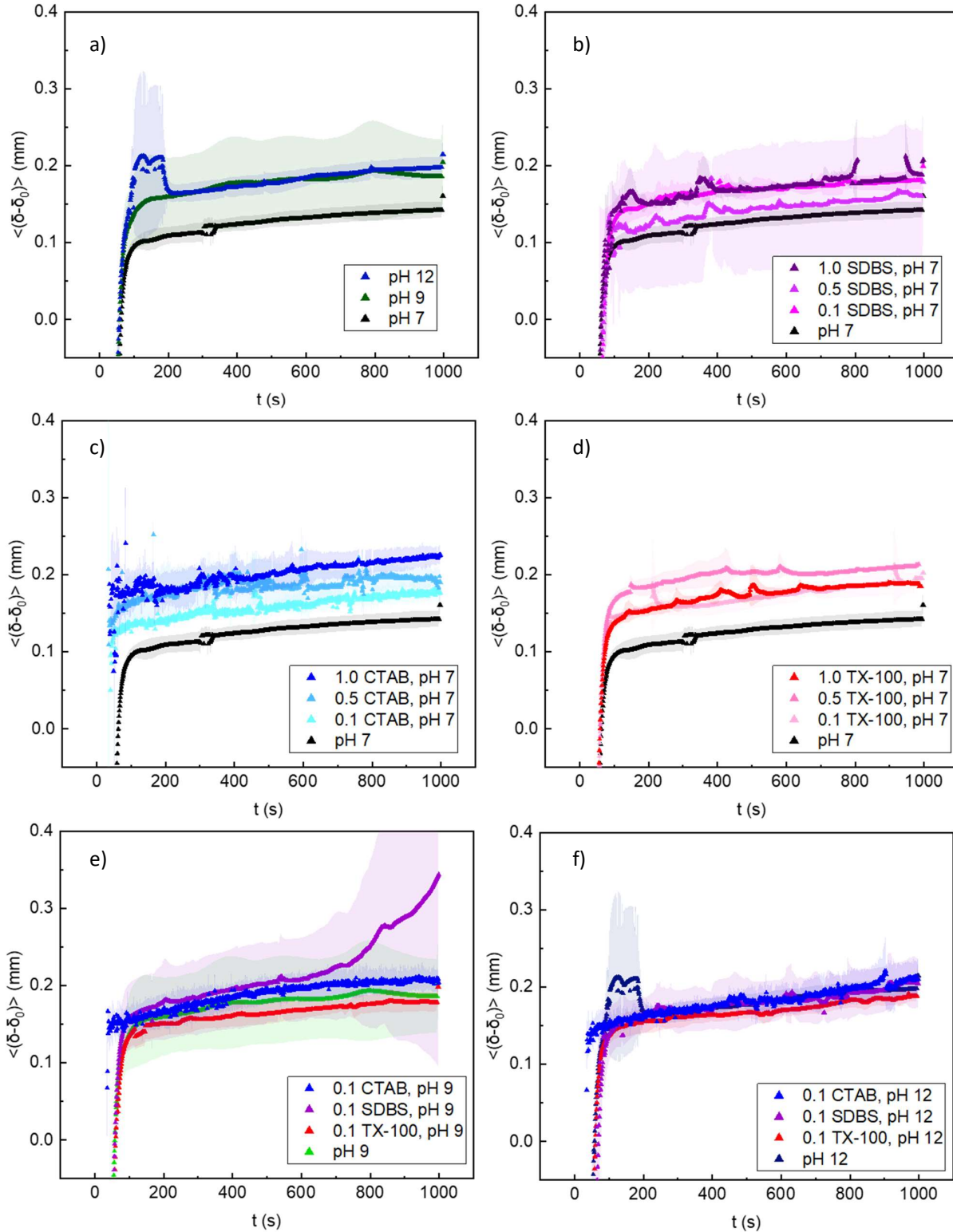


Figure 5.20: CTS swelling of CMS at 20 °C investigating the impact of (a) pH, (b) SDBS, (c) CTAB, (d) TX-100, (e) pH 9, with and without surfactants, (f) pH 12, with and without surfactants. Each test is an average of 3 repeats. Error bands show one standard deviation.

physical material limit at $\delta_{final} = 0.2$ mm as the majority of swelling results via all three methods tested plateaued at this point. Only in extreme cases e.g. high pH, high surfactant in SiDG did δ_{final} exceed this limit, to 0.3 mm.

Figure 5.20 (e, f) shows no synergistic effect of combining pH and surfactants for pH 9 and 12 at room temperature, in contrast to the SiDG results. Similar to Figure 5.17 (b), SDBS is shown to increase in an unstable manner after 800 s contact with the solution, although in that case the solution was at 50 °C whereas here it is at 20 °C.

The reason for the differences observed between the SiDG and the CTS are now considered. There are three key experimental differences between the SiDG and the CTS.

5.3.2.1 Impact of orientation

SiDG samples are mounted vertically and are therefore subject to gravity perpendicular to the swelling direction. The CTS is mounted horizontally with gravity collinear to the swelling direction. It is possible that a slightly higher magnitude of swelling occurs in the SiDG as material above the measurement region swells and sloughs downwards, increasing the thickness of the layer. In the CTS the material surrounding the measurement spot is unlikely to enter the frame of interest. This could explain why the maximum δ_{final} in the CTS was ~ 0.2 mm where it was higher in the SiDG, at 0.32 mm for pH 10 at 20 °C.

5.3.2.3 Measurement of δ_0

Feeler gauges were used to confirm the accuracy of the Mitutoyo micrometer (± 0.001 mm, Model ID-C112MB) used to measure δ_0 for the SiDG and the CTS under dry conditions. Figure 5.21 shows that while both slightly overestimate the thickness of the feeler gauges (Manufacturing accuracy of feeler thickness 0.03 – 0.15 mm; ± 0.005 mm; 0.20 – 0.50 mm; ± 0.012 mm; 0.60 – 1.00 mm; ± 0.020 mm) the Mitutoyo is more accurate. As the thickness of the feeler gauge approaches the range of interest (~ 0.3 -0.4 mm) the techniques agree. It is noted that feeler gauges are flat substrates whereas the CMS soils are rough. The Mitutoyo is known to overestimate the soil thickness as it measures the highest peak of the soil.

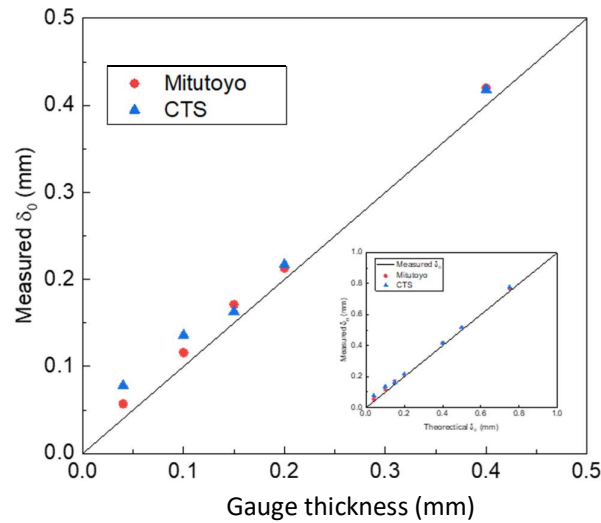


Figure 5.21: Comparison of δ_0 measured by Mitutoyo and CTS. Standards measured are feeler gauges of thickness 0.04, 0.1, 0.15, 0.2 and 0.4 mm. Inset: extended comparison including 0.5 and 0.8 mm.

5.3.2.4 Impact of measurement spot size

The CTS has a beam footprint of 9 μm diameter, whereas the SiDG diameter is 2 mm. CMS is a cracked soil and as such cracks will therefore be present with the SiDG footprint but they can be deliberately avoided in the CTS testing.

Direct comparisons between the SiDG and CTS swelling profiles of CMS submerged in pH 9 solution at 20 $^{\circ}\text{C}$ were conducted. Figure 5.22 shows four profiles obtained in SiDG tests and two obtained with the CTS. Both devices gave similar final extents of swelling (~ 0.16 mm) but there are noticeable differences in initial swelling behaviour. Each SiDG profile swells at a different rate, as do the CTS profiles. This is attributed to the presence of the surface cracks (Figure 5.12).

One CTS profile shows rapid hydration (over 0.1 mm) over the first 80 s, corresponding to the local measurement at a crack-free region. The second CTS profile shows a delay of approximately 500 s before noticeable swelling. In this test the 9 μm CTS light spot was deliberately located within a crack. The SiDG measurements exhibit swelling behaviour between the two CTS profiles. When submerged in solution the layers swell away from the substrate but also sideways to fill surface cracks. The initial delay in swelling is therefore associated with this crack filling. This was confirmed by Tsai (Tsai *et al.* 2019) via a 3-D simulation of the gauging flow on a surface with idealised cracks located beneath the nozzle.

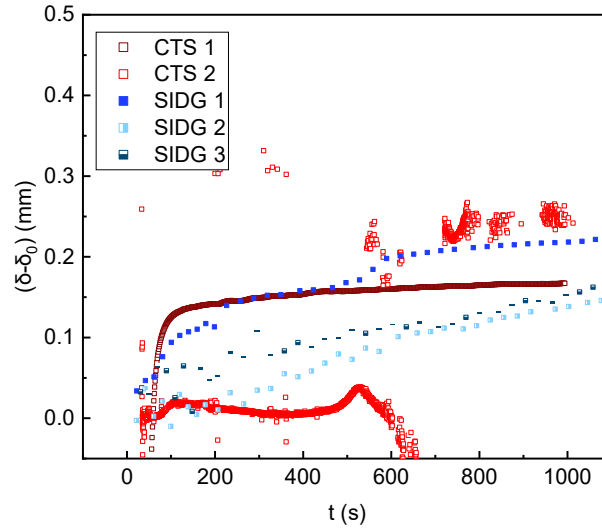


Figure 5.22: Comparison of swelling behaviour measured by the CTS and SiDG devices ($\dot{m} = 0.33 \text{ g s}^{-1}$) of CMS immersed in $\text{pH} = 9$ solution (δ_0 around $300 \mu\text{m}$), ejection mode. Red squares – CTS (2 repeats); blue squares – SiDG, ejection (3 repeats).

FDG measurements assume a smooth interface. The CMS layer is rough and features cracks of depth δ_0 . Wang *et al.* (2016) investigated the impact of surface roughness experimentally and showed that surface roughness leads to C_d being overestimated so that δ is underestimated. This is somewhat offset by the cracks providing flow channels for the solution to pass through which would cause an underestimation of δ as discussed previously.

The presence of a crack beneath the nozzle rim affected the flow pattern. For the simple case considered ($\dot{m} = 0.33 \text{ g/s}$, $h_0/d_t = 0.1$, representative of the experimental conditions used in these studies) the difference in suction mode was 8 % and in ejection mode 3 % (Tsai *et al.*, 2019).

5.3.3 CTS conclusions

The CTS can be used to monitor the swelling profiles of soils using a very small spot size. This is advantageous in cases of coherent, homogeneous soils however care must be taken when using heterogeneous soils that swell unevenly. CMS does not swell evenly and so location of the CTS focussing point greatly influences the results obtained, i.e. if focussed on a coherent section of soil, immediate swelling is recorded, if it lies on a crack, there is a time delay; and if it rests in between coherent soil and a crack then the light is reflected away at an angle and no measurement is recorded.

It was concluded based upon these measurements that the CTS provided valuable information about the impact of nozzle diameter choice for the SiDG. Since the measured change in thickness is an average of the distribution of soil thickness beneath the nozzle, a larger nozzle will average over a larger area and obtain one mean swelling profile, while a smaller d_t can provide another. Although

dynamic similarity suggests that the change in d_t can be compensated for by changing \dot{m} to give the same C_d , this will not always result in the same δ when testing cracked, heterogeneous soils.

5.4 Chapter conclusions

Three techniques were used in this chapter to investigate the swelling of CMS upon exposure to cleaning solutions of different temperature, pH and surfactancy.

Initial experiments conducted on the zFDG were confounded by inaccurate δ_0 data and the use of δ_i was not ideal for samples exhibiting rapid initial hydration due to the requirement to establish the location post-submersion. Investigations into the impact of temperature and pH using this device showed that the CMS swelled most above pH 9 at room temperature. This was attributed to OH⁻ ions interacting with starch molecules in the soil and causing internal repulsion to occur, expanding the soil network. Softening of the soil at higher temperatures resulted in the lower $\Delta\delta_{max}$ at 50 °C.

The SiDG technique was developed in order to elucidate the impact of hydration kinetics on the CMS layer. This technique demonstrated the ability to measure the initial swelling kinetics of soft solid layers immersed in a liquid environment. This development represents a significant advance over existing FDG techniques, which were unable to obtain data during this time period. Additionally, up to five readings can be taken per soiled sample (compared to one on the zFDG) allowing measurements to be repeated and operating conditions varied systematically.

Temperature was found to increase swelling rate constants until the temperature at which the soils fat components melt, above which little effect of temperature was noted. Little variation in $\Delta\delta_{max}$ was noted above 30 °C, only the timescale needed to reach $\Delta\delta_{max}$.

When hydration data were included, pH was shown to have a marked impact on the soil swelling kinetics. Tests conducted at room temperature showed that both the rate constant and $\Delta\delta_{max}$ increased with pH with pH 7 < pH 8, 9 < pH 10. Above pH 10 SiDG readings were not possible as the soil lost its integrity and sloughed down the sample plate. This is a significant drawback in the vertical mounting of the SiDG system. Hydration rate constants ($t < 10$ s) were found to increase linearly with the pH of the cleaning solution.

Surfactants demonstrated varied ability to promote swelling, dependent upon temperature, pH and soil coherency. At pH 7 surfactants doubled the $\Delta\delta_{max}$ of the soil and tripled the rate constant of swelling, however at 50 °C only marginal improvement was noted. The combination of increased pH, from pH 7 to 9, and the use of 0.1 wt.% SDBS gave a synergistic impact on the swelling rate of the CMS, and as such was the 'best' system tested. No significant differentiation of cleaning mode could be elucidated for different surfactant types.

A second technique to monitor swelling, using a LED confocal sensor, was developed. All measurement techniques were found to be sensitive to the layer macrostructure. Larger, wider cracks gave more inconsistent data on the zFDG and SiDG, associated with the large spot size of measurement. The thickness measurements are averaged over the total spot-size and therefore the presence of cracks will lead to underestimations in soil layer thickness. The CTS has a narrower spot size and therefore care must be taken with the initial positioning on a position free of cracks. A delay was observed where the soil swelled into the crack. Ultimately care is needed in interpreting both sets of data. The porous, rough, heterogeneous CMS layers pose challenges to both measurement techniques.

5.5 Timescales of cleaning

Here the timescale of cleaning was primarily dependent upon the soil macrostructure and pH. At pH 7 t_{asym} was approximately 1200 s, $\Delta\delta_{max} = 0.08$ mm, and the rate constant $k_{SiDG} = 0.91 \times 10^{-3} \text{ s}^{-1}$. An aqueous solution of 0.1 wt.% surfactant at 20 °C and pH 9 gave t_{asym} of ~ 800 s, $\Delta\delta_{max} = 0.27$ mm, and a rate constant of $k_{SiDG} = 3.97 \times 10^{-3} \text{ s}^{-1}$. These timescales are longer than those observed for CMS for pH 7 water on the microscope ($t_{asym} \approx 600$ s) however this discrepancy was known to be caused by the offset in δ_0 ($\delta_{0, CFM} = 0.2$ mm, $\delta_{0, SiDG} = 0.36$ mm).

6. Transfer of soil to solution

The release of oil from within the burnt soil layer to form droplets on the soil surface was first observed when undertaking zero discharge fluid dynamic gauging on the CMS formulation at 50°C (Figure 5.14(a, inset)).

The phenomenon was not observed in previous experiments conducted at room temperature (20°C). Differential scanning calorimetry of the CMS both before and after baking shows that melting of the soil components, likely the fat phase, occurs between 20 and 40 °C (Figure 3.4). Component release was observed under these conditions due to the decrease in the viscosity of the fat component in CMS at 50 °C (apparent viscosity of fat emulsion ~60 Pa s at 20 °C, ~2 Pa s at 50 °C, Figure 3.6), i.e. the fat melted.

Observation of the droplets during zFDG testing of soil swelling in the zFDG tests led to the hypothesis that the rate of droplet formation and solubilisation into the solution may be an important factor in determining the overall cleaning rate. Conversely, quantification of these release rates could allow features such as the timescale of swelling (and B/C transitions in MM3 testing, Chapter 7) to be explained. Preliminary testing was conducted to ascertain if there were observable differences in oil evolution rate under a range of thermal and mechanical conditions in simple cleaning solutions.

Submersion of a burnt CMS layer in deionised water at a temperature above the onset of the melting range of the fat component (around 40 °C) led to oil droplet formation at the soil-solution interface (Figure 6.1 (b)). The droplets were estimated to be up to 2 mm in diameter and grew gradually over a period of 5 – 10 minutes following submersion.



Figure 6.1: (a) Appearance of oil droplets on a CMS-SS sample submerged in cleaning solution in zFDG testing at 50°C. (b) Oil droplet formation on burnt CMS contacted with pH 7 deionised water at 50°C.

Droplet formation is indicative of water penetration into the soil, displacing the oil to the surface due to its lower density. At the surface the oil forms droplets indicating their removal via an oil ‘roll-up’

mechanism. The evolution of the oil droplets reflects a change in composition of the burnt CMS, and potentially its mechanical properties, and so two methods to monitor the oil loss were devised.

1. Oil recovery

Initial intentions to monitor the oil liberated from the solution focussed on separating the oil phase from the aqueous solution and measuring its mass. An activated carbon black filter was created and tested. However, water retention was too high to make the technique feasible. 10 g of 'oil' phase was collected over the duration of the test but the original soil mass was 0.8 g, of which about 47 % of which was oil based. More thorough drying before and after filtration did not significantly improve the systematic error in measurements. Separation of the oil component from the aqueous phase was therefore considered to be infeasible for high-throughput testing.

Methods of monitoring the oil concentration in the aqueous solution were then investigated and total organic carbon (TOC) analysis was chosen. It is important to note that this is a non-specific technique. The TOC does not differentiate between solubilised oil/fats and other organic matter such as proteins and starches. The organic carbon measured in this section is assumed to be primarily from fats and oils unless otherwise stated. Karl Fischer titration was considered but a working titrator was not available.

This technique was developed and improved upon over time and so there is some variation in the repeatability of the solutions tested (e.g. Figure 6.9 early data: (a, b) vs refined data (c, d)).

2. Image analysis of the droplets

The formation and evolution of droplets on the deposit surface was also monitored via image analysis for a period of 60 minutes after submersion, for a range of cleaning solutions. Photographs of the CMS surface were taken at 15 s intervals and an image analysis technique developed in order to monitor the droplet growth, the total volume of the droplets on the surface, and the influence of the cleaning solution composition on the rate of droplet formation and detachment. Two models based upon proposed mechanisms of oil displacement within the soil layer were developed and fitted to the data. Finally the impact of surfactants on droplet growth and release were investigated.

6.1 Oil recovery technique development

6.1.1 Experimental set-up

6.1.1.1 Sample preparation

Samples were prepared on polished 170 mm x 24 mm x 1.1 mm thick 316 stainless steel plates with roughness, R_q of 18.5 μm (measured using the CTS, Chapter 5) (Figure 6.2). Plates were pre-washed

in an ultrasonic bath whilst submerged in solutions of soapy $\text{NaOH}_{(aq)}$ solution (10 minutes), isopropyl alcohol (10 minutes), and acetone (10 minutes). Plates were scrubbed with a soft sponge between each step and afterwards dried in air at room temperature.

A target soiled section was defined for each sample plate using Sellotape™. Static samples were prepared with a 24 mm X 66 mm rectangular cross section (soil-substrate contact area: 1580 mm²). Samples for the flow rig had a soiled area of 160 x 10 mm (giving a soil-substrate contact area 1600 mm²) (Figure 6.2). Excess soil was deposited on the marked substrate and the drawdown device (Figure 3.2) passed over it with a clearance of 1.8 mm to generate a layer of thickness approximately 0.7 mm. This gave a target wet mass of 1.5 g.

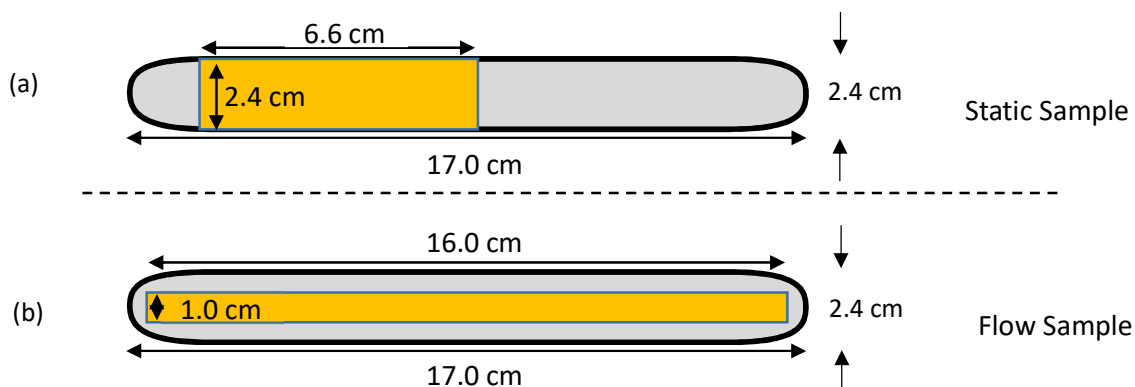


Figure 6.2: Schematics of soiled 'lollipop stick' plates for (a) static and (b) flow testing. Yellow colouring indicates soiled region.

The soil used in these tests was CMS prepared as described in Chapter 3. A fresh batch of CMS mix was used for each set of samples. Soils were applied to pre-weighed plates (4 decimal place balance, Precisa®, XB10200G), weighed within 1 min of application (fresh soil mass), left to evaporate in ambient air for at least 18 hours, weighed (post-evaporation mass), baked in a conventional oven (Carbolite®) for 7 min at 204 °C, removed from the oven, cooled in ambient air for > 1 hour to room temperature and subsequently weighed (post-baking mass). Soil layer masses averaged over 60 samples are given in Table 6.1.

Table 6.1: Soil sample preparation masses for 60 CMS soil plates.

Soil sample mass (+/- standard error) / g			
	Fresh	Evaporated	Baked
Soil mass	1.54 (0.17)	0.77 (0.10)	0.67 (0.10)
Mass loss		50 % (2.1)	56 % (2.8)
Coverage / kg m ⁻²		0.486	0.419

6.1.1.2 Solution preparation

Up to 3.6 L of solution (solution volume varied with flow rate) was prepared for each test. For tests conducted at 50 °C, 4 L of deionised water was heated in a 5 L glass beaker on a stirrer hot-plate with stirring at approx. 200 rpm. Its pH was measured using a pH probe (Jenway 3520) and raised through the dropwise addition of 0.1 M NaOH until the required pH was achieved. Surfactants, chelant and bleach were weighed out on a 4 decimal place balance (Precisa®, XB10200G), added, and stirred for 30 minutes. Solutions were maintained at the desired temperature on the hotplate before testing commenced.

6.1.1.3 Static System

Two 100 ml measuring cylinders, each containing 50 ml of cleaning solution, were maintained at a set temperature in a thermostatically controlled water bath. At $t = 0$ s, a stainless steel 'lollipop stick' ($17.0 \times 2.4 \times 1$ mm) soiled with burnt CMS ($6.6 \times 2.4 \times 0.3$ mm) (Figure 6.2 (a)) was lowered into the cleaning solution in solution chamber 1 (Figure 6.3) ensuring full soil submersion. After 5 minutes the substrate was moved from the initial solution to chamber 2. The solution from chamber 1 was collected, filtered ($450 \mu\text{m}$ syringe filter, Whatman®) and the filtrate stored for subsequent TOC analysis (TOC, Sievers InnovOx). The sample was moved between chambers after total elapsed times of 15, 30, 60 and 120 minutes. A baseline measurement of organic carbon in the cleaning solution was established using 'fresh' cleaning solution. Data are presented as mg of oil solubilised per gram of soil sample submerged (mg g^{-1}). Tests were conducted in triplicate. TOC analysis was conducted in triplicate with a fourth measurement made if required.

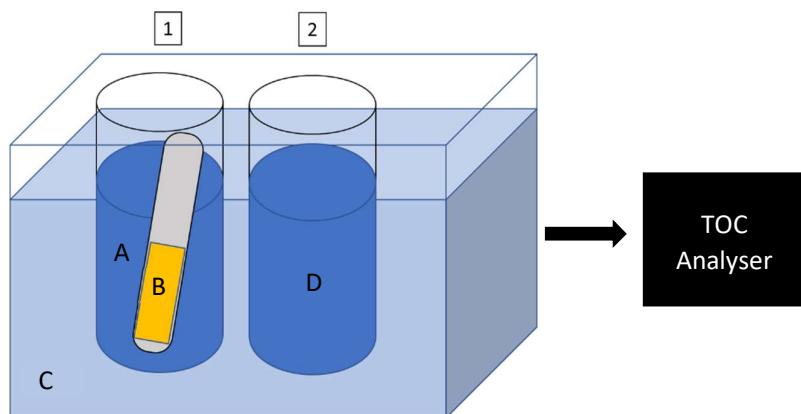


Figure 6.3: Static method of oil collection. A – 100 ml solution chamber, solution volume: 50 ml. [1] containing soil sample; B – soil on SS substrate (Figure 6.2(a)); C – thermostatted water bath; D – second solution chamber [2].

6.1.1.4 Flow system

It was thought that in flowing systems any liberated oil was likely to be removed by the shear flow across the soil surface. The system shown in Figure 6.4 was designed to test the impact of convection at the soil surface. Cleaning solution was held in a stirred reservoir (labelled A) and was heated to the required temperature using a hotplate. The solution was fed by peristaltic pump (labelled B) into the Perspex™ sample chamber (C). The substrate sat in a recess in the lower section of the chamber with the soil layer protruding into the flow. The solution was collected in a series of collection vials (D). For ease of comparison the time intervals used in static tests were repeated for flowing systems; 0 (baseline), 5, 15, 30, 60 and 120 minutes. Flow rates of 1, 3, 10 and 30 ml min⁻¹ were investigated. The eluent for each time interval was stirred to homogenise the solution before aliquots were taken. The effect of solution pH, chelants, surfactants and temperature were investigated.

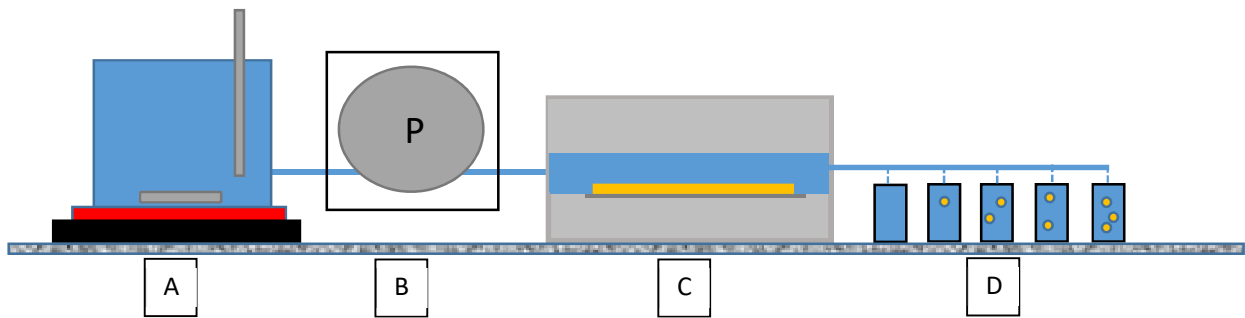


Figure 6.4: Schematic of Flow rig for investigating oil release of CMS samples. A) Temperature controlled solution reservoir, B) peristaltic pump, C) sample chamber, D) solution collection chambers.

A schematic of the sample flow chamber (Item C in Figure 6.4) is shown in Figure 6.5.

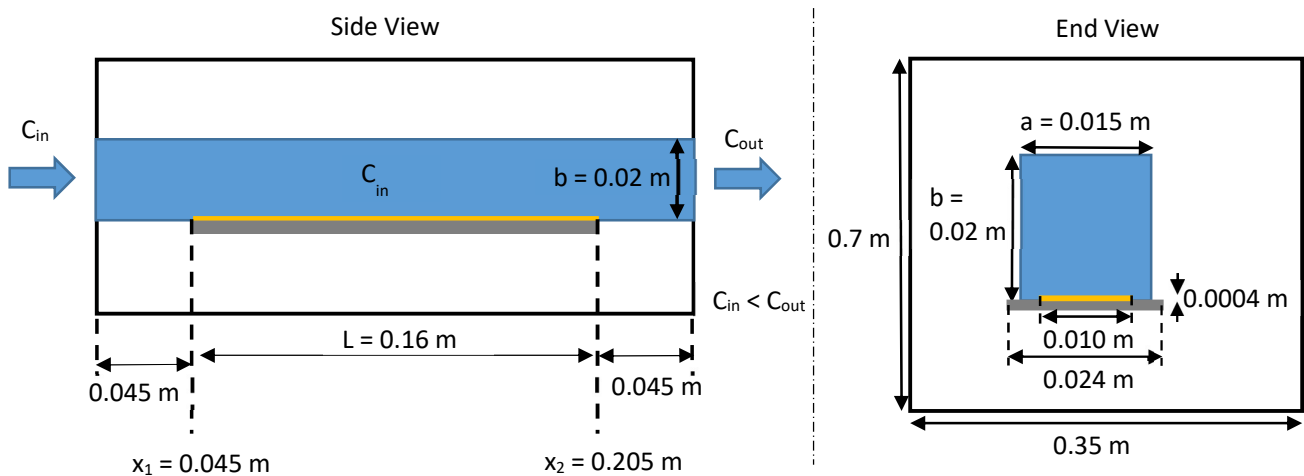


Figure 6.5: Schematic of sample chamber. $Q = 1 - 30 \text{ cm}^3/\text{min}$, $\bar{U} = 0.167 - 5.76 \text{ mm/s}$. Residence time = 2.5 - 75 min.

The mean Reynolds number in a square duct is given by

$$Re_{D_h} = \frac{\rho \bar{U} D_h}{\mu} \quad \text{Equation 6.1}$$

where \bar{U} is the average flow velocity, and D_h is the hydraulic diameter,

$$D_h = \frac{4A}{P} = \frac{2ab}{a+b} \quad \text{Equation 6.2}$$

where A is the area of the square duct of dimensions width a and depth b , and P is its wetted perimeter. In this case D_h was 0.017 m, giving Re_{D_h} values in the range of 0.9 to 52 (Table 6.2).

Table 6.2: Reynolds numbers associated with test flow velocities

Flow velocity / $m\ s^{-1}$	Re_{D_h}	
	22°C	50°C
5.56×10^{-5}	0.9	1.7
1.67×10^{-4}	2.8	5.2
5.56×10^{-4}	9.5	17.2
1.67×10^{-3}	28.5	51.6

These values are indicative of laminar flow. The transition from laminar to turbulent flow in a smooth cylindrical pipe or duct was experimentally defined by Osborne Reynolds in 1883 (Reynolds, 1883) as $Re_{cr} \approx 2,300$.

$$Re_{cr} = \frac{\rho \bar{U} D_h}{\mu} \quad \text{Equation 6.3}$$

For internal flows, such as those found in a duct, the flow is contained. There is an entrance region where the upstream flow converges, beyond which the velocity profile develops and becomes constant, at which point \bar{U} becomes an acceptable approximation for the flow velocity. Assuming that the fluid enters the duct from a rounded converging nozzle, and as such is characterised by a uniform velocity profile at the entrance, the length of the entrance region, L_e , can be approximated as (Langhaar, 1942) (Table 6.3).

$$\frac{L_e}{D_h} = 0.06 Re_{D_h} \quad \text{Equation 6.4}$$

Table 6.3: Length of entrance regions associated with test flow velocities

Flow Velocity m/s	Entrance region, L_e / mm	
	22°C	50°C
5.56×10^{-5}	0.976	1.77
1.67×10^{-4}	2.93	5.31
5.56×10^{-4}	9.76	17.7
1.67×10^{-3}	29.3	53.1

All entrance regions calculated bar one ($U = 1.67 \times 10^{-3} \text{ m s}^{-1}$, $T = 50 \text{ }^\circ\text{C}$, $L_e = 53.1 \text{ mm}$) are shorter than the 0.045 m spacing between the duct entrance and the start of the oil layer (x_1 , Figure 6.5). Testing was not conducted on the sample with a L_e greater than 0.045 m due to unrelated experimental difficulties. Therefore a simple analysis of fully developed flow can be used across the entire length of the soiled region.

The wall shear stress within the channel can be estimated using the Moody friction factor, a dimensionless parameter defined as (Moody, 1944)

$$f = \frac{-2 \left(\frac{dp}{dx} \right) D_h}{\rho \bar{U}^2} \quad \text{Equation 6.5}$$

For a fully developed laminar flow with average velocity U_m and Reynolds number, Re_{D_h} ,

$$f = \frac{64}{Re_{D_h}} \quad \text{Equation 6.6}$$

The average wall shear stress along the duct is given by (Muzychka and Yovanovic

$$f = \frac{8 \bar{\tau}_w}{\rho \bar{U}^2} \quad \text{Equation 6.7}$$

where $\bar{\tau}_w$ is the average wall shear stress along the duct. The average friction factors and wall shear stresses for each flow velocity and temperature are found in Table 6.4.

Table 6.4: Average wall shear stresses associated with test flow velocities

Flow Velocity m/s	22 °C		50 °C	
	f / -	$\bar{\tau}_w$ / Pa	f / -	$\bar{\tau}_w$ / Pa
5.56×10^{-5}	67.5	5.20×10^{-5}	37.2	1.42×10^{-5}
1.67×10^{-4}	22.5	1.56×10^{-4}	12.4	4.26×10^{-5}
5.56×10^{-4}	6.7	5.20×10^{-4}	3.7	1.42×10^{-4}
1.67×10^{-3}	2.2	1.56×10^{-3}	1.2	4.26×10^{-4}

The local wall shear stress at the beginning and end of the soil layer can also be estimated using a local Reynolds number Re_x , local friction factors, f_x and $C_{f,x}$, where x is the distance along the duct in the x -direction (Table 6.5).

$$Re_x = \frac{\rho \bar{U} x}{\mu} \quad \text{Equation 6.8}$$

$$f_x = \frac{64}{Re_x} \quad \text{Equation 6.9}$$

$$\tau_{w,x} = \frac{f_x \rho \bar{U}^2}{8} \quad \text{Equation 6.10}$$

Table 6.5: Local wall shear stresses associated with test flow velocities at a) x_1 and b) x_2 (Figure 6.5)

(a)	x_1 Flow Velocity m/s	22 °C			50 °C		
		Re_x	f_x	$\tau_{w,x} / \text{Pa}$	Re_x	f_x	$\tau_{w,x} / \text{Pa}$
	5.56×10^{-5}	2.5	25.7	9.9×10^{-6}	4.5	14.2	5.5×10^{-6}
	1.67×10^{-4}	7.5	8.6	3.0×10^{-5}	13.6	4.7	1.6×10^{-5}
	5.56×10^{-4}	24.9	2.6	9.9×10^{-5}	45.2	1.4	5.5×10^{-5}
	1.67×10^{-3}	74.7	0.9	3.0×10^{-4}	135.5	0.5	1.6×10^{-4}

(b)	x_2 Flow Velocity m/s	22 °C			50 °C		
		Re_x	f_x	$\tau_{w,x} / \text{Pa}$	Re_x	f_x	$\tau_{w,x} / \text{Pa}$
	5.56×10^{-5}	11.3	5.6	2.2×10^{-6}	20.6	3.1	1.2×10^{-6}
	1.67×10^{-4}	34.0	1.9	6.5×10^{-6}	61.7	1.0	3.6×10^{-6}
	5.56×10^{-4}	113.4	0.6	2.2×10^{-5}	205.8	0.3	1.2×10^{-5}
	1.67×10^{-3}	340.3	0.2	6.5×10^{-5}	617.4	0.1	3.6×10^{-5}

The drag force over the soil $F_D (x_2 - x_1)$ is calculated from;

$$F_D = \frac{C_D \rho \bar{U}^2 A}{2} \quad \text{Equation 6.11}$$

Where C_D is the drag coefficient for length $(x_2 - x_1)$ defined as $1.328 / \sqrt{Re_{(x_2-x_1)}}$, and A is the surface area of the soil in contact with the flowing solution (Table 6.6).

Table 6.6: Drag force over the soil associated with test flow velocities

F_D for soil Flow Velocity m/s	22 °C			50 °C		
	$Re_{x_2-x_1}$	C_D	F_D / N	$Re_{x_2-x_1}$	C_D	F_D / N
5.56×10^{-5}	8.9	0.45	1.98×10^{-5}	16.1	0.33	1.46×10^{-5}
1.67×10^{-4}	26.6	0.26	3.43×10^{-5}	48.2	0.19	2.52×10^{-5}
5.56×10^{-4}	88.5	0.14	6.26×10^{-5}	161	0.10	4.60×10^{-5}
1.67×10^{-3}	266	0.08	1.08×10^{-4}	482	0.06	7.97×10^{-5}

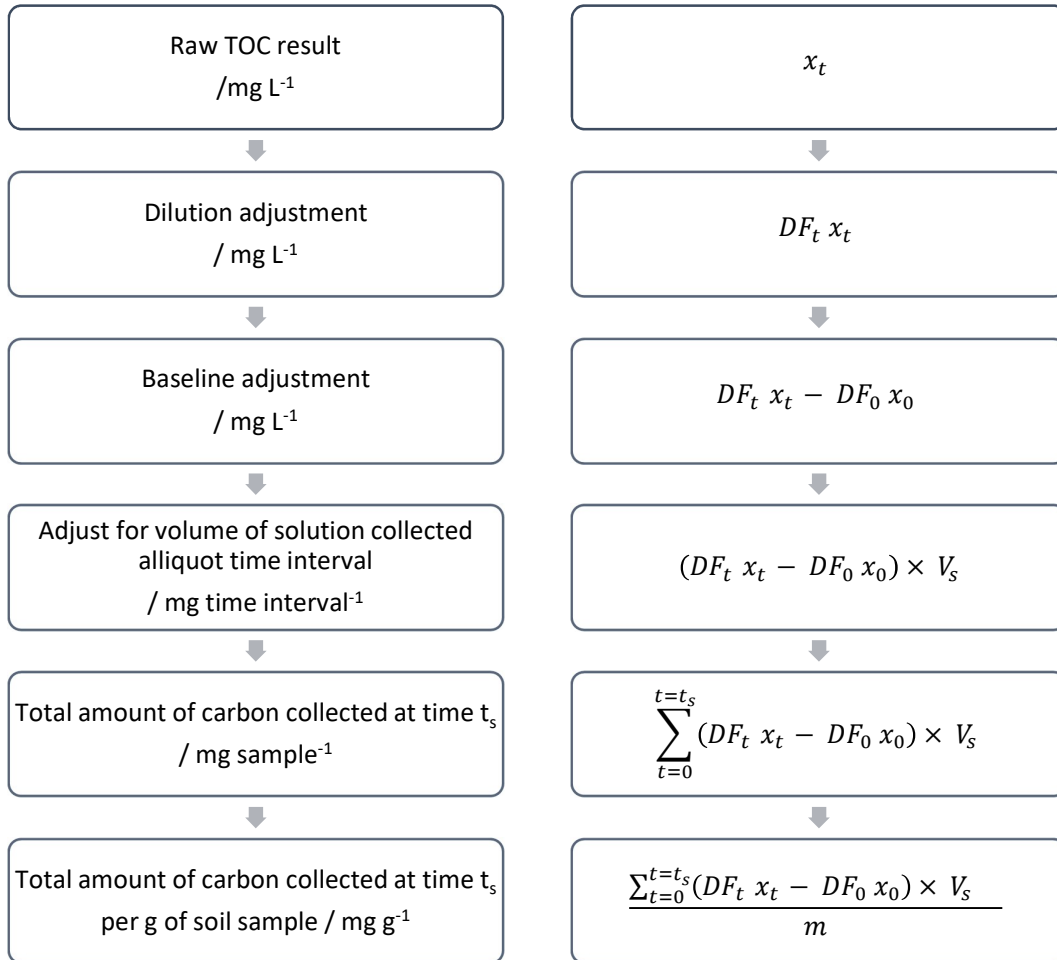
In all experiments the wall shear stresses and drag forces experienced by the soil are very low, on the scale of 0.01 mPa and 0.01 mN.

6.1.1.5 Data processing

TOC results for each aliquot were processed as shown in Flow Chart 6.1. The static and flow tests generated very different volumes of solution so solution volume was eliminated as a variable in order to facilitate comparison between the two apparatuses. It is important to note, however, that tests generating large volumes (e.g. 30 ml min^{-1}) resulted in relatively dilute solutions. Analysis of these dilute systems could be affected by the detection limits of the TOC, at 1 mg L^{-1} for a STDev 1.0 % (Limit of Quantification 0.14 ppm, 20 % STDev, 0.75 ppm 5.0 % STDev, Sievers InnovOx. Aliquots were diluted

to target a concentration of 20-200 ppm, however very high and very low flow rate tests gave solutions that measured in the 0 - 5 ppm range.

Flow Chart 6.1: Data processing chart for static and flowing systems described in Figure 6.3 and 6.4.



Where

t_s is the time at which the sample was taken. $t_s = \{0, 5, 10, 15, 30, 60, 120 \text{ min}\}$

x_0 is the TOC measurement in a sample at time t_0

x_t is the TOC measurement in a sample at time t_s

DF_t is the dilution factor of the TOC sample at time t_s as defined by;

$$DF_t = \frac{V_{\text{solution}} + V_{\text{DI water}}}{V_{\text{solution}}}$$

$V_{s,t}$ is the sample volume collected for a given time interval, t.

6.1.1.6 Data labelling

The data sets are labelled using the following convention;

Experiment type - solution pH – solution temperature – additive in solution.

where each marker can take the following values;

Experiment type: Batch (B), Static (S) or Flow (FXX) where XX denotes the flow rate in ml min⁻¹

Solution pH: 7, 10, or 12

Solution temperature: 22 to 50 °C

Additives: No additive (R), MGDA (M), SDBS (S), CTAB (C), bleach (B), full formulation (FF).

For example: the label 'F10-7-50-M' indicates a cleaning solution used in the flow test rig at 10 ml min⁻¹, at pH 7 and 50 °C, containing 0.1 wt. % MGDA.

6.1.2 Static results and discussion

6.1.2.1 Impact of temperature

The room temperature profiles in Figure 6.6 show almost linear release behaviour whilst data collected at T > 35 °C show asymptotic behaviour, which was fitted to

$$(TOC - TOC_{initial}) = TOC_{max} \left(1 - e^{-\frac{(t-t_0)}{\tau_{TOC}}} \right) \quad \text{Equation 6.12}$$

where TOC is the cumulative total organic carbon released at time t , $TOC_{initial}$ is the background organic carbon level present in the cleaning solution, TOC_{max} is the cumulative total organic carbon released by the end of the test, calculated through estimation of the asymptotic value, t_0 is the time at which immersion occurs, and τ_{TOC} is the half-life which yields a rate constant, k_{TOC}

$$k_{TOC} = \frac{1}{\tau_{TOC}} \quad \text{Equation 6.13}$$

Figure 6.6 shows the influence of temperature of temperature on oil release at pH 7 and pH 10 in the static tests. Increasing temperature increases the rate of carbon release, with a noticeable change from linear to asymptotic behaviour. The latter is associated with the approach to a limiting amount of available carbon. This limiting value can be compared with the initial amount of oil in the sample, determined as 316 mg (470 mg g⁻¹ from Chapter 3). Comparing this with the maximum value in Figure 6.6 (a) of 23 mg g⁻¹ over 120 min testing at 22 °C indicates that only 7 % of the oil, if the TOC measured oil alone, had been released. Figure 6.6 shows a detectable level of carbon release at 22 °C even though droplets were not observed. This value could be due to the presence of starch and sugars.

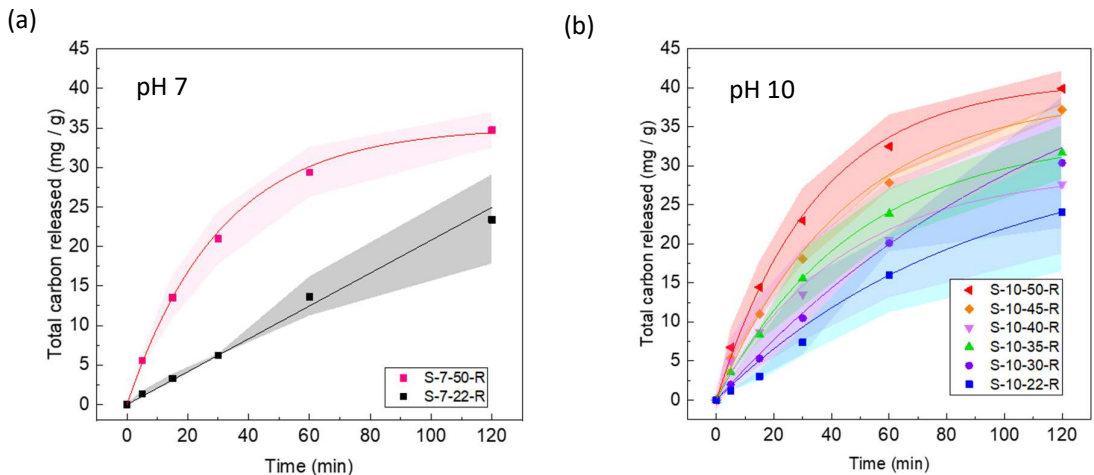


Figure 6.6: Effect of temperature on cumulative total carbon released from 0.67 +/- 0.1 g burnt CMS soil after submersion in cleaning solution at (a) pH 7 and (b) pH 10 in static tests. Lines: Experimental fits to Equation 6.12. Associated kinetic parameters given in Table 6.7.

The release data were fitted to Equation 6.12 and the parameters obtained are reported in Figure 6.7 and Table 6.7. Between 30 and 50 °C the rate constant of oil release is approximately constant at $0.36 \times 10^{-6} \text{ s}^{-1}$. At 50 °C this increases to approximately $0.5 \times 10^{-6} \text{ g s}^{-1}$ for both pH 7 and pH 10. This coincides with the decrease in the shear viscosity of the fat component which shows a sharp drop in viscosity between 26 and 34 °C before plateauing at 40 °C (Figure 3.6). As the heat from the cleaning solution is transferred to the soil, the fat components become more mobile and carbon release from the soil into the solution is enhanced. The amount of oil released generally increased both with time and temperature.

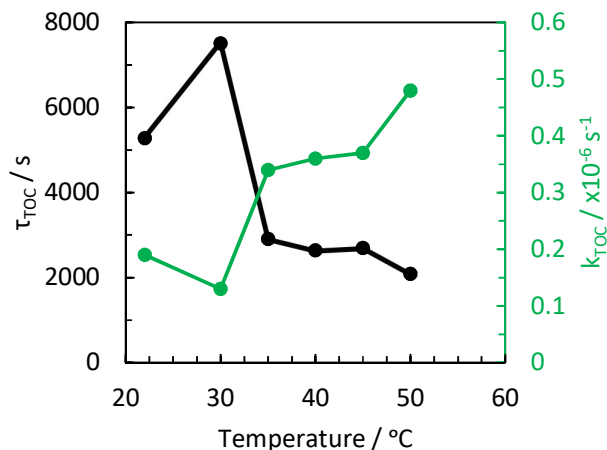


Figure 6.7: Kinetic parameters obtained from Figure 6.6 (b), pH 10.

Some quantitative checking was conducted. The fat content of the burnt CMS was measured using acid hydrolysis and liquid-liquid extraction (Test Method C-TM-007, Premier Analytical Services, Hemel

Hempstead) as 47.2 g/100 g. The average CMS sample mass is 0.67 g, resulting in a maximum total fat mass of 0.31 g fat per sample. Using an empirical formula of fat of $C_9H_{18}O_1$ gives a mass fraction of carbon of 76 % and a maximum carbon content of fat per sample of 240 mg. Comparing with Figure 6.6, the maximum fraction of fat equivalent, f_{FE} , i.e. the amount of oil released in a simple pH 10 solution after 2 hours at 50 °C, is 27.4 mg or 11 % of the total fat available. This shows that in the absence of surfactant, low levels of fat were released.

Table 6.7: Kinetic parameters from both data sets in Figure 6.6.

pH	T / °C	Sample	TOC_{max} / $mg\ g^{-1}$	T_{TOC} / s	K_{TOC} / $\times 10^{-6}\ s^{-1}$	f_{FE} / %	R^2
10	22	S-10-22-R	32	5280	0.19	9.0	0.999
	30	S-10-30-R	52	7510	0.13	14.6	0.999
	35	S-10-35-R	36	2910	0.34	9.5	0.991
	40	S-10-40-R	29	2640	0.36	8.0	0.980
	45	S-10-45-R	39	2700	0.37	11.0	0.990
	50	S-10-50-R	41	2090	0.48	11.4	0.998
7	22	S-7-22-R	16	-	-	-	0.999
	50	S-7-50-R	35	1840	0.54	9.8	0.999

Figure 6.8 shows that the pH has relatively little influence on the oil release in the absence of surfactant in static tests at 22 °C and 50 °C until pH 12, when the amount of oil released doubled in both systems. The test at 22 °C also deviates linear trends of the test conducted at lower pH. This is likely due to the breakdown of the soil matrix through hydrolysis that occurs at pH > 10.4 (shown in Chapter 7). This would increase the measured carbon release as the solution would then contain particles of burnt sugar and protein with particle sizes <450 μm , in addition to fats and oils. Note that f_{FE} is still small, at 18 %.

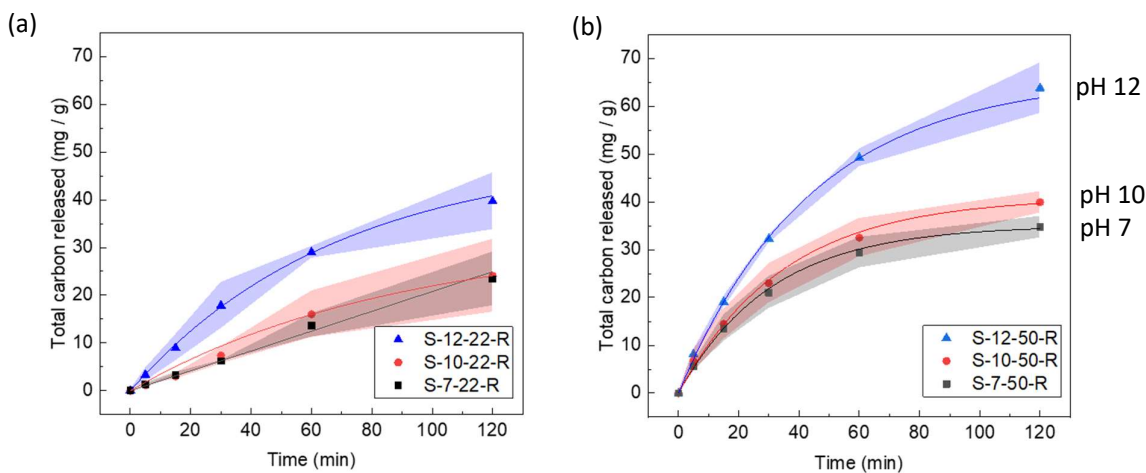


Figure 6.8: Effect of pH on total carbon release at (a) 22 °C and (b) 50 °C in static tests. Lines: Experimental fits to Equation 6.12. Associated kinetic parameters given in Table 6.8.

The data in Figure 6.8 were fitted to Equation 6.12 and the parameters obtained are reported in Table 6.8. The final amount of oil released increased significantly with pH to a maximum of 18.4 % of that within the sample. At T = 50 °C the maximum oil release was inversely related to the rate constant of release, k_{TOC} , decreasing from $0.54 \times 10^{-6} \text{ s}^{-1}$ to $0.38 \times 10^{-6} \text{ s}^{-1}$. Linear fits were used for pH 7 and 10 at 22 °C with the linear rate constant, k_L , interpreted as the initial rate of the exponential decay curve;

$$\frac{dTOC}{dt} = TOC_{max} \left(e^{-\frac{t-t_0}{\tau_{TOC}}} \right) \quad \text{Equation 6.14}$$

Giving the initial rate of change in TOC as;

$$\frac{dTOC}{dt} = k_{TOC} \times TOC_{max} = k_L \quad \text{Equation 6.15}$$

Table 6.8: Kinetic parameters from data sets in Figure 6.8. Data fitted to Equation 6.12 and Equation 6.15

Sample	pH	T / °C	TOC_{max} / mg/g	T_{TOC} / s	K_{TOC} / $\times 10^{-6} \text{ s}^{-1}$	k_L / $\times 10^{-6}$	f_{FE} / %	R^2
S-7-50-R	7	50	23.5	1850	0.54	12.7	9.8	0.999
S-10-50-R	10	50	27.4	2090	0.48	13.1	11.4	0.998
S-12-50-R	12	50	44.2	2640	0.38	16.8	18.4	0.998
S-12-22-R	12	22	33.1	4100	0.24	7.9	13.8	0.998
S-7-22-R	7	22	15.7	-	-	2.3	6.5	0.999
S-10-22-R	10	22	16.1	-	-	3.2	6.7	1

6.1.2.2 Impact of surfactants

Commercial cleaning formulations contain a range of additives to enhance cleaning. These additives include surfactants, chelates and bleaches. Solutions containing two common surfactants, the anionic SDBS (S) and cationic CTAB (C) were tested, along with a chelant (M) and an oxygen-based bleach (B). Figure 6.9 shows the impact of each type on the oil release behaviour in static tests. All tests were performed for two hours. There is a noticeable difference in standard deviation of the experimental data in Figure 6.9. This is an artefact of technique refinement and so care should be taken when mechanistically interpreting low repeatability. Figure 6.9 (a) and (b) are examples of early testing, while (c) and (d) examples of later testing.

Asymptotic behaviour was observed in all cases except that containing MGDA at 22 °C. Kinetic parameters for each test are reported in Table 6.9. For SDBS no significant improvement was observed over the reference solution (Figure 6.9(a)) at 50 °C ($TOC_{max} = 41 \text{ mg g}^{-1}$ at pH 7 vs 38.2 mg g^{-1} with

SDBS), however at 22 °C there was a shift from a linear to asymptotic behaviour, with an increase in TOC_{max} by 48 % with SDBS ($TOC_{max} = 16.1 \text{ mg g}^{-1}$ at pH 7 vs 30.8 mg g^{-1}).

Figure 6.9 (c) shows that CTAB significantly improved the carbon released over the reference, accessing approximately 1/3 of all available carbon from fat within the soil. There is a three-fold improvement over the reference solution at both temperatures tested. This release also occurs faster, with a 50 % increase in $k_{TOC} = 0.48 \text{ s}^{-1}$ at pH 7 vs 0.63 s^{-1} with CTAB. The enhanced oil release of CTAB containing cleaning solutions is consistent with observations of carbon release through image analysis (Chapter 6, Section 2) and the enhanced loss of soil adhesion strength to the surface demonstrated in Chapter 7 in millimanipulation testing.

Figure 6.9 (b) shows that the chelant, MGDA, had no significant impact on the carbon release at 50 °C ($f_{FE} = 10 \%$ with MGDA vs 11.4 % without), and a modest increase at room temperature ($f_{FE} = 7.8 \%$ with MGDA vs 4.5 % without). This indicates that the chelants are not involved in the solubilisation of the oils and fats within the soil. This is expected as chelants are added to coordinate with free ions such as Ca^{2+} , which would not be expected to play a role in the solubilisation of fats.

Bleach had a noticeable impact. At 50 °C an estimated equivalent of 60 % of all available carbon from the fats present in the mixture was released when bleach was present. At this pH and temperature bleach causes noticeable swelling (Chapter 9). It is thought that the enhanced swelling could open up the pore structure of the CMS. These wider flow channels would allow increased access by the cleaning solution driving the displacement of the mobile carbon material from within the soil. The soil also tended to lose its structural integrity in the presence of bleach (Chapter 9). Small particles of the deposit matrix smaller than the 450 μm filtration limit would contribute to the measured carbon release. For pH 10 water at 50 °C a plateau was reached at 25 mg after 80 minutes. The equivalent amount of carbon was released within the first 5 minutes of testing in a bleach containing solution. It is evident that bleach plays a significant role in the initial release of the oil and fats from the CMS.

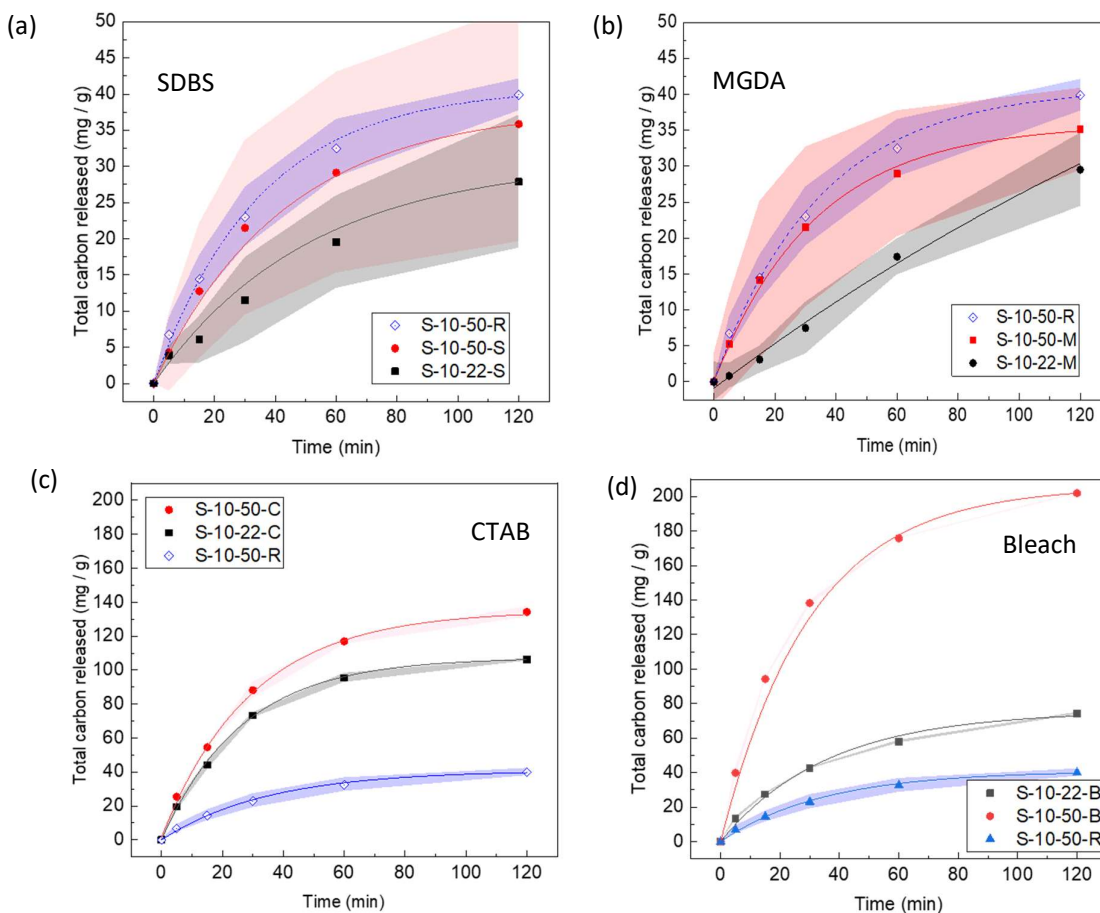


Figure 6.9: Effect of additives on cumulative total carbon release at 22 °C and 50 °C. SDBS (S), MGDA (M), CTAB (C), Bleach (B). Static test conditions. Note different y-axis scales. Lines: Experimental fits to Equation 6.12. Associated kinetic parameters given in Table 6.9. R = Reference. Data for SDBS and MGDA have larger error boundaries due to tests occurring at start of method development.

To take advantage of this fact bleach release could be two tiered; with the first release timed to occur early in the cleaning cycle to enhance swelling, and therefore oil release; followed by a later release enabling its functionality as a finishing agent.

Table 6.9: Kinetic parameters from both data sets in Figure 6.9. Data fitted to Equation 6.12.

Sample	Surfactant @ 0.1 %	Temp / °C	TOC_{max} / $mg\ g^{-1}$	T_{TOC} / s	k_{TOC} / $\times 10^{-6}\ s^{-1}$	f_{FE} / %	R^2
S-10-22-R	None	22	16.1	-	-	4.5	-
S-10-50-R		50	41	2090	0.48	11.4	0.998
S-10-22-S	SDBS	22	30.8	3060	0.33	8.6	1
S-10-50-S		50	38.2	2590	0.39	10.7	1
S-10-22-M	MGDA	22	28	-	-	7.8	-
S-10-50-M		50	35.9	1990	0.50	10.0	0.999
S-10-22-C	CTAB	22	107	1770	0.57	30.0	0.999
S-10-50-C		50	135	1590	0.63	37.7	0.996
S-10-22-B	Bleach	22	78.3	2150	0.46	21.3	0.999
S-10-50-B		50	202	1810	0.55	57.4	0.999

6.1.3. Flow testing results and discussion

The impact of flow rate, temperature, surfactant and chelant were subsequently explored using the flow rig described in Figure 6.4.

6.1.3.1 Impact of flow rate

The effect of flowing the solution over CMS on the oil release rate was investigated for flows ranging from 1 ml min^{-1} to 30 ml min^{-1} . All tests with flowing solutions give lower carbon release than static tests. Figure 6.10 shows that there is no clear relationship between the flow rate of the solution and the amount of oil released over 2 hours of testing. The shear stress imposed on an interface by the laminar flow of a Newtonian fluid increases with increased flow velocity. It would be expected that, in a system lacking surfactant molecules to promote oil roll-up, the driving forces for removal of mobile oils from the soil surface would be their buoyancy, oil displacement via pressure created by de-wetting in a capillary, and the shear stresses imposed on the soil from the solution flow. The latter leads to the expectation that higher flow rate would enhance the rate of oil removal. This was not observed. At room temperature testing the flow rate with greatest carbon removal was observed to be 3 ml min^{-1} , although the repeatability at this flow rate was low. Flows of 10 and 30 ml min^{-1} produced half as much organic carbon as the 3 ml min^{-1} test, with 1 ml min^{-1} producing half as much again. Similarly, at $50 \text{ }^{\circ}\text{C}$ 1 ml min^{-1} was observed to produce only 3 mg of organic carbon during testing with 3 and 10 ml min^{-1} generating approximately 10 mg. In the flow rig used here it was not possible to measure a flow rate of 30 ml min^{-1} at $50 \text{ }^{\circ}\text{C}$ as the equipment to warm the required 3.6 L of water required during testing was not available at the time.

There are several possible explanations for this unexpected result. The removal of the oil from the surface may have a detrimental impact of the displacement of oil from within the CMS bulk to the surface. As fat is highly hydrophobic it would preferentially remain within close proximity to other fat molecules than in proximity to the water. Water is likely to displace the fats within the soil layer due to preferential wetting of the water to the soil. This de-wetting of the fat layer drives displacement of the oils towards the cracks in the soil surface. If there is already a concentration of oil within the crack then the interfacial energies will be minimised by this accumulation. As the density of fats/oils is approximately $800 - 900 \text{ kg m}^{-3}$, lower than that of water (1000 kg m^{-3}), its relative buoyancy will cause it to move towards the surface of the soil. Removal of the oil by flow of water over the surface of the soil would prevent accumulation of the oil there and therefore lower the extent of interfacial energy minimisation. It would then be expected that slower flowing fluids, which allow for some oil accumulation to occur, would enhance the release of carbon/fat molecules from the CMS. This would explain why 3 ml min^{-1} removed more material than 10 and 30 ml min^{-1} . It is also corroborated by the

fact that the equivalent static systems (effectively the case of 0 ml min^{-1} , albeit with a vertically mounted plate in the static system, rather than a horizontally mounted one in the flow system) gave a total carbon removal of 16.1 mg at 22°C and 26.7 mg at 50°C , compared with 10.5 mg and 10.9 mg in flow tests, respectively.

It is possible that the low concentration of organic carbon in the 1 ml min^{-1} and 30 ml min^{-1} samples could lead to TOC being underestimated for these tests. As discussed above, the 30 ml min^{-1} solution was very dilute due to the large volume of cleaning solution involved during testing (0.3 L for static, 3.6 L for flow at 30 ml min^{-1}). A similar difficulty is encountered with the slow flow, 1 ml min^{-1} . For example, at the first data point only 5 ml of solution had passed through the chamber ($V_{\text{chamber}} = 48 \text{ ml}$). A minimum of 20 ml is required to conduct TOC testing, resulting in a minimum of $\times 4$ dilution of early solution samples. This could result in low calculated carbon loss if the concentration falls beneath the TOC detection threshold.

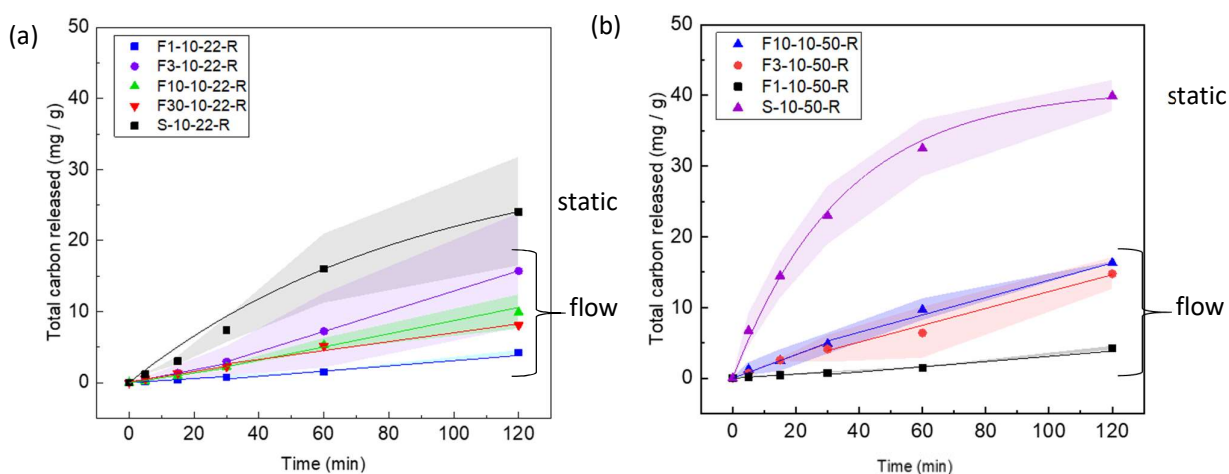


Figure 6.10: *Impact of flow rate at pH 10 and (a) 22°C and (b) 50°C .*

An additional experimental explanation is that a flow rate of 1 ml min^{-1} was not sufficient to remove the oil from sample chamber at any point during the test. Approximately 30 ml of solution per test sample remained in the sample chamber (Figure 6.4, Component C) at the end of the test, and the walls of the chamber appeared greasy. To test this theory the remaining solution was collected and measured for any residual organic carbon.

Figure 6.11 shows that flow velocity strongly impacts the amount of carbonaceous material remaining in the chamber. The lower the flow rate the higher the proportion of material that remained. Almost 70% of the total organic carbon measured at 1 ml min^{-1} was found to have remained within the sample chamber. At 10 ml min^{-1} the shear stresses and solution volume are sufficient for the fluid flow through the chamber to carry the released oil within it for collection.

This is consistent with the findings from oil video analysis in Section 2 of this chapter and the ADW testing in Chapter 9 which shows that at low shear stress conditions, skin friction forces keep the oil attached to the CMS surface. At higher flow rates the higher shear forces remove the soil as it approaches the soil surface which in this case appears to reduce the total oil released from the soil. This could be attributed to a wicking effect, i.e. the oil present on the surface acts to stabilise nearby hydrophobic material, increasing the rate of oil transport to the soil surface. This suggests that in order to maximise oil release the solution should not be agitated, however solution agitation will enhance other aspects of cleaning and likely provides an overall benefit to cleaning.

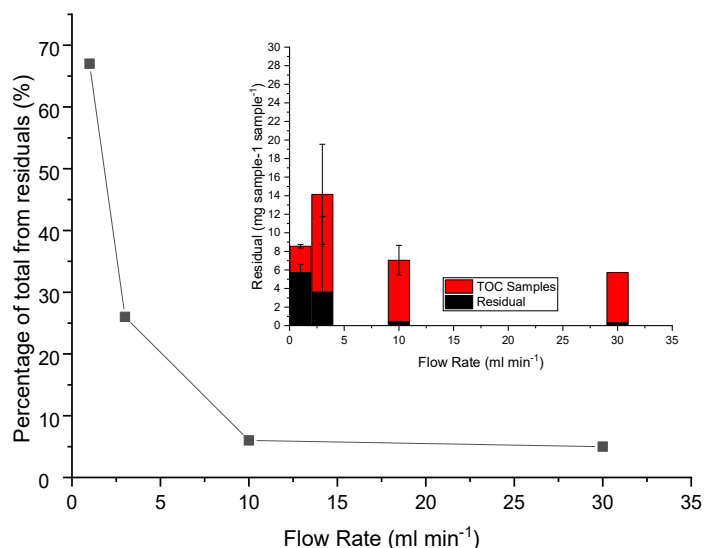


Figure 6.11: Percentage of total oil released that remained in the flow chamber at the end of the 120 minute test. Inset: measured residual carbon (black) as a proportion of total organic carbon (TOC, red + black) released throughout the test.

A flow rate of 10 ml min⁻¹ (Re = 9.5 at 22 °C) was selected for subsequent testing on the flow rig. This flow rate gave moderate volumes of solution, reasonably high TOC values, and little residual oil in the flow chamber.

6.1.3.2. Impact of temperature

Figure 6.12 shows that unlike the static case, temperature had negligible impact on the rate of organic carbon release from the CMS under flowing conditions. Testing at pH 12 may be preferential at 22 °C (Figure 6.12 (a)) over 50 °C (Figure 6.12 (b)) however it is impossible to state this with certainty due to the low repeatability of the test under these conditions (note by 120 minutes the error range spans the entire 0 - 30 mg region, Figure 6.12 (a, b)). Oil release appears to be predominantly linear though some shift in rate is noted between 0 - 30 min and 30 - 120 min sampling.

The rate of organic carbon release increased with increasing pH with average linear rate constants, k_i , of 1.16, 1.62 and 2.25 s^{-1} for pH 7, 10 and 12 at 50°C respectively. This trend is in agreement with the observations in static solutions, however k_i values are lower than at 22°C for static systems (2.32, 3.23, and 6.77 s^{-1} for pH 7, 10 and 12 respectively). This further supports the theory that static systems are advantageous to flowing ones for this particular cleaning phenomenon.

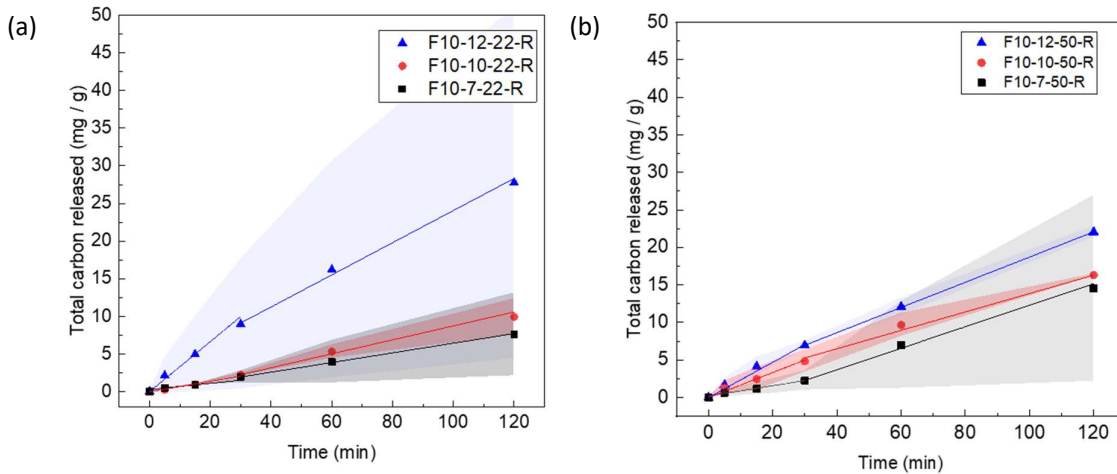


Figure 6.12: Effect of pH on the cumulative total carbon release at (a) 22°C and (b) 50°C in flow mode at 10 ml min⁻¹.

6.1.3.3 Impact of surfactants

Figure 6.13 (a) shows that SDBS enhanced release when the solution flowed (TOC_{max} at 10 ml min⁻¹ and 22 °C ~ 5 mg g⁻¹ at pH 7, ~100 mg g⁻¹ in 0.1 % SDBS). At both temperatures studied there is an almost seven-fold increase in the final amount of carbon released from the soil over static testing. The final value is equivalent to 28 % of the available fat from the CMS layer. As a surfactant the SDBS lowers the interfacial energy between the hydrophobic fats/oils and the water. This will enhance the displacement of the fats within the CMS layer. The oil is then transferred from the surface into the solution bulk, likely via a roll-up mechanism. Additionally the surfactant is continuously replenished throughout the duration of the test, allowing continuous removal of the oil from the CMS layer at a rate of 6.9 $\mu g s^{-1}$, 3-7 times faster than in solutions without the surfactant.

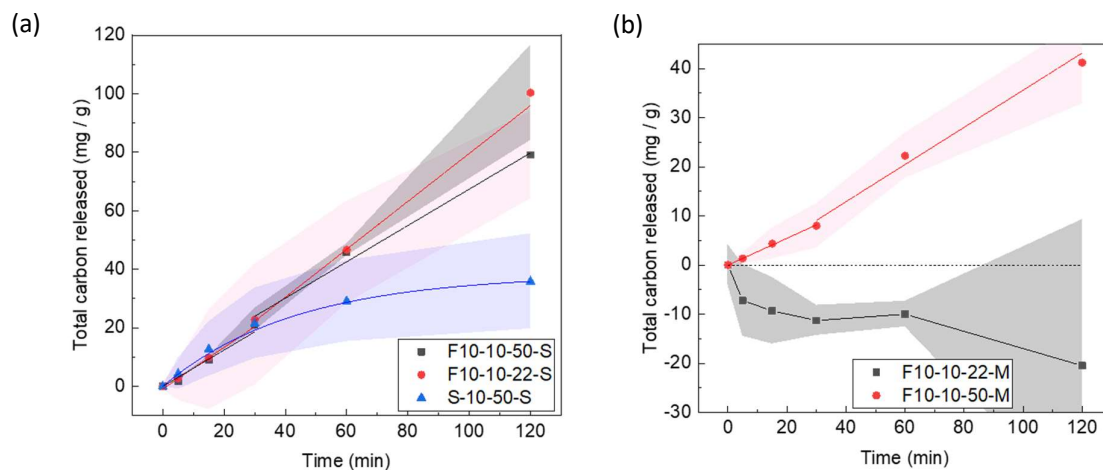


Figure 6.13: Cumulative total carbon release at 22 and 50 °C with (a) 0.1 wt.% SDBS (S), and (b) 0.1 wt.% MGDA (M). Flow apparatus, 10 ml min⁻¹.

6.1.3.4 Impact of chelant

In contrast the MGDA showed similar behaviour to other solutions tested at 50 °C (Figure 6.13 (b)). It demonstrated an approximately linear release, greater than that of simple water solutions (k_i 3.64 s⁻¹ for MGDA vs 1.62 s⁻¹ for pH 7). This is in line with the behaviour observed in static systems. However at 22 °C, negative results were consistently obtained. This indicates that the solution is *losing* carbon during testing. It was hypothesised that this is a base-line effect. MGDA is an organic molecule and therefore forms part of the background of the TOC removed during processing. However if the MGDA is entering the chamber and chelating to metal ions (such as Ca²⁺ from milk and Na⁺ from salt within the soil) in greater proportion than oil is being released, then organic carbon from the fats/oils will be masked by the loss of MGDA in the background signal. The cleaning solution contains 1 g L⁻¹ MGDA with only 30 mg of oil expected to be released into 1.2 L of cleaning solution over the course of the test making this highly probable. It is unclear why this effect was not observed at 50 °C. Both MGDA and metal complexes of MGDA are highly soluble in water at room temperature (up to 45 wt. % possible at pH 10 for MGDA in water, Trilon M, BASF) with no significant shift in solubility at elevated temperature. The soil's structural integrity is higher at lower temperatures so it is possible that metal ions, such as the calcium ions from the milk, are more firmly bound within the CMS structure. This would prevent the MGDA from solubilising the metal complexes into the bulk solution, lowering the organic carbon content baseline and resulting in the effect observed in Figure 6.13.

6.1.4 Oil recovery conclusions

Two techniques were developed here to monitor the transfer of oily material from the CMS into static and flowing cleaning solutions.

In static testing the release of organic carbon was found to be promoted at temperatures above the melting point of the fat component, shown by the marked increase in k_{TOC} between 30 °C and 40 °C. Increasing the pH of the cleaning solution was also shown to promote the rate and amount of oil material released into the cleaning solution. Finally the role of surfactants in promoting 'roll-up' of the mobile components in this type of deposit was found to be dependent upon surfactant type, i.e. the cationic one was more effective than anionic.

Of all additives tested (surfactants, a chelant, pH and an oxygen bleach) bleach was the most effective at releasing the oil from the CMS. Unfortunately bleach is opaque and so no image analysis of this solution could not be conducted.

Flowing the solution over the soil enhanced the oil release at 10 ml min⁻¹, however at lower flow rates the long residence time in the solution chamber meant that the oily material remained within the chamber instead of eluting for testing and at higher flow rates the volume of solution used diluted the released oil and increased the errors in the TOC measurement process. A flow rate of 10 ml min⁻¹ was therefore used in all subsequent testing.

In simple aqueous solutions of varying pH, static solutions showed enhanced oil recovery over flowing solutions. Conversely SDBS was significantly more effective in flowing solution than stagnant ones. This is thought to be due to minimisation of the oil-solution interfacial energies. In simple solutions the interfacial energy is high, and so there are significant energy gains from the oil droplets collecting together on the CMS surface, whereas in surfactant solutions the interfacial energy is lowered and so the oily droplets can be solubilised into the solution faster and eluted for testing.

MGDA was not appropriate for testing in flowing solutions at room temperature as the base line decreased to such an extent that it masked organic carbon released from within the soil layer. This was believed to be due to the MGDA complexing with the soil layer.

6.1.5 Timescales of cleaning

Here the timescale of cleaning was primarily dependent upon the flow rate and surfactancy of the solution. In static pH 7 water t_{asym} was >7600 s after submersion, reaching $TOC_{max} = 15.7 \text{ mg g}^{-1}$, with a rate constant of $k_{TOC} = 2.32 \times 10^{-6} \text{ s}^{-1}$. The solution of pH 10 water with 0.1 wt.% bleach at 50 °C gave the largest observed value of t_{asym} of ~4800 s and $TOC_{max} = 202 \text{ mg g}^{-1}$, with a rate constant of $k_{TOC} = 0.55 \times 10^{-6} \text{ s}^{-1}$. These timescales were significantly longer than that observed for the swelling of CMS in pH 7 water on the SiDG ($t_{asym} \approx 800\text{s}$) indicating that the soil swelling occurs before all the mobile components within the soil have been transferred to the cleaning solution.

6.2. Image analysis of droplets

The second technique used to monitor the release of mobile components from the CMS surface was image analysis of the evolution of droplets. The detection of droplets or circles in an image is a relatively common task. Zabulis *et al.* (2007) used circle detection to determine the distribution of air bubbles in a dense dispersion to establish a quantitative parameter for studying wet foams. Sargent (2018) similarly used image analysis to determine the both the size and spatial distributions of bubbles in the manufacture of instant coffee powers.

Some droplets, typically those with a high colour contrast between its contents and surrounding medium, are easily detectable and so straightforward techniques such as intensity and/or colour thresholding can be applied. However the droplets studied here featured a light brown organic liquid located on a slightly darker brown organic soil, submerged in solution. These featured poor contrast with the background media and so more refined image processing techniques are required. The droplet illumination conditions are also important: the correct lighting conditions can change a droplet from having blurred dark edges to well-defined, ring-like, bright edges via contrast reversal and multiple interreflections (Strokina *et al.*, 2016).

There are two main approaches in the image analysis of circular features;

1. Geometry-based: a circle is defined by its centre and radius.
2. Appearance-based: a template of the object to be found is mapped onto the image and convolved. The local maxima of the resultant convolution are taken to be the edges of the target circle.

The appearance-based approach is conceptually similar to that of cross-correlating the image (Girod, 2013) and is identical if the kernel employed is symmetric such as Gaussian or Laplacian kernels. As the radius of the circle, r , to be detected in these studies was not constant appearance-based approaches were not optimal. A geometry-based approach, within a given range of r , was therefore adopted.

6.2.1 Experimental set-up

A transparent, open-topped box with a rectangular cross-section (26.1 x 26.1 x 15.0 cm) was filled with 3.5 L deaerated cleaning solution and heated to temperature (20 – 50 °C) using copper heating coil connected to a water-heater-circulator (Julabo MP5) which circulated water heated to a pre-specified temperature (Figure 6.14).

A webcam (Logitech™ C920 Pro Stream Webcam connected via USB to a PC Intel Core i5-7260U, 7th Generation, Windows 10, 8.00 GB RAM, 256 GB Hard drive) was used for image acquisition. The

camera was mounted on a retort stand and was held approximately 5 cm above the surface of the solution, directly above the sample. The focus, brightness, white balance and aperture were manually adjusted via Logitech™ webcam software (Logitech Capture for Windows). A photograph of a blank sample plate marked with adhesive measurement tape was used to calibrate distances for each sample plate. The webcam has better image quality when taking still images than video (5168×2907 pixels in picture mode against 1920×1080 pixels in video mode), so time-lapse imaging at intervals of 15 s was conducted using MurGee, Mouse Auto Click software.

A light reflector was fitted above the apparatus to block out light from the halogen strip lights in the ceiling. A flexible light ring (8.7 cm outer diameter, 5.3 cm inner diameter) was mounted 3 cm above the surface of water, over the sample, to provide a coherent white light source and illuminate the droplets as they formed. Additional lighting was provided via three LED USB desk lamps (Plugable 2.0 USB).

A cylindrical sample holder (6.9 cm diameter, 5.0 cm height) was placed at the centre of the container beneath the camera and light ring at a height such that the sample was submerged approximately 1 cm below the surface of the water.

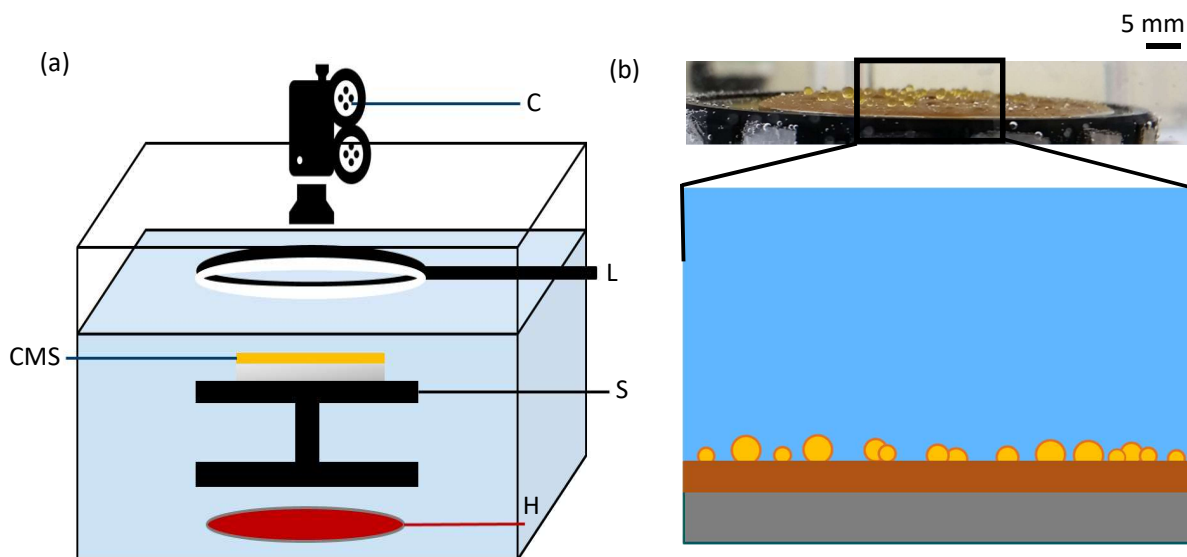


Figure 6.14: (a) Experimental set-up for droplet image analysis. H – heating coil, S – stand, L – light ring, C – camera. (b) side view of soiled plate with after droplets formed on the surface.

6.2.1.1 Test Solutions

pH 7 water was deaerated by boiling in a kettle (Sainsbury's, 1.7 L). The water was then left to cool to room temperature. Once cool, formulation components were added and the pH measured (Fisherbrand™ Accumet™ AB15 Basic). The pH was adjusted by adding 1 M NaOH, and the solution

then stirred for 30 minutes. Table 6.10 shows the range of solution compositions and conditions tested. A minimum of 3 repetitions was run for each test solution.

Table 6.10: *Conditions investigated using droplet imaging.*

pH	Temperature	Surfactant	Surfactant concentration / %
7	30 °C	SDBS	0.01
8	35 °C	CTAB	0.1
9	40 °C	TX-100	
10	45 °C		

6.2.1.2 Test soils

CMS soil was prepared as described in Chapter 3. The slurry was placed on 50 mm diameter, 1 mm thick 316 stainless steel discs, dried and baked. The wet soil thickness, δ , was $300 \pm 4 \mu\text{m}$, and the average mass of the slurry layers typically $1.6 \pm 0.05 \text{ g}$, giving an initial coverage on the discs of 0.82 kg m^{-2} .

6.2.1.3 Test Protocol

The solution was added to the container and brought to the required temperature then equilibrated for at least 30 minutes.

A soiled sample plate was submerged and located on the sample mount using forceps. The timer was started at first contact between the soil and the solution and time-lapse photography started within 30 seconds of submersion. Images were acquired every 15 seconds for one hour. At the end of the experiment the test solution was emptied via a drain located at the base of the box, the sample removed and the equipment cleaned.

6.2.2 Image analysis protocol

6.2.2.1 Droplet identification

Image analysis was conducted assuming that the droplets were spherical. This assumption was supported by side-view images in Figure 6.14 (b) which show the spherical caps formed by the oil droplets once they formed on the CMS surface. The image processing technique and modelling were developed in collaboration with MPhil ACE student Nathan Ravoisin as part of his research project.

Images were first processed using the imaging processing tools based on ImageJ. The final frame ($t = 60 \text{ min}$) from each experiment was used to identify the location of stable droplets manually at the end of the test. Regions of interest (ROI) were then drawn around each droplet and the location saved in

a separate log. An image from $t = 55$ min was then loaded into the viewer and the ROIs overlaid on the images to identify ROIs for droplets that had formed then detached during testing. This was then repeated for $t = 50$ min, 45 min etc. The central portion of the test plate (radius 15 mm, see Figure 6.15 (b)) was used for droplet tracking: beyond this the images were subject to blurring.

Once the ROIs had been established over the entire test, a macro was run that looped over all the ROIs, and produced a small image of each droplet at each time interval. A Laplacian-of-Gaussian (Mexican Hat) filter of radius 3 pixels was used to highlight the edge of the droplets. The macro then looped over all the frames captured in the experiment before saving a set of processed, small-sized frames in chronological order for each droplet (Figure 6.15 (c)).

6.2.2.2 Location of the droplets

The droplets were observed to grow directly over the cracks present in the burnt CMS. The white strips within the circle of the soil on Figure 6.15 (a, i) are due to reflection of light from the metallic substrate surface and denote the location of cracks within the soil. After submersion the soil swells (see Chapter 5) and the cracks close. Figure 6.15 (b, ii) shows an example of CMS on a borosilicate glass plate that was videoed from beneath. It can be observed that the oil is gathering within the cracks (the liquid was identified as oil first due to its lighter colour than the surrounding burnt structure and later via DSC profile matching with the fat component added to CMS during soil preparation, data not shown). When observed from above (Figure 6.15 (a,ii)) the CMS image analysis plate shows droplets forming above the location of the cracks as they swell closed until they are no longer visible (Figure 5.15 (a, iii)). This phenomenon is also visible in Figure 6.15 (c) which shows the growth of a single droplet (identified in the red square on Figure 6.15 (a,i)) above a closed crack.

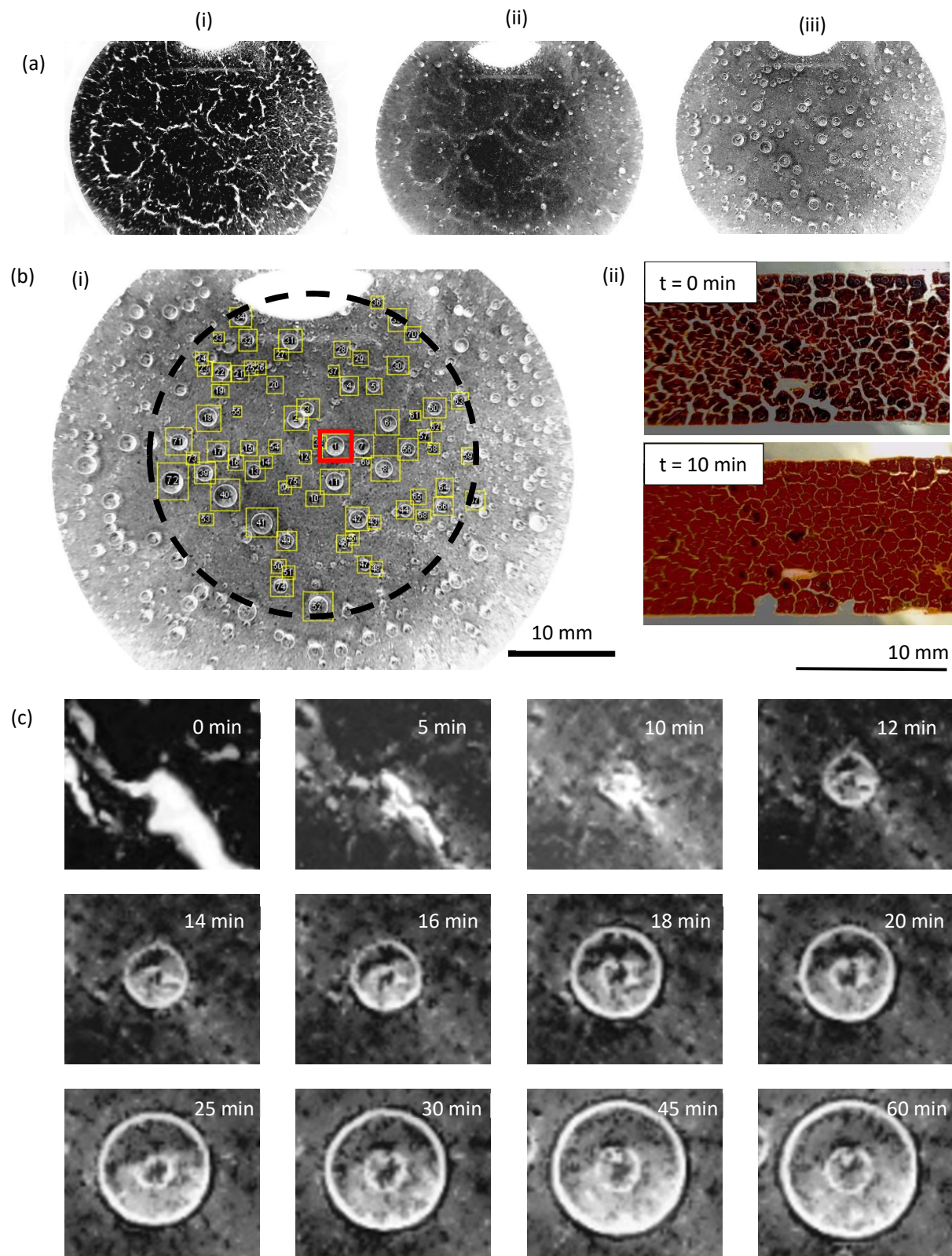


Figure 6.15: (a) Images acquired at (i) $t = 0$ min, start of test, (ii) $t = 5$ min, after swelling but before oil evolution and, (iii) $t = 60$ min, end of test. (b) (i) CMS imaging plate submerged in pH 7 water at 40 °C. Dashed circle shows region analysed. (ii) CMS on glass slide viewed from beneath showing crack closure and transfer of oil into cracks. (c) Example of droplet growth over time intervals. Test 25: pH 7, 40 °C.

6.2.2.3 Circle Hough Transform

A common method of detecting circles in image analysis is the circle Hough Transform (CHT, Hough, 1962, Duda and Hart, 1972). This technique is carried out via a voting procedure within a set parameter space. In a 2D image a circle can be described by;

$$(x - a)^2 + (y - b)^2 = r^2 \quad \text{Equation 6.16}$$

If the centre of the circle (x, y) is fixed in space then a 3 dimensional parameter space can be defined (a, b, r) of which all real values lie within an inverted right-angled cone of apex $(x, y, 0)$. The intersection of a set number of conic surfaces can then be used to identify the target 2D circle's parameters. This is completed via a 2 step process.

1. Fix the radius r , and solve for a , and b .

Each point (x, y) on the target circle can be defined as the centre of a secondary circle of radius r . the intersection point of each of a minimum of three secondary circles corresponds to the centre point of the target circle (a, b) (Figure 6.16). A voting system, with each radial point of the circle being assigned a value of 1 and each coordinate summed in space, is used until a clear maximum is produced. This step allows for parameters a and b to be estimated for a given r .

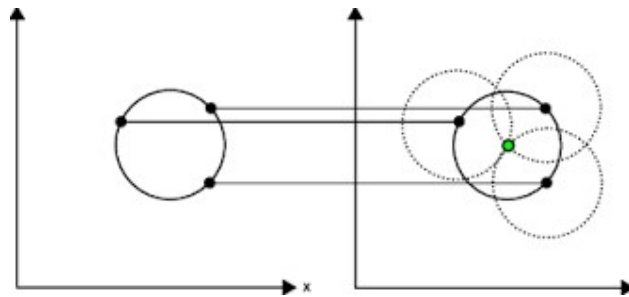


Figure 6.16: Diagram of the Hough Transformation Principle: step 1

2. Iterate for a range of r

Typically the radius of the target circle is unknown. An estimated range for r , based upon practical scaling of the experiment, can be used to set a parameter space within which step 1 is performed. A secondary voting system then takes place, in the same manner as the first described above. A range of maxima for each tested r is then generated and the coordinate with the highest maximum of each tested r was taken as the final centre point and r of the target circle respectively. In the experiments conducted here the range of r values iterated through was set based upon the image pixel density i.e. for an image with a pixel cross-section of 100 pixels, r be iterated for values ranging 0 – 50.

This method, although effective and relatively robust towards noise, is computationally expensive to run. It requires large storage requirements and processing power to achieve high accuracy detection.

To mitigate this a series of modifications to the Transform have been developed (Kälviäinen *et al.*, 1995). Kimme *et al.* (1975) used arcs in place of full circles to reduce the computational loading for image processing. Improving upon this, Minor and Sklansky (1981) plotted multiple points on a line in the edge direction, then utilised a voting system to determine intersections of edges. This approach eliminates the need to fix r , reducing the parameter space from three dimensions to two and enabling multiple circles of different radii to be identified simultaneously. A final improvement was made by Atherton and Kerbyson (1993) who used complex phase coding along the length of each spoke. This creates a complex accumulator space in which constructive accumulation can occur when spokes intersect with the same phase. This allows a circle radius to take decimal values rather than integer ones, improving both the noise tolerance of the Hough transform and its detection rate. This is the method utilised in this work due to its accuracy, noise tolerance, low computational requirements, and ease of use.

6.2.2.4 Droplet tracking

MatLab™ was used to determine the growth of the droplet over time. A circular Hough transform using the built-in command *imfindcircles* was applied to each frame of a given ROI.

The *imfindcircles* command has four adjustable parameters:

1. Radius Range: This parameter sets the limits on the radii of the circle the Hough transform seeks. Resolvable droplets were found to have radii between 20 and 120 pixels dependent upon camera location and resolution. The algorithm requires that the radius range is such that the maximum radius measured is no more than three times the minimum radius specified, i.e. if the minimum is set to $r = 20$ then the maximum radius detectable is $r = 59$.

Two separate instances of the *imfindcircles* function were therefore required: one with radius range set between 20 and 59 for early droplet detection, and the other between 41 and 122 to track the droplets as they grew. The resolution of the camera was such that it was not possible to identify and track the early, small droplets reliably (<20 pixels).

2. Object Polarity: This specifies whether the edges to be fitted are brighter or darker than the background and was set to 'bright'.
3. Sensitivity: This specifies the minimum score required by a given pixel to be accepted as the centre of a circle (i.e. how lenient the algorithm should be when detecting circles) and takes values between zero and one, with lower values translating to only well-defined circles being identified while higher values result in less apparent circles being detected but also increase the number of false positives. This parameter was set to 0.89 to ensure detection in the early

stages of droplet growth. False positives were removed during a later stage of image processing.

4. Edge Threshold: This parameter specifies the difference in intensity between pixels at the edge of the droplet and the background pixels. Setting a value of this parameter to a minimum (0.01) gave the best results.

Following droplet identification and tracking, the diameters were converted to lengths using the calibration image recorded at the start of the test.

6.2.2.5 Data filtering

Data were filtered first through automated processing, then through manual filtering to remove any remaining false positives.

One common false positive was the identification of a ghost droplet of small radius within the real droplet. This occurred due to total internal reflection of some of the light from the light ring which generated an image of a droplet at the centre of the oil droplet being tracked (See Figure 6.15(c)). To filter out these smaller reflected droplets the number of circles was identified in each frame. If more than one circle had been identified then the centres of the circles were identified. Each centre was evaluated against each other centre, one at a time, for all possible combinations of pairs (MATLAB™ *nchoosek*). If one of the circles evaluated was located within the other then the distance between the two centres would be less than the larger of the two radii. In this case the smaller circle was deleted.

Another common false positive was the false identification of circles in a different location to that of the droplet being tracked. The centre of the droplet in each frame was evaluated and logged, along with its radii, over the length of the experiment. The average radius and centre of the droplet was then evaluated after the droplet had stabilised in size and could be tracked reliably. All previous centres of circles identified during the growth phase were then evaluated against this and those which did not match up (within a 0.9 - 1.1 threshold) were deleted. In addition, if the radius had grown or shrunk by more than 10 % between frames (15 s per frame) then the circle was considered a false fit and removed.

The data were then exported to Microsoft Excel and each droplet growth profile evaluated manually. Droplets that grew and stabilised (Figure 6.17 (a)) were labelled (1) for further processing. Droplets that grew then detached (Figure 6.17 (b)) were labelled separately (2). All data points from after the droplet detached were deleted and the growth data was then regrouped with (1). Finally droplets that grew, detached, and then regrew (Figure 6.17 (c)) were labelled as (3). Each data set in this group was

split into its individual droplets with the diameter values before and after the droplet set to 0 before being reintegrated with group (1).

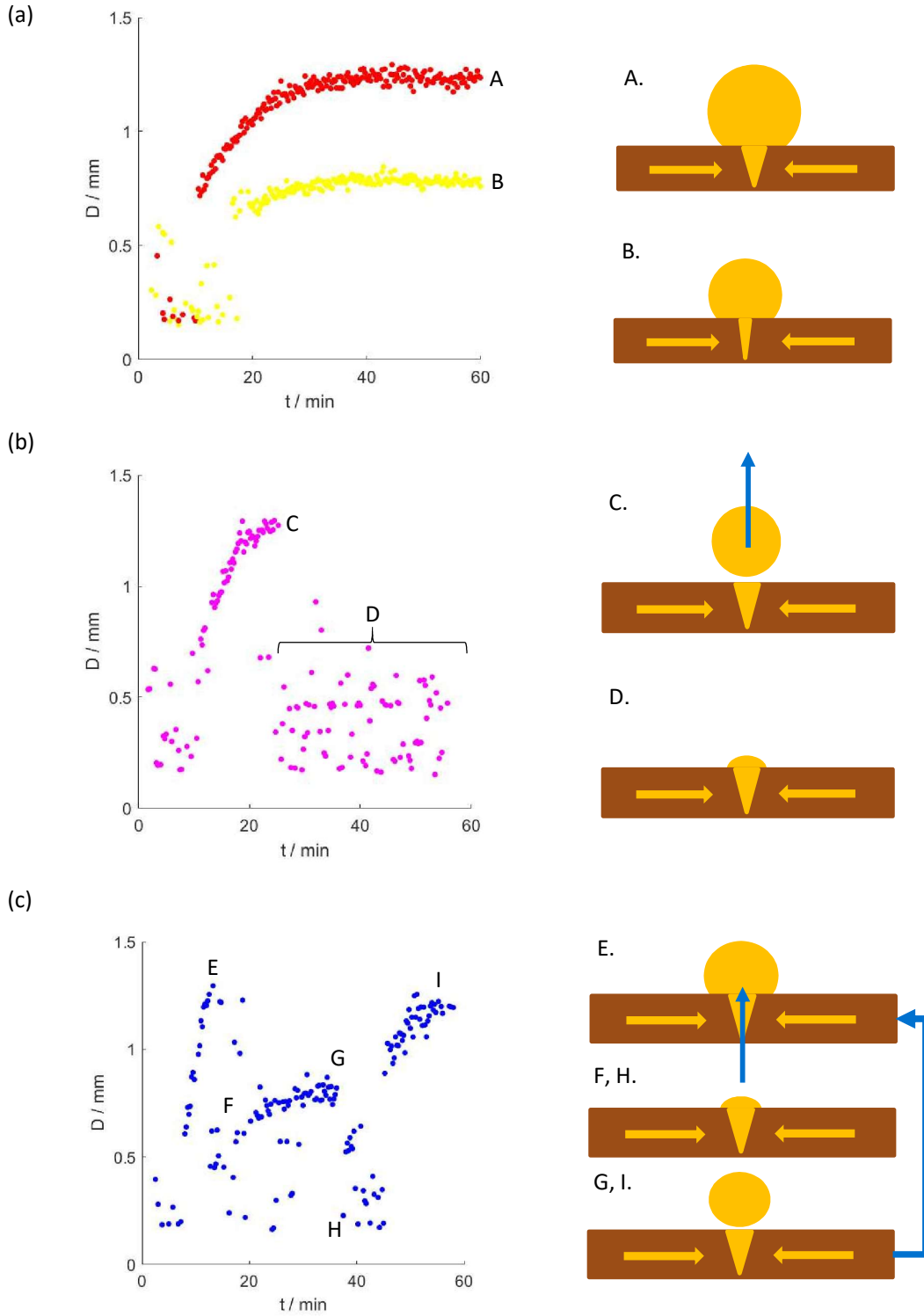


Figure 6.17: Types of oil droplet evolution; (a) variations in equilibrium droplet size, (b) growth and detachment and, (c) growth, detachment and regrowth.

6.2.3 Data processing

The data processing protocol is demonstrated for a CMS sample submerged in pH 7 water at 50 °C for 60 minutes.

6.2.3.1 Size distribution

The droplets were first evaluated in terms of their size distribution over the duration of the test (Figure 6.18). This gave indications of the rate of droplet growth and whether all droplets were formed simultaneously or whether new droplets formed throughout the test. Histograms of the droplet diameter, d , were generated at 5 to 10 minute intervals with the first plot generated at 5 minutes after submersion. The total number of droplets, regardless of their size was also plotted and is included as an inset for each histogram for reference purposes (Figure 6.18 (inset)).

At early stages of the experiment (Figure 6.18, $8 \text{ min} < t < 10 \text{ min}$) numerous very small droplets form on the CMS surface, with $d < 0.5 \text{ mm}$. Over time these droplets grow at slightly different rates giving a wider size distribution. During these early stages new droplets are also forming, although not at the same rate as at the start of the test. After 25 minutes few new droplets formed and droplet growth dominates before the droplets either stabilise at a given diameter ($d < 1.6 \text{ mm}$ for pH 7 water at 50 °C) or detach from the surface.

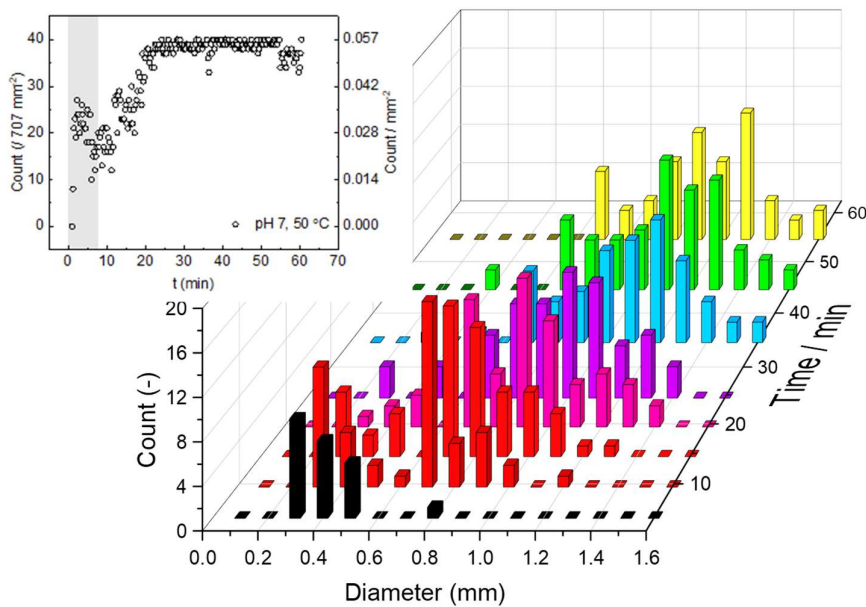


Figure 6.18: Histograms of droplet growth on 707 mm² CMS after submersion in pH 7 water at 50 °C. Inset: evolution of the total number of droplets on the CMS surface. Larger version available in Figure 6.21 (b).

6.2.3.2 Droplet detachment

The detachment of a droplet from the CMS surface is caused by buoyancy, arising from the difference in the density between the fat-based droplet and the surrounding solution, and the surface tension keeping the droplet attached to the soil. Knowledge of the properties (e.g. density difference, $\Delta\rho$, the interfacial tension between the droplet and the solution (γ_{ow}), and the contact angle between the droplet and the soil (θ , defined in the more dense fluid) allows the maximum volume the droplet can reach to be estimated. Figure 6.19 shows a drop of the critical radius (R_{crit}) at the point of detachment.

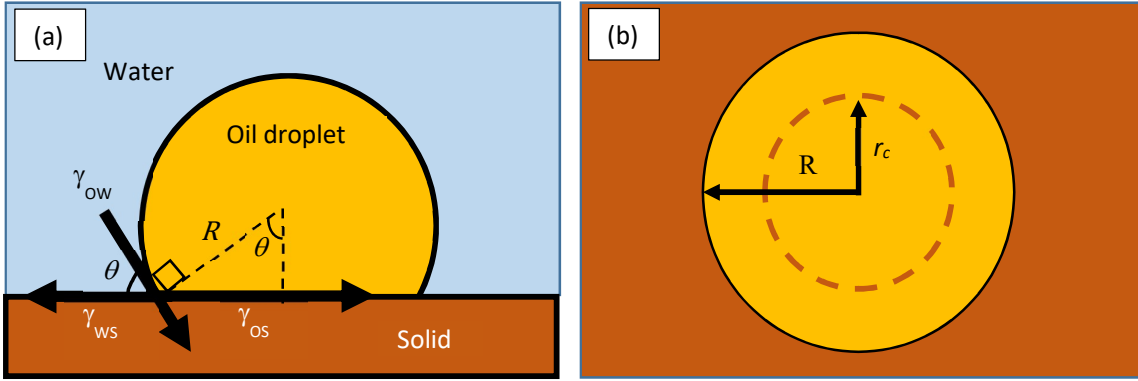


Figure 6.19: Schematics of oil droplet on CMS surface submerged in solution. r_c is the radius of the contact line of the spherical cap on the CMS, R is the droplet radius, γ_{ow} , γ_{so} , γ_{wo} are the oil-water, oil-soil and water-oil interfacial tensions respectively. (a) side view, (b) plan view. Contact angle defined in the denser phase.

The buoyancy forces (F_B) and surface tension forces (F_{SF}) are, respectively,

$$F_B = V_D \Delta\rho g \quad \text{Equation 6.17}$$

and

$$F_{SF} = 2 \pi r_c \gamma_{OW} \sin \theta \quad \text{Equation 6.18}$$

where V_D is the droplet volume, g is the gravitational constant, and

$$r_c = R \sin \theta \quad \text{Equation 6.19}$$

At the point of detachment $R = R_{crit}$, $F_B = F_{SF}$, giving

$$V_D \Delta\rho g = 2 \pi r_c \gamma_{OW} \sin \theta \quad \text{Equation 6.20}$$

V_D is therefore a function of the radius and contact angle on the soiled surface (assumed to be flat).

$$V_D = \frac{\pi}{3} R_{crit}^3 (4 - (2 + \cos \theta)(1 - \cos \theta))^2 \quad \text{Equation 6.21}$$

Substituting V_D and Equation 6.18 into Equation 6.20 gives

$$\frac{\pi}{3} R_{crit}^3 (4 - (2 + \cos \theta)(1 - \cos \theta))^2 \Delta \rho g = 2 \pi R_{crit} \gamma_{ow} \sin^2 \theta \quad \text{Equation 6.22}$$

Rearrangement and substitution gives;

$$R_{crit}^2 = L_c^2 \frac{6 \sin^2 \theta}{2 + 3 \cos \theta - \cos^3 \theta} \quad \text{Equation 6.23}$$

where L_c is the capillary length,

$$L_c = \sqrt{\frac{\gamma_{ow}}{g \Delta \rho}} \quad \text{Equation 6.24}$$

The characteristic length of a droplet submerged in pure water is 5.8 mm (γ_{ow} estimated using sunflower oil pendant drop tests using a DSA drop shape analyser). This corresponds to a critical radius of $R_{crit} = 6.0$ mm, well above the maximum radius of the droplets formed experimentally. This is consistent with experimental observations that little droplet detachment was observed in stagnant water.

6.2.3.3 Sphericity of the droplet

The detachment model assumes (i) $\theta < 90^\circ$ and (ii) the droplet is spherical. The second assumption can be validated by considering the Bond number, Bo . This describes the ratio of gravitational forces to capillary forces (Equation 6.25). A low Bond number (< 1) indicates an interface that is dominated by surface tension forces, a high one (> 1) indicates a system that is dominated by gravity.

In the modelling conducted here the droplets are assumed to be spherical, therefore the Bond number should be less than or equal to 1. R_1 here is the radius of a droplet for which $Bo = 1$.

$$Bo = \frac{\text{hydrostatic pressure}}{\text{capillary pressure}} \quad \text{Equation 6.25}$$

giving
$$Bo = \frac{(R_1 + R_1 \cos \theta) \Delta \rho g}{2 \gamma_{ow} / R_1} \quad \text{Equation 6.26}$$

setting
$$\frac{\Delta \rho \times g}{\gamma_{ow}} \frac{1 + \cos \theta}{2} R_1^2 \leq 1 \quad \text{Equation 6.27}$$

yields
$$R_1^2 \leq L_c^2 \frac{2}{1 + \cos \theta} \quad \text{Equation 6.28}$$

A contact angle of 53° (see Figure 6.18) was used to estimate the Bond numbers for a range of expected droplet sizes in water at 50°C . All Bond numbers were found to be $\ll 1$ in water at the length scale used in these tests, validating the spherical assumption (Table 6.11).

Table 6.11: Bond number estimations for range of potential R_1 values in water, $\theta = 53^\circ$

	$R_1 = 0.5$ mm	$R_1 = 0.75$ mm	$R_1 = 1.0$ mm	$R_1 = 1.5$ mm
L_c	5.8 mm	5.8 mm	5.8 mm	5.8 mm
Bo	0.006	0.013	0.024	0.053

6.2.3.4 Effect of contact angle

Using Equations 6.23 and 6.28 we can establish the ratio of R_{crit}/R_1 to determine the effect of the contact angle on the validity of the spherical modelling assumption.

$$\left(\frac{R_{crit}}{R_1}\right)^2 \leq \frac{L_c^2 \frac{6 \sin^2 \theta}{2 + 3 \cos \theta - \cos^3 \theta}}{L_c^2 \frac{2}{1 + \cos \theta_s}} \quad \text{Equation 6.29}$$

Rearrangement and cancellation gives:

$$\left(\frac{R_{crit}}{R_1}\right)^2 \leq \frac{3(1 + \cos \theta - \cos^2 \theta - \cos^3 \theta)}{2 + 3 \cos \theta - \cos^3 \theta} \quad \text{Equation 6.30}$$

This can be used to determine the theoretical detachment contact angle (Figure 6.20). If $R_1 < R_{crit}$, the droplet will not be spherical at the modelled point of detachment and the model will be inaccurate.

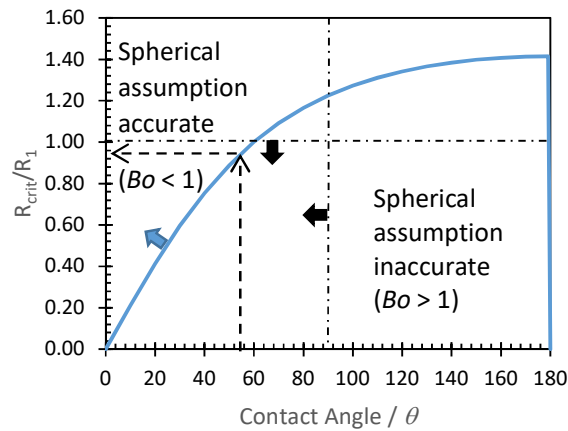


Figure 6.20: Effect of contact angle on validity of spherical modelling assumption. Blue line: Equation 6.30.

The average measured contact angle in pH 7 water was $53^\circ \pm 6$, giving R_{crit}/R_1 of ~ 0.9 . This implies that the assumption of a Bond number less than or equal to one was valid. As cleaning agents such as surfactants are added γ_{ow} will decrease. This will cause the Bond number to increase for a fixed R_1 and L_c to decrease. If L_c decreases either R_{crit} must decrease or $\cos \theta$ must increase. If $\cos \theta$ increases, θ is decreased, i.e. the tendency of water to wet over oil is increased. This enhanced wetting enhances oil displacement, driving droplet formation. Alternatively the critical radius of the droplet decreases,

causing detachment to occur at lower oil volumes. This implies that the droplets will form quickly and detach before they grow to size at which they would be non-spherical in all surfactant containing cleaning solutions to be studied in this work.

6.2.3.5 Volume of droplets

The volume of the droplets can be estimated using the assumption validated above that the droplets formed are truncated spheres. Visual observation (Figure 6.14 (b, ii)) also supports this assumption. If the droplet is taken to be a sphere of diameter d as measured from above, then its volume can be calculated as the volume of the sphere minus a spherical cap with an associated contact angle θ . The contact angle was estimated here through imaging of multiple droplets from the side and taking an average. The volume is then calculated using Equation 6.31.

$$V_{j,k} = \frac{\pi}{24} d_{j,k}^3 (2 + 3 \cos \theta - \cos^3 \theta) \quad \text{Equation 6.31}$$

where $V_{j,k}$ and $d_{j,k}$ are the volume and diameter, respectively, of droplet k at frame j . As the analysis is conducted on a fixed surface area of the soiled plate the volume is presented as the total volume of oil on the surface, V_s , at time t , both as $\mu\text{l} / 707 \text{ mm}^2$ and as $\mu\text{l mm}^{-2}$.

The total volume of all the droplets in the sampled region could then be plotted. Figure 6.21 shows that for CMS submerged in pH 7 water at 50 °C there is an induction period, t_i , of approximately 8 min before a significant volume of droplets form on the surface. The drops grow on the surface over a period of approximately 30 min until the volume reaches a plateau of approximately 20 $\mu\text{l} / 707 \text{ mm}^2$ at (t_{asym}). 40 min after submersion the total volume of material starts to decrease as the droplets detach and are replaced with new, smaller droplets. After 50 minutes the rate of droplets detaching from the surface surpasses the rate of new droplet formation (Figure 6.21 (b)).

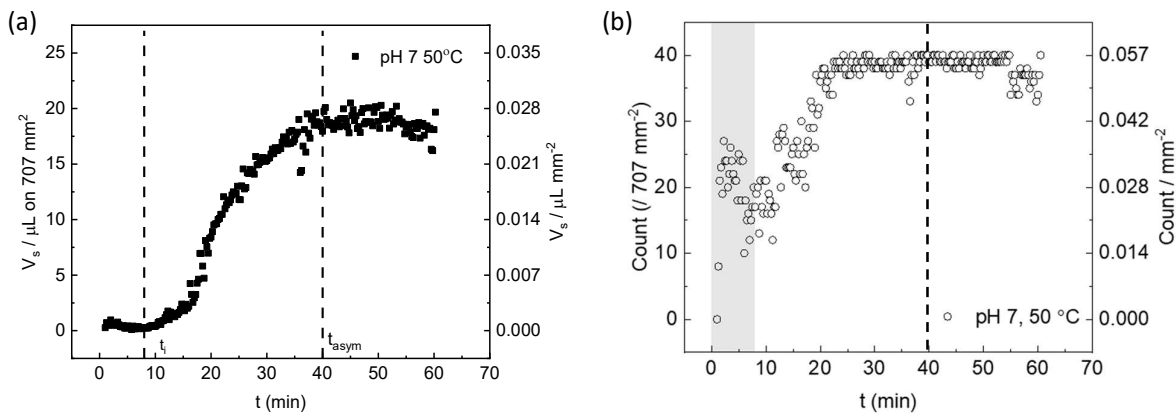


Figure 6.21: Evolution of (a) total volume and (b) number of droplets on 707 mm² of CMS surface after submersion in pH 7 water at 50 °C.

The fat content of the burnt CMS was measured as 47.2 g/100 g. The average CMS sample mass in these experiments was 0.76 g, giving a maximum total fat mass of 0.35 g or 350 mg fat per sample. Only a section of the plate is monitored in the image analysis section due to focussing constraints. Assuming the droplets form uniformly over whole soil then this section corresponded to 36 % of the total soiled area ($r_{\text{plate}} = 25 \text{ mm}$). Inspecting Figure 6.21, the maximum amount of fat released in pH 7 water after 60 minutes at 50 °C was 19 μl , or 17.3 mg (assuming a fat density of 910 kg m^{-3}). The surface adjusted percentage would therefore be approximately 14 % of the total fat available in the CMS. This is higher than the f_{FE} of 11.4 % calculated for an equivalent sample in the oil recovery work. However, this is likely an overestimation as the droplets are more likely to form in the centre of the plate, both due to the presence of more cracks in the soil providing channels for the material to transport through and due to the fact that the droplets can accumulate material from all directions in the soil plane, unlike at the edge where the mobile material can only be sourced from one side. The second factor that could cause a discrepancy between the oil recovery work and the droplet imaging is the detachment of the droplets over time. Figure 6.21 shows the volume of the droplets attached to the surface and does not account for lost material, thereby underestimating V .

6.2.3.6 Scaled analysis.

The scaled diameter of a droplet j at frame k was calculated from:

$$d_j^* = \frac{d_{j,k}}{\max_j(d_j)} \quad \text{Equation 6.32}$$

With the average scaled volume, V_j^* calculated in the same fashion as d_j^* .

Figure 6.22 (a) shows the evolution of d^* for 40 droplets after submersion in pH 7 water at 50 °C. A consistent increase is evident until approximately 23 minutes, after which the droplets reach their individual maximum. There is considerable scatter in the onset time (here between $2 \text{ min} < t_{\text{onset}} < 10 \text{ min}$) at which the droplets start to form (indicated by red dashed lines in Figure 6.22 (a)). In order to calculate an average rate of droplet growth, independent of onset time, the start of growth was identified for each droplet. The adjusted time, t_{adj} , was calculated for each droplet as $t_{\text{adj}} = t - t_{\text{onset}}$. d_j^* was then averaged for all droplets as a function of t_{adj} (Figure 6.22 (b)). The average onset time and one standard deviation is included in Table 6.13 for reference. At $t < t_{\text{onset}}$, Figure 6.22 (b), and subsequent plots, show scattered data. These are false readings. To show this the region of $t < t_{\text{onset}}$ has been shaded out.

A simple asymptotic fit (Equation 6.33), was found to give a good description of the growth data.

$$(d_j^* - d_0^*) = d_{j,\text{max}}^* \left(1 - e^{-\frac{(t_{\text{adj}})}{\tau_{\text{droplet}}}} \right) \quad \text{Equation 6.33}$$

where d_j^* is the scaled droplet diameter, d_0^* is the initial droplet scaled diameter (here, zero), $d_{j,max}^*$ is the final scaled diameter (here this will be 1), and $\tau_{droplet}$ is the half-life which yields a rate constant, $k_{droplet}$ (s^{-1}), via

$$k_{droplet} = \frac{1}{\tau_{droplet}} \quad \text{Equation 6.34}$$

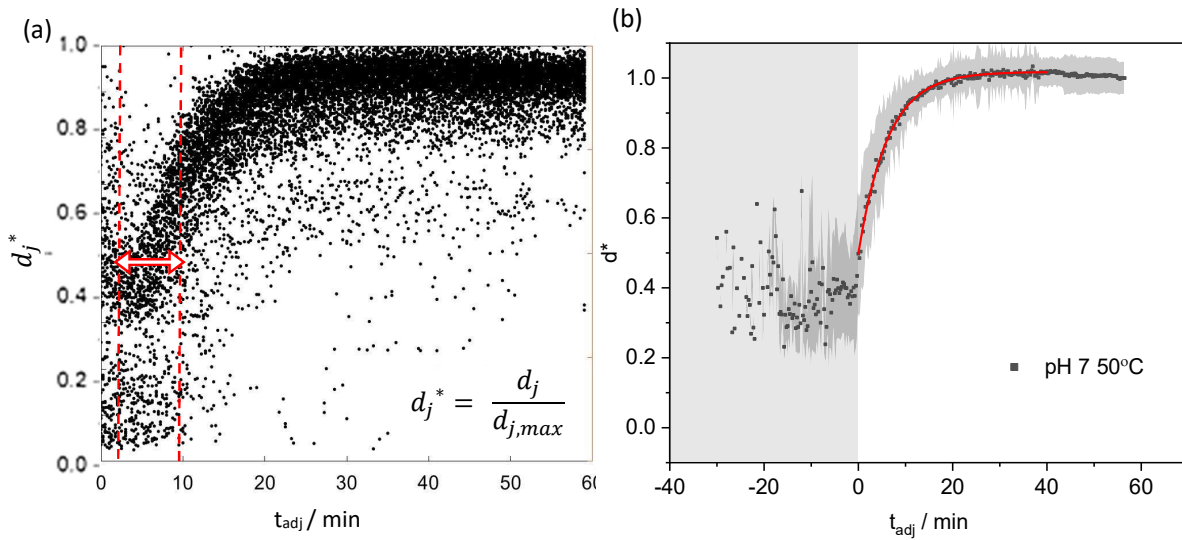


Figure 6.22: (a) Evolution of scaled droplet diameter d_j^* , all droplets, t_{adj} . (b) average scaled droplet diameter data set. Shaded region shows one standard deviation. Smooth red line shows the fit to Equation 6.33, parameters reported in Table 6.13.

6.2.4 Mathematical modelling

Two possible mechanisms by which the droplets form on the surface of the CMS are now considered.

- I. Solution penetration: the solution penetrates down into the soil from the soil-solution interface, displacing the oil within the soil as it moves towards the substrate (Figure 6.23 (a)), with the displaced material collecting at sites which favour droplet formation.
- II. Solution ingress: the solution moves into the soil from the edge of plate or from large cracks, displacing the oil as it progresses into the bulk. This mechanism assumes a homogenous, coherent soil layer (Figure 6.23 (b)).

A combination of these two mechanisms (I + II) could also occur. Simple mathematical models for these two mechanisms are now considered.

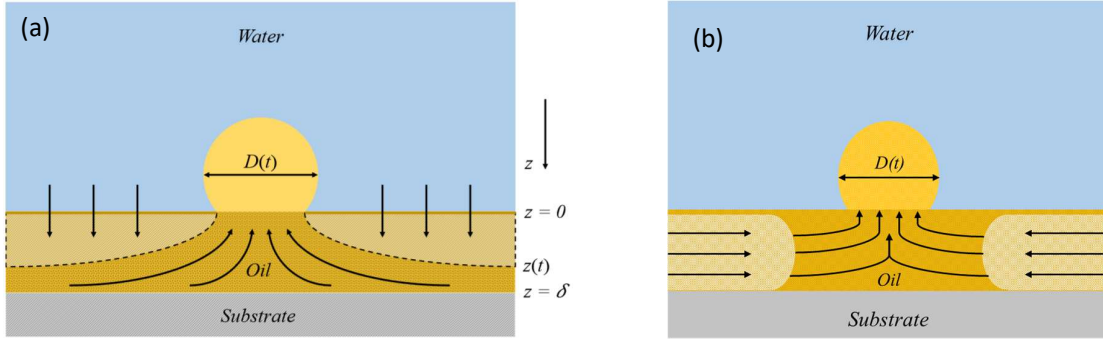


Figure 6.23: (a) Schematic cartoon representations of a penetration displacement mechanism, (b) water ingress mechanism.

6.2.4.1 Model I: solution penetration

The example considered here is CMS submerged in pH 7 water at 50 °C. At this temperature the viscosity of the fat phase is approximately 2 Pa s (Figure 3.6). It is assumed that the displacement of the fat phase is not rate-limited by its mobility. A volume balance approach can therefore be taken.

$$\frac{dV}{dt_{adj}} \approx \pi a^2 \phi_{oil} \frac{dz}{dt_{adj}} \quad \text{Equation 6.35}$$

Where V is the droplet volume, t_{adj} is droplet onset time, $2a$ is the average distance between two droplets at steady-state, ϕ_{oil} is the volume fraction of mobile fat within CMS, and z is the distance from the soil-solution interface (See Figure 6.23 (a)). In this simple model swelling is assumed to occur behind the solution front.

For a soil of thickness δ the rate of water penetration is assumed to be inversely proportional to z (Equation 6.36).

$$\frac{dz}{dt_{adj}} = \begin{cases} \frac{c}{z}, & 0 < z < \delta \\ 0, & z = \delta \end{cases} \quad \text{Equation 6.36}$$

Integration of (Equation 6.36) for $0 < z \leq \delta$ yields;

$$\int_{\sim 0}^z z dz = c \int_{\sim 0}^{t_{adj}} dt_{adj} \quad \text{Equation 6.37}$$

$$\Rightarrow z = \sqrt{2ct_{adj}} \quad \text{Equation 6.38}$$

The time taken for the solution to penetrate the entire soil layer, t_p at $z = \delta$, can be estimated as

$$t_p = \frac{\delta^2}{2c} \quad \text{Equation 6.39}$$

Setting t^* as $\frac{t_{adj}}{t_p}$ and substituting into the volume balance in Equation 6.35 gives;

$$\int_0^V dV \approx \frac{\pi a^2 \delta \phi_{oil}}{2} \int_0^{t^*} \frac{1}{\sqrt{t^*}} dt^* \quad \text{Equation 6.40}$$

which yields

$$\Rightarrow V(t^*) \approx \begin{cases} \pi a^2 \delta \phi_{oil} \sqrt{t^*}, & 0 \leq t^* \leq 1 \\ \pi a^2 \delta \phi_{oil}, & t^* > 1 \end{cases} \quad \text{Equation 6.41}$$

Interpreting $\pi a^2 \delta \phi_{oil}$ as the total amount of oil present within the control volume of soil, V_{total} , and setting $V^* = \frac{V}{V_{total}}$, Equation 6.41 can be written as;

$$V^*(t^*) \approx \begin{cases} \sqrt{t^*}, & 0 \leq t^* \leq 1 \\ 1, & t^* > 1 \end{cases} \quad \text{Equation 6.42}$$

Using Equation 6.42 as an expression of the volume of a truncated sphere this can be converted to an expression for the droplet diameter as a function of dimensionless time:

$$d \approx \begin{cases} \sqrt[3]{\frac{24 a^2 \delta \phi_{oil}}{(2 + 3 \cos \theta - \cos^3 \theta)} \cdot t^{\frac{1}{6}}}, & 0 \leq t^* \leq 1 \\ \sqrt[3]{\frac{24 a^2 \delta \phi_{oil}}{(2 + 3 \cos \theta - \cos^3 \theta)}}, & t^* > 1 \end{cases} \quad \text{Equation 6.43}$$

The scaled droplet diameter, d^* , is then:

$$d^*(t^*) \approx \begin{cases} \sqrt[6]{t^*}, & 0 \leq t^* \leq 1 \\ 1, & t^* > 1 \end{cases} \quad \text{Equation 6.44}$$

Figure 6.24 shows the fit of this model to the averaged data in Figure 6.22 (b) with t_p set to 22 minutes giving the penetration rate constant, c , as $3 \times 10^{-11} \text{ m}^2 \text{ s}^{-1}$. The model fits within the variation of the experimental results, however it does not describe the final approach to an asymptote as t^* approaches 1.

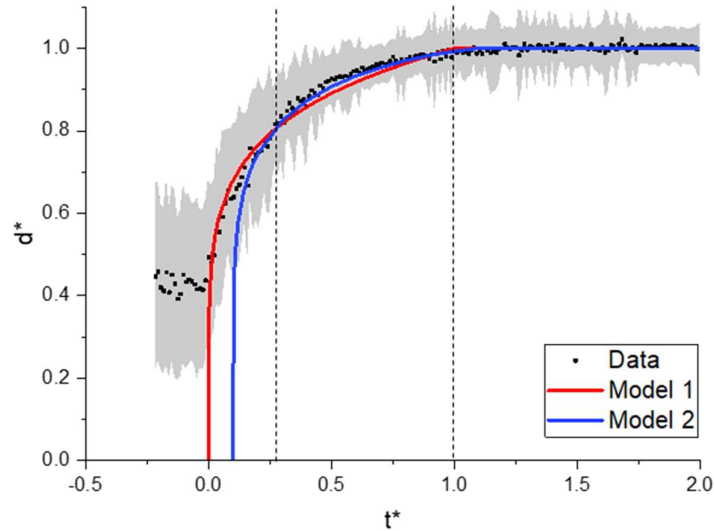


Figure 6.24: Fits of models I and II to droplet formation data for CMS submerged in pH 7 water at 50 °C

The model assumes that the droplet is a spherical cap. Inspection of images supports this assumption however there may be some cases, especially above cracks that did not completely fill after swelling, in which the droplet is pinned along a contact line and therefore is more ellipsoidal in shape. Lubarda and Talke (2011) explored the mathematical implications of gravitationally induced ellipsoidal droplets and the impact on the contact angle estimation. The Bond number estimation of this system (Figure 6.20) demonstrates that in this system gravity does not affect the droplet shape. However, the geometrical implications of ellipsoidal droplets formed due to gravity vs ellipsoidal droplets formed due to contact line pinning are compatible. Lubarda and Talke described V as a function of the contact angle θ in an ellipsoidal droplet as;

$$V \propto \frac{(1 - \cos \theta)(3 + \cos \theta)}{4 + (2 + \cos \theta)} \quad \text{Equation 6.45}$$

This has the consequence of decreasing the effective contact angle dependency, which would increase the estimation of d^* . It is outside the scope of this work to determine the curvature of each individual droplet, however should the technique be used further, this would be the recommended avenue to explore.

6.2.4.2 Model II: Solution ingress

In this model the water is assumed to be displaced by water penetrating from the soil edges. Each droplet will be formed from the mobile components contained within a soil disc of radius a , where a is the maximum radial distance that the mobile component travels from (Figure 6.25). This model

assumes that the solution penetrates as a front of radius r . Penetration through the top surface is considered here to be negligible.

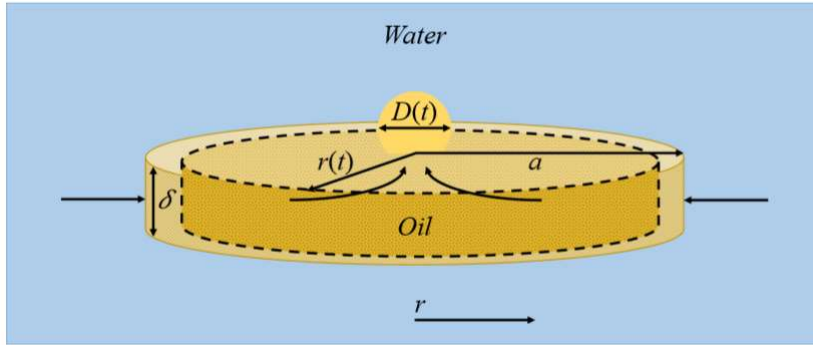


Figure 6.25: Schematic of the solution ingress model.

A volume balance in this system takes the form;

$$\frac{dV}{dt_{adj}} \approx -2\pi\delta\phi_{oil}r \frac{dr}{dt_{adj}} \quad \text{Equation 6.46}$$

The flow rate of the solution into the soil, Q , through the disc can be expressed in terms of the superficial velocity, u_m :

$$Q = 2\pi r\delta u_m \quad \text{Equation 6.47}$$

Let P be the gauge pressure. This allows the superficial velocity to be written in terms of the pressure drop, $\frac{dP}{dr}$, across the disc using the Carman-Kozeny equation, assuming laminar flow of water within the soil pores:

$$\frac{dP}{dr} = -180 \frac{(1-\varepsilon)^2}{\varepsilon^3} \frac{\mu}{d_{pore}^2} u_m = -\alpha u_m \quad \text{Equation 6.48}$$

where ε is the porosity of the sample, μ the viscosity of solution, d_{pore} the diameter of the pore and α is a lumped constant. Assuming instantaneous steady-state;

$$\frac{dP}{dr} = -\frac{\alpha Q}{2\pi\delta r} \quad \text{Equation 6.49}$$

Integration of this function from 0 to $-\Delta P_c$ (the suction induced capillary pressure difference) across a section from a to r and rearranging gives:

$$Q = \frac{2\pi\delta\Delta P_c}{\alpha \ln\left(\frac{r}{a}\right)} \quad \text{Equation 6.50}$$

This can then be set as equivalent to Equation 6.47. Given $u_m = \frac{dr}{dt}$ this becomes:

$$\frac{dr}{dt} = \frac{\Delta P_c}{\alpha r \ln\left(\frac{r}{a}\right)}, \quad 0 < r \leq a \quad \text{Equation 6.51}$$

Setting $r^* = \frac{r}{a}$ and integrating from $r^* = 1$ at $t = 0$ to $r^* = r^*$ at $t = t_{adj}$ gives:

$$\frac{(r^*)^2}{2} \left(\ln(r^*) - \frac{1}{2} \right) + \frac{1}{4} = \frac{\Delta P_c}{\alpha a^2} t_{adj} \quad \text{Equation 6.52}$$

Equation 6.52 can be solved for r^* by utilisation of the Lambert W or product log function (Corless *et al.*, 1996) and Equation 6.46. This solution is shown in Appendix 12.1. By defining $t^* = \frac{4\Delta P_c}{\alpha a^2} t_{adj}$ and substituting into the solution of Equation 6.52 gives;

$$V(t^*) \approx \begin{cases} \pi a^2 \delta \phi_{oil} \left(1 - \frac{t^* - 1}{W_{-1}\left(\frac{t^* - 1}{e}\right)} \right), & 0 \leq t^* < 1 \\ \pi a^2 \delta \phi_{oil}, & t^* \geq 1 \end{cases} \quad \text{Equation 6.53}$$

With dimensionless form:

$$V^*(t^*) \approx \begin{cases} 1 - \frac{t^* - 1}{W_{-1}\left(\frac{t^* - 1}{e}\right)}, & 0 \leq t^* < 1 \\ 1, & t^* \geq 1 \end{cases} \quad \text{Equation 6.54}$$

The diameter is thus expressed as:

$$d(t^*) \approx \begin{cases} \sqrt[3]{\frac{24a^2 \delta \phi_{oil}}{(2 + 3 \cos \theta - \cos^3 \theta)} \left(1 - \frac{t^* - 1}{W_{-1}\left(\frac{t^* - 1}{e}\right)} \right)}, & 0 \leq t^* < 1 \\ \sqrt[3]{\frac{24a^2 \delta \phi_{oil}}{(2 + 3 \cos \theta - \cos^3 \theta)}}, & t^* \geq 1 \end{cases} \quad \text{Equation 6.55}$$

with dimensionless form:

$$d^*(t^*) \approx \begin{cases} \sqrt[3]{1 - \frac{t^* - 1}{W_{-1}\left(\frac{t^* - 1}{e}\right)}}, & 0 \leq t^* < 1 \\ 1, & t^* \geq 1 \end{cases} \quad \text{Equation 6.56}$$

Figure 6.24 shows the appropriate fit models I and II for CMS in pH 7 water at 50 °C with t_p set to 22 minutes. An adjustment of $t^* + 0.1$ was required to fit model II to the data. This could indicate that the mechanism by which model II occurs, i.e. ingress of water from the side of the soil occurs later than the driving force caused by water penetration into the surface of the soil. If the disc model is assumed to be appropriate, then neither model represents the data perfectly, however a combination

of the two mechanisms does adequately describe the data. This implies that first the droplet is formed after being displaced by the pressure of the water penetration into the soil before the pore pressure from water ingress through the soil channels becomes the dominant mechanism until the soil is fully wetted and the droplet stabilises (or in some cases detached). This change in mechanism occurred at approximately $t^* = 0.3$ which corresponds to a t_{onset} of 6 – 7 minutes calculated using the estimated penetration rate constant $c = 3 \times 10^{-11} \text{ m}^2 \text{ s}^{-1}$. At this point the water would have progressed approximately 2 – 2.3 mm into the soil. The crack distribution of CMS was estimated to be 2.5 ± 0.4 mm which is approximately consistent however the solution should be penetrating from all radial directions making this an overestimation. The inconsistency could be due to a number of factors:

1. The assumption of instantaneous steady-state is likely an over-simplification.
2. The oil is displacing into more than one droplet per 'island' caused by cracks. This would slow the oil uptake per droplet.
3. The cracks do not penetrate the soil to the surface. This would decrease the available solution-soil contact line through which the water can penetrate.
4. If some oil has already been displaced by the water penetrating into the CMS from the surface, there is a lower concentration of oil to be displaced into the droplet by the sideways forces in model II, slowing oil uptake via this mechanism.

The appropriateness of each of these models to describe the droplet formation on CMS can be further investigated via alteration of the solution system e.g. the addition of surfactants, pH or alterations in temperature.

6.2.5 Results and Discussion

6.2.5.1 Impact of temperature

The effect of temperature on the formation of droplets on the CMS surface after submersion in pH 7 water was investigated for the range 20 - 50 °C at intervals of 5 °C. No droplet formation was observed below 35 °C despite carbon analysis of the cleaning solution showing that material is removed from the soil into the solution at these temperatures (Figure 6.6). At 35 °C the fat component within the soil is still undergoing a phase transition to its liquid state and has a higher viscosity of approximately 11 Pa s (Figure 3.6).

Figure 6.26 (a) shows a comparison between the average scaled drop diameter by t_{adj} for $T > 35$ °C. It is evident that as the temperature of the cleaning solution increases from 35 °C to 50 °C the rate of droplet growth increases ($k_{droplet} / \text{s}^{-1}$: 4.5 → 6.5 → 8.4 → 9.9, Table 6.13) as this increases the final drop diameter ($d^* = 1$). This is reflected in both the droplet volume estimation (Figure 6.26 (b)), which shows a slower initial rate of droplet growth at lower temperature. The droplet size distributions at

35 °C and 50 °C (Figure 6.26 (c)) suggest that there is a smaller maximum droplet diameter to which the droplets will grow at 35 °C compared to 50 °C (~1.3 mm vs 1.5 mm). It is also evident from Figure 6.26 (c, insert) that there are fewer droplets formed at lower temperatures with a larger number of stable, smaller droplets. A slight down-tick in the total droplet volume was recorded at $t_{adj} > 50$ minutes for pH 7 at both 35 °C and 50 °C; this is attributed to there being a higher degree of droplet detachment from the surface than there is droplet growth after this time.

The average droplet onset time (~ 16 minutes) and the total volume of the droplets present on the plate (~ 20-25 μL) are reasonably insensitive to changes in temperature within this range (Table 6.13). The rate at which the droplets form and stabilise that changes between temperatures. This is reflected in the modelling in Figure 6.26 (d). The behaviour of the average droplet growth curve at 40 °C is similar that of 50 °C, i.e. model I, until $t^* = 0.2$ after which point model II describes the data more closely. At 35 °C neither model is adequate. This is thought to be due to the initial assumption that the displacement of the fat phase is not rate-limited by its mobility when at this lower temperature it will still have a higher viscosity than at 50 °C (11 Pa s vs 2 Pa s).

The time taken for the solution front to penetrate the whole CMS layer, t_p , decreased with increasing temperature ($t_p = 22$ minutes at 50 °C, and 40 min at 35 °C, Table 6.13). This corresponds to an increasing water penetration rate constant from $1.85 \times 10^{-11} \text{ m}^2 \text{ s}^{-1}$ at 35 °C up to $3.4 \times 10^{-11} \text{ m}^2 \text{ s}^{-1}$ at 50 °C.

A pseudo-Arrhenius plot was used to determine the dependency between the temperature and the rate constants of oil evolution calculated for the data in Figure 6.26.

$$\ln(k) = \ln(A) - \frac{E}{R_g T} \quad \text{Equation 6.57}$$

Here E is an activation energy, and R_g is the gas constant. Here it gives an indication of the driving force of water penetration. Using four data points ($T = 35 - 50$ °C) an energy of penetration was calculated to be 44 kJ mol^{-1} , with $R^2 = 0.98$. This value indicates a mixed mechanism, higher than expected for diffusion driven penetration, but lower than expected for chemically driven penetration. The mixed mechanism is likely due to the heterogeneity and porosity of the CMS soil.

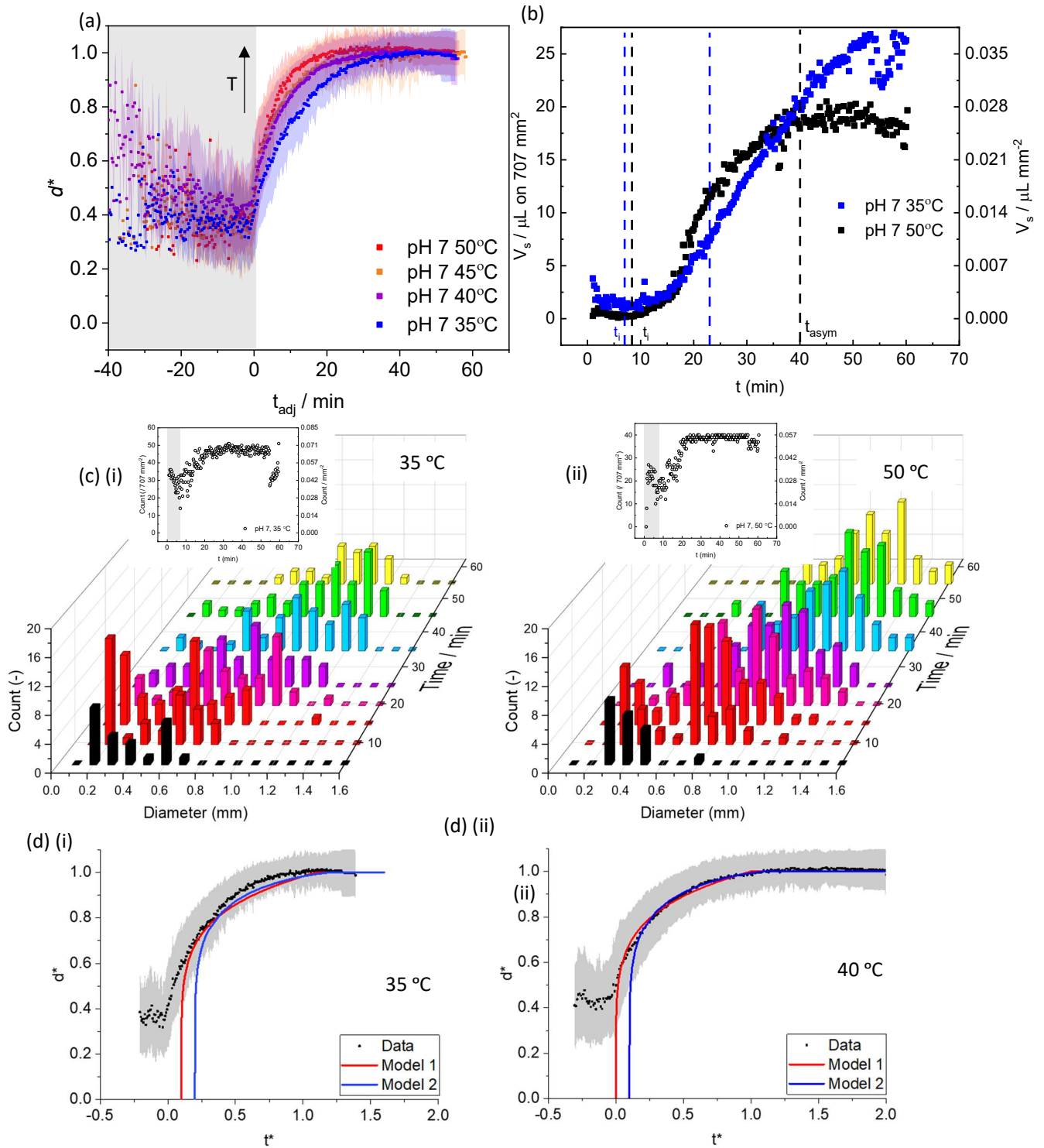


Figure 6.26: (a) Evolution of averaged scaled diameter. (b) Total volume of the droplets. (c) Histograms of droplets formed on CMS after submersion in pH 7 water at (i) 35 °C and (ii) 50 °C. Inset: total number of droplets by time, (d) Model fits of CMS submerged in pH 7 water at (i) 35 °C, t_p here is 40 minutes and (ii) 40 °C, with t_p set to 27 minutes. Model fit to 45 °C not shown. Shaded regions show one standard deviation of three repeats. Model parameters for fits to Equation 6.44 and Equation 6.56 are recorded in Table 6.13.

6.2.5.2 Impact of pH

The impact of pH was explored for solutions starting at pH 7 water up to pH 10. Higher pH promoted the swelling and breakdown of the bulk soil to the extent that imaging of droplets formed over time was impractical. Figure 6.27 compares pH 7, pH 8 and pH 9 solutions.

Figure 6.27 (a) shows a small impact of pH on the growth of a droplet ($k_{droplet} = 9.9, 9.4$ and 8.0 for pH 7 water, pH 8 and pH 9 cleaning solutions respectively, Table 6.13). The solution penetration time, t_p , was constant, at approximately 22 minutes, corresponding to a penetration rate constant of $\sim 3.4 \times 10^{-11} \text{ m}^2 \text{ s}^{-1}$.

Figure 6.27 (b) shows that the volume of droplets on the surface stabilises at an approximately constant $V_{max} \approx 20 - 23 \text{ } \mu\text{L}$, with a faster rate at higher pH ($t_{asym} \sim 24$ minutes at pH 9, 37 minutes at pH 8, and 40 minutes in pH 7 water). This corresponds to a faster average droplet onset time at higher pH with $\langle t_{onset} \rangle$ decreasing from 16 minutes in pH 7 water to 10 minutes at pH 9 (Table 6.13). The increased rate of swelling of the soil at higher pH would contribute to the lower $\langle t_{onset} \rangle$. Visual observation of the droplet location shows that they most often formed above the cracks in the soil. As water ingresses into the matrix, the soil swells, closing the cracks. The volume of mobile material that must accumulate within the crack before forming a droplet therefore decreases, causing droplets to start forming sooner than they would in pH 7 water, even though the rate of growth after t_{onset} is unchanged (Figure 6.15 (b, ii)). The distribution of droplet sizes after 5 minutes of submersion at pH 9 is significantly wider than in pH 7 water alone (Figure 6.27 (c)) indicating that in some cases the droplets are forming almost immediately after submersion.

The maximum droplet diameter recorded at pH 9 was 1.2 mm (compared to 1.5 mm in pH 7) indicating that either the droplets are stabilising at this size (possibly due to a change in surface charge) or that detachment of the droplet occurs at a lower size than in pH 7 water. In pH 9 solution the number of droplets after 55 minutes is lower than that after 25 minutes indicating the later explanation is the most likely. Additionally, due to the higher degree of swelling at pH 9 the cracks will be smaller, causing a narrower pinning line of the soil for the droplet to attach to, giving a sharper θ . Equation 6.30 shows that if a droplet has a smaller θ its R_{crit} will also be smaller, and the drop will detach sooner.

Modelling of the average scaled droplet growth indicates a potential change in dominant cleaning mechanism between pH 8 and pH 9 (Figure 6.27 (d)). At pH 8 the combination of models used to describe the behaviour of the water penetration/ingress in pH 7 water is still valid, however at pH 9 neither model adequately fits the experimental data. This is likely due to changes in the soil internal structure after contact with OH^- ions. Experimental observations in Chapter 5 demonstrated that as the pH increases the CMS rapidly increases in volume for a period of approximately 50 s, with swelling

occurring at a slower rate for a further 1500 s. This swelling would influence the internal structure of the soil layer. The models used here do not include swelling. Both models assume a constant porosity and thickness of the soil matrix. It is therefore expected that as the pH of the cleaning solution increases the appropriateness of the water ingress/penetration models used here changes.

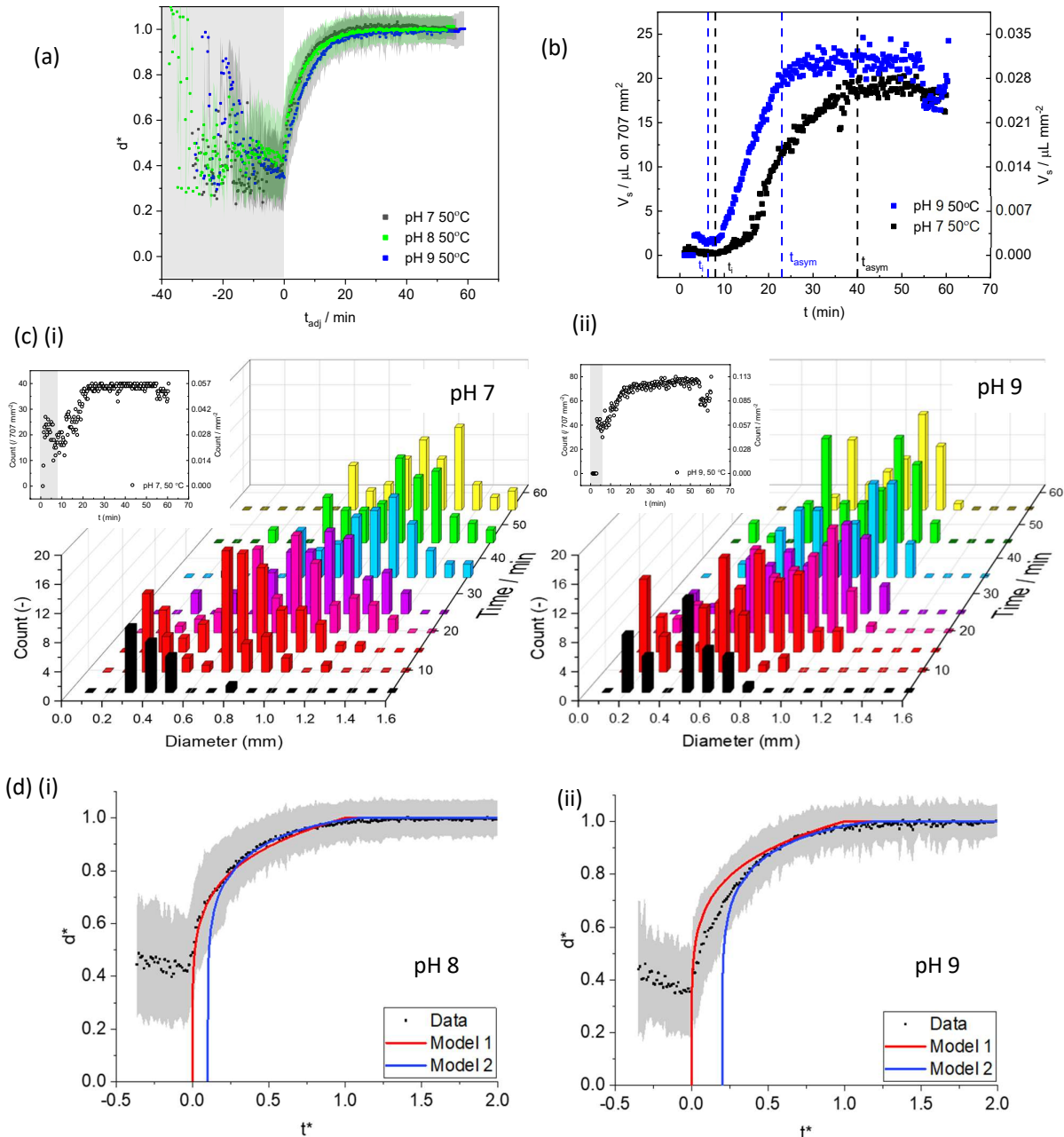


Figure 6.27: (a) Effect of pH on evolution of averaged scaled diameter. (b) Volume of the droplets. (c) Histograms of droplets formed on CMS after submersion at 50 °C in (i) pH 7 water and (ii) pH 9, inset: total number of droplets by time. (d) Model fits of CMS submerged at 50 °C in (i) pH 8 solution, with t_p set to 22 minutes and (ii) pH 9, $t_p = 23$ minutes. Shaded regions show one standard deviation of three repeats. Model parameters for fits to Equation 6.44 and Equation 6.56 are recorded in Table 6.13.

6.2.5.3 Impact of surfactants on droplet detachment

The critical radii for the surfactants tested are shown in Table 6.12. Interfacial tension estimations were made on a DSA pendant drop shape analyser using sunflower oil on CMS in 0.1 wt.% surfactant solutions. The contact angle was set at 53°, which is the average of multiple droplets imaged during testing and will likely be an overestimate in the case of the surfactant containing solutions. Critical radii of droplets with smaller contact angles have been calculated. It was not possible to accurately measure the contact angle of a sessile droplet on the CMS in the presence of surfactants using a drop shape analyser due being unable to attach a sunflower oil droplet to the CMS surface. The droplet must form from within the soil to be attached to the CMS surface. $\Delta\rho$ was 77 kg m⁻³.

Table 6.12: (a) Bond number estimations for droplets sized $0.5\text{ mm} < R_1 < 1.5\text{ mm}$ in surfactant solutions (b) Estimations of the critical radius for droplet detachment from CMS submerged in an aqueous cleaning solution at 50 °C. $d_{crit} = 2R_{crit}$.

Solution	Characteristic length	Bond Number			
		$R_1 = 1.5\text{ mm}$	$R_1 = 1.0\text{ mm}$	$R_1 = 0.75\text{ mm}$	$R_1 = 0.5\text{ mm}$
Contact angle 53°	L_c / mm				
0.01 % SDBS	4.7	0.08	0.04	0.02	0.01
0.01 % TX-100	3.8	0.13	0.06	0.03	0.01
0.01 % CTAB	2.0	0.46	0.21	0.12	0.05
0.1 % SDBS	2.0	0.44	0.20	0.11	0.05
0.1 % TX-100	2.0	0.46	0.20	0.11	0.05
0.1 % CTAB	0.7	3.50	1.56	0.88	0.39

Solution	d_{crit} / mm			
	53°	40°	30°	20°
Contact angle →				
pH 7 water	12.0	9.4	7.2	4.8
0.01 % SDBS	9.7	7.6	5.8	4.0
0.01 % TX-100	7.8	6.1	3.7	3.2
0.01 % CTAB	4.1	3.2	2.4	1.7
0.1 % SDBS	4.2	3.2	2.4	1.6
0.1 % TX-100	4.2	3.2	2.4	1.6
0.1 % CTAB	1.4	1.2	0.8	0.6

The impact of the change in θ with increasing surfactant concentration can be estimated using the oil-water surface tension. Young's Equation states that:

$$\gamma_{OS} = \gamma_{OW} \times \cos \theta + \gamma_{WS} \quad \text{Equation 6.58}$$

Therefore

$$\cos \theta = \frac{\gamma_{OS} - \gamma_{WS}}{\gamma_{OW}} \quad \text{Equation 6.59}$$

If we assume that the surface interactions between the droplet and CMS, and the CMS and the solution, are constant throughout the experiment (for each individual solution) then only the surface interactions between the droplet and the solution change. We can determine γ_{OW} using pendant drop analysis.

$$\gamma_{OS} - \gamma_{WS} = \gamma_{OW} \times \cos \theta \quad \text{Equation 6.60}$$

If we define system (1) as the simple water system and (2) as the system containing surfactant then

$$\frac{\cos \theta_2}{\cos \theta_1} = \frac{\gamma_{OW,1} (\gamma_{OS} - \gamma_{WS})_1}{\gamma_{OW,2} (\gamma_{OS} - \gamma_{WS})_2} \quad \text{Equation 6.61}$$

Since γ_{OW} decreases on the addition of surfactant $\frac{\gamma_{OW,1}}{\gamma_{OW,2}}$ will be greater than 1. Similarly, $\frac{(\gamma_{OS} - \gamma_{WS})_1}{(\gamma_{OS} - \gamma_{WS})_2}$ will be greater than 1 because the surfactant reduces the surface energy so the difference in surface tensions will be smaller. This implies that $\cos \theta_2 > \cos \theta_1$ and so $\theta_2 < \theta_1$. Therefore, we expect a decreasing contact angle with increasing surfactant concentration.

However, γ_{WS} is unlikely to remain constant with increasing surfactant concentration. In the limiting case, where γ_{WS} decreases to zero, (system (3)) then

$$\gamma_{OS} = \gamma_{OW} \times \cos \theta \quad \text{Equation 6.62}$$

Giving

$$\frac{\cos \theta_3}{\cos \theta_1} = \frac{\gamma_{OW,1} (\gamma_{OS})_1}{\gamma_{OW,3} (\gamma_{OS} - \gamma_{WS})_3} \quad \text{Equation 6.63}$$

If surfactant lowers γ_{OW} to the same extent, then $\cos \theta_3 > \cos \theta_2$, and $\theta_3 < \theta_2$. θ is therefore an overestimate in cases where surfactant is used, but γ_{WS} is not altered in the modelling. However as mentioned previously, experimental observations (not shown) show that the γ_{WS} interactions dominate over the γ_{OS} interactions as the droplet will not re-attach to the surfactant covered soil. This is consistent with the experimental observations that oil is mobilised at a faster rate in the surfactant containing cleaning solutions during the image analysis testing. The surfactant preferentially wets the

soil matrix forcing the oil into the cracks and buoyancy forces drive oil to form a droplet on the soil surface. i.e.

$$\gamma_{ws} < \gamma_{ow}, \gamma_{os} \quad \text{Equation 6.64}$$

This suggests that the approximation in Equation 6.26 is applicable.

When utilising this approximation it is important that the initial value for θ must be $<90^\circ$, i.e. the water must wet the soil more strongly than the oil in the absence of surfactant.

A surfactant that can decrease the interfacial tension of the system at a faster rate, such as CTAB (Figure 3.7), will be more capable of creating the driving force for the removal of the oil from the soil at lower concentrations and shorter time scales. This is evidenced by the over three-fold increase in organic carbon measured during static oil recovery testing when the soil is contacted with 0.1 % CTAB solution (135 mg g^{-1}) over other surfactants tested such as 0.1 % SDBS (38.2 mg g^{-1}).

6.2.5.4 Experimental impact of surfactants

The impact of surfactants on the evolution of oil within the soil was investigated using SDBS, TX-100 and CTAB. The droplets that formed on the CMS surface were noticeably smaller ($r_{max} = 0.8 \text{ mm}$ for 0.1 % SDBS compared to 1.6 mm for pH 7 water, Figure 6.28 (c)), complicating the image analysis. This was especially the case for CTAB containing solutions, to the extent that the technique was incapable of resolving droplets effectively (See Appendix 12.2). Higher resolution imaging equipment as well as increased processing power would be required to solve this problem. For this reason CTAB data are not presented (Picture of CMS submerged in CTAB in Appendix 12.2).

Another factor that required additional processing steps was the fact that the droplets were readily detached from the surface via a surfactant-enhanced roll-up mechanism, conflating the calculated initial $\langle t_{adj} \rangle$ with a large proportion of droplets which formed at the same site as a previous droplet. For this reason, studies were conducted at the standard surfactant of 0.1 wt.%, and at a lower surfactant loading (0.01 wt.%). This lower concentration was targeted to provide sufficient surfactant to resolve a change in behaviour from pH 7 water, but chosen to avoid early droplet detachment. Figure 6.28 shows representatives of both surfactant concentrations; experiments requiring that droplets be present over a relatively long period of time (e.g. rate of droplet growth data. Figure 6.28 (a), (d)) use 0.01 % surfactant, else the standard concentration of 0.1% was used.

Figure 6.28 (b) shows that the total volume of the droplets on the CMS surface in the presence of surfactant at any given time decreased as the experiment progresses. This is interpreted to be a function of the availability of mobile material. Within 5 minutes of submersion a number of droplets of relatively large diameter, up to 0.8 mm (Figure 6.28 (c,i)), form on the CMS surface. The surfactant

solution then promotes roll-up of the droplet and it detaches from the surface. A new droplet will then form in its place (e.g. Figure 6.17 (c)). The presence of droplets with $d \leq 0.2$ mm (i.e. the detection threshold) throughout the entire test time indicates that this detachment-regrowth process occurred throughout the test. Figure 6.28 (b) however indicates that the rate of replenishment of the droplets on the soil surface slows, likely due to exhaustion of the available mobile material.

Models I and II were fitted to systems containing low surfactant concentrations. These systems demonstrated similar behaviour to that of pH 7 water, however, with a shorter $\langle t_{onset} \rangle$, t_i and, in the case of 0.01 % SDBS, t_{asym} . This indicates that the surfactants are promoting the de-wetting of the oil from the soil layer, enabling the mobile components to move towards the CMS surface on a shorter time-scale than in water alone.

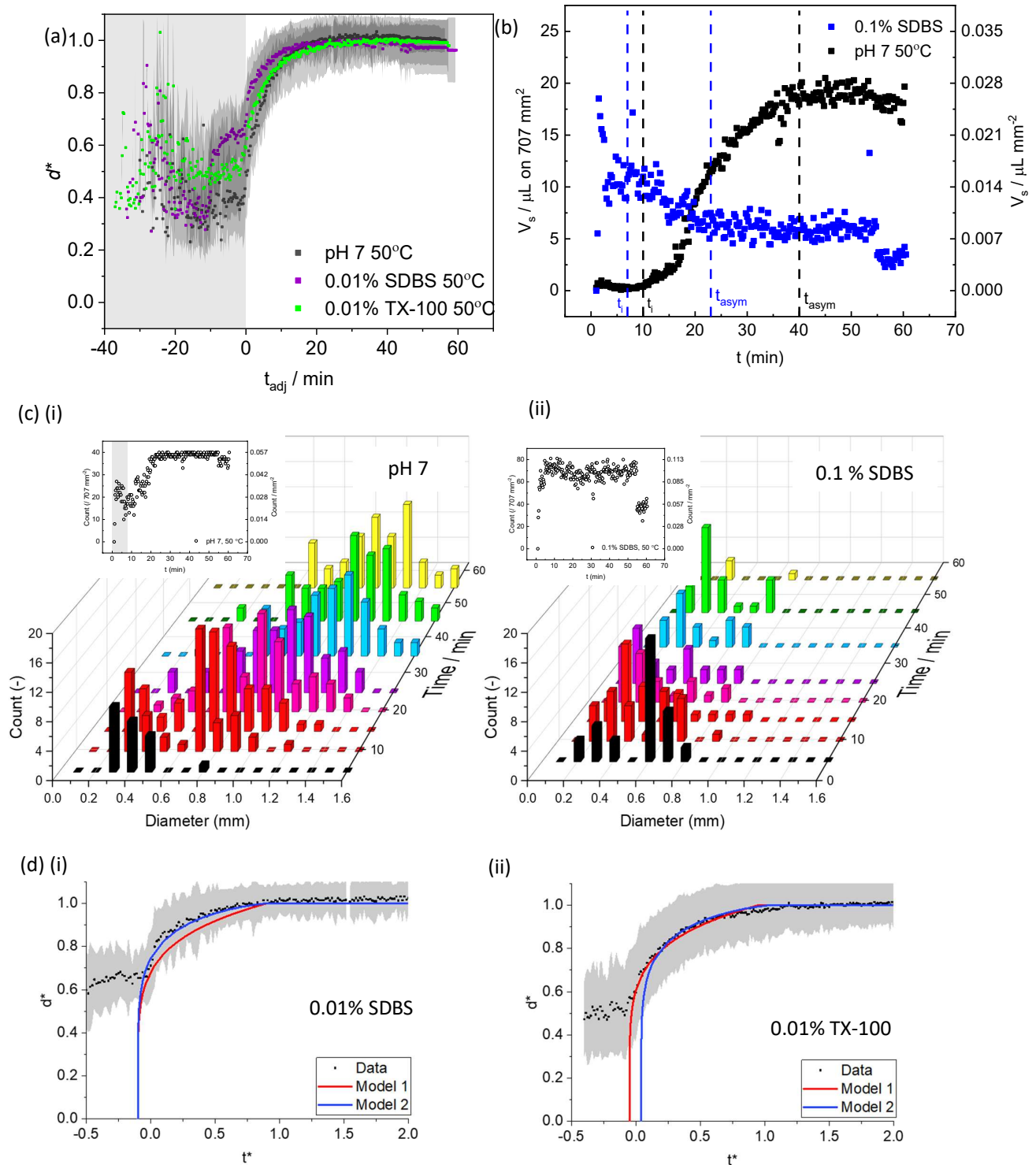


Figure 6.28: Effect of surfactant on droplet evolution (a) averaged scaled diameter. (b) Total volume of the droplets formed over the test time. (c) Histograms of droplets formed on CMS after submersion in at 50 °C in (i) pH 7 water and (ii) 0.1% SDBS, inset: total number of droplets by time. (d) Model fits of CMS submerging at 50 °C in (i) 0.01% SDBS solution, with t_p set to 16 minutes and (ii) 0.01 TX-100, $t_p = 20$ minutes. Shaded regions show one standard deviation of three repeats. Model parameters for fits to Equation 6.44 and Equation 6.56 are recorded in Table 6.13.

6.2.6 Overarching observations

Table 6.13 provides a summary of the relevant parameters measured throughout this range of testing. It is evident from this table that each parameter tested, temperature, pH and surfactancy, play a different role in influencing the formation and growth of droplets on the CMS. Modelling indicates that temperature has the most significant influence on the rate of water penetration into the soil, as well as the rate of growth of the droplets once they start to form (Table 6.13: Modelling; t_p , c , t_2^*). This implies that it is predominantly influencing the mobile components within the soil.

pH has little impact on the growth of the droplets but increasing pH does play a role in reducing the $\langle t_{onset} \rangle$ of droplet growth. This is evident in both the tracking of individual droplets and of the bulk volume of droplets on the CMS surface (Table 6.13: Droplet onset and Volume of droplets; $\langle t_{onset} \rangle$, t_i and t_{asym}) and indicates that the pH is influencing the interaction between CMS solid matrix and the cleaning solution, likely through enhancing the osmotic pressure, causing an increase in the volume and rate of soil swelling (Chapter 5).

Surfactants, even at very low concentrations, both decrease $\langle t_{onset} \rangle$ and the maximum size of the droplet forming on the surface. This indicates that the surfactant acts on both the soil by promoting the de-wetting of the oil from the solid matrix, and on the detachment of the resultant droplets, likely via lowering the interfacial tension between the soil components and the cleaning solution.

This was the first known development of this technique to track the evolution of oil droplets from heterogeneous soils and required significant development in the generation and processing of data. As such there was insufficient time to look into further combinations. The impact of combining these parameters is therefore recommended for further study.

Table 6.13: Table of parameters for image analysis of droplets study.

Solution	Temperature	pH	Surfactant	Droplet onset		Maximum volume of droplets			Kinetics		Modelling		
				$\langle t_{onset} \rangle$	$\langle t_{onset} \rangle SD$	t_i	t_{asym}	V_{total}	$k_{droplet}$	$\tau_{droplet}$	t_p	Model I	Model II
				min	min	min	min	$\mu\text{l} / 707 \text{ mm}^2$	s^{-1}	s	min	$\text{m}^2 \text{ s}^{-1}$	t_2^*
	/ °C		0.01 wt. %										
Water	35	7	-	16	± 7	10	53	25	4.5	0.22	40	1.85	0.2
	40	7	-	18	± 8	10	40	32	6.5	0.16	27	2.8	0.1
	45	7	-	14	± 6	6	44	20	8.4	0.12	25	3	0.1
	50	7	-	16	± 5	8	40	20	9.9	0.10	22	3.4	0.1
NaOH _{aq}	50	7	-	16	± 5	8	40	20	9.9	0.10	22	3.4	0.1
	50	8	-	13	± 7	6.6	37	23	9.4	0.11	22	3.4	0.1
	50	9	-	10	± 5	5.5	24	17	8.0	0.13	23	3.3	0.2
Surfactants	50	7	-	16	± 5	8	40	20	9.9	0.10	22	3.4	0.1
	50	7	SDBS	12	± 5	5.6	23	19	11.8	0.08	16	4.7	-0.1
	50	7	TX-100	9	± 5	4	43	27	10.0	0.10	20	3.8	0.04

6.3 Conclusions

In the second part of this chapter an image analysis method was developed to track the evolution of mobile components from CMS submerged in a cleaning solution. A set of key parameters were established in order to study the influence of the cleaning solution composition on the solubilisation of CMS from stainless steel substrates. These include: (i) t_{onset} , the time after submersion at which the first detectable droplet forms; (ii) t_{asym} , the time at which the rate of droplet formation/growth is equal to the rate of droplet detachment; (iii) V_{total} , the total volume of the droplets at a given time within a 707 mm² surface area of the CMS layer; and (iv) $k_{droplet}$, the rate constant of scaled droplet growth.

Oil droplets were found to form on the top surface of the CMS, the size and stability of which was dependent upon the temperature, pH and surfactancy of the cleaning solution. The temperature influenced the mobility of the oily components and so more droplets formed, at a faster rate, and larger size at 50 °C than at 35 °C. Below 35 °C no droplets were observed.

pH affected the soil matrix, with a higher pH causing more soil expansion, and increasing the volume of oily material that was released. A limit to the droplet size of $d = 1.2$ mm was noted and attributed to (I) changes to the surface energy of the soil, decreasing the contact angle of the soil to the droplet, and (II) the closure of the cracks above which the droplets form, pinning the droplet attachment point to a smaller width and therefore decreasing the contact angle of the droplet to the substrate, which at pH 9, caused larger droplets to detach from the surface.

Surfactant acted on the both the droplet and the soil layer. Droplets formed almost immediately in surfactant solutions and consistently grew to a smaller maximum droplet size, of < 0.8 mm. The smaller size was attributed to surfactants promoting the detachment of the droplets into the cleaning solution. Surfactants that lowered the droplet-solution interfacial tension more were effective at promoting droplet detachment.

Two models were proposed to describe the mechanism of solution infiltration into the soil matrix, i.e. solution ingress vs solution penetration. The applicability of each model to the different solutions was analysed, as was the sphericity of the droplets in different systems.

6.4 Timescales of cleaning

Here the timescale of cleaning was primarily dependent upon the temperature and surfactancy of the solution. In static pH 7 water t_{asym} for droplet formation was around 2400 s after submersion giving $V_{total} = 20 \mu\text{l} (707 \text{ mm})^{-2}$, with a scaled rate constant of $k_{droplet} = 9.9 \text{ s}^{-1}$. The best solution tested contained 0.01 wt.% SDBS at 50 °C gave a $t_{asym} \sim 1380$ s and $V_{total} = 19 \mu\text{l} (707 \text{ mm})^{-2}$, with a rate constant

of $k_{droplet} = 11.8 \text{ s}^{-1}$. As with the oil recovery testing, including the delay time t_{onset} , these timescales are longer than the swelling timescales observed in pH 7 water on the SiDG ($t_{asym} \approx 800\text{s}$), indicating that the soil swelling occurs before all the mobile components within the soil have been solubilised into the cleaning solution. However the droplet timescales are shorter than those for oil mobility ($t_{asym} = >7600 \text{ s}$), indicating that even after the droplets have stopped forming and detaching, organic material is being released into the solution. This is attributed to the solubilisation of the solid network into the solution after all the mobile material has been depleted.

7. Soil removal forces

The use of controlled deformation devices in the field of fouling and cleaning was pioneered by Zhang *et al.* in their study of the deformation (1991) and mechanical properties (1992) of biofilms. They developed a ‘micromanipulation’ device (Liu *et al.*, 2002) consisting of a horizontal bar (30 x 6 x 1 mm) which was moved through the biofilm at a set velocity and clearance from the substrate. The force on the bar as it moved was measured and the deformation of the soil was imaged. Adjustment of the clearance at which the bar was pulled through the layer determined whether the forces measured were representative of soil-soil or soil-substrate interactions. Several forms of this concept have since been developed.

One form is the millimanipulation device (Figure 7.1, Ali, 2015(a)) which pushes a vertical blade through the layer. The force measured, f , is composed of the forces required to (I) deform material in the layer, f_I ; (II) displace the deformed material, usually either upwards along the face of the blade or outwards around the edge, f_{II} ; and, (III) overcome the shear resistance imposed on the bottom edge of the blade, f_{III} , such that;

$$f = f_I + f_{II} + f_{III} \quad \text{Equation 7.1}$$

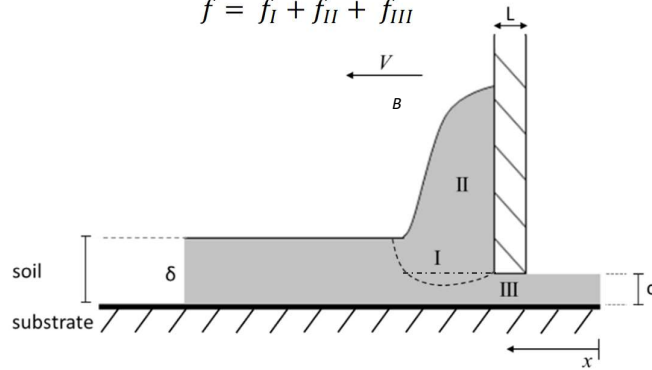


Figure 7.1: Schematic of millimanipulation deformation testing. A flat blade of thickness L is pulled at velocity, V_b , through a soil sample of initial thickness, δ , at clearance, c , leaving a residual layer of notional thickness c . The blade displacement, relative to the point of first contact is x . Region (I) denotes material ahead of the blade (boundary, dashed, not known a priori); (II) displaced material collected in front of the blade; and (III) material beneath the blade. Reproduced from Ali (2015(a)).

In an idealised soil-substrate system in which the soil fails adhesively, with c set close to 0 ($c \approx 50 \mu\text{m}$), allowing, for incompressible materials, f_I to be approximated as 0. Additionally, δ is kept small ($\delta < 400 \mu\text{m}$), minimising f_{II} . $f_{adhesive}$ would therefore be associated with f_{III} i.e. the work done to overcome the adhesive binding strength between the soil and the substrate ahead of the blade. It is noted that in this mode moving the blade along the surface, i.e. $c = 0$, is likely to invite contributions from surface friction. When removal occurs purely by adhesive failure, f provides a measure of the work required to peel a deposit away from a surface and this can be related to forces (or momentum) applied to a layer by a tool or a flow.

When removal occurs by cohesive breakdown, f_i is non-negligible and so a quantitative model of the deformation is needed to isolate the contributions from rheological parameters such as yield strength and elastic compression to the measured force. How the material properties are related to the forces required to complete a cleaning operation can then be investigated. For cleaning in pipe flows, these are typically related to fluid shear but in cleaning by impinging jets or liquid films, shear and extensional forces can act depending on the geometry and whether the liquid film is confined or has a free surface. At a coarse level, f can be used to gauge the change in material strength or adhesion.

Ali's (2015) work on burnt lard soils prompted the development of a new 'millimanipulation' device to study greater adhesion strengths (up to 420 J m^{-2}) than those accessible on micromanipulation devices ($0.3 - 80 \text{ J m}^{-2}$, Zhang *et al.* 2014).

Magens developed the current iteration, named Millimanipulation Mk III (MM3, Magens *et al.*, 2017). This device differs from the micromanipulation devices developed by Zhang as well as the millimanipulation developed by Ali (2015(a)) in a number of ways; (i) the Mk III is distinguished by a switch of the moving and stationary sections; the sample is now moved against the blade which transmits the force to a stationary force transducer; (ii) an automated z-axis was installed so that the sample can be raised and lowered, which allows the blade to be located at different heights through the sample relative to the substrate easily and (iii) the sample is located in a 100 ml bath to allow submersion in liquid (Figure 7.2) and for liquid to flow across the sample.

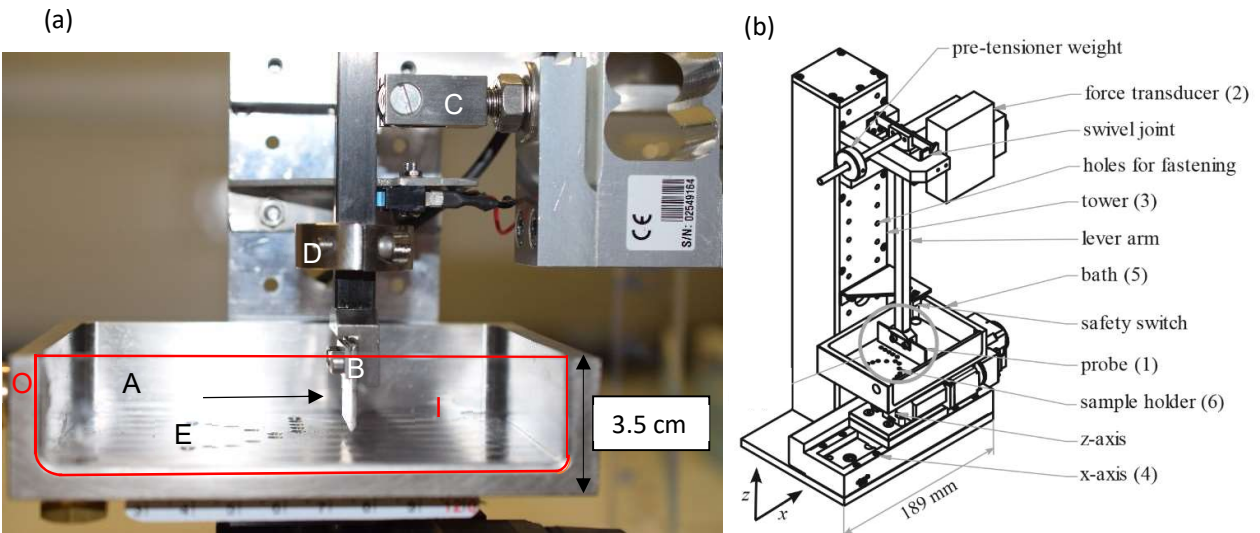


Figure 7.2: (a) Side view of the millimanipulation device with flow chamber fitted. Labels: A, Perspex viewing wall, outlined in red; B, stainless steel blade; C, force transducer; D, counterweight; E, sample mounting station; I, solution inlet; O, solution outlet. Dashed arrow indicates direction of sample motion. (b) Schematic of the MM3, taken from Magens *et al.* (2017). Components not shown: axis controllers and force transducer amplifier. Modifications to allow study of immersed systems not shown. Copyright permission obtained for MM3 drawing.

A study using the MM3 was conducted using a simple food soil (lard). This work showed that the forces required to remove the soil were dependent upon the baking time of the soil, its unsaturation level and type, and the speed of the MM3 blade as it passed through the soil layer. Oscillations were noted in the removal profile and were hypothesised to be a function of the compressibility of the soil, which would be determined by the degree of polymerisation that occurred within the soil upon baking. The work is not included in this thesis due to word limitations.

In this chapter the millimanipulation device described by Magens *et al.* (2017) (Figure 7.2) was utilised, first with dry samples submerged in separate solutions then transferred into the MM3 for testing (Section 1), before later being modified to include a solution circulation system (Section 2).

7.1 Complex Soils

The mechanical forces required to remove complex food soils was studied as a function of (i) the substrate they are bound to, and (ii) the temperature, pH and surfactancy of the solution they are submerged in.

7.1.1 Substrate effects

In practice food soils are generated on surfaces differing in chemical compositions and surface energy. Here square substrates (50 x 50 x 2 mm) of polished 304 stainless steel, borosilicate glass, and a glazed ceramic, sourced from a commercial kitchen tile, were tested. Copper plates were also tested, however these substrates were made by stamping and proved to be too curved for MM3 testing.

Figure 7.3 indicates that dry CMS binds to ceramic substrates more strongly ($\bar{F}_w = 251 \text{ N m}^{-1}$) compared to stainless steel ($\langle \bar{F}_w \rangle = 163 \text{ N m}^{-1}$) and glass ($\langle \bar{F}_w \rangle = 149 \text{ N m}^{-1}$). The MM3 was unable to remove the soil consistently for either of the two ceramic substrates (failure at $x/\delta \approx 15 - 30$; the red dashed line on Figure 7.3 indicates blade lift-off, denoted 'L'), precluding it from being used in further testing here. Adhesion to glass and stainless steel were similar. Oscillations present in the profiles were attributed to the roughness of the surface and the presence of visible cracking of the CMS layers (Chapter 3). For consistency stainless steel was selected as the substrate for subsequent testing on the CMS soil.

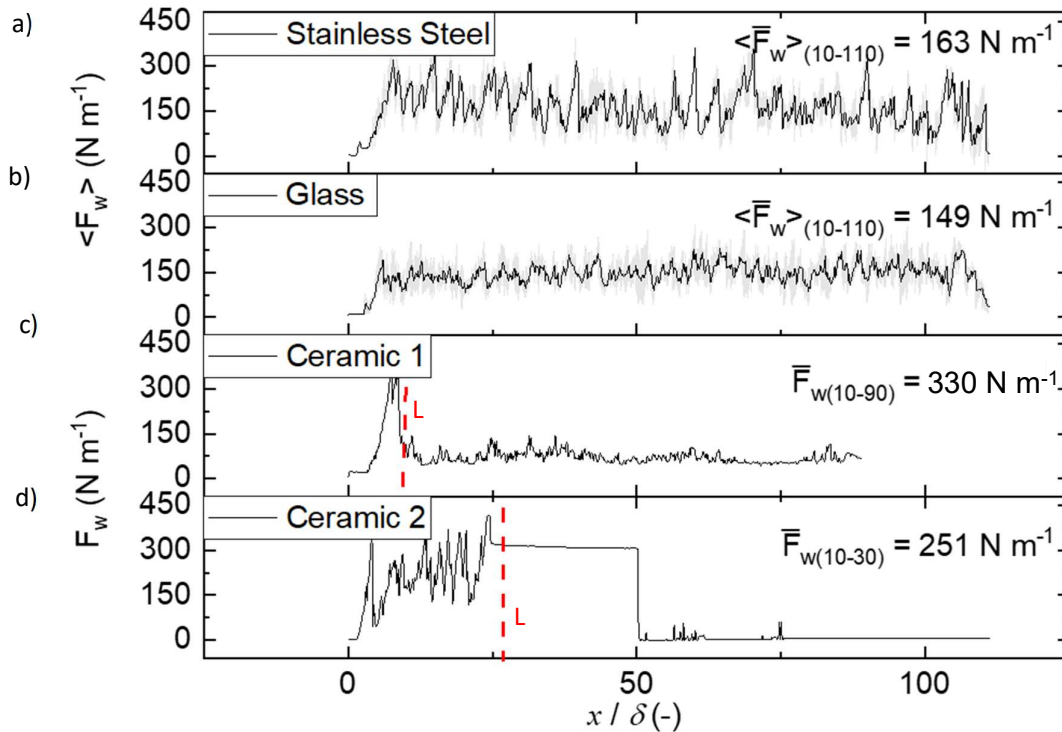


Figure 7.3: Effect of substrate on removal force of dry CMS baked at 204 °C for 7 minutes. Shaded region is standard deviation between 3 repeat samples for (a) stainless steel, (b) glass. (c, d) show individual samples of soiled glazed ceramic. Red dashed lines (L) show point of failure of the MM3 test on the soiled glazed ceramic samples.

7.1.2 Effect of contact with simple cleaning solutions for set time

During early testing the method for preparing consistent soil layers was still undergoing refinement. This led to high variability between tests. To compensate for sample-to-sample variation in adhesion strength of the dry soil to the substrate, it was decided that the pre- and post-soaking measurements would be conducted on the same disc each time and the difference between the two values taken as an indicator of the cleaning effectiveness of the solution.

The experience gained from testing on the simple oil-based soils was used to devise the CMS testing protocol. Square stainless steel plates (50 x 50 x 3 mm) were used as substrates in order to minimise edge effects and warping. The MM3 blade was set with a clearance of 50 μm above the substrate surface to favour the adhesive contributions to the measured forces over cohesive ones. The velocity was set at 0.1 mm s^{-1} to maximise the relaxation of the soil during testing, minimising f_{ii} .

The dry samples were mounted in the solution chamber with no liquid present and F_w measured for 200 s, giving $X_{\text{dry}} = 20 \text{ mm}$ (region A in Figure 7.4). Solution was then introduced to the chamber for periods ranging from 1 - 60 min with the sample stationary, after which F_w was measured for a further 200 s, giving $20 \text{ mm} < X_{\text{wet}} \leq 40 \text{ mm}$. A section of undisturbed material 10 mm long remained.

Tests were performed in triplicate. Removal profiles such as Figure 7.6 feature the average value of F_w plotted against blade-soil displacement, x . Later profiles show $\langle F_w \rangle$ plotted against time in contact with cleaning solution, t_{soak} ; since V is constant in these tests, the abscissa is readily converted between x and t .

Figure 7.4 (b) shows an example of a square plate following testing with 1 wt.% SDBS solution at pH 10 and room temperature. There is a noticeable amount of residual material on the substrate in region A (dry removal) compared with region B (following soaking), indicating that the adhesion of the soil to the substrate had decreased significantly.

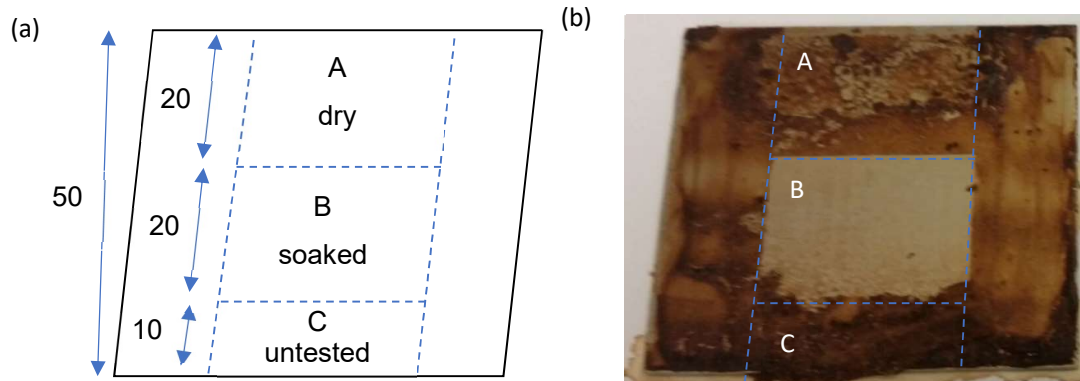


Figure 7.4: Effect of contact with cleaning solution on residual soil on substrate. (a) schematic of testing regions; (b) photograph of plate after testing with (conditions for B: 5 minutes soaking in 1 wt.% SDBS solution at room temperature). All dimension in mm. Blade clearance: 50 μm .

The change in soil behaviour was also evident in the form of the removed soil. Figure 7.5 (a) shows that, prior to soaking, removal is characterised by the chipping away of small chunks of material by the blade, characteristic of a brittle material (Kovrizhnykh, 2009). After soaking, the removed soil becomes more ductile, forming a weakly cohesively-bound heap ahead of the blade (Figure 7.5 (b)) indicative of viscous deformation (Tsai *et al.*, 2019). The absence of residual material on the substrate indicates that adhesion of the soil layer was reduced more than cohesive interactions within the layer.

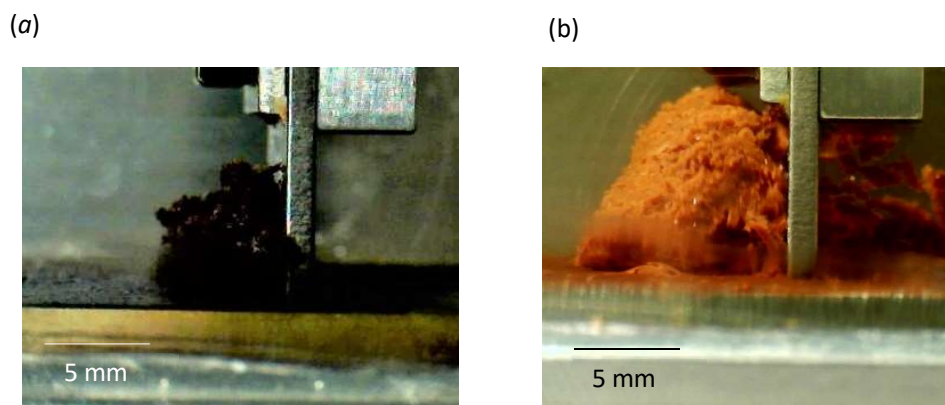


Figure 7.5: Side-on view of the removal of an example of (a) dry soil and (b) soil immersed in surfactant solution. Identical CMS with differences in lighting conditions due to submersion in solution causing apparent colour differences.

The importance of mechanical action is demonstrated by the presence of the residual material in region A and the original soil layer in region C. Both remained in place, unchanged, after soaking, indicating that the (weak) shear force associated with the flow of solution was not large enough to disrupt them.

The corresponding dry and soaked F_w profiles are shown in Figure 7.6. The dry profiles exhibit a cut-off at 430 N m^{-1} , which corresponds to the maximum force that could be measured for this setting of the transducer (see Figure 7.2(b)). The range can be extended by adjusting the transducer position, at the expense of reducing the sensitivity for weaker layers. The oscillations evident in the dry F_w profiles arise from the cracked nature of the soils, giving inhomogeneous coverage. Regions free of deposit did not contribute to the force on the blade, and the periodicity was roughly consistent with the average measured crack spacing of 2.3 mm (Chapter 3). The average value of F_w for dry samples was consistent between tests, at approximately 400 N m^{-1} (1 s.f.). This is comparable with the $\langle F_w \rangle$ values reported by Ali *et al.* (2015(c)) for baked lard (up to 430 N m^{-1} for soils cooked for 5 hr at 220°C).

The F_w profiles for samples soaked at pH 10 at room temperature in Figure 7.6 (b) show similar oscillation, associated with inhomogeneous coverage, and a general reduction in absolute amplitude with time. The relative amplitude of oscillation is consistent at approximately 20 % of the mean F_w value indicating the impact of the cracking is consistent over the test duration. The values are larger than those reported by Akhtar *et al.* (2010) and Bobe *et al.* (2007) of 0.1 – 0.3 and 1.3 N m^{-1} for fresh caramel and yeast layers, respectively. With extended soaking they approach those reported by Ali *et al.* (2015(c)) for unbaked oil soils with thickness ranging from 0.3 to 0.6 mm, of 0 – 20 N m^{-1} .

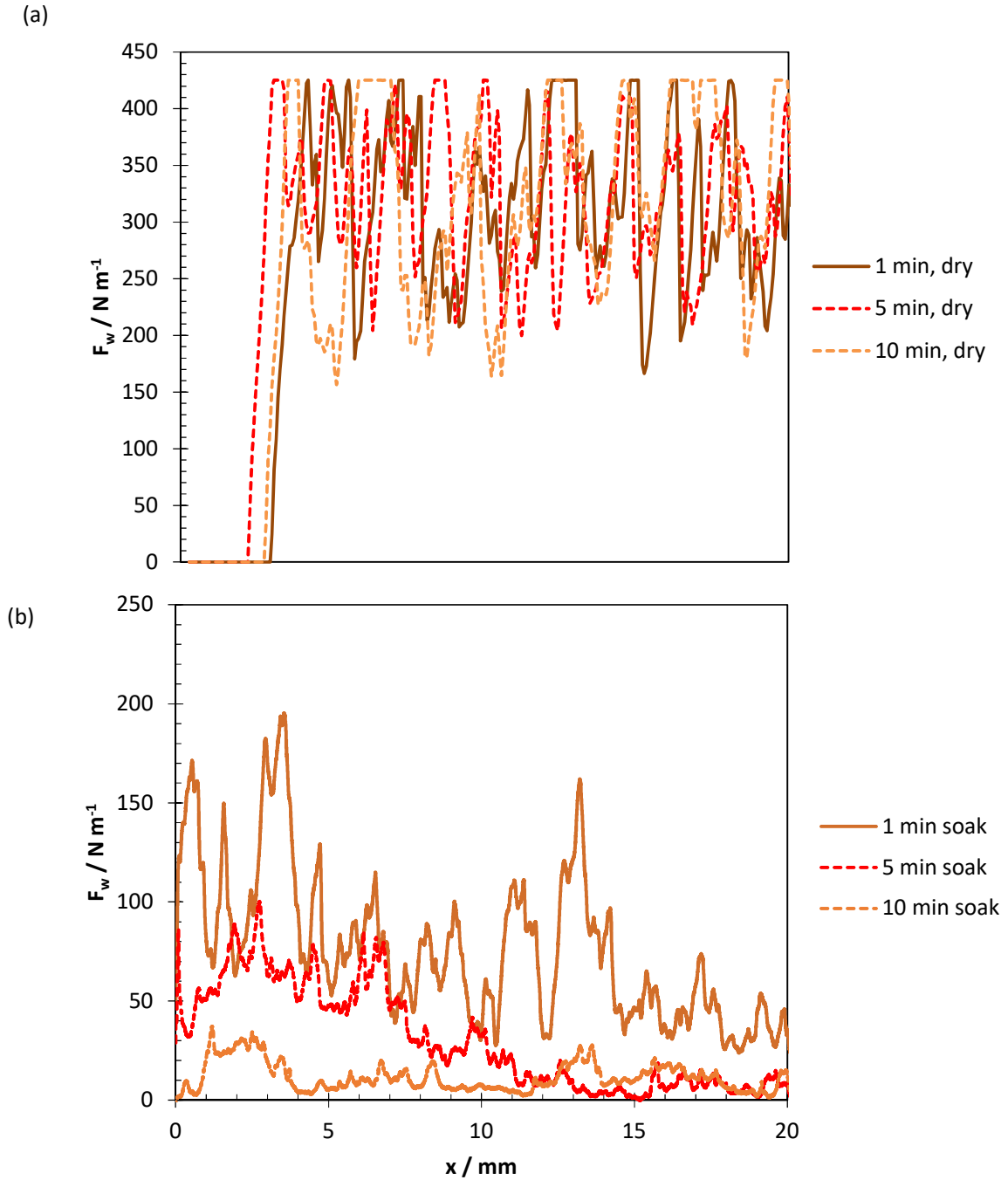


Figure 7.6: F_w profiles (a) before (region A in Figure 7.4) and (b) after soaking in 1 wt.% SDBS solution at pH 10 at room temperature (region B in Figure 7.4). The transducer range sets a limit on F_w of 430 N m^{-1} causing the truncation in (a). Legend denotes start time of the test. $V = 0.1 \text{ mm s}^{-1}$

The average F_w value is plotted against soaking time in Figure 7.7, normalised by the dry value. After 10 minutes of soaking there was virtually no variation in $\langle F_w \rangle$. Much of the weakening of the adhesive forces occurred within the first 10 minutes of soaking, and there is a noticeable reduction in F_w for the test started after 5 minutes of soaking, indicating that changes were occurring over this timescale.

Subsequent testing focused on shorter soaking periods, measuring F_w continuously for 500 s after the soil contacted the solution.

Figure 7.7 also shows the average $\langle F_w \rangle$ values measured after soaking in 1 wt% SDBS solution at the same temperature and pH. There is no significant effect of this anionic surfactant, as both data sets exhibit an almost exponential decay to $\langle F_{w,wet} \rangle / \langle F_{w,dry} \rangle = 0.05$ after 10 minutes. The $\langle F_w \rangle$ value obtained with SDBS after 60 minutes was larger than at 10 minutes, which was attributed to this sample having swollen more and having absorbed more water. Similar results were obtained for SDBS solutions at pH 11 and 12 (not shown).

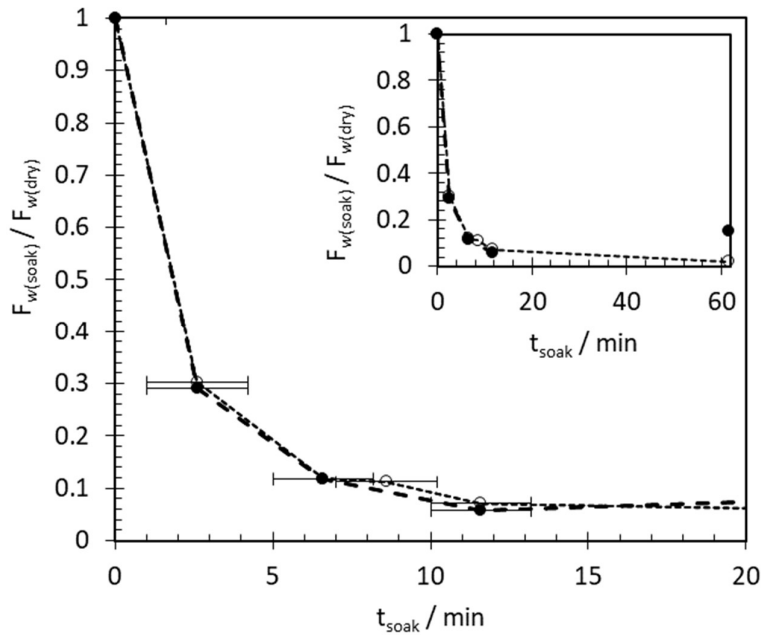


Figure 7.7: Effect of soaking at pH 10 at room temperature with (solid circles) and without 1 wt.% SDBS (open circles). Insert: full data containing 60 min data points. Error bars show time scale of averaged data points.

Preliminary studies (Figure 7.7) show the surfactant solution does not appear to have an impact on the soaking time required for effective cleaning of the CMS under these conditions. Variability in the results due to the increased roughness of the CMS layer is expected. After 10 minutes soaking the forces required to remove the CMS layer are small.

7.1.3 Impact of drying

The reduction in $\langle F_w \rangle$ upon wetting was shown to be a reversible process. These tests were conducted after refinement of the MM3 sample preparation technique CMS. The refined soils gave lower, more consistent $\langle F_w \rangle$ values (Figure 7.8 (a)). The CMS samples were immersed in 1 wt.% SDBS solution at pH 7, 20 °C for 30 minutes. The samples were then removed and dried in air for $t_{dry} = 0, 15, 30, 60, 120$

and 180 minutes. Figure 7.8 shows that $\langle F_w \rangle$ recovered to 140 N m^{-1} , which is similar to the value for the dry samples for this batch of CMS.

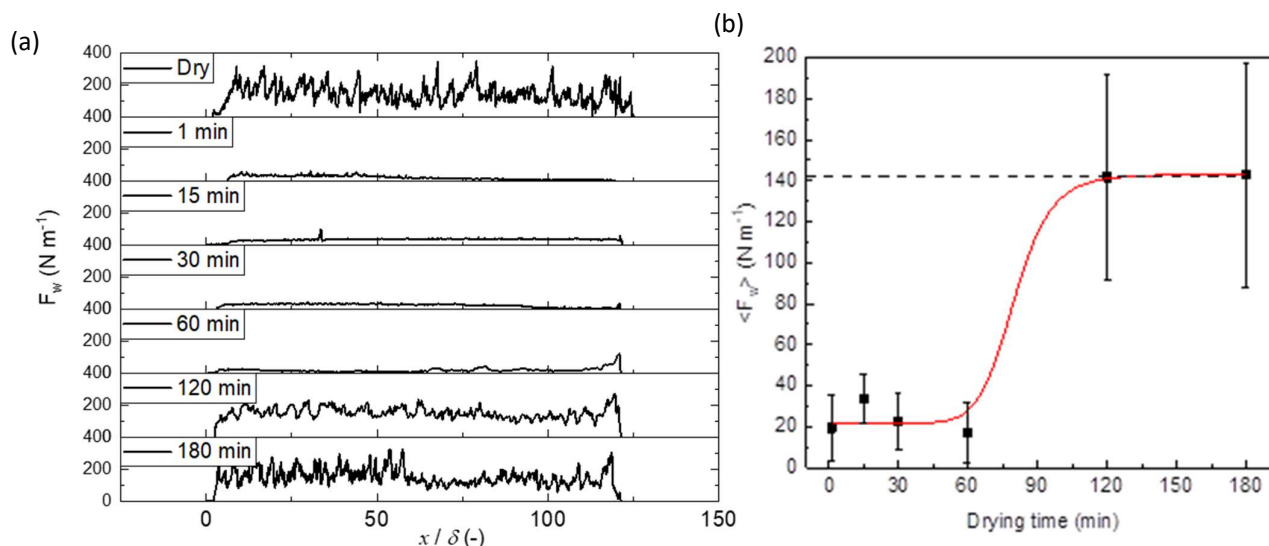


Figure 7.8: Effect of air drying at room temperature after soaking for 30 minutes in 1 wt.% SDBS solution at pH 7. (a) Representative plots of CMS plates dried in air for 1, 15, 30, 60, 120 and 180 minutes. (b) Average force of removal per unit blade width. Dashed line is a dry reference sample. The line shows a generalised logistic function fitted to the data. Error bars show standard deviation of the F_w within each sample.

7.2 Development of a flow system for the MM3

7.2.1 Experimental set-up

One difference between the zFDG described in Chapter 5 and the MM3 tests is the fact that in the MM3 the solution was static whereas in the zFDG there is fluid motion. This mimics the procedure performed in households of soaking dishes with troublesome soiling layers prior to placing them in the dishwasher. It is this step that is intended to be minimised by the project sponsors. A commercial dishwasher uses around 12 L/cycle (Rosa *et al.* 2012) of cleaning solution. The concentration of surfactant and $[\text{OH}^-]$ will decrease over time. To mimic this, a flow system was set up to allow for a larger volume of solution to be circulated whilst the sample was located within the MM3 chamber. This removed the need for manual removal and replacement of either the cleaning solution or the soiled substrate.

Figure 7.9 shows the millimanipulation device (Figure 7.2) modified to include a solution circulation system. A stirred 1 litre jacketed vessel served as the solution reservoir. Liquid is delivered at a set flow rate by a peristaltic pump to the base of the sample chamber (total volume of $D + B = 1.5 \text{ L}$, Figure 7.9 (b)). The solution passes across the chamber and leaves via the outlet located on the far wall before draining back to the reservoir under gravity. The reservoir contents are heated by recirculation of hot

water through the jacket. The temperature of the solution is monitored by a thermocouple located in the sample chamber. Changes to solution composition are made in the reservoir. The volume of solution held in the chamber after locating the sample is approximately 87 ml.

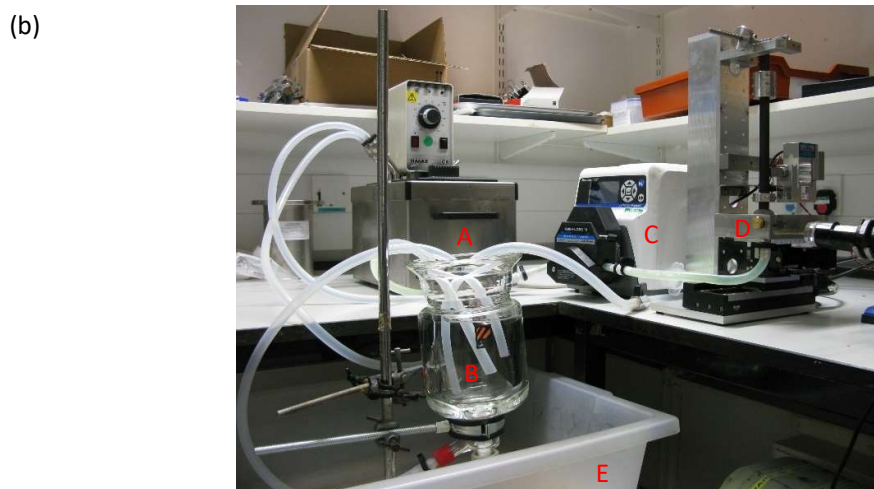
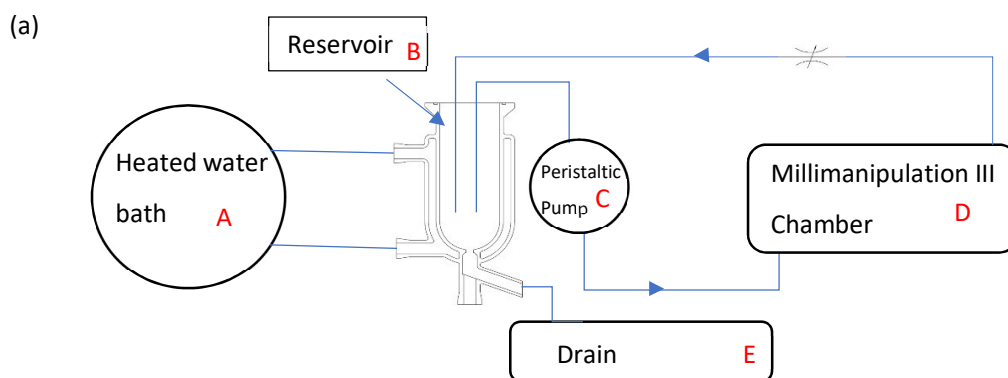


Figure 7.9: (a) schematic and (b) photograph of flow system for MM3. A – heater-circulator water bath, B – solution reservoir, C – peristaltic pump, D – sample chamber, E – Drainage system. Labels on photo correspond to items in schematic.

The tests reported here featured a solution flow rate of 100 ml min^{-1} , giving a space time in the chamber of approximately 53 s. The time taken for a change in solution chemistry to take effect in the chamber was determined by a simple residence time test whereby the conductivity of the solution in the reservoir was altered by adding a 10 mL dose of 1 M NaOH and monitoring the conductivity of the liquid leaving the chamber. Figure 7.10 shows that breakthrough is observed after approximately 30 s, followed by a two-step change in conductivity which could be modelled approximately as plug flow over the top of the sample in parallel with a mixing element. The inset in Figure 7.10 shows that the change in conductivity was complete after 150 s at this flow rate.

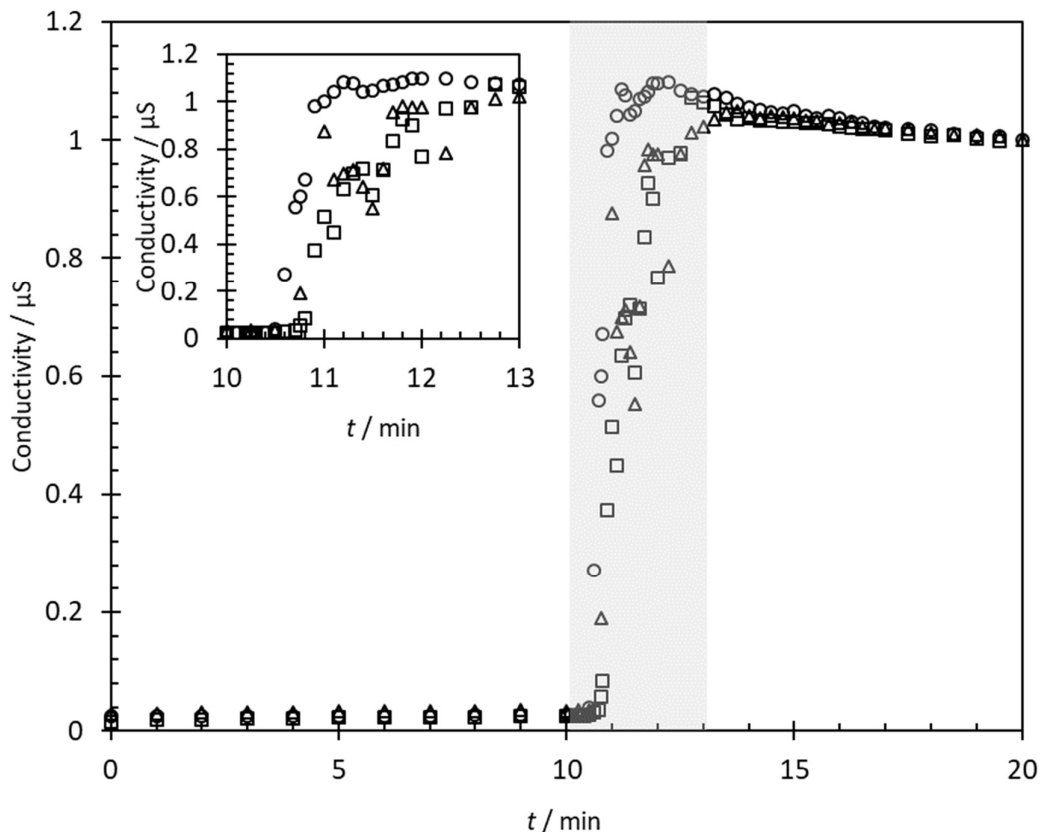


Figure 7.10: Conductivity of solution leaving test chamber before and after addition of NaOH solution to the reservoir at $t = 10$ min. Data from three repeats. The grey area indicates the section plotted in the inset. Solution flow rate 100 mL min^{-1} .

7.2.1 Flow system test protocol

Cleaning solution was initially circulated through the empty chamber to bring it to the required temperature. Flow was then stopped, the solution allowed to drain, the dry sample swiftly mounted in place, and the millimanipulation blade located to pass over the substrate with a $50 \mu\text{m}$ gap. Solution was then reintroduced and pumped through the chamber at a rate of 100 mL min^{-1} . Once the surface of the layer was immersed, the blade motion was initiated. The blade moved across the sample at velocity V_B for a set time t_s to give a total displacement $X = V_B t_s$. In these tests V_B was 0.1 mm s^{-1} and the force on the blade was recorded at 151 Hz . For ease of plotting, the data are truncated on a 1:100 basis.

7.2.1.2 Test solutions in flow system

Tests solutions were prepared in batches using 1 L deionised water and the pH adjusted to 7, 9 or 12 using 1 M aqueous NaOH. Surfactant solutions were prepared at $1 \text{ wt.}\%$ loading using sodium dodecyl benzene sulfonate (SDBS, anionic, critical micelle concentration (CMC) 0.1 g L^{-1} (Sanz *et al.* 2003), hexadecyltrimethylammonium bromide (CTAB, cationic, CMC 0.334 g L^{-1} (Previdello *et al.* 2006), and

t-octylphenoxy polyethoxyethanol (TX-100, non-ionic; CMC 0.0131 g L⁻¹ (Ruiz *et al.* 2001). All solutions therefore featured surfactant concentrations above their CMC. The mixtures were prepared by stirring at 50 °C for 30 minutes before being left to cool to room temperature.

7.2.2 Results and Discussion

7.2.2.1 Effect of solution temperature

Figure 7.11 (a) shows examples of removal profiles obtained with no pre-soaking in water at pH 7 and 20 °C, with no surfactant present. The initial F_w values are noticeably smaller than the average of 400 N m⁻¹ for dry deposits evident in Figure 7.6 (a). This arises from the nature of the layer at the edge of plates differing from that in the interior. When the slurry is applied to the plate the layer is pinned at the edges so the layer is thinner there and subject to a different drying and baking history. Data obtained for $t < 40$ s (labelled A on the Figure) and $t > 460$ s (labelled D) were therefore excluded from comparisons.

It is evident that stage A masks a rapid reduction in removal force caused by hydration following initial contact with solution. The F_w values measured after 60 s (stage B) lie in the range 100 – 150 N m⁻¹, which is larger than that observed at pH 10 (Figure 7.6): the effect of pH is discussed in the next section. In stage B there is a slow decrease in F_w with time which in Figure 7.11 (a) is masked by the scatter in the data: this feature is clearer in Figure 7.11 (b), obtained at 50 °C, and subsequent plots.

After 360 s at 20 °C, there is a transition to a faster decay in F_w (labelled stage C): the transition time is labelled t_c . At 50 °C, Figure 7.11 (b), $t_c \sim 220$ s and F_w decreases more quickly, with noticeably less scatter. The data could be fitted to an exponential decay expression with characteristic decay time, D , $\sim 125 \pm 3$ s, as well as less scatter.

The photographs in Figure 7.11 show that the transition is accompanied by a change in the amount of soil remaining on the substrate, with a significant fall in residual material after t_c . These findings indicate that the adhesion of the soil to the substrate changes at t_c : the soil is still removed as a coherent layer, with cohesion within the soil (which may be decreasing due to the uptake of water) stronger than the adhesion to the substrate.

The B/C transition is more likely to arise from water penetrating through the soil (*i.e.* related to absorption and diffusion) rather than being due to ingress of water at the soil-substrate interface. The latter would start as soon as there was contact with solution via the network of cracks in the layer.

Figure 7.11 confirms that temperature is an important parameter in cleaning of the CMS material, as Sinner's circle indicates. 50 °C is a standard operating temperature in domestic dishwashers, though

it can take some time for the machine to reach 50 °C. This temperature is above the temperature estimated for the fat-rich phase in the CMS to become more fluid. The time taken for a 200 μm thick soil layer to reach 50 °C after contacting the solution can be estimated by considering conduction through a slab of baked material with a thermal diffusivity of $2 \times 10^{-7} \text{ m}^2/\text{s}$ (Rask, 1989). This gives a heating time of order 1 s, which is negligible. The initial F_w values are larger at 50 °C than at 20 °C (but subject to considerable scatter), which may be due to faster swelling. The B/C transition occurs earlier, which is consistent with faster diffusion, while the presence of mobile fat is likely to facilitate adhesive failure. A pseudo-exponential decay in stage C was not observed at 20 °C. This may be because the solution was not in contact with the solution for long enough at this lower temperature.

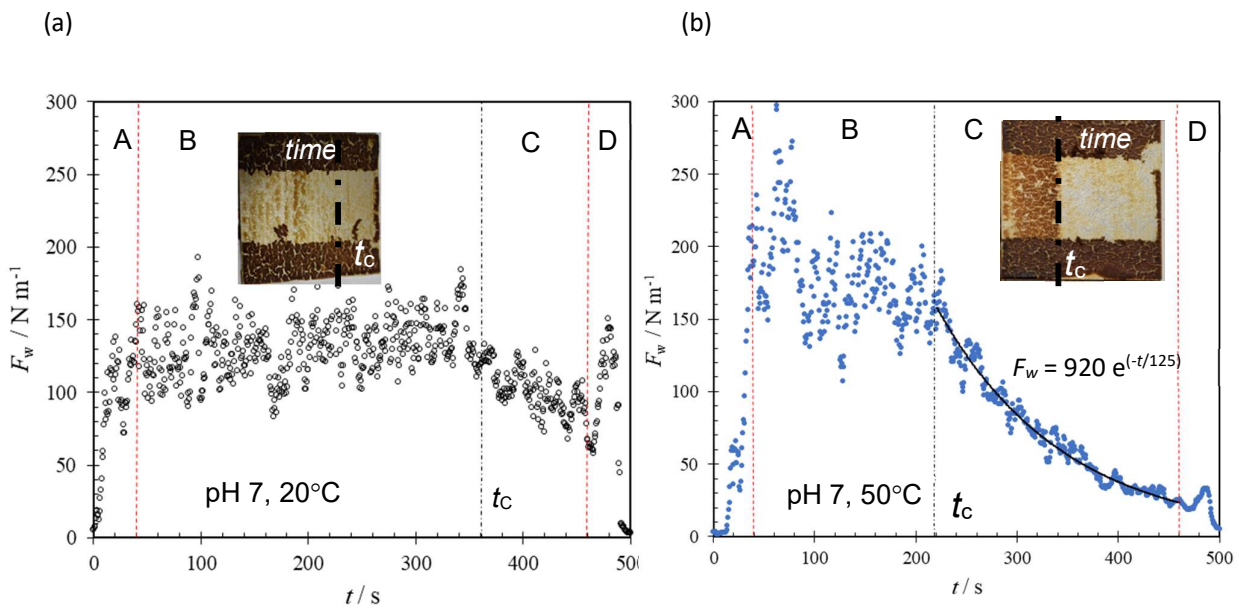


Figure 7.11: Effect of temperature on removal force following contact with pH 7 solution at $t=0$ at (a) 20 °C; (b) 50 °C. Dashed vertical lines mark initial and final regions subject to edge effects from material baking whilst pinned at the edge of the sample plate. This data is therefore discounted, the indicators are repeated in subsequent plots. Vertical dot-dashed lines speculate on location of B/C transition observed at time t_c : photograph insets show the plate after testing. Solid line in (b) shows fit to exponential decay $F_w = 920 \exp[-t/125]$.

7.2.2.2 Effect of solution pH

The impact of pH on removing CMS layers was investigated primarily with water at pH 7 and aqueous NaOH solutions (pH 9 and 12) at 20 °C and at 50 °C.

Figure 7.12 shows that pH had little influence at 20 °C. The removal profiles are similar, with initial F_w values following hydration between 140 and 200 N m^{-1} , followed by a slow linear decay. The B/C transition evident at pH 7 was not observed at pH 9 and occurred later, around 410 s, at pH 12. As a

result the non-edge data were fitted to a simple linear trend: the decay rate was greatest at pH 9. Chapter 5 showed that considerable swelling of the soil occurs during the first 500 s however at 20 °C this did not appear to significantly influence the F_w . The relationship between swelling and F_w is discussed in Chapter 8.

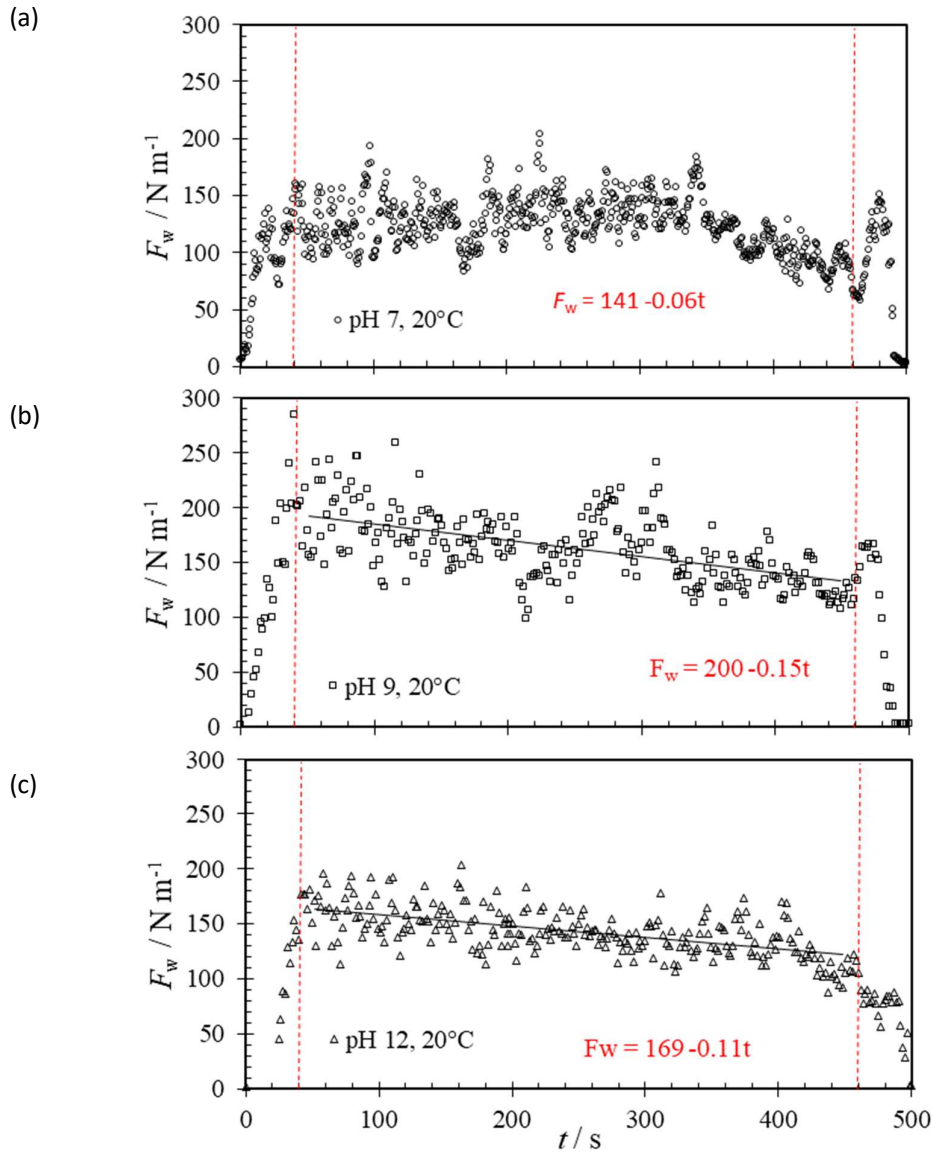


Figure 7.12: Effect of pH on removal profiles at 20 °C. Solid loci show linear regression to data in the range $50 < t < 350$ s. Vertical dashed lines mark initial and final regions subject to edge effects.

The removal profiles at 50 °C at pH 9 and pH 12 in Figure 7.13 do not show the marked transition evident at 220 s at pH 7 (Figure 7.11(b)). Decay profiles measured at pH 6 and 8 were similar to those at pH 7 (not shown). The initial F_w values are similar to those at 20 °C and the linear decay rates were faster at this higher temperature, at $0.51 \pm 0.01 \text{ N m}^{-1} \text{ s}^{-1}$ (pH 7) and $0.26 \pm 0.01 \text{ N m}^{-1} \text{ s}^{-1}$ at pH 9 and

12. Whereas F_w decayed almost exponentially in stage C at pH 7, the decay at pH 9 is close to linear until $t \sim 420$ s and at pH 12 F_w does not decay strongly until around 300 s. The inset photographs as show a gradual change in residual soil on the substrate, which is consistent with the removal profiles.

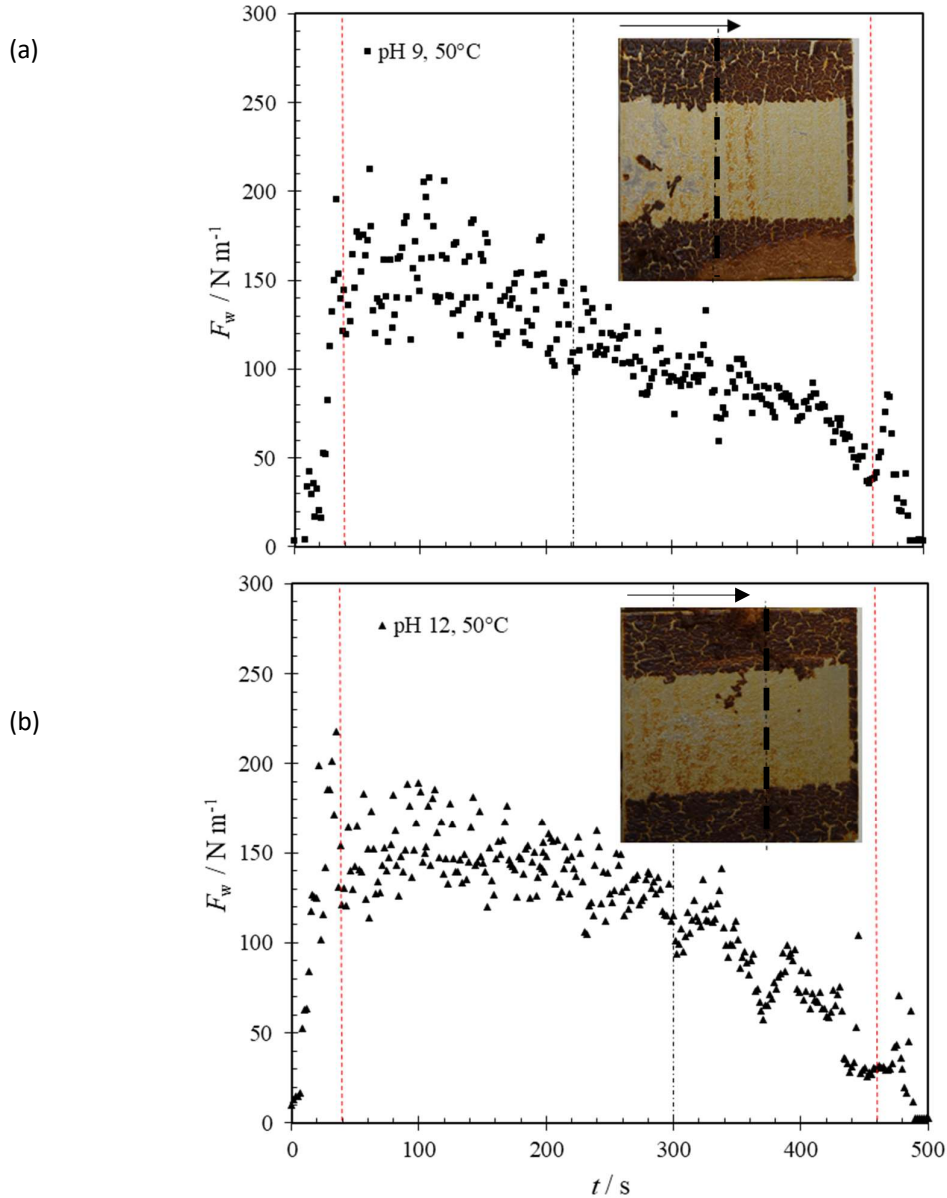


Figure 7.13: Effect of pH on removal profiles at 50 °C. (a) pH 9, (b) pH 12: pH 7 data given in Figure 7.11 (b). Vertical dashed lines mark region A and D (edge effects). Vertical dot-dashed lines speculate on location of B/C transition observed at pH 7 at 220 s. Photographs show substrate after testing.

The effect of alkali at 50 °C is unexpected, as higher pH often accelerates cleaning of proteinaceous food soils (Morison and Thorpe, 2002; Fryer and Asteriadou, 2009), although some proteinaceous soils exhibit an optimal pH in alkaline cleaning (Mercade-Prieto *et al.*, 2006). In the absence of surfactants

the cleaning agents active in this case are water (hydrating starch and proteins, dissolving soluble components), hydroxyl ions (indicative of pH) and Na⁺ counterions (both of which contribute to ionic strength/osmotic effects). Alkali conditions are known to cause unbaked protein layers to swell and promote erosion at the soil-solution interface (Tuladhar *et al.*, 2000; Christian and Fryer, 2006). Swelling would be expected to enhance transport of water to the substrate/soil interface and weaken the soil adhesion. Similarly, Otto *et al.* (2016) reported that unbaked starch deposits are expected to become more negatively charged at high pH and therefore be repelled from stainless steel surfaces which are similarly charged under these condition (isoelectric points typically pH 4-5 for 304 stainless steel (Lefèvre *et al.*, 2009) and 5.1 for starch from wheat flowers (Kemp, 1936).

The results indicate that the hydroxyl ions are retarding the weakening of the adhesive interactions, which could be due to hydrolysis of the fats or inhibiting the mobility of the mobile fat phase, thereby retarding the access of water to the soil-substrate interface. The material at the interface is a complex mixture which has been subject to the oven temperature for 7 minutes (as a result of fast conduction through the steel). Further work is required to identify the components and processes active at this interface.

7.2.2.3 Effect of surfactant

The effect of 1 wt.% surfactant was studied at pH 9 at 20 °C and 50 °C, representing standard dishwasher operating conditions. Figure 7.14 shows that the non-ionic (TX-100) and anionic (SDBS) surfactants gave no enhancement in removal, with similar changes in F_w over the test period (linear decay rates of $0.14\text{-}0.15 \pm 0.01 \text{ N m}^{-1} \text{ s}^{-1}$). This is consistent with Figure 7.12 (pH 9 and 20 °C). This finding could be explained by the surfactant acting via an erosive/emulsification cleaning mechanism. Erosive cleaning has been shown by Gillham *et al.* (1999) and Chen *et al.* (2012) to be less effective for burnt materials due to their increased cohesive strengths and cross-linked polymeric structures relative to their unburnt counterparts.

In contrast the cationic agent, CTAB had immediate impact, giving almost exponential decay behaviour (initial decay rate $0.42 \pm 0.01 \text{ N m}^{-1} \text{ s}^{-1}$), similar to pH 7 at 50 °C, and without an evident B/C transition. The latter transition could have occurred at $t < 40 \text{ s}$, suggesting that either (i) CTAB aided the penetration of water through the soil to the substrate, and/or (ii) the reduction in adhesion was caused by ingress at the soil-substrate interface via the many cracks present in the soil layer. The photograph of the cleared region shows little residual material on the substrate, confirming that CTAB had promoted adhesive failure. The enhanced penetration of the cleaning solution is also consistent with findings in soil image analysis that shows that CTAB generated many small droplets of oil rapidly

after submersion in the cleaning solution. The ability of CTAB to promote removal at room temperature brings immediate advantages in terms of energy consumption.

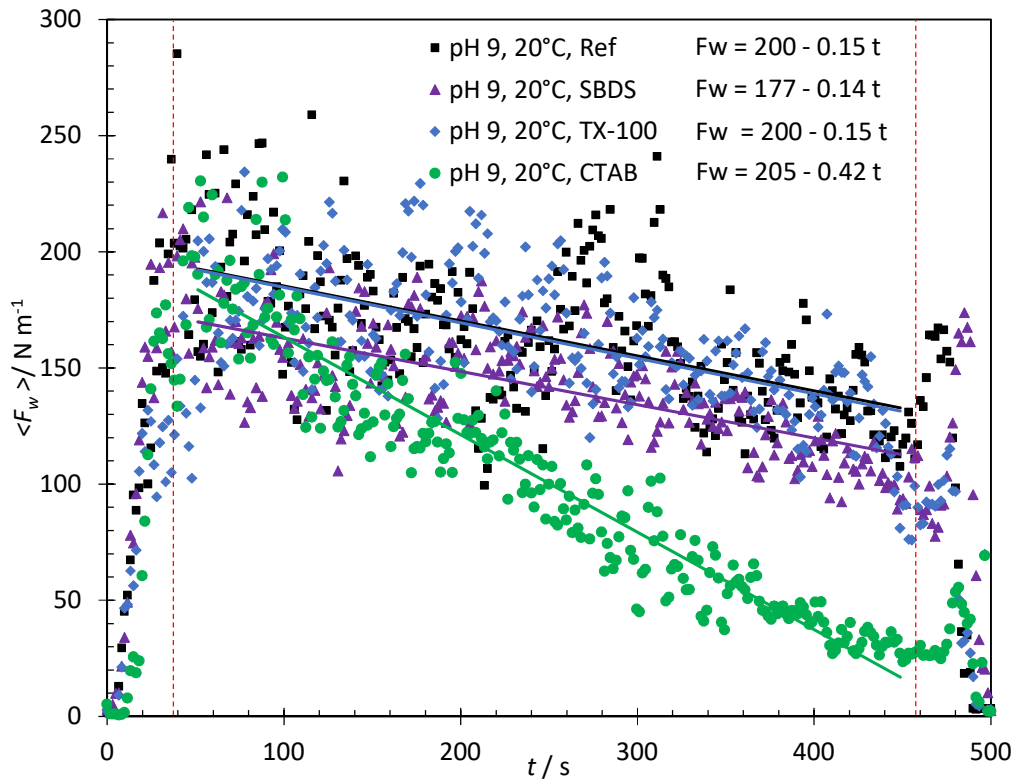


Figure 7.14: Effect of surfactant on removal force at 20 °C. Soil is contacted with pH 9 solution at $t = 0$. Lines show linear regression to data in the range $50 < t < 350$ s. Vertical dashed lines mark initial and final regions subject to edge effects.

Figure 7.15 shows that all three surfactants promoted removal at 50 °C at pH 9 compared to a simple alkaline solution. The removal profile for CTAB (Figure 7.15 (a)) is similar to that at 20 °C: fitting the data sets to simple exponential decay relationships gave an exponential decay time, $t_D = 213 \pm 4$ s and 238 ± 5 s at 20 °C and 50 °C, respectively. Temperature does not appear to have affected the CTAB mechanism. Determining the mechanism involved requires further work, but two possible explanations are (i) the cationic surfactant being attracted to the negatively charged starch-based moieties within the soil at pH 9; and (ii) the cationic surfactant having greater affinity for the stainless steel surface (which acquires a negative charge at pH 9), disrupting the adhesive bonding between the soil and the substrate at the interface and therefore lowering F_w even at room temperature. Hypothesis (ii) could be tested by using substrates with a different IEP but similar surface energy and heat conduction properties. Hypothesis (ii) suggests that the effectiveness of a CTAB-based formulation in practice would vary between surfaces.

The removal profiles for TX-100 and SDBS are both similar to that for water at pH 7, 50 °C (Figure 7.11 (b)), but with earlier B/C transition: t_c for TX-100 is markedly shorter, at approximately 80 s, while F_w

decays more rapidly than with CTAB, with $t_D = 139 \pm 3$ s. SDBS behaviour is very similar to the surfactant-free solution until $t_c = 200$ s, after which F_w decays exponentially, unlike the alkaline solution, with $t_D = 120 \pm 3$ s. The final F_w values for TX-100 and SDBS (*i.e.* at $t = 460$ s) are both smaller than that observed with CTAB.

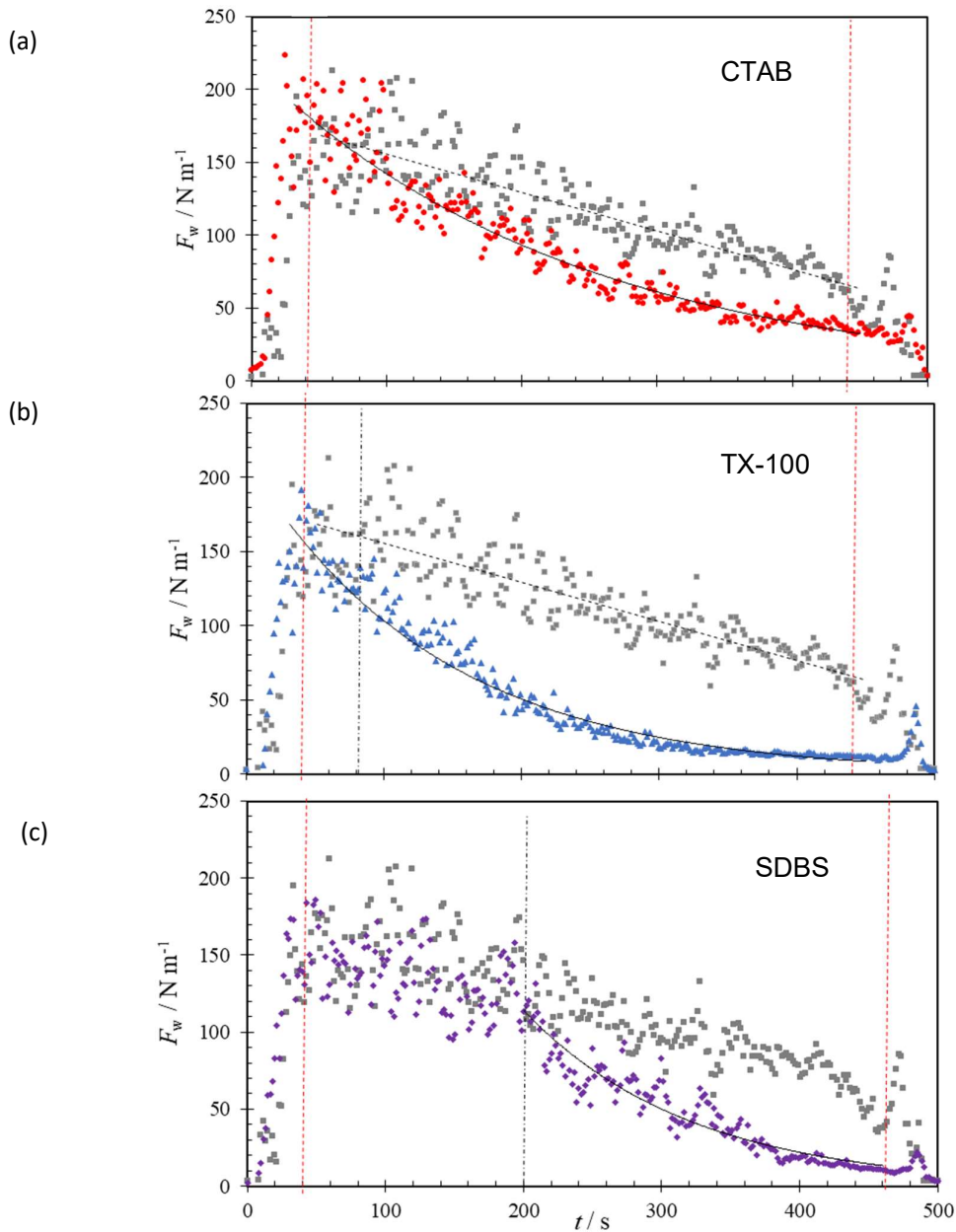


Figure 7.15: Effect of 1 wt.% surfactant on removal profiles at pH 9 and 50 °C. (a) CTAB, (b) TX-100, (c) SDBS solution. Grey symbols show profile obtained without surfactant common to each plot. Vertical dashed lines mark initial and final regions subject to edge effects. Vertical dot-dashed lines speculate on location of B/C transition observed. Solid lines show fit of data in stage C to a simple exponential decay.

The decay behaviours and decay rate parameters are summarised in Table 7.1. The existence of the B/C transition, faster decays and lower final F_w values all indicate that a different mechanism is involved in softening of the soil layer by the non-ionic and anionic surfactants.

Table 7.1: Summary of rate of change of adhesion forces over 500 s testing. Uncertainty parameters based on one standard deviation.

pH	surfactant (1 wt%)	t_c		linear decay rate		t_D	
		/s		/N m ⁻¹ s ⁻¹		/s	
		20°C	50°C	20°C	50°C	20°C	50°C
7	-	-	220	0.06±0.007	0.51±0.01	-	125±3
9	-	-	220	0.15±0.02	0.26±0.01	-	-
12	-	-	300	0.11±0.01	0.26±0.01	-	-
9	SDBS	-	200	0.14±0.01	0.41±0.01	-	120±3
9	CTAB	40	40	0.42±0.01	-	213±4	238±5
9	TX-100	-	80	0.15±0.01	-	-	139±3

The reason why TX-100 and SDBS promote behaviour observed at pH 7, essentially inhibiting the effect of higher pH, is now considered. SDBS will increase the solution ionic strength, while TX-100 will have little effect on this quantity. The observation that these surfactants are not effective at 20 °C, when the fat phase is immobile, indicates that the mechanism is linked to the solubilising of fat globules present in the soil. Non-ionic surfactants are known to be effective at removing oily soils from synthetic fibres (Williams, 2007), whereas anionic surfactants are effective at removing (positively charged) particles. Since the fat slows the ingress of water through the soil matrix, agents which promote the removal of this phase will enhance penetration of water and hydration at the soil-substrate interface. Removal of the oil phase will also affect the rheology of the hydrated soil, which will be manifested in the cohesive contribution to the force measured by the millimanipulation blade. This mechanism would not be directly affected by the nature of the substrate to the same degree as that promoted by CTAB. The substrate would have an indirect effect in terms of wetting characteristics towards components in the soil, heat transfer etc. and therefore microstructure of the fouling layer at the soil-substrate interface (see Magens *et al.*, 2017).

These results demonstrate how the different agents effect cleaning, reducing the strength of the soil at the soil-substrate interface via different mechanisms. The same length of time may be required to

remove the CMS layers studied here from a stainless steel surface, but knowledge of the mechanisms – whether ingress or penetration – allows one to gauge whether or not the agent will give similar efficacy for other soils on different substrates.

The cleaning mechanism and behaviour is ultimately determined by the nature and microstructure of the soil. For example, Ali *et al.* (2015(a)) studied the cleaning of polymerised lard soil layers on stainless steel and reported that solutions of TX-100 and LAS at pH 10.4-11 promoted solution ingress and soil detachment at the lard soil-substrate interface, while CTAB promoted penetration through the soil layer: with CMS CTAB promoted ingress. These differences illustrate how, like coatings to prevent deposition and fouling, detergent solutions need to be matched to the soil and substrate.

7.3 Conclusions

Millimanipulation was used to investigate the mechanical aspect of cleaning of burnt complex soils as a function of soaking time and solution composition. The millimanipulation technique was modified to allow the forces at the soil-substrate interface to be measured whilst being immersed and soaked in cleaning solutions in real time. The complex model food soil tested comprised burnt fats, starch and proteins in a cracked layer on stainless steel. It was not possible to prepare uniform thin layers of this soil. The adhesion forces decreased noticeably on hydration.

The soils exhibited cohesive or adhesive failure during removal, depending on the cleaning agent. Temperature had a uniformly beneficial effect on cleaning, with water at pH 7 at 50 °C exhibiting a transition between cohesive and adhesive failure after an initial soaking period. The length of this initial soaking period was reduced when TX-100 or SDBS was present. This behaviour is attributed to the fat in the soil being mobile at 50 °C. CTAB, the cationic surfactant, promoted adhesive failure at 20 °C and 50 °C, indicating that its action involved a different removal mechanism.

The pH of the solution had little influence at 20 °C. At 50 °C, high pH gave slower cleaning than at pH 6-8, even though alkaline conditions promoted swelling and weakening of proteins in the deposit. All three surfactants studied promoted removal at high pH, with TX-100 giving greatest reduction in soil strength. The results provide quantitative evidence that different cleaning mechanisms are promoted by the different cleaning agents, and allow their role in Sinner's circle to be quantified in terms of the extent and rate of change of the soil-substrate interactions.

7.4 Timescales of cleaning

Here the timescale of cleaning was primarily dependent upon the surfactancy of the solution. In static pH 7 water a weak B/C transition, indicating the onset of cleaning, was observed after 360 s. Increasing the temperature of the solution from 20 °C to 50 °C increased the degree of the inflection

whilst also reducing the onset to 320 s. $\langle F_w \rangle$ then decreased, with a rate constant of $k'_{MM3} = 0.06 \text{ s}^{-1}$ at 20 °C and 0.51 s^{-1} at 50 °C. The most effective solution considered of 0.1 wt.% TX-100 at 50 °C has a B/C transition after 80 s and $\langle F_w \rangle$ decay with a rate constant of $k'_{MM3} = 6.1 \text{ s}^{-1}$. These time scales are faster than those observed for both swelling and oil release, indicating either that the reduction in adhesive and cohesive strength of the soil is a function of solely of soil wetting and occurs during the swelling of the soil, before it reaches its maximum height, or that the forces on the MM3 are bigger than those exerted by a flowing liquid.

8. Data fusion

The wetting of food soils, even in the absence of alkali, enzymes and surfactants, has long been understood to promote effective cleaning. The dominant mechanisms for common soil types, e.g. roll-up for oil films, have been established. The factors that determine the dominant cleaning mechanism are often related in terms of Sinner's cleaning circle, where the temperature and chemical composition of a solution, in combination with imposed mechanical forces, govern the time taken for sufficient decontamination to take place.

In the case of burnt food soils containing a mixture of components, such as the burnt CMS studied here, the mechanism(s) of action is less clear. The promotion of a single mechanism has been proven not to be effective at removing these soils within the bounds of mechanical action generated in consumer dishwashing devices. Several processes are involved in the removal of CMS from the substrate. The cleaning mechanisms may act in series, one step following the other, or in parallel, synergistically or antagonistically. The levers dictated by Sinner's Circle promote each mechanism to a different extent, over different timescales.

Four techniques were used in this work to monitor how the time in contact with a cleaning solution, of fixed temperature and chemistry, affect the mechanical force required to remove the soil from the substrate. The change in soil volume and solution composition was measured separately. This information can be used to identify formulations which could give faster cleaning.

8.1 Techniques

The techniques used were: (i) millimanipulation (MM3), used to monitor the change in adhesive strength between soil and substrate (as well as soil cohesion); (ii) sideways zero discharge fluid dynamic gauging (SiDG), quantifying the swelling behaviour under shear and in static conditions; and two oil collection techniques, namely (iii) bulk oil recovery, measuring carbonaceous material that has been transferred into solution, (Labelled: Oil R); and (iv) image analysis of mobile soil components that form droplets on the soil surface (Labelled: Oil M).

8.2 Collation of data

For ease of comparison data are presented as evolution of the measured quantity in scaled form, along with the fitted kinetic model, *i.e.*

$$\text{Millimanipulation: } \frac{\langle F_w \rangle}{\langle F_{w,max} \rangle} \quad \langle F_w \rangle = \langle F_{w,max} \rangle - k'_{MM3} t \quad \text{Equation 8.1}$$

$$\text{SiDG: } \frac{\delta - \delta_0}{\delta_{max}} \quad (\delta - \delta_0) = \Delta\delta_{max}(1 - e^{-k_{SiDG}(t-t_0)}) \quad \text{Equation 5.8}$$

$$\text{Oil recovery: } \frac{TOC}{TOC_{max}} \quad (TOC - TOC_0) = TOC_{max}(1 - e^{-k_{TOC}(t-t_0)}) \quad \text{Equation 6.12}$$

$$\text{Image analysis: } \frac{d}{d_{max}} \quad (d_j^* - d_0^*) = d_{j,max}^*(1 - e^{-k_{droplet}(t_{adj})}) \quad \text{Equation 6.33}$$

Equation 6.33 was used to back-predict the onset of droplet formation as this could not be determined directly owing to the detection limit of the image analysis software (See Figure 8.1). Oil recovery data were not available for 0.1 % TX-100 solutions due to failure of the TOC equipment. Furthermore, as explained in Chapter 6, image analysis testing for surfactant solutions was conducted at 0.01 wt.% (all other tests conducted at 0.1 wt.% surfactant). At higher concentrations the droplets formed were too small and grew too fast for the image analysis method.

The kinetic parameters are summarised in Table 8.1. The individual values have been discussed in previous chapters.

8.3 Results and Analysis

Figure 8.1 shows the evolution of the four parameters for the base case, namely soaking in pH 7 water at 50 °C. This demonstrates the importance of monitoring different factors in identifying and linking chemical and physical phenomena that occur following contact with the cleaning solution. Significant changes to the soil's adhesion strength, thickness, and composition all occur within the first 900 s of contact.

The particular region of interest in this case is 0 – 500 s. A significant drop in adhesion strength ($MM3$, $\langle F_w \rangle_{500s} = 0.1 \langle F_w \rangle_0$, $k'_{MM3} = -0.51 \text{ s}^{-1}$) coincided with the approach to the swelling plateau (SiDG, $t_{asym} = 800 \text{ s}$) and the appearance of droplets on the soil surface ($t_{droplet, onset} \approx 700 \text{ s}$). Oil droplets large enough to be detected by the image analysis software did not appear until $\sim 960 \text{ s}$ after submersion, when most of the swelling had taken place. The transfer of carbonaceous material into the bulk solution, which here is taken as an overall indicator of the removal of soil, is seen in Figure 8.1 to be a more gradual process than either the weakening of the adhesive forces, or penetration of the solution into the CMS.

Table 8.1: Summary of kinetic constants and timescales obtained from the different measurement techniques.

(i)	Millimanipulation	SiDG	Droplet Imaging	Solution analysis	MM3	Droplet Imaging	SiDG	Droplet Imaging	Solution analysis
	$Linear\ k'_{MM3}$	k_{SiDG}	$k_{droplet}$	k_{TOC}	t_c	t_{onset}	t_{asym}	t_{asym}	t_{asym}
	/ s^{-1}	/ $10^{-3} s^{-1}$	/ $10^{-3} s^{-1}$	/ $10^{-6} s^{-1}$	/ s	/ s	/ s	/ s	/ s
<i>pH 7 50 °C</i>	-0.51	3.26	2.8	0.54	220	960	800	2400	4800
<i>pH 7 45 °C</i>	-	-	2.3	0.37	-	840	-	2640	6300
<i>pH 7 40 °C</i>	-	1.58	1.8	0.36	-	1080	1000	2400	6000
<i>pH 7 35 °C</i>	-	-	1.3	0.34	-	960	-	3180	6600
<i>pH 7 30 °C</i>	-	4.03	-	0.13	-	-	700	-	>7200
<i>pH 7 22 °C</i>	-0.06	0.91	-	0.19	n/a	-	>1600	-	>7200
(ii)									
<i>pH 7 50 °C</i>	-0.51	3.26	2.8	0.54	220	960	800	2400	4800
<i>pH 8, 50 °C</i>	-0.26	3.4	2.5	-	160	780	700	2220	-
<i>pH 9, 50 °C</i>	-0.41	2.67	2.4	0.48*	220	600	600	1440	5400
(iii)									
<i>pH 7 50 °C</i>	-0.51	3.26	2.8	0.54	220	960	800	2400	4800
<i>0.1 % SDBS, 50 °C</i>	-0.41	2.09	3.3*	0.39	200	720*	800	1380*	6600
<i>0.1 % TX100, 50 °C</i>	-0.61	4.95	2.3*	-	80	540*	500	2580*	-
<i>0.1% CTAB, 50 °C</i>	-0.53	2.87	-	0.63	40	-	800	-	4200

* 0.01 wt.% surfactant was used in oil droplet imaging studies.

The transfer of material into the solution continued to occur even after the swelling and oil droplet formation had reached their limits ($t_{SIDG, asym} = 800$ s, $t_{SIDG, asym} = 2400$ s and $t_{TOC, asym} = 4800$ s). This sequence of events was observed for all conditions tested.

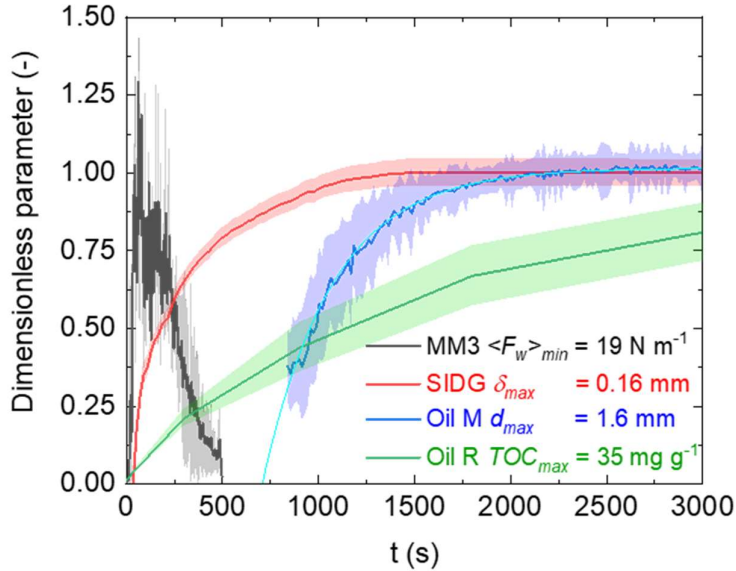


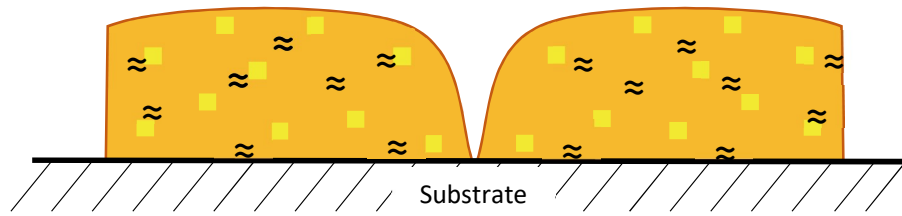
Figure 8.1: Data fusion plot for CMS submerged in deionised water at 50 °C. Data plotted as scaled parameters on the y-axis for millimanipulation (MM3), fluid dynamic gauging (SiDG), oil recovery via solution analysis (Oil R_B), and image analysis of droplet on the CMS surface (Oil M).

The sequence of events observed in Figure 8.1 can be rationalised mechanistically as follows. The dry soil, at room temperature (20 °C), can be considered to be a porous soil matrix of proteins and starches containing a multitude of solid fat inclusions (approx. 40 % of the soil) with a semi-permeable surface layer (due to increased exposure of the outer edges to heat and oxygen during baking). This ‘crust’ allows the penetration of water into the soil but is less or im-permeable to oils and fats (Figure 8.2 (a,i)).

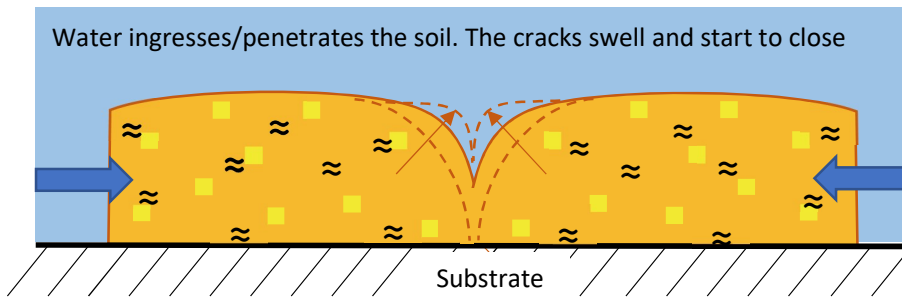
Immersion of the dry soil first results in hydration of the soil through an osmotic pressure difference between the soil and the surrounding solution (see SiDG, 0–60 s and Figure 8.2 (a, ii)). The absorption of water causes the soil to swell, both upwards, away from the substrate surface, and laterally into the soil cracks (Figure 8.2 (a,ii)). The uptake of water also alters the bulk rheology of the soil and weakens the adhesive bonds between soil and substrate, leading to a reduction in $\langle F_w \rangle$. As the warmed solution penetrates into the soil, it transfers thermal energy, melting the mobile fats and low molecular weight carbon chains (generated by thermal decomposition of starches, sugars, fibres and proteins during baking), creating the oil phase (Figure 8.2 (b,i)). A period of slower soil swelling then follows.

The expansion of the soil due to swelling increased the pore size and structure, changing the capillarity of the soil. When the soil reached its maximum height, here after approximately 800 s, the water had saturated the solid matrix and melted the fats, increasing their mobility. The water also preferentially wets the solid matrix, progressively displacing the oil (Figure 8.2 (b,ii)). Roll-up and/or coalescence of the oil occurred causing accumulation within the pores, potentially blocking them (Figure 8.2 (b,ii)). However the oil phase is less dense than the water phase and this differential gave rise to buoyancy, causing the collected oil to rise through the soil layer. As the surface of the soil has low permeability to the oil phase, the oil instead collected within the cracks, which acted as a sink for the oil within the matrix (Figure 8.2 (a,iii)). Once enough oil had accumulated, buoyancy forces caused the oil to grow upwards as droplets (Figure 8.2 (a, iv)). The rate of displacement of the oil from within the soil matrix determined t_{onset} of droplet formation. These droplets then grew over time until they reached a critical volume (see Chapter 6) subsequently detaching from the CMS surface into the bulk solution, where they and any dissolved components were counted by the solution analysis (Oil R, TOC_B).

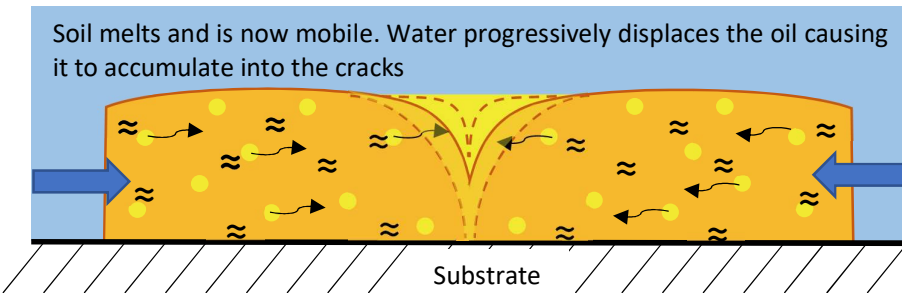
(a) (i) Dry soil is a porous structure containing solid fat inclusions. The outer 'crust' is a semi-permeable surface: less or impermeable to fats/oils



(ii) Water ingresses/penetrates the soil. The cracks swell and start to close



(iii) Soil melts and is now mobile. Water progressively displaces the oil causing it to accumulate into the cracks



(iv) Buoyancy causes oil to grow up as droplets on the soil surface. The cracks function as a sink for droplets to move in the matrix

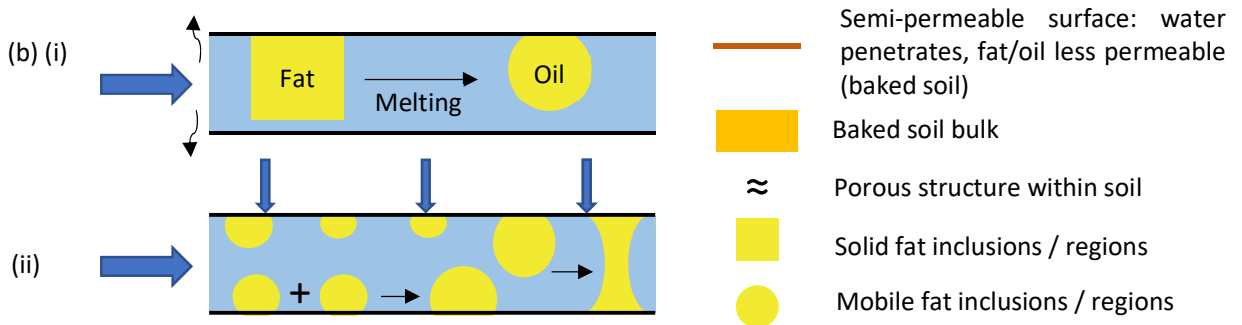
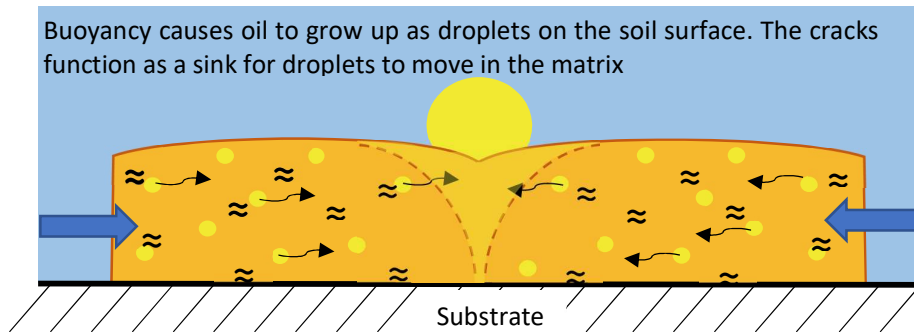


Figure 8.2: Schematics of stages in cleaning of CMS. (a) bulk soil, (b) within a pore.

8.3.1 Effect of temperature

Figure 8.3 (a) and (b) demonstrates the effect of raising the temperature from 20 °C to 50 °C. No droplets of mobile soil formed within one hour of submersion. In the absence of cleaning agents, raising the temperature increased the oil release rate constant ($k_{TOC} = 0.19 \times 10^{-6} \text{ s}^{-1}$ at 20 °C, $0.54 \times 10^{-6} \text{ s}^{-1}$ at 50 °C) and reduced the adhesion strength of the soil over 500 s ($\langle F_w \rangle_{min} = 70 \text{ N m}^{-1}$ at 20 °C, 19 N m^{-1} at 50 °C). This demonstrates that the warmed solution was required to cause the mobilisation of components from within the soil (Oil R: $TOC_{max} = 23 \text{ mg g}^{-1}$ at 20 °C, 35 mg g^{-1} at 50 °C).

The extent of soil swelling was greater at higher temperature ($\delta_{max} = 0.10 \text{ mm}$ at 20 °C, 0.16 mm at 50 °C). This can be attributed to structural changes within the soil. The melting of hydrophobic fats within the soil enhanced the wetting and hydration of the solid matrix through easier displacement of the mobile oil. The removal of the oil phase may also have exposed more of the hydrophilic molecules such as starches and proteins, reducing the soils net hydrophobicity, thereby enhancing solution penetration and the displacement of the mobile oil. This hydration promotes the disruption of soil-substrate adhesive bonds (as well as soil cohesion) as evidenced by the decrease of the force required to displace the soil from the substrate ($k'_{MM3} = 0.91 \times 10^{-3} \text{ s}^{-1}$ at 20 °C and 3.26 s^{-1} at 50 °C), promoting faster and more effective cleaning.

Figure 8.3(a) shows that the scaled rate of CMS swelling measured by zFDG and SiDG was consistent at 20 °C. The δ_{max} values varied between the techniques (zFDG, $\delta_{max} = 0.17 \text{ mm}$; SiDG, 0.10 mm). The SiDG gave better repeatability for the systems tested here (See discussion in Chapter 5 and error bars of one standard deviation on Figure 8.3(a)). SiDG data are thus reported in subsequent plots.

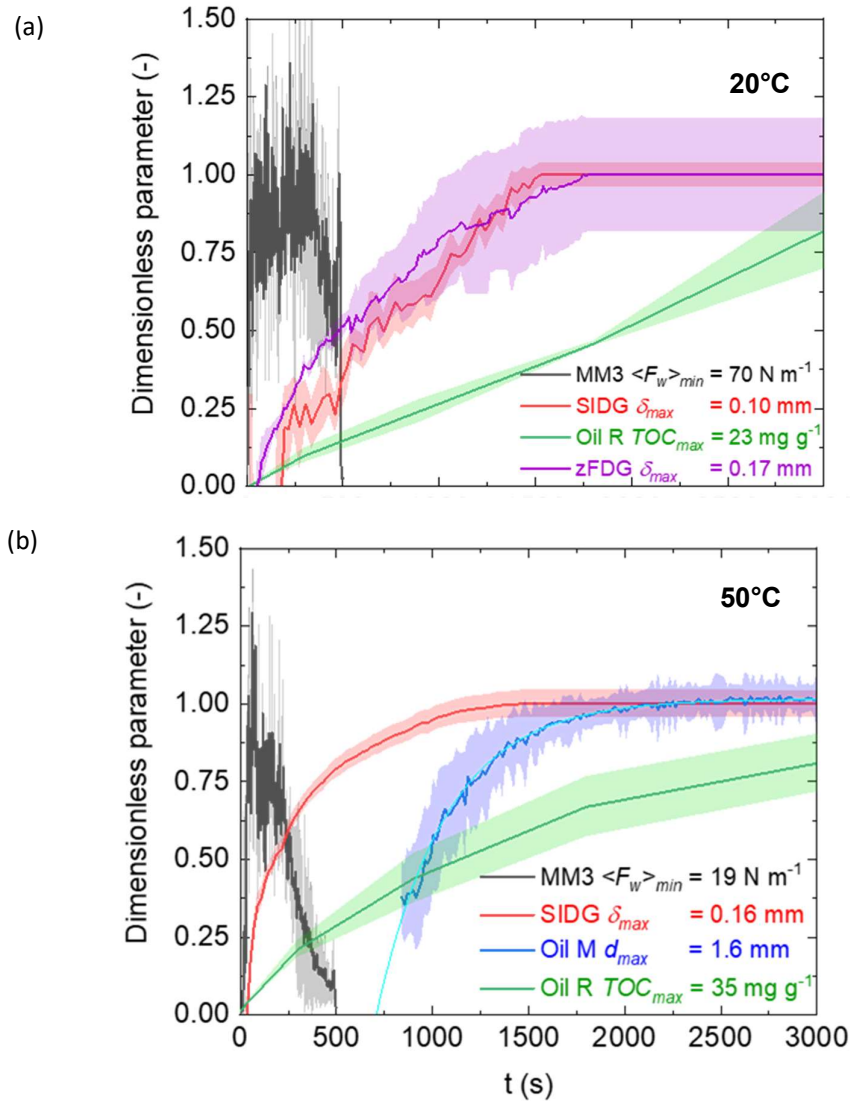


Figure 8.3: Effect of temperature. Deionised water at pH 7 and (a) 20 °C and (b) 50 °C.

8.3.2 Effect of pH

Figure 8.4 (a) and (b) shows the effect of raising the pH from 7 to 9 at 50 °C. The rate constant denoting the weakening of soil was lower at pH 9 (k'_{MM3} : -0.51 s^{-1} at pH 7, -0.41 s^{-1} at pH 9, rate constants calculated after t_c). This decrease was accompanied an increase in the final measured $\langle F_w \rangle$, showing that after 500 s the soil was more strongly bound to the substrate in the pH 9 solution than when submerged in water alone ($\langle F_w \rangle_{500s} = 19 \text{ N m}^{-1}$ at pH 7 and 50 N m^{-1} at pH 9). The normalised swelling rate constant was also lower at pH 9 (k_{SIDG} : $3.26 \times 10^{-3} \text{ s}^{-1}$ at pH 7 vs $2.67 \times 10^{-3} \text{ s}^{-1}$ at pH 9) but the extent of swelling was greater ($\delta_{max} = 0.10 \text{ mm}$ at pH 7 and 0.16 mm at pH 9). pH did not affect overall carbon transfer into the solution significantly ($TOC_{max} = 35 \text{ mg g}^{-1}$ at pH 7 and 40 mg g^{-1} at pH 9).

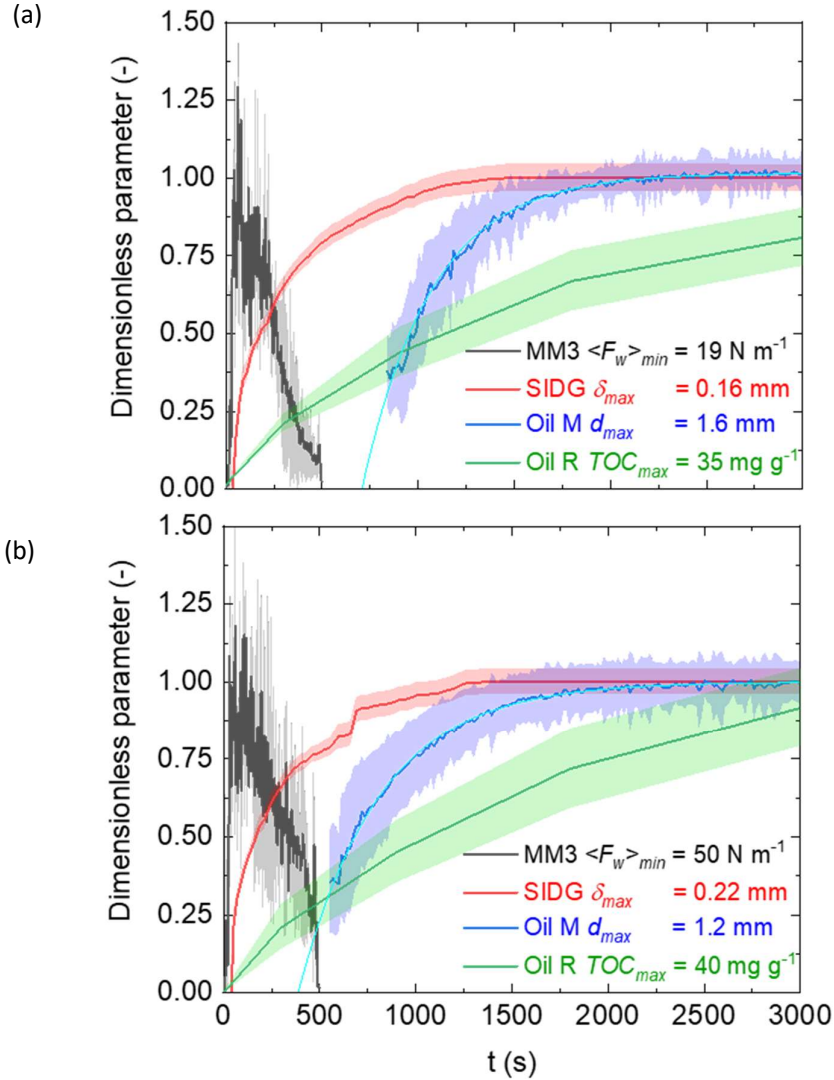


Figure 8.4: Effect of pH. Deionised water at 50 °C at (a) pH 7 and (b) pH 9.

Although the total carbon transfer was similar in both systems, the onset of formation and size of the droplets ($d_{max} = 1.6 \text{ mm}$ at pH 7 vs 1.2 mm at pH 9) differed. Oil was released earlier at pH 9 ($t_{onset} = 960 \text{ s}$ at pH 7 vs 600 s at pH 9), however the normalised rate constant of release appeared to be faster at pH 7. This can be rationalised mechanistically; alkaline solutions are known to enhance the expansion of protein and starch networks through charge repulsion and osmotic effects (Tsai *et al.* 2019). This is shown in Figure 5.15 in which initial swelling ($t < 10 \text{ s}$), δ_i , was found to increase linearly with hydroxide concentration. The higher δ_i due to the presence of hydroxides in the pH 9 solution promotes oil loss at 50 °C (due to larger pore size promoting the displacement of the mobile oils within the matrix, Figure 8.2 (b,ii)). This in turn improves access of more OH^- ions to the burnt CMS network, further enhancing swelling and oil displacement. The feedback nature of this behaviour, in combination with the increase in δ_{max} , explains the lower k_{SIDG} at pH 9.

The formation of smaller droplets on the surface can be explained both by the change in surface energy of the soil (causing a change in wetting behaviour of the soil to the soil matrix) and the increase in swelling at pH 9. As the soil swelled it did so in all directions i.e. it swelled into the crack space as well as into the solution. It was demonstrated in Chapter 6 that the droplets form at the site of cracks. If the cracks were smaller after swelling, a smaller volume of oil could collect in them before the formation of a droplet, contributing to the decrease in t_{onset} (Figure 8.2 (a,iii)).

8.3.3 Impact of surfactants

Figure 8.5 (a) and (b) shows the impact of adding surfactant (0.1 % SDBS, TX-100 and CTAB) at 50 °C. Initial comparisons were made between pH 7 water and 0.1 % SDBS (Figure 8.5(a, b)). The decrease in both the extent ($\langle F_w \rangle_{500s} = 19 \text{ N m}^{-1}$ for pH 7; 12 N m^{-1} for 0.1 % SDBS) and the normalised adhesion rate constant ($k'_{MM3} = 0.51 \text{ s}^{-1}$ for pH 7, 0.41 s^{-1} for 0.1 % SDBS) in the SDBS solution was similar to that of the pH 7 only solution. In both cases the adhesion strength decreased to approximately 10 % of the starting adhesion strength within 500 s.

Oil droplet formation started earlier in the surfactant solutions, and prior to the swelling reaching its asymptote. For SDBS solution the predicted onset was approximately 300 s (compared to 700 s in pH 7) at which point the soil had swollen to 60 % of its final extent. Both droplet formation and swelling plateaued around 1500 s. This suggests that the surfactants promoted oil mobilisation and recovery before the solid soil network had stopped swelling. This represents a significant difference in the sequence of the cleaning mechanism from water alone, i.e. in place of swelling, then oil release, the two phenomena are occurring simultaneously after only 300 s. This can be rationalised as the surfactants promoting the de-wetting and displacement (likely via roll-up) of the oil from the pores in the matrix into the cracks (Figure 8.2 (b, ii)). In addition to this, the surfactants lower the interfacial energy between the oil and the surrounding solution, potentially promoting the formation of droplets on the soil surface over the accumulation of oil within the cracks (Figure 8.2 (a, iv)).

The normalised swelling rate constant was lower in SDBS solutions ($k_{SIDG} = 2.09 \times 10^{-3}$ vs $3.26 \times 10^{-3} \text{ s}^{-1}$). The timescale of swelling was similar in both cases ($t_{asym, SIDG} = 800 \text{ s}$). This can be explained as the contributions to the layer height are a combination of both the soil and the water that has penetrated into the soil bulk. If the penetration rate of the water into the soil is similar, but the oil is being displaced from within the soil simultaneously (i.e. forming as droplets on the surface), then the overall timescale of swelling would be similar, but the rate constant associated with the layer height increase, k_{SIDG} , would be lower.

CTAB behaved in a similar fashion to SDBS in terms of swelling. It exhibited an earlier lowering of adhesion strength ($t_c = 40 \text{ s}$ in CTAB vs 200 - 220 s in pH 7 and SDBS) although it did not decrease to

the same extent ($\langle F_w \rangle_{500s} = 26 \text{ N m}^{-1}$ in CTAB vs 12 N m^{-1} in SDBS). This was accompanied by a shorter oil recovery time (4200 s vs 4800 s), a larger amount of oil recovered (134 mg g^{-1} vs 36 mg g^{-1}) and the rapid formation of small oil droplets (too small to be captured by image analysis).

The differences between SDBS and CTAB can be attributed to 0.1 wt.% CTAB reducing the oil-water interfacial tension by a factor of 10 more than 0.1 wt.% SDBS or 0.1 wt.% TX-100 ($\gamma_{OW,pH 7} = 26 \text{ N m}^{-1}$, $\gamma_{OW,0.1\% CTAB} = 0.38 \text{ N m}^{-1}$, $\gamma_{OW,0.1\% SDBS} = 3.1 \text{ N m}^{-1}$, $\gamma_{OW,0.1\% TX-100} = 3.0 \text{ N m}^{-1}$). This lowering of the interfacial tension between the oil and the water promoted the de-wetting and displacement of the hydrophobic soil components (i.e. fats and oils) through the soil network. Additionally a lower concentration of CTAB would have been required for roll-up to start to occur within the pores.

There was also a higher rate of removal of the oil droplets on the surface, likely also through surfactant promoted roll-up of the droplets causing faster detachment. The ability of the CTAB to more effectively promote oil mobilisation was predicted by the droplet detachment model in Chapter 6.

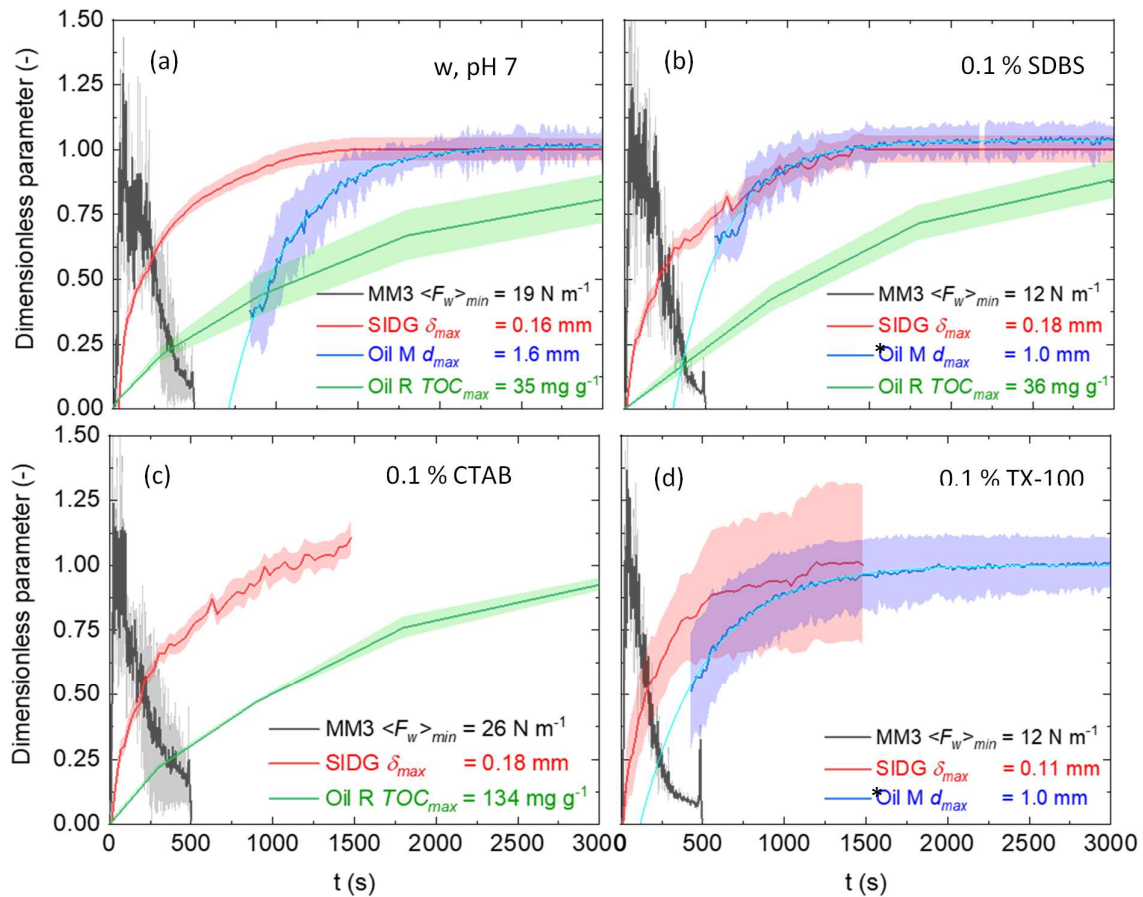


Figure 8.5: Effect of surfactants. Deionised water at $50 \text{ }^\circ\text{C}$ with (a) no surfactant, (b) $pH 7 + 0.1\%$ SDBS (MM3, Oil R and SiDG) and $pH 7 + 0.01\%$ SDBS (Oil M), (c) $pH 7 + 0.1\%$ CTAB (MM3, Oil R and SiDG) and (d) $pH 7 + 0.1\%$ TX-100 (MM3, Oil R_B and SiDG) and $pH 7 + 0.01\%$ TX-100 (Oil M). * denotes samples at 0.01 wt.% surfactant.

The shorter millimanipulation inflection time with CTAB is thought to be linked to the solution penetrating at the soil-substrate interface as the soil swelling characteristics are similar (implying the bulk soil behaviour similar). This behaviour would account for the short induction time on the MM3 as the soil at the interface would be wetted more quickly and therefore lose structure on a shorter timescale.

Soils exposed to 0.1 % TX-100 solutions did not swell to the same extent as other surfactants ($\Delta\delta_{final} = 0.11$ mm vs 0.18 mm in CTAB and SDBS, and 0.16 mm at pH 7). This lower extent of swelling explains the normalised kinetics and timescale; in TX-100 solutions the normalised swelling rate constant was larger than in pH 7 ($k_{SIDG} = 4.95 \times 10^{-3} \text{ s}^{-1}$ vs $3.26 \times 10^{-3} \text{ s}^{-1}$) and $t_{asym, SIDG}$ was shorter. The soil swelled less and so, when scaled, it appeared to swell with a faster normalised rate constant even though the absolute rate of swelling was lower (Figure 5.16 (b)). In CTAB solutions the reverse holds. Soils exposed to 0.1 % CTAB exhibited slower normalised swelling rate constants ($k_{SIDG} = 2.09 \times 10^{-3} \text{ s}^{-1}$ vs $3.26 \times 10^{-3} \text{ s}^{-1}$) and reached their maximum thickness after approximately 800 s, but swelled to a larger extent than when in pH 7 solution.

At the soil-substrate interface 0.1 % TX-100 solutions behaved similarly to the 0.1 % CTAB solutions i.e. they have a short t_c (80 s vs 220 s in pH 7), the rate of decrease of adhesion strength was faster ($k'_{MM3} = -0.61 \text{ s}^{-1}$ vs -0.51 s^{-1}), and the onset of oil droplet formation was earlier (predicted $t_{onset} < 250$ s vs ~ 700 s). This is consistent with the findings of Jurado-Alameda *et al.* (2015) who reported that lipase activity during the cleaning of oily soils was affected by the nature (non-ionic or anionic) of the accompanying surfactant. They demonstrated that non-ionic surfactants adsorbed preferentially at the water-soil interface, decreasing cleaning effectiveness at high surfactant concentrations by preventing enzymes from entering the soil. For anionic surfactants, this effect was less pronounced.

While the onset of oil release was enhanced with TX-100, the normalised rate constant of release was similar to that of water ($k_{droplet} 2.3 \times 10^{-6} \text{ s}^{-1}$ vs $2.8 \times 10^{-6} \text{ s}^{-1}$ at pH 7). This can be explained by the fact that at 0.01 % the TX-100 (the concentration used in the oil release tests) was below its CMC (Figure 3.7). As the TX-100 concentration was reduced by absorption to the soil matrix, the absence of micelles mean that there was less surfactant available to adsorb onto the oil droplets and promote roll-up.

8.4 Overall cleaning mechanism

The cleaning mechanism can be broken into two distinct stages: (I) the hydration and swelling of the CMS after exposure to aqueous solutions and (II) the displacement of oils and fats from within the soil structure to the soil-solution interface. The use of hydroxide ions has been shown to increase the extent of swelling in stage (I) as well as shorten the timescale on which it occurs. Surfactants then

enhance the de-wetting and displacement of mobile oils by lowering the interfacial tension (as well as changing the oil-matrix and solution-matrix contact angles) between the soil and solution (II). This change in interfacial tension enhances the displacement of the oils and fats into the bulk solution. The interplay between these two stages of cleaning can be monitored using the four techniques outlined in this thesis, and solutions formulated to promote effective cleaning on short timescales.

Upon submersion the CMS interacts with the solution both in the bulk, characterised by soil swelling as well as mobilisation of the oil phase, and at the soil-substrate interface, denoted by the reduction in MM3 forces. No direct link was established between the removal of the fat fraction and the reduction in MM3 forces. Figure 8.3 demonstrates that a reduction in $\langle F_w \rangle$ occurred the solution temperature was raised to 50 °C. This temperature is above the onset of melting of the fat fraction, causing an increase in the displacement of the fat phase. Figures 8.4 and 8.5 can be inspected in order to establish whether there is a link between the two phenomena; it has been established that the addition of either surfactants promoting roll-up of hydrophobic components in the soil, or pH promoting swelling of the soil, increases the speed and magnitude of displacement of the fat fraction. However neither Figure 8.4 nor 8.5 exhibits a beneficial effect on $\langle F_w \rangle$ suggesting that the two cleaning phenomena are distinct from one another, i.e. in the simple surfactant/pH systems tested here there is no direct benefit of promoting the removal of the fat fraction on the removal of the soil as a whole.

8.5 Conclusions

A suite of techniques has been developed to investigate the structural and chemical changes that occur in a complex model food soil upon contact with aqueous solutions. The complex model food soil tested comprised burnt fats, starch and proteins in a cracked layer on stainless steel. Combination of the findings of each of these techniques, described in Chapters 4 – 7, provides insight into the staged cleaning mechanism that needs to take place to removal burnt soils from stainless steel substrates.

This chapter demonstrated that in simple pH 7 water solutions at 50 °C swelling and the drop in adhesive strength of the soil to the substrate occur on the same timescale. Figure 8.1 showed that both processes reached their respective t_{asym} after approximately 500 s, indicating that they are either both a function of the same occurrence e.g. solution penetration, or that one directly impact the other, i.e. as the soil swells it exerts a force on the soil-substrate interface, weakening the measured adhesion strength. It was only after the above sequence occurred that the formation of oil droplets was observed.

At lower temperatures $\langle F_w \rangle$ decreased and δ increased over a much longer timescale. Additionally no oil mobilisation occurred. These factors explain why the overall volume of carbon material released

into the solution after submersion, used here as an indication of cleaning effectiveness, was significantly lower for solutions at room temperature than at 50 °C.

Testing at a higher pH decreased the rate of reduction in $\langle F_w \rangle$ but hastened soil swelling and droplet formation, indicating that the adhesion and soil swelling are not direct results of one another but instead both change as a function of solution ingress. The decrease in induction time for oil mobilisation also decreased the amount of time for the overall cleaning effectiveness (measured by solution analysis) to reach its maxima. Overall it was shown that alkaline conditions increase swelling, which had knock on effects on oil mobilisation and total carbon material release, hastening transfer of soil components into the solution.

Surfactants were shown to enhance the weakening of adhesive and cohesive strength of the soil significantly, as well as promote oil displacement and droplet formation whilst the soil is still swelling. The faster overall rate of soil layer cleaning can be attributed in this case to the rate of oil mobilisation within the CMS. However this rate is dependent upon surfactant type; the surfactants act on the solid matrix and the liquid hydrophobic components in different ways: SDBS and CTAB promoted both displacement and detachment of the mobile components, whilst TX-100 primarily promoted wetting of the soil matrix, enhancing the displacement of the oils/fats towards the soil surface.

These insights into the stages of cleaning and the mechanisms involved can be used to enhance the cleaning effectiveness of commercial cleaning formulations.

9. Application to commercial formulations

The wider focus of this work was to determine the impact of key components within a cleaning formulation on the overall cleaning rate and effectiveness on the removal of burnt food soils. This was intended to inform formulation design for complex commercial cleaning formulations, such as those used by the project sponsors. The cross-applicability of this work to P&G® formulations was therefore investigated. This was done via two methods.

The first was the testing of simple cleaning solutions used in this thesis i.e. different pH, temperature and surfactant solutions (Section 1) on a standard P&G® test apparatus. This was done firstly to relate the findings of this thesis to a device used regularly by the project sponsors, and secondly to demonstrate how the project learnings support formulation design. This work was completed during a 3 month working visit to the P&G's Newcastle Innovation Centre.

In Section 2 P&G® provided two commercial cleaning formulations (denoted CCF1 and CCF2) for testing with the MM3, zFDG and solution analysis. The formulations were provided without the bleach and chelant components, allowing tailoring of the concentrations. The surfactant levels used in the CCFs remained constant throughout testing. These formulations contained enzymes and so the oil recovery technique was adapted to ensure that denaturation of the enzymes did not occur. The adapted oil recovery technique is described in Section 3.

9.1. Multichambered Automatic Dish Washing Rig

9.1.1 Test set-up

The multichambered automatic dish washing rig (ADW rig) was developed and commissioned in March 2015 at Procter and Gamble®, Newcastle-upon-Tyne, by research scientist James Goodwin. The aim was to create a system to replicate the conditions in a domestic automatic dishwashing system to assess the effectiveness of new chemistries developed for the commercial formulation.

A schematic of the ADW rig is shown in Figure 9.1. The rig consists of four chambers, each containing a sample mount, a water jet nozzle of diameter 2 mm positioned perpendicular to the sample mount on a reciprocating stage, two heating blocks, a magnetic stirrer, and a solution recirculation system. The walls of the chamber are stainless steel with a half-panel Perspex® viewing window at the front. The window is interchangeable, allowing the chamber to be completely enclosed for use with hazardous cleaning solutions, e.g. those containing sensitizers such as enzymes.

Two Nikon® D5600 cameras are situated on moveable arms in front of the rig, each capturing photos of two chambers. The cameras are controlled using a desktop PC (Dell® Precision Tower™ 3420, Intel®

Core™ i7-7700 CPU 3.6 GHz processor, 16 GB RAM, Windows® 10) running DigiCamControl OpenSource software to take photographs for a set test time at pre-defined intervals. In this work the test time was 2 hours, unless otherwise stated, with an interval time of 10 s. Videos were generated using Windows Movie Maker Software® with a frame rate of 0.016 photos per second, giving an approximate playback ratio of 1 minute to 1 hour.

The ADW rig system allows automatic control of the oscillation period, *i.e.* the time taken for the nozzle to traverse from one side of the sample plate to the other, re-circulation speed, *i.e.* flow rate, magnetic stirrer rotation speed and temperature. Table 9.1 shows the conditions used in this work. A minimum of three repeats were conducted for each soil-solution permutation.

Table 9.1: *Settings used in ADW rig.*

Variable	Samples 1-13	Samples 14-152
<i>Oscillation period (s⁻¹)</i>	0.13	0.13
<i>Recirculation time (min)</i>	6	6
<i>Mass flow rate (g/s)</i>	10	10
<i>Magnetic stirrer rotation (%)*</i>	32	32
Temperature (°C)	22	50
<i>Solution volume (L)</i>	3.5	3.5

* % here refers to the proportion of power supplied to the stirrer. The project sponsor was unable to supply absolute speed in rpm.

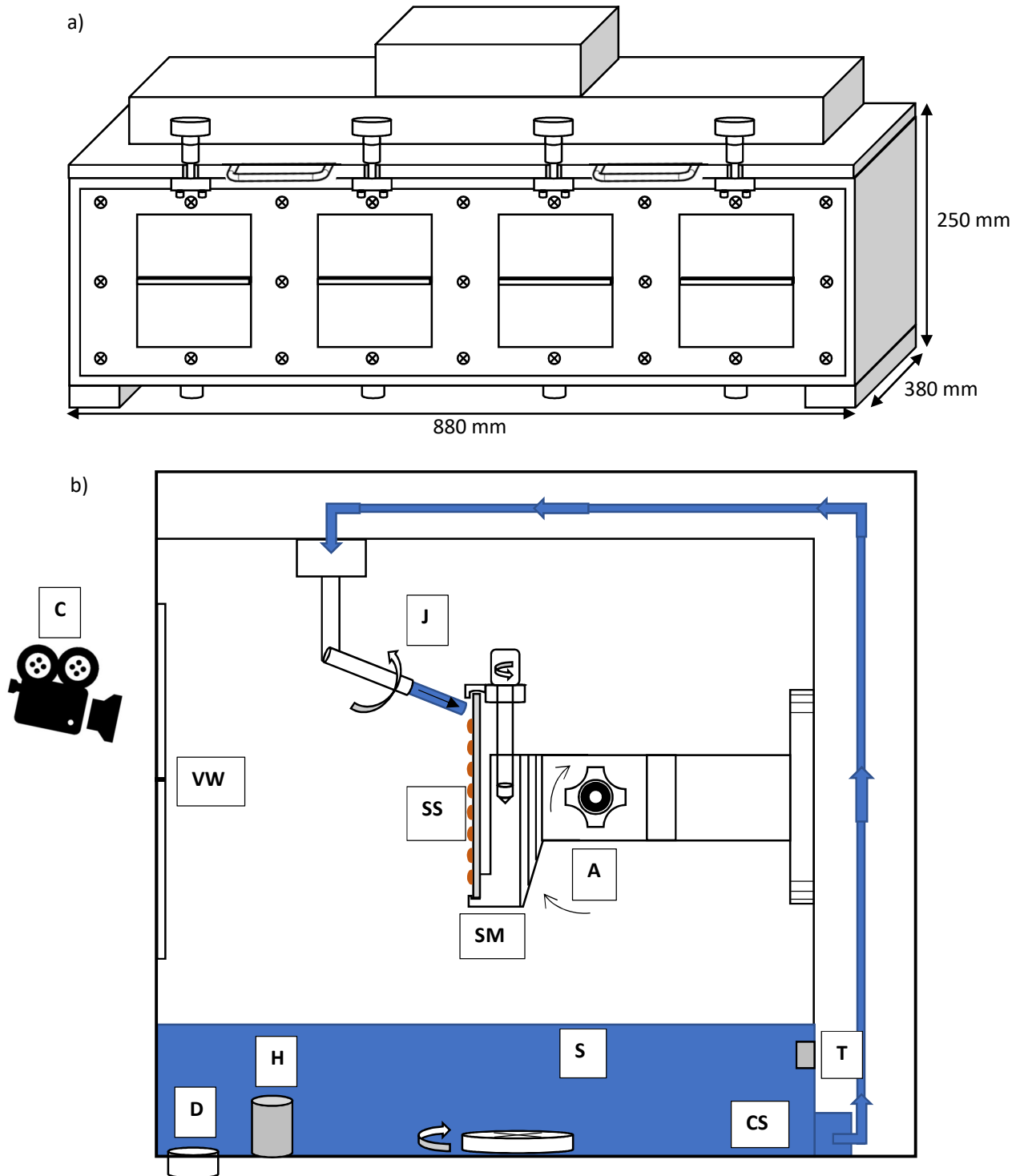


Figure 9.1: Schematic of the ADW Rig. a) Front View b) Side view inside a chamber. Labels: A; Sample mount angle adjuster; C; Camera; CS; circulation system; D; drain; H; heating block; J; water jet; S; cleaning solution; SM; sample mount SS; plate with soil sample; T; temperature sensor; VW; viewing window. Water is circulated from the reservoir, through the circulation system and out through the jet at a set flow rate. The jet reciprocates at a set frequency across the top of the sample plate to wet the entire surface.

9.1.1.1 Sample preparation

Samples were prepared on polished 98 mm x 98 mm x 4 mm 304 stainless steel plates (SlickSteel®) with roughness, R_{q} , of 2.69 μm . Plates undergo a pre-wash in an automatic dishwasher (Bosch®) on a 2.25 hour intensive cycle with approx. 5 g citric acid dose. The citric acid is used to remove any glue residue from the protective covering used for shipping the plates. A stainless steel stencil (Figure 9.2 (a)) was used to generate a grid pattern consisting of 80 soil dots of diameter 7 mm and thickness 0.8 mm in 8 rows of 10 dots, spaced 2 mm apart, giving a sample test area of 90 mm x 70 mm (Figure 9.2 (b)).

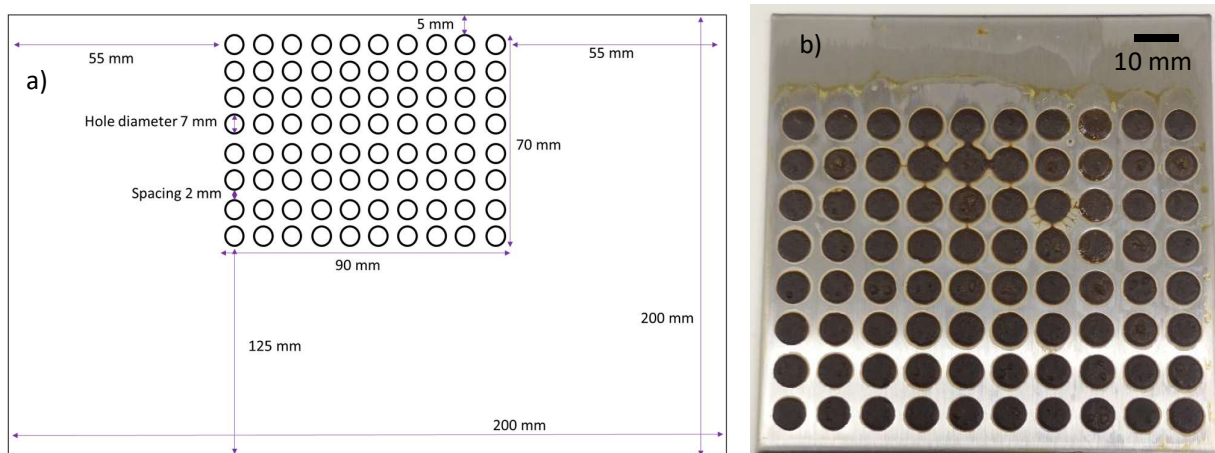


Figure 9.2: (a) stainless steel stencil for generating uniform soil dots (b) photograph of CMS sample plate.

The soil used in this test was CMS prepared via the method described in Chapter 3 with the exception that the fat portion (I can't believe it's not butter®) was melted in a microwave instead of on a hotplate. A fresh batch of CMS mix was used for each set of samples. Soils were applied to pre-weighed plates (2 decimal place balance, Sartorius BP 3100S), weighed within 1 min of application (fresh soil mass), left to evaporate in ambient air for at least 18 hours, weighed (post-evaporation mass), baked in a conventional oven (Philip Harris Ltd.) for 7 min at 204 °C, removed from the oven, cooled in ambient air for > 1 hour to room temperature and subsequently weighed (post-baking mass). Soil layer metrics for 152 samples are shown in Table 9.2. The soils here had an average mass loss of 62 ± 8 wt.% between the fresh charge of CMS mix and the final baked layer. This is consistent with the mass loss of samples generated at Cambridge of 67 ± 6 wt.%.

Table 9.2: Soil sample preparation masses for 152 CMS plates.

	Average mass / g	Standard deviation / g
<i>Sample plate</i>	56.14	0.25
<i>Fresh soil</i>	2.74	0.30
<i>Post-evaporation</i>	1.19	0.17
<i>Post-baking</i>	1.05	0.15

9.1.1.2 Solution preparation

3.5 L of solution was prepared for each test. For tests conducted at 50 °C, 1.5 L of deionised water was boiled at 100 °C in a kettle (Asda Smartprice®, KE7519) and added to 2 L deionised water at room temperature in a 5 L plastic beaker on a stirrer plate with stirring at approx. 200 rpm. pH was measured using a pH probe (Jenway 3520) and raised through the dropwise addition of 10 g/L of aqueous NaOH until the required pH was achieved. Surfactants and chelants were weighed out on a 4 decimal place balance (Salter ANDFX-40), added and stirred until visibly dissolved plus 5 minutes. Solutions were poured into the sample chambers and heated to 50 °C, with stirring, before testing commenced. For room temperature testing the same procedure was used with the exception of boiling the water beforehand and preheating the rig.

9.1.1.3 Test protocol

Once the solution was at the required temperature the sample plates were attached to the sample holders and the lid of the chamber screwed shut. The cameras were located in position and the auto-focus function used to set the focus before auto focus was switched off to ensure consistency throughout the 2 hours test time. The camera's time lapse protocol was initiated with the first photo taken being that of the dry sample located within the chamber. The solution circulation and nozzle oscillation systems were then started. Once testing was completed all systems were shut off, the samples removed from the chamber. The ADW rig cleaning protocol would then commence. The samples were left to dry in air for at least 18 hours before being weighed (post-test mass).

9.1.1.4 ADW rig cleaning protocol

The cleaning tests aim to test the effectiveness of surfactants and chelants within a dishwashing environment. To avoid cross-contamination a rigorous cleaning protocol for the ADW rig was required to ensure that no contaminants remained after testing. The rig was cleaned as follows:

- (i) All solution was allowed to drain out of the chamber
- (ii) With the drain left open, 4 L hot tap water was poured into the chamber down the chamber walls and collected for disposal
- (iii) 4 L hot tap water was poured into each chamber and pumped through the circulation system for 15 minutes then drained
- (iv) Visual inspection, with repeats of stages (i)-(iii) if required.

In order to monitor the cleanliness of the filter and circulation system, water was collected from the jet for 15 s before testing to check flow rates were within expected limits. Removal of filters and deep clean of the ADW rig was performed by P&G® researcher James Goodwin approximately every 50 samples.

9.1.1.5 Test metrics

The efficacy of the cleaning solution was monitored using 2 metrics:

- (i) Gravimetrically: the soil mass was weighed before and after testing. The percentage mass loss over the course of the test was calculated.
- (ii) Visually: The rate of soil dot drop off was recorded to within 10 s through analysis of the photographs. Soil dots were considered to have been removed if > 90 % of the soil area was missing from the dot's initial location. Transfer of the dot from one section of the plate to another was recorded as removed as it was no longer affixed to the plate, merely lodged on another section of soil.

9.1.2 Results and analysis

Testing conducted on the ADW rig included studying the impact of temperature, pH, surfactants, chelants, and combinations thereof. Mass loss was used as a metric where no soil dots were removed, in all other cases the rate of dot loss was used as the primary metric.

9.1.2.1 Impact of temperature and pH

Initial tests were conducted with top water at pH 7, 8, 9, 10, 10.5, 11 at room temperature and at 50 °C. The small mass loss between the start and end of testing. Figure 9.3 shows that up to pH 11, pH alone had little impact on the effectiveness of soil removal in the ADW rig.

In room temperature tests no single dot was completely removed. There was an $8.0 \pm 1.9\%$ mass loss over the 2 hour test period. Increasing the temperature to $50\text{ }^{\circ}\text{C}$ resulted in an increase in soil mass loss to $29 \pm 3.2\%$, with a small number of dots removed at pH 11. A mass loss of approximately 30% corresponds to that observed in solution analysis testing at pH 7 (fat fraction = 350 mg g^{-1} , Chapter 3) and is attributed to the proportion of the soil which becomes mobile at $50\text{ }^{\circ}\text{C}$ i.e. the fats. The hot water runs down the plate, and therefore around and over the soil, transferring heat to the soil, and melting the fats contained within it. The fats are then displaced by the solution to the soil surface before being transferred via shear flow forces into the bulk solution where it is collected below. The remainder of the burnt heterogeneous soil mixture remains adhered to the substrate unless cleaning agents are used.

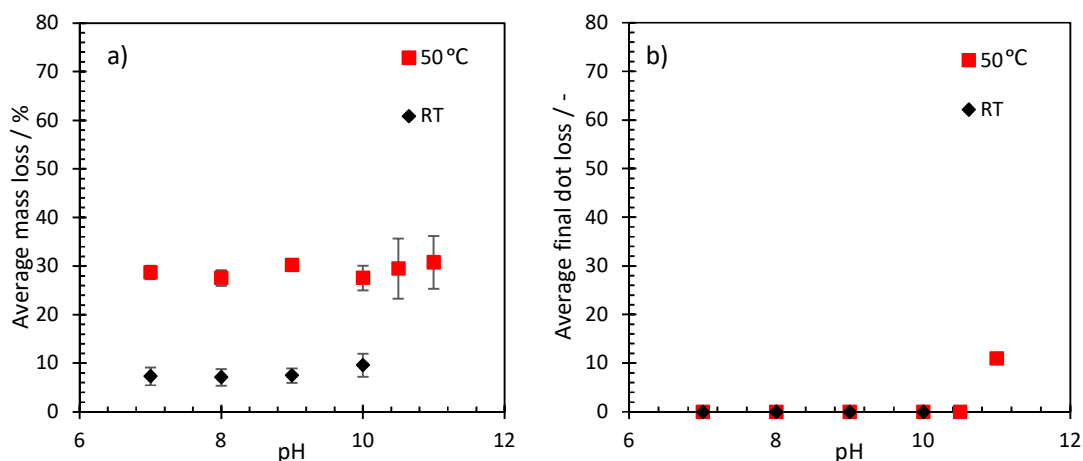


Figure 9.3: ADW data showing impact of temperature and pH. (a) average mass loss as a percentage of total sample mass over 120 min test with 3-4 samples per point. Error bars indicate sample standard deviation, (b) Final average dot loss over 120 min test with 3-4 samples per point. Error bars indicate sample standard deviation.

9.1.2.2 Impact of surfactants

Addition of surfactants at both pH 7 and pH 10 at $50\text{ }^{\circ}\text{C}$ showed little to no impact on cleaning for TX-100 and CTAB (Figure 9.4). A slightly higher mass loss was recorded with SDBS, with limited soil dot loss at pH 10 for two of the three samples tested. It is likely that the surfactants act only upon the mobile fatty material, and not the solid soil network. If this was the case then there would be no observable benefit over simple hot water solutions via end point testing. When the benefits from both enhanced solubility from the presence of surfactants and pH are combined, i.e. 0.1% SDBS at pH 10, the number of dots that detached out-performed all other conditions tested in terms of dot loss (22 dots at $50\text{ }^{\circ}\text{C}$, 2 dots at $20\text{ }^{\circ}\text{C}$ vs no dots in any other system). The performance of SDBS is counter to

the findings from oil mobility, oil recovery and millimanipulation testing (Chapters 6 and 7) which indicated that CTAB ought to provide enhanced oil recovery and lowering of soil attachment to the substrate, thereby providing enhanced clean-ability. One possible explanation for this was that a film was noticeable on the solution surface in tests containing CTAB solutions. This could indicate that the CTAB was interacting with the steel casing of the test equipment. Furthermore there was enhanced foaming of the CTAB test solution; the solution was drawn from the base of the vessel into the recirculation system so it is possible that there was a reduced concentration of CTAB in the solution that contacted the soil dots.

A second explanation is that the primary mechanism by which the surfactants interact with each phase of the heterogeneous soil is different. It was reported in the Chapter 8 that, when adhesion, swelling and oil mobilisation data were analysed together, TX-100 and CTAB predominantly interacted with soil at the soil-substrate interface and the solution ingress at this interface caused an upward movement of both the solid soil network and the mobile fatty components. SDBS, on the other hand, interacted primarily with the hydrophobic fats within the soil, enhancing solubilisation of these from the soil into the solution. In the ADW system the soil is never completely submerged, as the water film passes over each section of the soil in turn. This would affect the ability of the solution to penetrate or ingress to within the soil as it was never fully saturated with solution. Mechanistically, a surfactant that acts by removing a hydrophobic component from within the soil would enhance the wetting of the solid network, enabling access for the OH⁻ to react with the protein and starch moieties, weakening its structural integrity, and eventually causing it to succumb to the gravitational forces acting upon the soil in this vertical substrate arrangement.

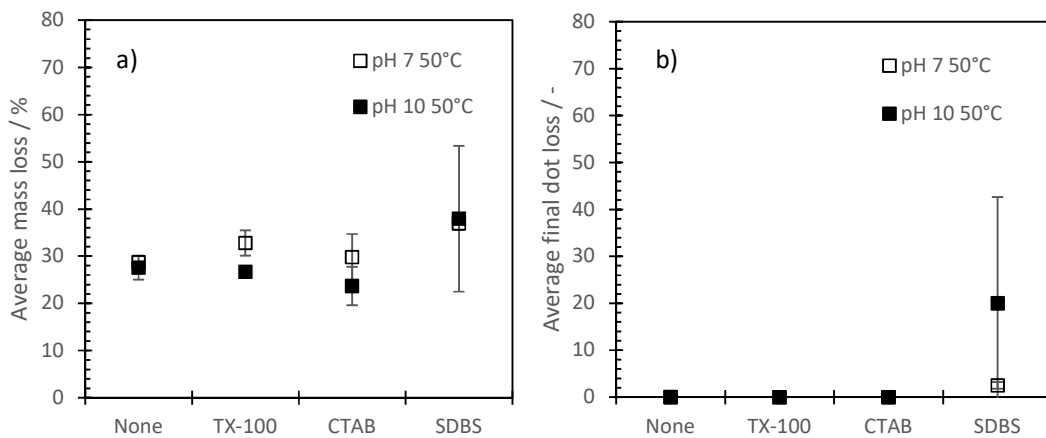


Figure 9.4: Impact of surfactant on cleaning of CMS as tested in ADW rig at 50 °C. a) Average mass loss as a percentage of total sample mass, b) average final dot loss after 120 min. Error bars are sample standard deviation. 3-4 sample per test.

9.1.2.3 Falling films

Falling liquid films are used throughout industrial cleaning processes. In a commercial dishwasher a rotating spray arm is used to recirculate the cleaning solution within a closed environment. Water is pumped into the spray arm and leaves through a series of holes drilled at an angle along the arm. Typical rotating spray arms have 3 – 4 holes on each arm. These generate water jets at an angle of 45 – 70° from the roof of the dishwasher (depending on manufacturer). Newton's third law dictates that as the water is ejected, an equal but opposite force is imposed upon the arm itself, causing it to rotate at a frequency in the region of 25 – 45 rpm (Brambilla and Ugel, 2013) .

The length of time the jet spray makes contact with a typical plate stacked in a standard commercial dishwasher has been determined by positron emission particle tracking (PEPT) to be a maximum of 1.5 % of each rotation of the spray arm. (Pérez-Mohedano *et al.* 2016). The shear stresses (12 – 65 Pa, Pérez-Mohedano *et al.* 2016) imposed by direct impact cannot therefore be relied upon to perform significant cleaning during a 1 – 2 hour dishwashing cycle. The falling films generated by the gravity flow of liquid from jet impact above a target area, including the ceiling of the dishwashing unit, instead provide the means to transport the cleaning agents, such as surfactants and enzymes, to the soiled surface.

Adequate wetting across the target surface is key to contacting the cleaning agents with the soil. Surfactants are used to enhance wetting on the dish surface and maximise the contact area. As water drains, its surface tension and contact angle on the solid surface, as well as the topography of the aforementioned surface, dictate the fluid flow pattern, i.e. whether the water drains as a sheet or as rivulets.

Figure 9.5 shows the impact of 0.1 wt.% SDBS on the drainage pattern of the film. Each plate was impacted by the jet in a standard test run of the ADW rig. The drainage profile of the water was monitored for the first minute of testing. After 10 s of contact with the reciprocating jet, i.e. one complete cycle, the cleaning solution containing SDBS achieved complete coverage of the test plate. Each soil dot appears to be experiencing equal contact time with the solution. With DI water, coverage is not even. The draining film is complete only in the region close to the jet impact point and quickly forms rivulets lower down the plate.

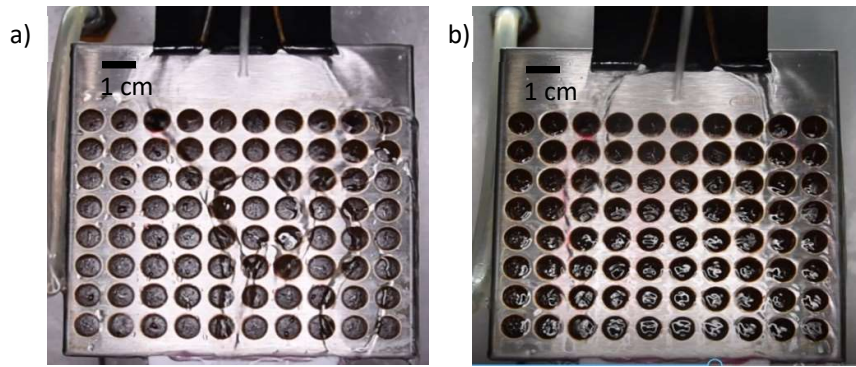


Figure 9.5: Photographs of film flow over stainless steel plate soiled with CMS, contacted with (a): DI water: inadequate coverage. (b): 0.1 % SDBS in water: full film coverage. Both pictures taken after one cycle of the water jet. $T = 50\text{ }^{\circ}\text{C}$.

Rivulets, such as those observed in Figure 9.5, arise when the surface tension narrows the film, which is when surface tension acting horizontally is greater than the inertia of the liquid falling vertically. Their formation is dependent upon a balance of contact angle (i.e. the wettability), the topography of the solid, and the Weber number (related to the velocity of the fluid flow) (Slade, 2013). The lower the wettability of the solution the lower the stability of the fluid flow down the surface. In order to reduce the surface area (and the energy associated with it) to a minimum, the solution will collect into long thin finger-like structures. These structures can be considered analogous to the surface energy minimisation process found in jet break-up into droplets; by forming rivulets the system minimises the higher energy contact area between the solution and the substrate. Silvi and Dussan (1985) demonstrated that the pattern of rivulet formation was determined principally by the wetting characteristics. Hocking *et al.* (1990) later showed that the instability causing rivulet formation closely follows that of a modified Rayleigh-Taylor model due to its dependency on gravity and the strong influence of surface tension.

The rivulets in Figure 9.5 do not follow a direct path down the soiled plate. This is due to changes in the fluid inertia and anisotropy of the friction between the rivulet and the soiled substrate (Daerr *et al.* 2011). Undulating topography on the surface plate can serve to stabilise fluid flows at moderate surface tension values (Weber number ($We \geq 30$)) but tends to cause increased destabilisation at the higher end ($We < 30$) (D'Alessio *et al.* 2009).

As a consequence of the rivulet formation all soil dots cannot be considered to be wetted equally in solutions with high surface tension, such as surfactant-free water. This explains why the dots do not detach starting from the top row which would theoretically have the most contact with the film flow under stable film flow conditions (Figure 9.6).

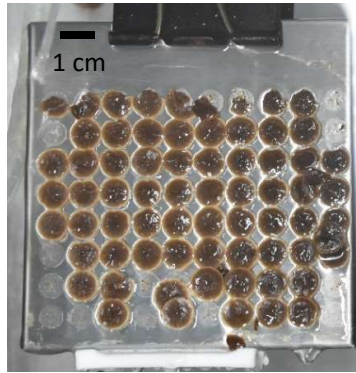


Figure 9.6: CMS soiled substrate after 120 minutes contact with pH 11 cleaning solution.

9.1.2.4 Impact of chelant

The role of chelant (MGDA) was evaluated both in isolation and in parallel with three surfactants at 50 °C (Figure 9.7). MGDA alone promoted removal of soil over pH-only cleaning solutions. The combination of MGDA and raised pH (pH 10) gave enhanced dot drop off over pH 7.

Addition of surfactants and chelant gave varied responses. SDBS/MGDA promoted additional soil removal at pH 7 but gave no improvement above MGDA-alone at pH 10; TX-100 gave no additional benefit over MGDA-alone; and CTAB/MGDA caused a significant volume of visible ‘scum’ to appear in the cleaning solution. This was due to the formation of a co-precipitate, i.e. an insoluble ion pair, between the cationic CTAB and anionic MGDA, removing MGDA from solution, impeding its access to the soil. Up to 3 CTAB ions can co-precipitate with each MGDA molecule (BASF, 2007).

These findings are consistent with findings by Ali (2015(a)) for polymerised lard soils. MGDA was shown to promote adhesive removal of that soil through ingress at the soil-substrate interface. This was characterised by the formation of blisters in the soil when subject to suction during fluid dynamic gauging. In the ADW rig this ingress is marked by the peeling and lifting of soil at the edge of the dots in contact with the substrate (Figure 9.8). With MGDA as the primary cleaning agent, soil was removed as a coherent piece due to adhesive strength weakening at a faster rate than the cohesive breakdown of the soil. With 0.1 % SDBS alone the soil was broken down over time and detached from the substrate in small chunks. This is supported by the oil recovery data obtained for MGDA solutions: oil recovery was negative for MGDA due to the baseline carbon, present due to the carbon in the MGDA molecule, being lost over duration of the test. This was due to the absorption of the MGDA from the solution, into the soil as it interacts (or reacts) strongly with the soil structure and/or the substrate, instead of solubilising the material into the solution.

A power law function can be fitted to the data in Figure 9.7;

$$\left[\frac{N_0 - N}{N_0} \right]^n = k_{ADW}(t - t_{onset}) \quad \text{Equation 9.1}$$

where N is the average number of dots attached at time t , N_0 is the total number of soil dots at the start of the test, k is a kinetic constant and t_{onset} is the time at which the first dot falls from the plate. In this case, experimental data suggest $n = 0.5$. Fits are shown in Figure 9.7 (c, d), parameters in Table 9.3.

This equation of best fit shows an inversion in the profile of soil behaviour. In swelling, oil imaging and oil recovery studies the rate of change in the measured phenomenon is rapid after the onset time, then slows to an asymptote. Here the dot loss starts slowly but the rate of cleaning steadily increases with soaking time until there is relatively rapid dot loss after 120 min submersion. This may be a function of the intermittent contact with the cleaning solution. As dots fall off, they no longer impede the flow of cleaning solution to the dots beneath, and so these dots will be cleaned more rapidly now that they are in the direct line of the solution flow.

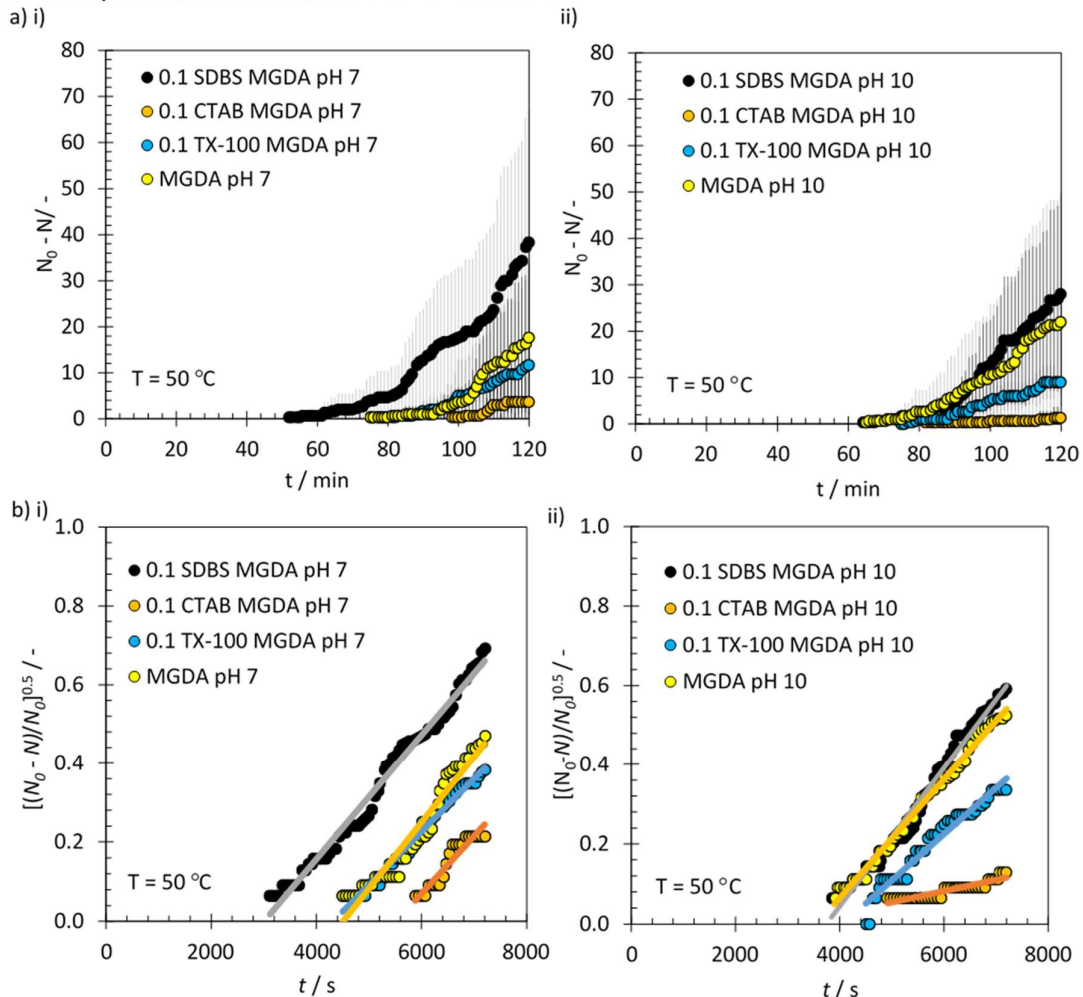


Figure 9.7: (a) Average dot loss over time for solutions of 0.1 % MGDA plus 0.1 % surfactant at 50 °C and (i) pH 7 and (ii) pH 10. (b) Normalised average dot loss against time plotted in the form of Equation 9.1. (i) pH 7 and (ii) pH 10. Total number of dots = 80. Error bars are sample standard deviation of 3-4 samples. Trendlines are linear regression fits.

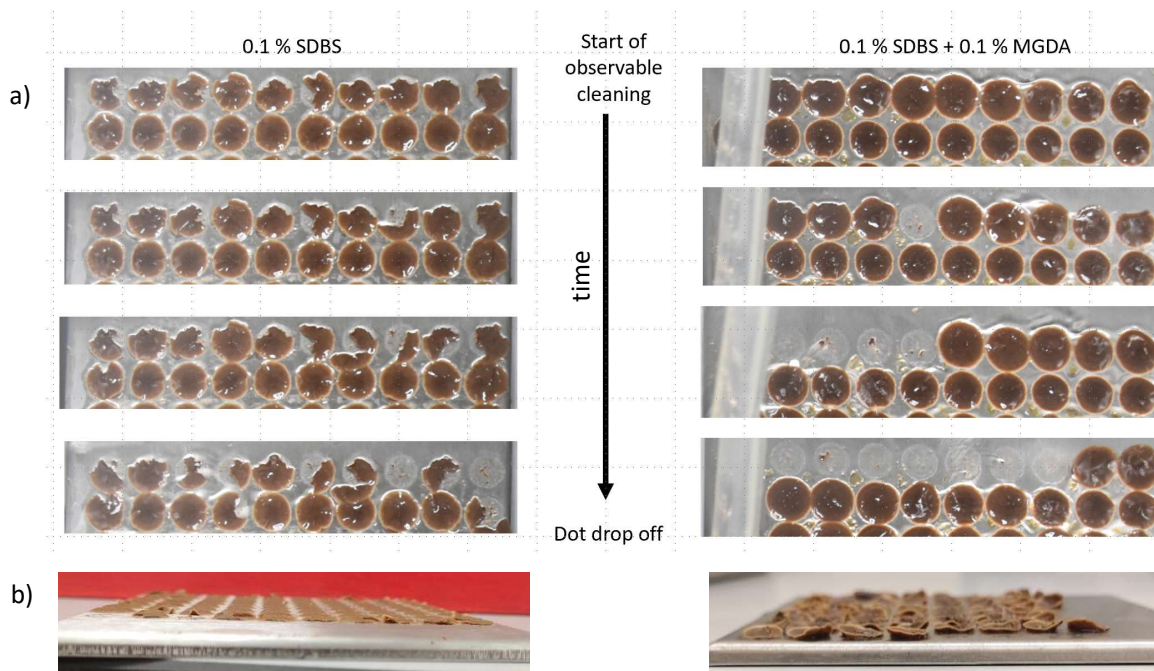


Figure 9.8: Photographs of a) top two rows of soil dots over time in the ADW rig. LHS 0.1 wt.% SDBS RHS 0.1 wt.% SDBS + 0.1 wt.% MGDA. b) side view photos showing wet soil curling away from the surface in 0.1 wt.% MGDA + 0.1 wt.% SDBS solution.

Table 9.3: Kinetic parameters of data in Figure 9.7 fitted to Equation 9.1 for solutions of 0.1 wt.% MGDA with 0.1 wt.% surfactant, 50 °C

		t_{onset} / s	$k_{\text{ADW}} (\times 10^{-4})$ / s^{-1}	R^2
pH 7	Reference	4500	1.67	0.94
	SDBS	3010	1.57	0.99
	TX-100	4330	1.34	0.98
	CTAB	5530	1.45	0.91
		t_{onset} / s	$k_{\text{ADW}} (\times 10^{-4})$ / s^{-1}	R^2
pH 10	Reference	3550	1.49	0.99
	SDBS	3750	1.73	0.98
	TX-100	4040	1.16	0.96
	CTAB	3050	0.28	0.83

At pH 7 all combinations of surfactant and MGDA gave similar cleaning rate constants, in the region of $1.5 \times 10^{-4} \pm 0.15 s^{-1}$. The main influence of the additives is on the onset of cleaning. The ‘induction time’ or delay between the first contact of the solution and the first dot to be removed depends on heat transfer (to melt fats within the soil), the diffusion of water, surfactants and ions into the soil layer, their ingress between the soil layer and the substrate and, potentially, the rate of removal of

the mobile elements within the soil, increasing the porosity of the soil layer. Assuming that the heat transfer process is common, it follows that at pH 7 the primary factors effecting cleaning rate are penetration of solution into, and the removal of the mobile components from, the soil.

The transfer of solution into the soil will be dependent upon the adsorption and absorption characteristics of the surfactant i.e. its wettability and penetration behaviour. LAS-type surfactants, such as SDBS, have been reported in the literature to be effective at solubilising fatty components (Dunstan and Fletcher, 2014). The enhanced removal of the mobile fats enables the MGDA to access the soil-solution interface earlier and as such decreases the induction time. At pH 10 the expected increase in porosity could be attributed to OH⁻ enhanced swelling as demonstrated by FDG data in Figure 5.15. SDBS therefore would no longer provide enhanced benefit over MGDA-alone, as observed in Figure 9.7 (b, ii).

TX-100 delays the onset time and cleaning rate of the soil at pH 10, possibly due to hydration of the polyethylene glycol (PEG) within TX-100. Competition between the TX-100 and the soil for OH⁻ ions could reduce the swelling of the soil, inhibiting the MGDA access. Similarly, CTAB gives a low rate of cleaning at pH 10 likely due to the formation of co-precipitates with both the OH⁻ ions and MGDA.

9.1.2.5 Step increase in pH

It was posited that delaying the addition of OH⁻ ions to the cleaning solution may enhance the cleaning rate of surfactant solutions in the absence of chelants. It was observed, in Figure 9.7 and during adhesion testing on the millimanipulation device (Chapter 7), that the induction time between contact of solution with the soil and the first measurable point of cleaning, determined by residual analysis, is shorter at pH 7 than at pH 10.

To investigate this phenomenon, solutions of 0.1 wt.% SDBS in deionised (DI) water were used to clean CMS dots in the ADW rig. A step increase of pH, achieved by adding 1.4 ml of aqueous 10 g/L NaOH solution was used to raise the pH of the cleaning solution to pH 10 at a set time. The rate of dot loss was plotted both from the start of solution contact (Figure 9.9 (a)) and from the addition of alkali (Figure 9.9 (b)). Analysis of the cleaning after 120 min shows that the hypothesis does not hold: the cleaning solutions that spent the longest time at pH 10 show faster cleaning over those that started at pH 7.

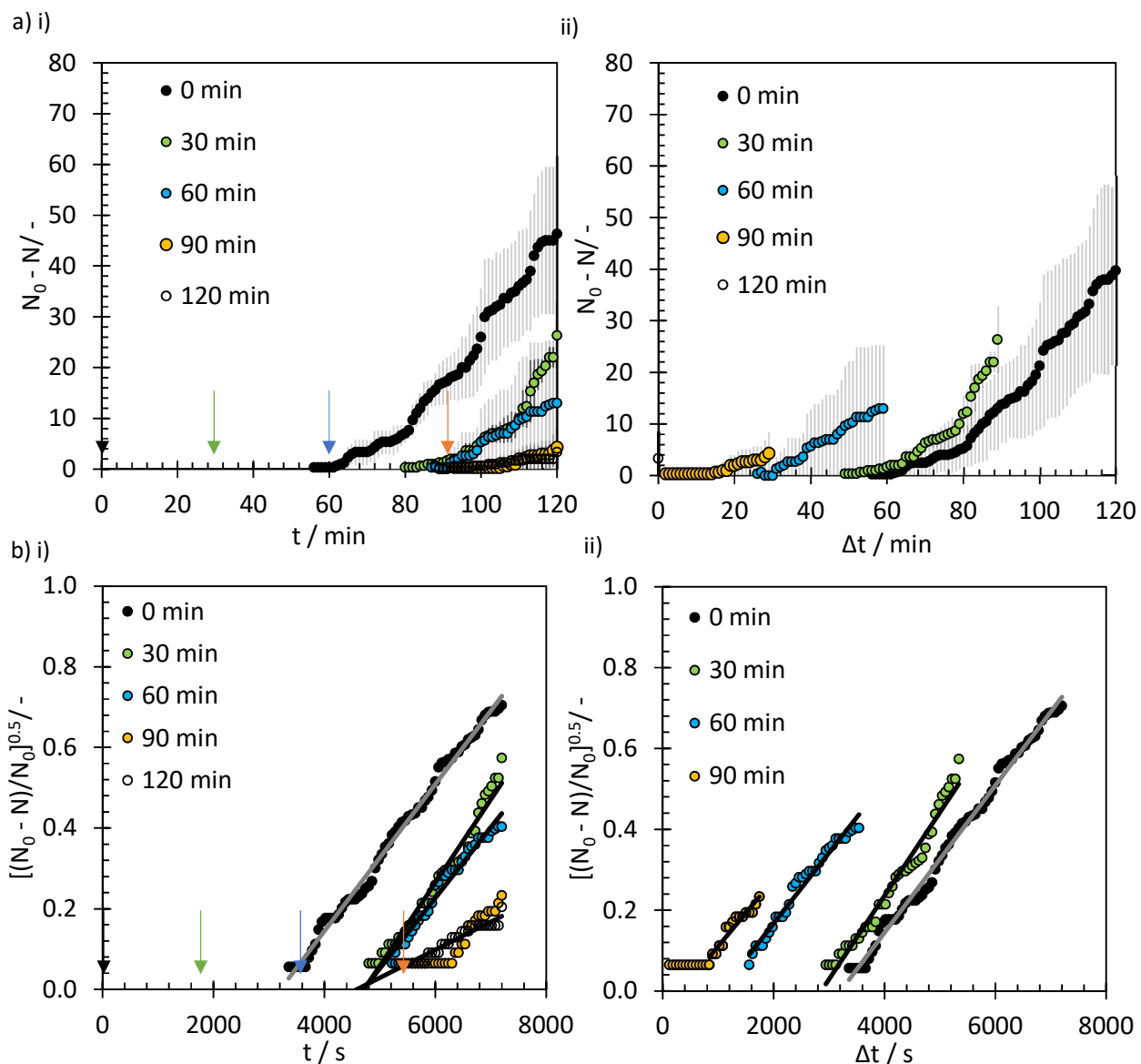


Figure 9.9: (a) Effect of step increase in pH from 7 to 10 at set time intervals. Data plotted as (i) time since start of test and (ii) time after addition of alkali. (b) Kinetic plots of normalized average dot loss plotted in the form of Equation 9.1 for (i) time since start of test and (ii) time after addition of alkali. Error bars indicate sample standard deviation of 3-4 samples. Arrows indicate dosage time. Lines show fit to Equation 9.1. Parameters in Table 9.4.

The rate of cleaning shows the same trend as Figure 9.7. The cleaning rate constant is similar for all samples, at approximately $1.85 \times 10^{-4} \text{ s}^{-1}$ (Table 9.4). This implies that the mechanism of cleaning after OH^- addition is consistent for all samples tested. The differences in the extent of cleaning after 120 min can therefore be attributed to differences in the induction time. The rate constants in these tests are a factor of 10 lower than that of those for swelling and image analysis of oil loss ($k_{\text{SIDG}} \sim 3 \times 10^{-3} \text{ s}^{-1}$, $k_{\text{droplet}} \sim 2 \times 10^{-3} \text{ s}^{-1}$). This is indicative of a slower cleaning process, likely due to the fact that the contact time with the solution is reduced. The soil is contacted with the solution once every 7.6 s. Scaling the

kinetic data to equivalent soil-solution contact time would increase the rate constant to approximately $1.4 \times 10^{-3} \text{ s}^{-1}$, which is in agreement with the other phenomena studied.

Table 9.4: Kinetic parameters of data in Figure 9.9 calculated using Equation 9.1 for pH 7 solutions doped up to pH 10 at set time intervals.

Time of pH step	$t_{\text{onset}} / \text{s}$	$\Delta t_{\text{onset}} / \text{s}$	$k_{ADW} (\times 10^{-4}) / \text{s}^{-1}$	R^2
0 min	3200	3200	1.8	0.99
30 min	4700	2900	2.1	0.97
60 min	4800	1000	1.8	0.97
90 min	5300	330	1.7	0.92

9.1.2.6 Effect of pH jump

The cleaning mechanism can be considered as involving the stages in Figure 9.10. Stages I and II are influenced by two factors, namely heat transfer and soil wetting. These can be considered to be dependent on liquid flow rate, interfacial tension (i.e. surfactancy), temperature of the cleaning solution, and soil characteristics. These are assumed to be independent of the pH of the solution and as such stage I will be independent of addition time. The removal of the fats is dependent primarily on the surfactancy of the solution. However, some dependence upon the pH could be considered due to the relationship between OH^- ions and swelling rate (Tsai *et al.* 2019), providing access for the surfactants to encounter and solubilise the fats. Stage III is constant throughout the pH only experiments (as k_{ADW} is constant). This stage would be impacted by the presence of surfactant, assisting in the solubilisation and removal of solid particulates.

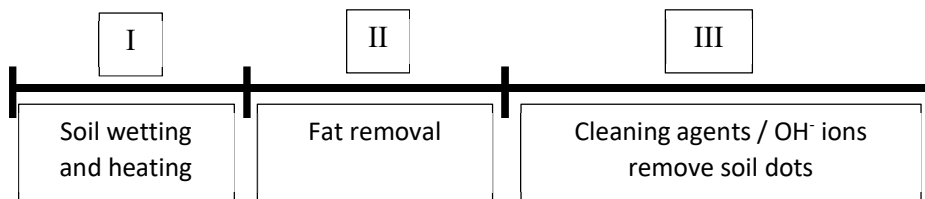


Figure 9.10: Simplified cleaning behaviour timeline

From Table 9.4 $t_{\text{onset}} = 3200 \text{ s}$ for pH 10 solutions. In this case (soil material, shape...) this indicates that Stages I and II requires a minimum of 3200 s to occur. For tests with doping at 30, 60 and 90 minutes, t_{onset} has been extended to approximately 5000 s, regardless of the time the pH is raised. This indicates that the OH^- ions are key to a process involved in cleaning that occurs a minimum of 300 s before the onset of measurable dot drop off, and is likely a function of swelling, but the significant bulk of the induction time was independent of pH. This concept of distinct stages in the cleaning process was

observed during FDG testing after a pH jump was introduced to the system (Chapter 5). In that test the soil swelled in pH 7 to a stable state then, when NaOH was added to raise the pH to 12, swelling was re-started and the soil swelled to a new, higher extent (Figure 5.10).

Knowledge obtained from studies on the MM3 and oil recovery testing (Chapter 8) suggests that in order to minimise t_{onset} of the cleaning process, surfactants should be introduced immediately to assist in the removal of oily substances, enhancing access for other cleaning additives. Figure 9.7 shows that the most effective of those tested is the anionic surfactant SDBS (also shown in Chapter 8 to be the surfactant most likely to act on the soil instead of the soil-substrate interface). Introducing this surfactant at the start of the test reduced t_{onset} significantly. Once dot removal had started the pH could then be boosted to enhance the cleaning rate constant ($k_{ADW} \sim 1.5 \times 10^{-4} \text{ s}^{-1}$ in surfactant solutions, $\sim 2 \times 10^{-4} \text{ s}^{-1}$ in pH 10). Figure 9.9 demonstrates that this cleaning rate is consistent regardless of addition time. Due to time constraints this proposal could not be tested.

9.1.2.7 Commercial detergent formulations

Two commercial dishwashing detergent products were tested in the ADW rig. These contain up to 13 different cleaning components, including but not limited to, surfactants, chelants, enzymes, bleach, shine agents, and anti-foamants. Commercial detergents were tested in the rig in order to benchmark results for model systems with commercial detergents, as tested in the ADW rig. Due to the presence of enzymes in the solutions, and the risk of denaturing them, the solutions were dissolved and heated for a fixed time (5 minutes) to ensure equal risk of denaturation. The two solutions have been denoted as commercial cleaning formulation 1 (CCF1) and commercial cleaning formulation 2 (CCF2) in randomised order to maintain commercial confidentiality requirements.

The dot-based cleaning profiles in Figure 9.11 show that the two commercial detergents gave very different cleaning profiles. The (average) first soil dot was removed at the same time (within the 10 s time resolution of the test). For CCF1 this was followed by linear removal, whereas for CCF2 the same rate relationship as the simple (pH, surfactant and chelant only) solutions reported above was observed, i.e. Equation 9.1 with $n = 0.5$.

The rates of cleaning can be quantified from the gradients of the trend-lines in Figure 9.11 (green for CCF1 at $n = 1$ and purple for CCF2 at $n = 0.5$) (Table 9.5). When comparing the initial rate of cleaning, after t_{onset} , for both solutions using the parameter $n = 1$ in Equation 9.1, Figure 9.11 (a) shows that whilst both formulations have the same onset times ($t_{onset} = 2640 \text{ s}$) CCF1 has a markedly higher rate constant for dot drop-off than CCF2 ($k'_{ADW} = 1.9 \times 10^{-4} \text{ s}^{-1}$ vs $0.35 \times 10^{-4} \text{ s}^{-1}$).

Comparison of initial cleaning rate constants between CCF1 and the best single system surfactant, SDBS, with $n = 0.5$ shows that CCF1 has both a higher cleaning rate constant ($k_{ADW} = 4.1 \times 10^{-4} \text{ s}^{-1}$ for CCF1 vs $1.57 \times 10^{-4} \text{ s}^{-1}$ for SDBS) and an earlier onset time ($t_{onset} = 2640 \text{ s}$ vs 3010 s for SDBS), indicating superior cleaning performance for the highly formulated system, with $\sim 90\%$ of all dots removed from the surface after 7000 s in this test. CCF2, whilst featuring an earlier onset time than SDBS solution ($t_{onset} = 2640 \text{ s}$ for CCF2 vs 3010 s for SDBS), has a lower rate constant ($k_{ADW} = 1.0 \times 10^{-4} \text{ s}^{-1}$ vs $1.57 \times 10^{-4} \text{ s}^{-1}$) and removed fewer dots from the substrate by the end of the test ($\sim 60\%$ vs $\sim 70\%$ for SDBS-only).

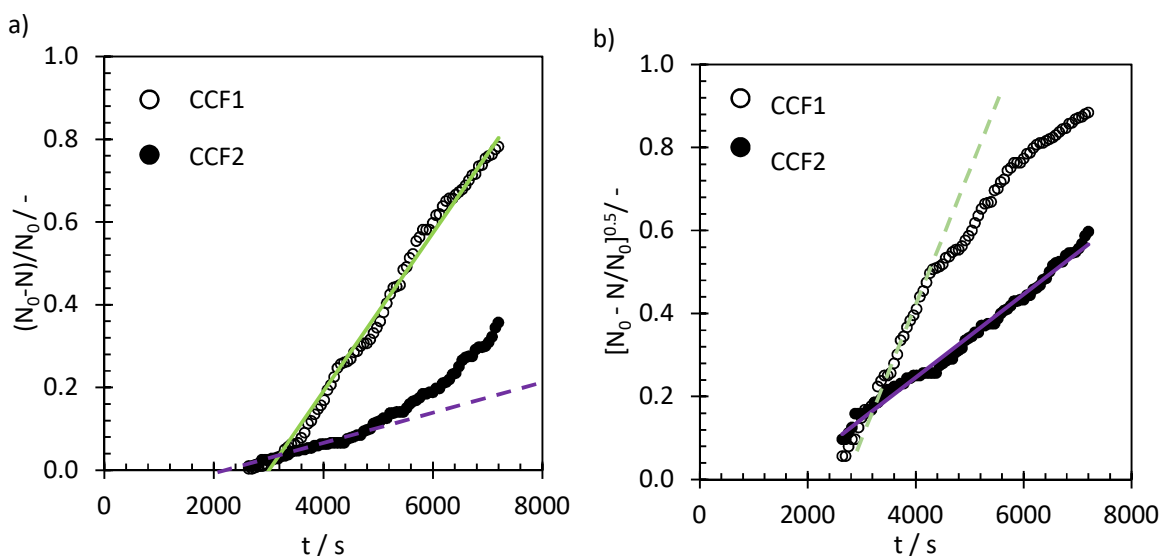


Figure 9.11: Average cleaning of CMS dots with commercial detergents on the ADW rig, plotted in the form of Equation 9.1 with (a) $n = 1$ and (b) $n = 0.5$. Solid trendlines show linear fits. Dashed trendline shows fit to initial data. Parameters tabulated in Table 9.5. 4 repeats per solution. 80 soil dots per plate. $T = 50 \text{ }^\circ\text{C}$, $\text{pH } 10.4$

It is not possible to explain this difference in cleaning effectiveness between the two formulations mechanistically without full knowledge of their compositions. However it is clear that there is a difference between the two commercial formulations. Of all the devices used in this work the ADW rig is expected to reproduce the conditions encountered in a dishwasher most faithfully. Research into any possible antagonisms between the detergent system used in CCF2 and the other components within the formulation is recommended. The poor performance of CCF2 compared to the SDBS-alone suggests that inhibition of the surfactant action is occurring.

Even with the fully formulated solutions, stages I and II (Figure 9.10) still require almost 45 minutes on the ADW rig. This delay should be considered when comparing timescales of cleaning between the ADW rig and the MM3 or SiDG; in those tests the sample is fully submerged in pre-heated solution,

whereas on the ADW the soil is contacted with the solution periodically as the jet cycles across the sample plate. This intermittent contact is not sufficient to explain the difference between t_{onset} on the ADW rig and the other techniques tested (t_{onset} for DI at 50 °C = 3640 s for ADW, 220 s for MM3, 960 s for droplet formation and <6 s for swelling). Further work is required to explain the difference in cleaning onset times, e.g. differences in the (i) substrate, (ii) the level of cross-polymerisation of the CMS dots upon baking (the dots have a higher surface area to volume ratio and would therefore be expected to burn at a faster rate), (iii) CMS preparation method (using a microwave to melt the fat component before mixing vs using a hotplate) etc.

Table 9.5: Kinetic parameters obtained by fitting Equation 9.1 to data generated in Figure 9.11 for commercial cleaning detergents. k' denotes $n = 1$, k denotes $n = 0.5$.

	n	t_{onset}	$k'_{ADW} (\times 10^{-4})$ / s^{-1}	$k_{ADW} (\times 10^{-4})$ / s^{-1}	R^2
CCF1	1	2640	1.9	(4.1)	0.99
CCF2	0.5	2640	(0.35)	1.0	0.99

9.1.3 Shear Forces

Millimanipulation forces can be compared with the shear forces acting in the ADW rig. The shear forces acting on the surface beneath each dot can be estimated as the sum of the dot's weight and the force applied by the falling film, F . The upthrust from the falling film is considered negligible. These forces are given by;

Equation 9.2

$$F = M_d g + M_w D$$

where M_d is the mass of the dot, D is the diameter of the dot and M_w is the rate of flow of momentum of the falling film per unit width, estimated using

$$M_w = \frac{\dot{M}}{L} \cdot \frac{\dot{M}}{\rho_s L h} = \frac{\dot{M}^2}{\rho_s L^2 h}$$

Equation 9.3

Here \dot{M} is the mass flow rate of the falling film, ρ_s is the density of the cleaning solution, L is the width of the falling film, and h is the height of the falling film.

The average shear stress acting at the interface of the soil with the wall is;

$$\tau_{dot} = \frac{4}{\pi D^2} [M_d g + M_w D]$$

Equation 9.4

This gives τ_{dot} of 3.5 Pa at first contact between soil and solution. Over time τ_{dot} will increase linearly as the soil swells and absorbs solution. The soil volume was estimated using SiDG data to increase by 160 % in 400 s, giving a $\tau_{dot, 500s}$ of 5.5 Pa. The shear stress that was applied to remove the soil predicted using the MM3 at this time was 4 kPa. This is a factor of 10^3 larger than the forces present on the dot after 400 s. Using a rate of decay for the shear stress of CMS, calculated based on data from tests of CMS submerged in pH 7 solution at 50 °C, it was estimated that the shear stress applied by the falling film surpassed the adhesion strength of the soil to the substrate after approximately 62 minutes. After this time the soil dot is expected to fall under its own weight. This assumes that the soil is submerged in the cleaning solution which is not the case on the ADW rig.

It was estimated that the jet contacts an average of 5 out of 10 dots at any one time during each oscillation, which would increase the t_{onset} estimation to 124 minutes, which lies beyond the experiment period. In the presence of surfactants the adhesion strength to the soil is being decreased by the action of cleaning chemistry, as well as the water uptake. Predictions based upon the MM3 cleaning profile of CMS submerged in SDBS solution at 50 °C give an estimated t_{onset} of 78 minutes. This is an overestimate of the recorded t_{onset} of 52 minutes. This difference is likely due to either error in the exponential decay profile estimated from MM3 data, or from the fact that, if the solution is refreshed regularly, the availability of additives to perform actions associated with enhanced cleaning may not be exhausted between each cycle. There is general agreement between the trends on the MM3 and the ADW rig. A second source of error is the wetting behaviour of the solutions. A solution containing 0.1 % SDBS will exhibit enhanced wetting of the dots over the pH 7 solution, which was not factored into the prediction, and could contribute to the overestimation in t_{onset} .

9.1.4 Stage 1 conclusions

The ADW rig was utilised to investigate the impact of pH, surfactancy and chelants on the removal of CMS from stainless steel substrates. There was an induction time of approx. 3000 s before any visible cleaning occurred, longer than that of any experimental conditions tested in this work. This is likely due to the requirement to heat the soil and transfer agents to and from the soil before the adhesive bonds at the interface are sufficiently weakened to enable soil detachment. The onset of cleaning, here quantified in terms of dot removal, can be related to the shear induced stresses on the soil-substrate interface arising from its vertical mounting i.e. after sufficient water is absorbed and adhesive weakening has occurred, the weight of the soil provides the mechanical force required to detach the soil from the substrate.

pH alone was shown to have little impact on the cleaning rate or magnitude. The use of surfactants and chelants provided visible benefit in the ADW rig. When used with SDBS, increasing pH reduced the induction time for the onset of visible cleaning. SDBS was the most effective of all surfactants tested, possibly due to its low surface tension and strong wetting of both stainless steel and CMS.

MGDA was found to act at the soil-substrate interface in a different manner than the surfactants, enhancing dot removal ten-fold. It promoted ingress and peeling at the soil-substrate interface, indicating that the chelant is capable of penetrating into the soil layer and disrupting the adhesive bonding between soil and substrate.

Finally the stability of the falling film was determined to be important for dishwasher operation due to its effect on the contact time between cleaning solution and soil.

9.2 P&G formulations on Cambridge Rigs

Although surfactants have proved effective in reducing the soil-substrate adhesive forces under the right conditions (Chapter 7), commercial detergent formulations can contain up to 13 components within each dose. Agents such as bleaches, chelates and shine agents are all surface active and will interact strongly with both the soil and the substrate under standard conditions. These interactions may be either synergistic or antagonistic in nature.

Two commercial formulations were provided by P&G for testing on the rigs developed in this work. One was a 'liquitab' that dissolved readily in hot water with stirring. The second came in tablet form, which required grinding into a powder before being added to 5 L hot water. Due to the presence of enzymes the time between dissolving the formulation and testing on each rig was set to 5 minutes.

Tests on the MM3 and SiDG were conducted using CCF1, with and without the oxygen bleach component sodium percarbonate. This component forms 10 % of the concentrated cleaning formulation. This formulation was tested to investigate the impact of bleach on cleaning. To replicate common consumer environments the testing was conducted both on 316 stainless steel and borosilicate glass substrates at 22 °C and 50 °C. Both CCF1 and CCF2 were tested via an adapted solution analysis technique, described in section 3. The ADW rig was not used.

9.2.1 Commercial formulation testing

9.2.1.1 Effect of commercial formulation and bleach on stainless steel

Figure 9.12 (a) demonstrates the impact of bleach on CCF1. At 22 °C the commercial formulation, with and without bleach, shows little interaction with the soil-substrate interface as characterised by the

late B/C transition, similar to those observed at pH 7 ($t_c = 330$ s with bleach and 370 s without, vs ~ 330 s at pH 7). After t_c both solutions present relatively high linear decay rates ($k_{MM3} = -0.46$ and -0.48 N $m^{-1} s^{-1}$ respectively vs 0.06 N $m^{-1} s^{-1}$ for pH 7, Figure 7.11 (a)).

At 50 °C (Figure 9.12 (a) (iii, iv)) bleach has a significant impact. When bleach is present in the CCF1 formulation there is a B/C transition at 260 s then a linear decrease in $\langle F_w \rangle$ to ~ 60 N m^{-1} until the end of the test. When the bleach is not present $\langle F_w \rangle$ decreases rapidly for 90 s before plateauing at 130 N m^{-1} until 380 s where a sharp B/C transition is observed.

Figure 9.12 (b, i) shows that the swelling profiles CMS submerged in CCF1 are affected by bleach. Swelling of CCF1 without bleach reaches $\Delta\delta_{i,max}$ of 0.19 mm with a rate constant of $k_{zFDG} = 2.55 \times 10^{-3} s^{-1}$, similar to that observed for a pH 7 water-only system at 20 °C on the zFDG ($\Delta\delta_{i,max} = 0.19$ mm and $k_{zFDG} = 1.71 \times 10^{-3} s^{-1}$) though with a slightly faster rate constant. The cause of this was discussed with P&G® and a detrimental interaction between MGDA (a common chelant) and the bleach was identified by in-house testing conducted at P&G®.

The swelling profile of CCF1, in the absence of MGDA, was also investigated. Figure 9.12 (b, ii) shows that there is an increase in the extent of swelling ($\Delta\delta_{i,max} = 0.26$ mm vs 0.19 mm for CCF1) and a decrease in the rate constant ($k_{zFDG} = 0.84 \times 10^{-3} s^{-1}$ vs $k_{zFDG} = 2.55 \times 10^{-3} s^{-1}$) for CCF1 without MGDA or bleach. When bleach is included there is a reduction in swelling magnitude ($\Delta\delta_{i,max} = 0.18$ mm vs 0.26 mm without bleach). Rate data were not obtainable for this system due to what is believed to be a soil blister formed under the nozzle which bursts at 500 s. This blister implied that the initial soil hydration/swelling was sharp for the bleach containing solution even though the final $\Delta\delta_{i,max}$ was lower.

It is evident that the bleach has a detrimental impact on the swelling of CMS in a fully formulated system, even without the observed antagonism with MGDA (which also had a detrimental impact on soil swelling). In order to determine if this impact was based upon inhibitive interactions with other components within the formulation or a function of the mode of action of the bleach itself, tests were performed on simple combinations of MGDA and bleach.

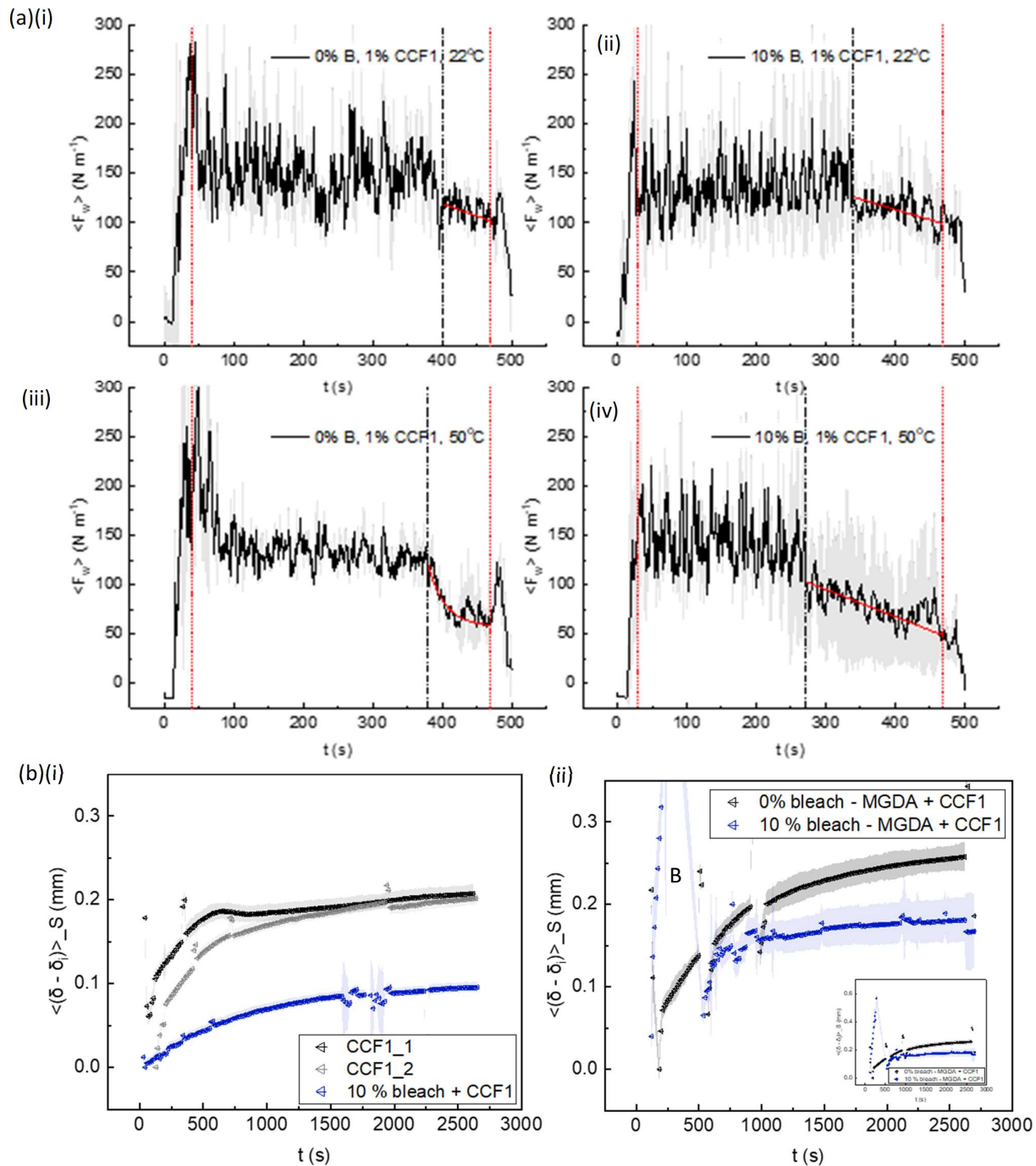


Figure 9.12: (a) MM3 testing showing the effect of temperature on average removal force of CMS from stainless steel following contact with 1 % CCF1 solution at $t = 0$ and (i) 0 % bleach, 22 °C (ii) 10 % bleach, 22 °C (iii) 0 % bleach, 50 °C (iv) 10 % bleach, 50 °C. Dashed lines mark initial and final regions subject to soil edge effects from soil pinning at the edge of the plate. Data outside these lines are discounted, repeated in subsequent plots. Dot-dashed lines mark the transition in decay behaviour at t_c . Solid red line in (i, ii, iv) shows fit to linear decay, red line in (iii) shows fit to exponential decay. Shaded grey area region is range of 2 repeat samples. Parameters reported in Table 9.6. (b) SiDG testing at 20 °C showing the effect of effect of (i) CCF1 with and without bleach (ii) CCF1, without MGDA, with and without bleach on soil swelling suction mode. B – blister.

9.2.1.2 Effect of MGDA and bleach on CMS on stainless steel

MGDA solutions at 22 °C gave $\langle F_w \rangle = 150 - 200 \text{ N m}^{-1}$, with a B/C transition at 200 s, faster than that of pH 7 water (B/C = 360 s in pH 7 water, Figure 9.13 (a, i)) with a steady linear decay rate of $-0.72 \text{ N m}^{-1} \text{ s}^{-1}$. At 50 °C (Figure 9.13 (a,iii)) the benefit of MGDA is pronounced with the B/C transition occurring within the initial edge effect period and exponential decay, with $t_d = 393 \pm 12 \text{ s}$ similar to profiles obtained for both TX-100 and SDBS at 50 °C (Figure 7.15 (b, c)), though with a steeper gradient, due to the larger $\Delta \langle F_w \rangle$.

The use of 0.1 % MGDA and bleach together showed the opposite behaviour. This formulation (Figure 9.13 (a, ii)) differed little from a pH 7 only solution (Figure 7.11 (a)) at room temperature. The removal profiles are similar and pH 7 water, with initial $\langle F_w \rangle$ values following hydration between 100 and 150 N m^{-1} and the B/C transition at 320 s and 360 s, respectively. At higher temperatures, (50 °C, Figure 9.13 (a, iv)), the B/C is slightly earlier than at 22 °C (290 s vs 320 s) however it is later than at pH 7 alone (Figure 7.11 (b)) which showed a B/C transition at 220 s followed by an exponential decay. The MGDA and bleach case decays linearly.

These results indicate that the MGDA is adept at acting at the soil-substrate interface, with the effect of weakening the soil-substrate bonds, most likely as it absorbs to the steel itself, providing an inhibitive buffer between soil and solution. This effect is delayed by 250 s in the presence of bleach, either through competition for the substrate surface, or via interaction with the MGDA itself.

The swelling profiles in MGDA and bleach (Figure 9.13 (b, i, ii)) were not strongly affected by the presence of either component. Both MGDA and bleach containing solutions caused the same extent of swelling of CMS after 2500 s ($\Delta \delta_{i,max} \approx 0.2 \text{ mm}$) however the bleach solution achieved this more slowly ($t_{asym, zFDG} = 2500 \text{ s}$ vs 800 s for pH 7 only). This indicates that the mechanism by which both MGDA and bleach inhibit the swelling of the soil in CCF1 is formulation based and not a function of its direct interaction with the soil layer. Without detailed knowledge of the full formulation composition it was not possible to determine the exact antagonism that takes place. This demonstrates the careful balance that must be struck when utilising both components to maximise the cleaning effectiveness in full scale testing.

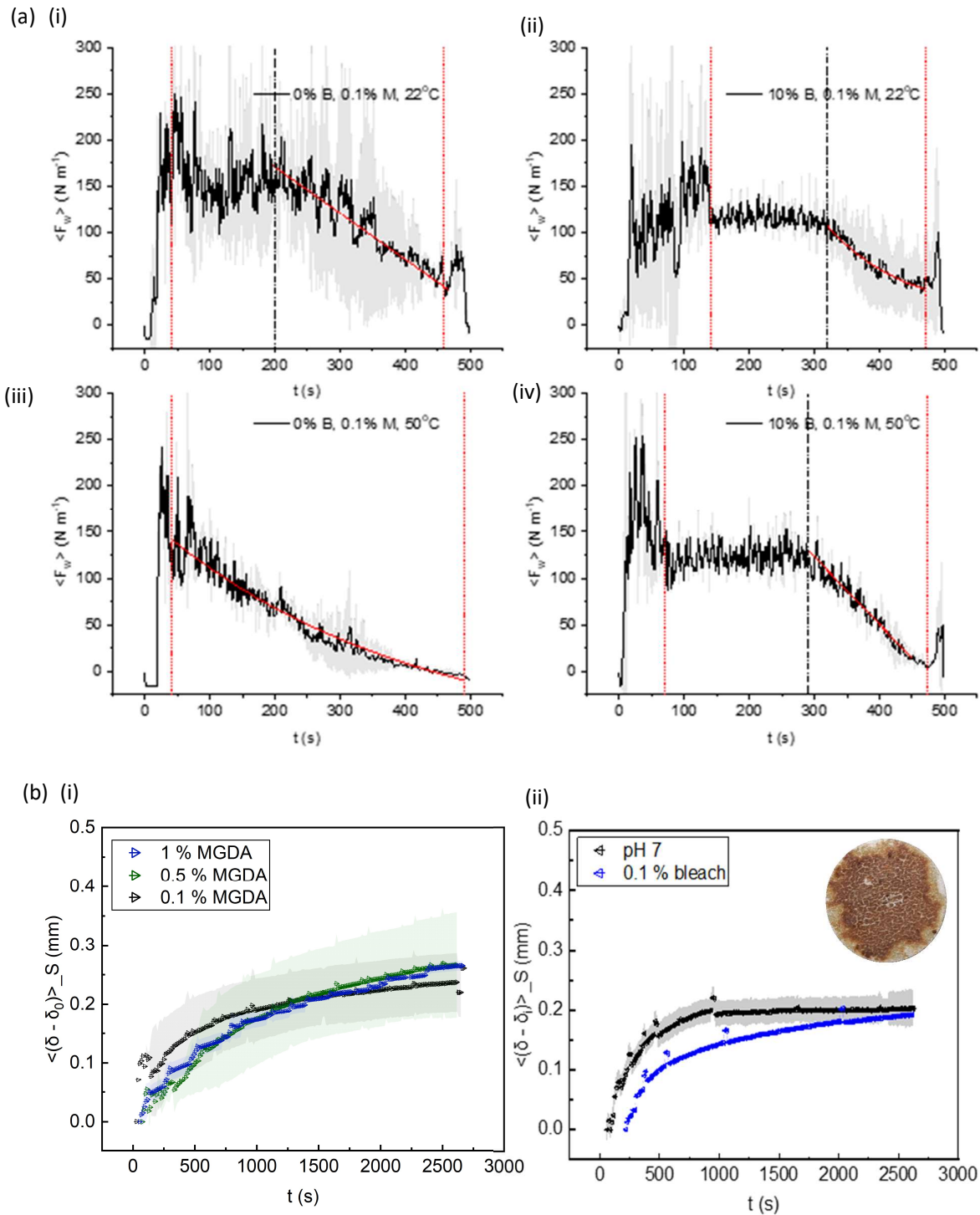


Figure 9.13: (a) MM3 testing showing the effect of temperature on average removal force of CMS from stainless steel following contact with 0.1 wt% MGDA solution at ($t = 0$) and (i) 0% bleach, 22 °C; (ii) 10% bleach, 22 °C (iii) 0% bleach, 50 °C (iv) 10% bleach, 50 °C. Dot-dashed lines mark the transition in decay behaviour at t_c . Solid red line in (i, ii, iv) shows fit to linear decay, red line in (iii) shows fit to exponential decay. Shaded grey area region is range of 2 repeat samples. Parameters reported in Table 9.6. (b) SiDG testing showing the effect of (i) MGDA and (ii) bleach, on soil swelling using suction mode. Inset in (b, ii) photograph of CMS soil after testing with bleach showing discolouration.

9.2.3 Glass Substrates

The impact of CCF1 on the cleaning of CMS from borosilicate glass substrates was investigated. Soil swelling was not investigated as the primary change in behaviour was expected to occur at the soil-substrate interface and not within the bulk soil itself.

Previous testing has shown that CMS binds slightly less strongly on glass substrates ($\langle F_w \rangle = 149 \text{ N m}^{-1}$) than to stainless steel ($\langle F_w \rangle = 163 \text{ N m}^{-1}$) (Figure 7.3). However as the two substrates have different surface energies it is likely that cleaning agents have differing affinities for the surface and their behaviour may be different at soil-substrate interface.

The function of the cleaning agents would vary because (i) removal is by ingress (adhesion \rightarrow direct influence) or (ii) the overall cleaning rate is affected by the weaker soil adhesion to glass substrates.

9.2.3.1 Effect of commercial formulation and bleach on glass

Figure 9.14 demonstrates the impact of CCF1 with and without bleach on CMS-borosilicate glass. At both 22 °C and 50 °C, CCF1 with bleach shows poor interaction with the soil-substrate interface characterised by late B/C transitions (270-400 s) and low linear decay rates ($k_{MM3} = 0.21 - 0.25 \text{ N m}^{-1} \text{ s}^{-1}$). However at 50 °C, the solution containing bleach showed a decrease in $\langle F_w \rangle$ to $\sim 50 \text{ N m}^{-1}$ after 460 s whereas in all other samples $\langle F_w \rangle$ remained high ($> 100 \text{ N m}^{-1}$) with slow linear decay rates after the B/C transition.

Formulations without bleach showed similarly poor performance, with a later B/C transition of $\sim 400 \text{ s}$ in both cases, accompanied by a small reduction ($\sim 30 \text{ N m}^{-1}$) in $\langle F_w \rangle$ at 22 °C and a larger reduction at 50 °C ($\sim 70 \text{ N m}^{-1}$).

It can be observed therefore that, even though the overall adhesion of CMS to the glass is lower than for the stainless steel, the rate and weakening of adhesion is reduced in both cases, more so at 50 °C. This observation indicates that both the bleach and the MGDA function, either directly or indirectly at the soil-substrate interface and may have a lower affinity for borosilicate glass than for stainless steel. As the CMS layer composition is assumed to be unchanged when baked onto glass or stainless steel, it is assumed that the weakening of cohesive strength in the CMS after submersion that contributes to $\langle F_w \rangle$ will be constant in comparisons of $\langle F_w \rangle$ between stainless steel and glass substrates. Experiments were subsequently conducted with only bleach and MGDA in combination, in order to investigate this effect (Figure 9.15).

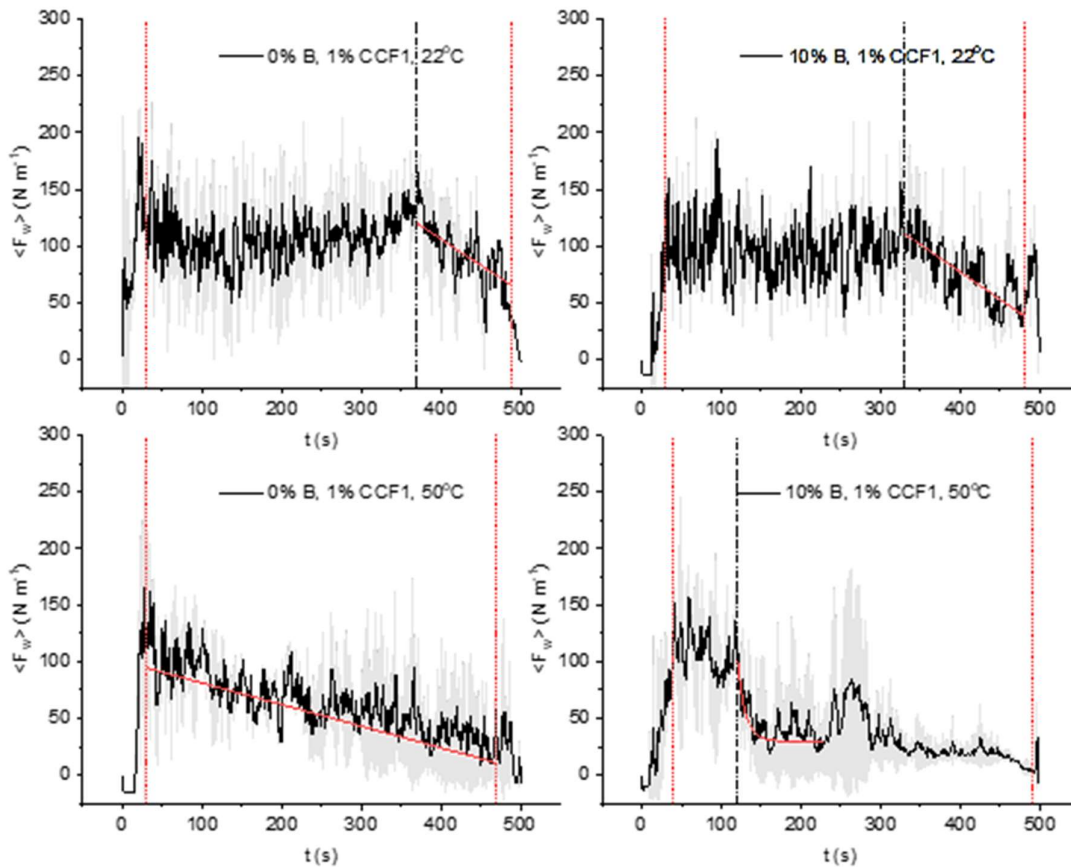


Figure 9.14: MM3 tests showing the effect of temperature on average removal force of CMS from glass following contact with 1 % CCF1 solution at $t = 0$ at (i) 0 % bleach, 22 °C (ii) 10 % bleach, 22 °C (iii) 0 % bleach, 50 °C (iv) 10 % bleach, 50 °C. Dot-dashed lines mark the transition in decay behaviour at t_c . Solid red line in (i-iii) shows fit to linear decay, red line in (iv) shows fit to exponential decay. Shaded grey area region is the range of 2 repeat samples. Parameters reported in Table 9.6.

9.2.3.2 Effect of MGDA and bleach on glass

Figure 9.15 shows the impact of the removal of bleach on the removal forces of CMS submerged in MGDA solutions. At 22 °C neither solution containing MGDA exhibited strong adhesion decay profiles. The MM3 profiles are similar to those of simple aqueous solutions at pH 9 and 12 (Figure 5.15), and CCF1 (Figure 9.14 (a) (i, ii)), where there is a weak reduction in $\langle F_w \rangle$ and late, weak B/C transitions (300 s and 400 s).

At 50 °C (Figure 9.15 iii, iv) the impact of bleach is the opposite of that seen on stainless steel. The B/C transition occurs after 190 s with solutions of MGDA alone but is faster in solutions containing both bleach and MGDA ($t_c = 120$ s vs 290 s). Both profiles also show linear decay ($k_{MM3} = 0.29$ N m⁻¹ s⁻¹ and 0.33 N m⁻¹ s⁻¹ without and with bleach, respectively). This indicates that the bleach and MGDA are functioning cooperatively to reduce the MM3 forces at the interface and as such indicates that the

inhibitive effect on the cleaning in CCF1 is a formulation effect, through interactions with other additives and not a function of the bleach or MGDA actions on the soil themselves. Alternatively it could be a function of the change in the de-wetting of the oil component within the soil, which is mobile at 50 °C.

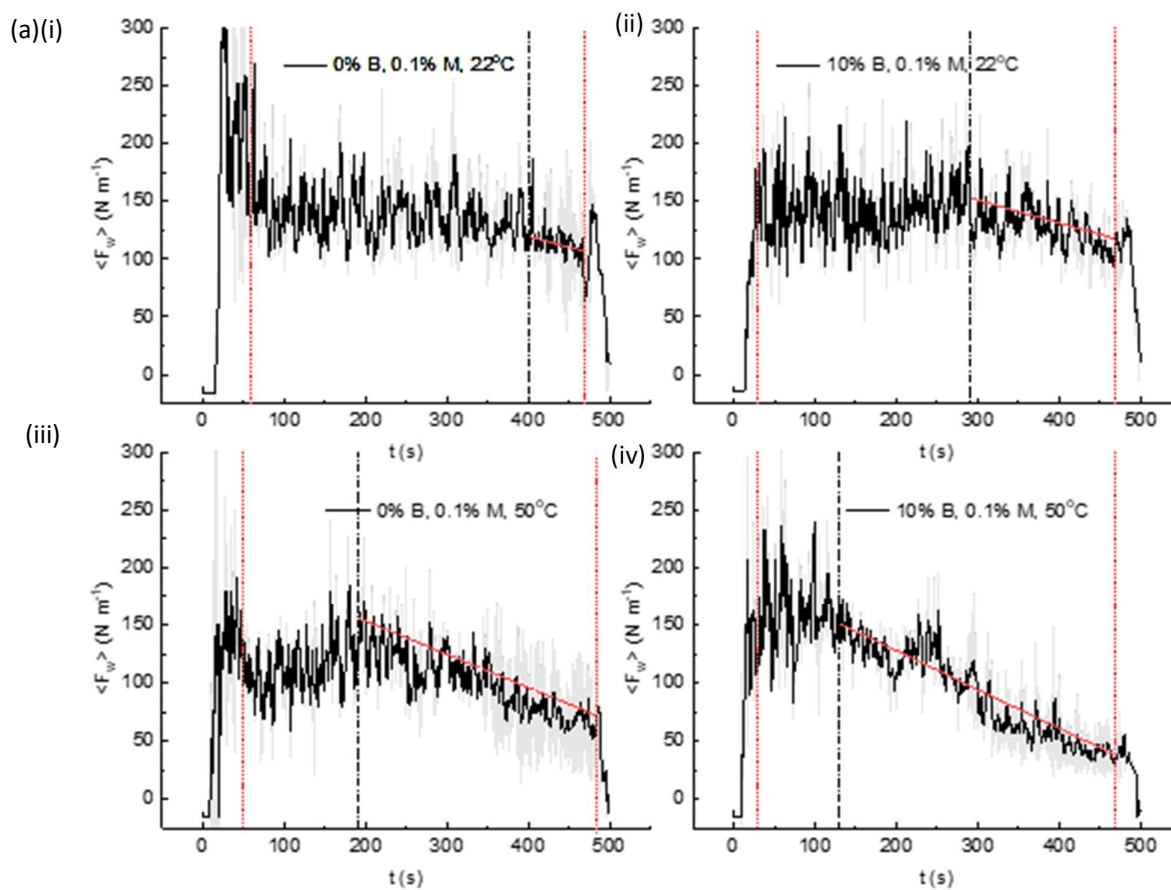


Figure 9.15: Effect of temperature on average removal force of CMS from glass following contact with 0.1 wt% MGDA solution at $t = 0$ at (i) 0 % bleach, 22 °C (ii) 10 % bleach, 22 °C (iii) 0 % bleach, 50 °C (iv) 10 % bleach, 50 °C. Dot-dashed lines mark the transition in decay behaviour at t_c . Solid red line in (i-iii) shows fit to linear decay, red line in (iv) shows fit to exponential decay. Shaded grey area region is the range of 2 repeat samples. Parameters reported in Table 9.6.

The decay behaviour and decay rate parameters from Figures 9.12 through 9.15 are summarised in Table 9.6. The cleaning agents have different effectiveness in weakening the soil-substrate adhesion on glass and stainless steel.

Table 9.6: Summary of rate of change of MM3 forces over 500 s testing in Figures 9.12 - 9.15. Uncertainty parameters were based on one standard deviation.

Plate	Bleach / %	MGDA / %	CCF1 / %	t_c / s		k / N m ⁻¹ s ⁻¹		t_D / s	
				20°C	50°C	20°C	50°C	20°C	50°C
SS	pH 9 reference			-	220	0.15±0.02	0.26±0.01	-	-
SS	0	0.1	-	200	40	-0.45 (± 0.0005)	-	-	393 (± 12)
	10	0.1	-	320	290	-	-0.72 (± 0.002)	120 (± 15)	-
SS	0	-	1	370	-	-0.46 (± 0.003)	-0.19 (± 0.001)	-	-
	10	-	1	330	120	-0.48 (± 0.002)	-	-	9.62 (± 0.89)
Glass	0	0.1	-	400	190	-0.18 (± 0.07)	-0.29 (± 0.0002)	-	-
	10	0.1	-	290	130	-0.20 (± 0.002)	-0.33 (± 0.009)	-	-
Glass	0	-	1	400	380	-0.25 (± 0.001)	-	-	24.37 (± 2.33)
	10	-	1	340	270	-0.21 (± 0.01)	-0.28 (± 0.01)	-	-

9.2.4 Overview of results

The reason why bleach and MGDA show antagonism at 50 °C on stainless steel is now considered. MGDA alone behaves similarly to Tx-100 and CTAB at 50 °C, exponentially reducing the required shear forces required to remove soil from substrate. At pH 7 MGDA will have two negatively charged sites (MGDA pKa: 1.6, 2.5 and 10.5; BASF, 2007) and should be considered a strongly anionic molecule with a high affinity for positively charged metallic ions. Removal of Ca²⁺ (present in the CMS from the milk component) as well as counter ions such as Na⁺ may promote swelling and soil weakening which will be manifested in a drop in the cohesive contribution to the force measured by the millimanipulation blade.

At room temperature access of the MGDA to the soil matrix would be inhibited by the solid hydrophobic fat within the soil preventing ingress of both water and the highly polar MGDA. The earlier B/C transition indicates that the MGDA also interacts with the metals on the substrate surface, displacing bonds between the soil and substrate, weakening its overall adhesive strength.

Sodium percarbonate (2 Na₂CO₃ · 3 H₂O₂) dissolved in water forms a polar, negatively charged molecule (CO₃²⁻) that is expected to interact both with the soil matrix and with stainless steel surfaces (Bäck *et al.* 2004). It is possible that competitive inhibition is occurring as both molecules compete for the same sites. If the percarbonate is displacing the MGDA for sites on the substrate surface then the

MGDA would preferentially bind with the free metal ions contained within the soil, e.g. Ca^{2+} , rather than the substrate surface, preventing it from acting to weaken the soil-substrate bonds.

This hypothesis is supported by the fact that MGDA is significantly less effective on glass substrates than stainless steel, even though the soil binds more weakly to glass than steel. MGDA is not known to interact strongly with silica-based structures and as such would not displace the soil at either temperature tested.

CCF1 demonstrated no marked increase in effectiveness other than that of the CCF1 + 10 % bleach, at 50 °C, on SS substrates. In this system a sharp decrease in $\langle F_w \rangle$ was noted. This is unsurprising as the formulation consists of agents designed to perform several functions. The comparison is being made between the agents expected to function at the adhesive interface and the commercial formulation containing components irrelevant to the observable interface, which may be impacting their behaviour in the solution. The most notable result was the variation between the substrates. This demonstrates the importance of testing a range of substrates as its efficacy may not be similar for similar soils on other substrates.

9.2.5 Stage 2 conclusions

The millimanipulation flow device was used to investigate the forces at the soil-substrate interface for in commercial cleaning formulations. The complex model food soil exhibited adhesive weakening during testing, depending on the cleaning solution chemistry.

Common cleaning agents MGDA and bleach exhibited an antagonistic interaction, inhibiting the reduction of $\langle F_w \rangle$ when used at concentrations relevant to consumer formulations. Possible mechanisms of this antagonism are proposed. Fully formulated cleaning solutions were demonstrably less effective than surfactants or chelants alone, potentially due to bulk solution interactions or competition for active sites to perform cleaning action.

Glass substrates were shown to give weaker binding to CMS but also exhibited reduced clean-ability defined in terms of timing and rate of reduction of $\langle F_w \rangle$, demonstrating the importance of formulating for a range of surface chemistries.

9.3. Oil Recovery - Batch System

In a commercial dishwasher the cleaning solution is recirculated within the automated unit. A dishwashing tablet (or liquitab) containing up to 13 components is added to the cleaning solution early in the dishwashing cycle. These tablets are often designed to promote a staged release mechanism, with some components, e.g. surfactants, bleaches, alkali, released early on in the dishwashing cycle whilst others, e.g. shine agents, are released towards the end. In the static system described in Chapter 6, the cleaning solution is continuously replenished and therefore does not replicate dishwasher action.

9.3.1 Test set-up

A batch test system, similar to the static system, was devised (Figure 9.16). A larger volume of solution (640 ml for batch vs 300 ml for static) was placed in a thermostatted reservoir heated by an external heater-circulator to the required temperature. 50 x 50 mm soiled substrates were suspended centrally in the solution chamber, fully submerged throughout the test. 40 ml aliquots were removed periodically. The solution was not replenished.

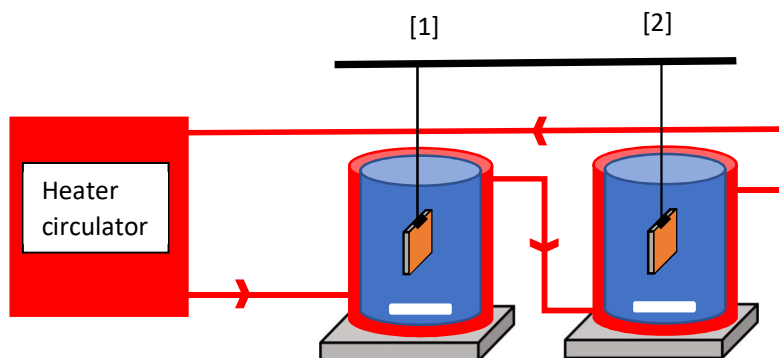


Figure 9.16: Schematic of batch rig for investigating oil release of CMS samples. Solutions are stirred by a magnetic stirrer bar (SB) at 300 rpm.

9.3.1.1 Substrates

50 x 50 mm ($\delta = 1.89$, $R_q = 1.6 \mu\text{m}$) polished 316 stainless steel substrates, similar to those used in MM3 testing, were soiled with 1.8 ± 0.07 g CMS. The soil was then left to evaporate for 24 hours (CMS mass = 0.8 ± 0.03 g, 55 % mass loss), before being baked at 204 °C for 7 minutes. Cracks formed upon baking. The final burnt CMS plates had a soil mass of 0.77 ± 0.03 g with an overall mass loss of 57 %. This is similar to other CMS samples.

9.3.1.2 Test solutions

Test solutions were prepared in batches using 5 L deionised water and 1 tablet of commercial cleaning formulation. A further pH 9 buffered solution was prepared using Reagecon buffer solution (pH 9 ± 0.01 at 20°C, \sim pH 8.8 at 50°C). The mixtures were prepared by stirring at 50 °C for 30 minutes before

being left to cool to room temperature. 640 ml of solution was used per test prepared a maximum of 5 minutes before test commencement.

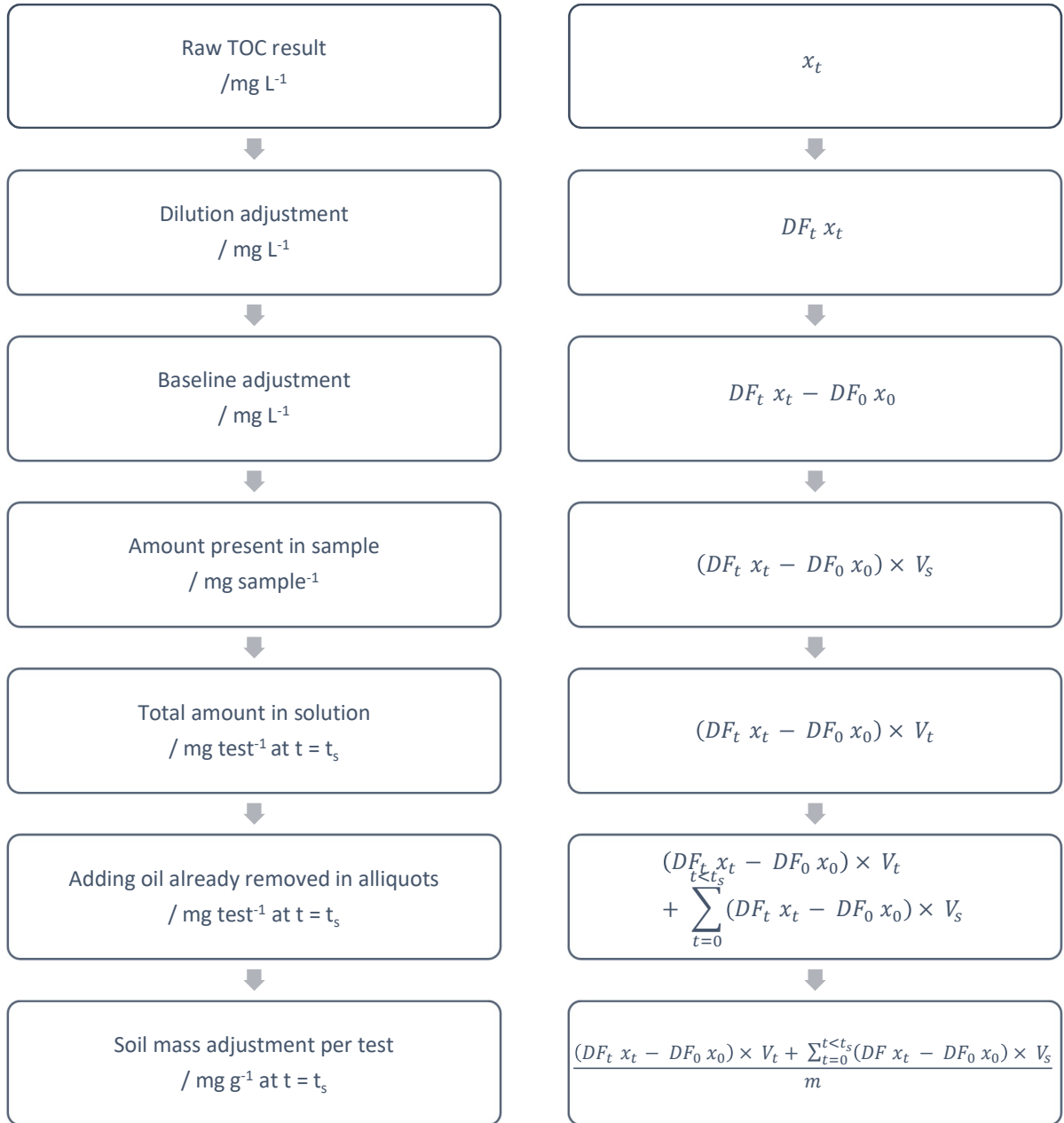
9.3.1.3 Batch test protocol

1. Pre-heat apparatus to $50\text{ }^{\circ}\text{C} \pm 3\text{ }^{\circ}\text{C}$
2. Pre-heat 640 ml test solution to $50\text{ }^{\circ}\text{C}$ in separate water bath
3. Use measuring cylinder to transfer 600 ml of test solution to chamber 1. Stir at 300 rpm.
4. Start timer.
5. Filter remaining 40 ml through Sartorius $0.45\text{ }\mu\text{m}$ mesh cellulose acetate syringe filter into labelled 50 ml plastic centrifuge tube to generate a baseline sample.
6. Remove 40 ml aliquots after 5, 10, 15, 30, 60, 120 min. Filter each sample through clean $0.45\text{ }\mu\text{m}$ cellulose acetate syringe filter (Whatmann®) into a plastic centrifuge tube. The sample remained fully submerged in the cleaning solution throughout the test.
7. Samples of the commercial cleaning solutions require dilution. pH 9 solution and DI water do not require dilution in standard TOCs. Solution samples containing commercial cleaning solutions require 90 % dilution. Dilution is conducted with DI water of known carbon content.
8. A minimum of 3x TOC measurements made per aliquot collected in 5 and 6. A fourth measurement is taken if the variation between 3 runs is $> 3\%$. Mean TOC values are plotted. The error bar shows standard deviation of repeat samples. Differences between TOC results on the same sample were negligible in comparison and so are not plotted.
9. The substrate was immediately removed from the chamber at the end of the test, dried overnight in a desiccator, weighed and photographed.
10. 4 repeats were conducted for each test solution. Fresh test solution was used in each repeat.

9.3.1.4 Data processing

The data recovered from the TOC measurements must be standardised between different oil recovery methods. The flow chart (Flow chart 9.1) gives a step-by-step account of data processing that occurred between TOC results and final value.

Flow chart 9.1: Data processing chart for batch systems described in Figure 9.16.



Where;

t_s is the time at which the sample was taken. $t_s = \{0, 5, 10, 15, 30, 60, 120 \text{ min}\}$

x_t is the total organic carbon content measured in a sample at time t_s

DF_t is the dilution factor of the TOC sample at time t_s given by;

$$DF_t = \frac{V_{\text{samp}} + V_{\text{DI water}}}{V_{\text{sample}}}$$

V_s is the sample volume

V_t is the test volume at time t_s

m is the original mass of the dry soil sample

9.3.2 Results and Discussion

9.3.2.1 Total carbon testing

The total amount of organic carbon present in the cleaning solution (after filtering at 450 μm) is shown in Figure 9.17. The total recovered carbon in CCF1 was approximately 650 mg/g, which is significantly greater than CCF2 at 270 mg/g after 2 hours. Increasing the pH of the water to pH 9 showed no appreciable difference in carbon released. The oil release data for pH 9 and pH 7 water were fitted to Equation 6.12 and there was good agreement between the calculated rate constants between the batch and static tests, considering the change in test conditions (Batch vs static; DI water at 50°C: k_{TOC} : 0.71 vs 0.54 s^{-1} , pH 9/10 at 50°C: k_{TOC} : 0.55 vs 0.47 s^{-1}).

The expected maximum fat/oil content was 360 mg g^{-1} . The values for CCF1 are larger than expected for the fat/oil content of the CMS, indicating that a fraction of the protein and starch content in the burnt CMS has been solubilised (diameter < 450 μm suspensions due to filter size during processing) into the cleaning solution. This result was observed in 3 of the 4 tests with CCF1. The fourth gave even larger values and was discounted. An unusually low TOC baseline was considered as a possible cause of this outlying set of data.

The uncertainty in the amount of recovered organic carbon for the CCF1 and CCF2 solutions is notably larger than that of pH 9 and DI water. This is due to a combination of commercial cleaning solutions having a higher baseline TOC value, due to the organic carbon already present within the solution prior to contact with the soil, as well as a 1:9 dilution requirement for the TOC. Any errors in the TOC measurement are therefore amplified 10-fold by dilution compensation. Additionally, if the cleaning agents, such as enzymes, promote breakdown of the soil structure into particles smaller than 450 μm , this will be a random effect, and will lead to large uncertainties.

Figure 9.17 shows cumulative soil mass recovered within the cleaning solution over time. Although not directly comparable with alternative forms of oil mobility testing (the mass of soil varied between test types) this provides insight into the cleaning effectiveness. 0.7 g of carbon was recovered per gram of soil used in the tests with CCF1, indicating that the soil has been solubilised effectively into particles <450 μm in diameter over the 2 hour test. In contrast, DI water only recovered 0.2 g/g (~20 %) of the soil, with the remainder either remaining on the substrate or being removed in larger chunks that were filtered out in the TOC preparation.

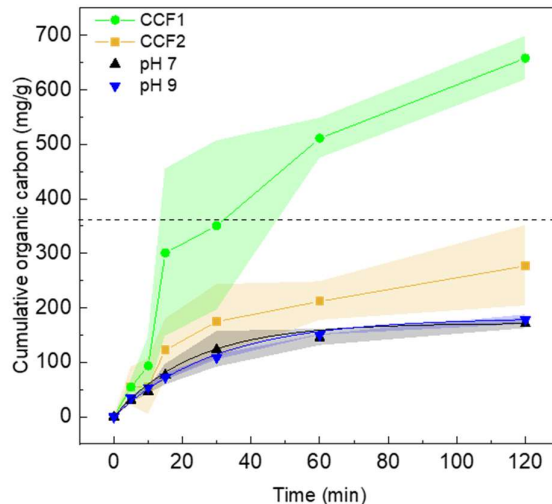


Figure 9.17: Recovered organic carbon for CMS submerged in cleaning solutions for 120 min. Horizontal dashed line shows amount of oil/fat present in the deposit. Batch configuration. Lines for pH 7 and pH 9 are fits to Equation 6.12.

The commercial cleaning agent tests were repeated due to concerns that denaturation of the enzymes in CCF2 led to poorer performance. Similar results were obtained with a fixed exposure time and temperatures compatible with enzyme chemistry during solution preparation. The enzymes were considered to be intact during the testing sequence.

Nitrogen analysis (TON, NWG Scientific Services) of the test solution was also conducted on selected samples to measure protein solubilisation. All results lay below the resolution limit of the available test equipment (< 1 mg difference between samples).

9.3.2.2 Residual material

9.3.2.2.1 Gravimetric analysis

Figure 9.18 shows the percentage of soil mass remaining on the plate after 2 hours submersion. The values for DI water and pH 9 buffered solutions are similar, at 10.1 wt.% \pm 6.2 and 10.7 wt.% \pm 4.4, respectively. CCF1 showed superior effectiveness to simple systems, with 2.1 wt.% \pm 0.9 remaining. CCF2 similarly performed well, with 1.1 wt.% \pm 0.4 remaining at the end of the test.

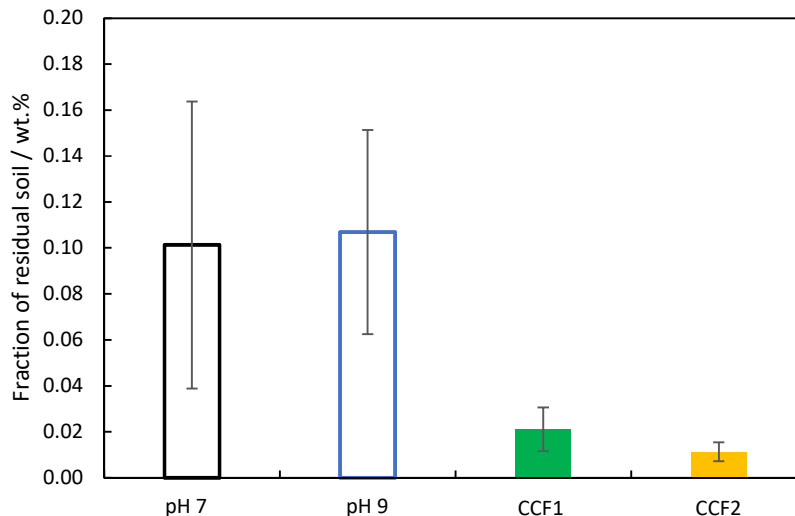


Figure 9.18: Gravimetric analysis of soil samples after 2 hours submersion in cleaning solutions and drying overnight in a desiccator. Masses presented as a percentage of the initial burnt soil mass. Error bars are of 4 repeats per sample. CCF1: commercial formulation 1, CCF2: commercial formulation 2.

9.3.2.2.2 Image analysis of residual deposit

The pattern of any residue remaining on the surface after a cleaning test provides information about the effectiveness of the cleaning regime on the individual components in the complex soil mixture. Figure 9.19 shows that for soils cleaned with DI water or pH 9 buffered solution, the cracking pattern generated during drying of the CMS was still present. Strongly burnt material such as at the edge of cracks will have been drier, harder, and more strongly adhered to the substrate. DI water and pH 9 cleaning solutions, in combination with the mechanical forces provided by the stirring of the solutions during testing, were unable to remove is strongly adhered material from the substrate surface. Large chunks of CMS remained adhered to the substrate itself. Visually it appeared that there was significant amounts of fat remaining on the substrate in the pH 9 buffered solutions, denoted by the white misshapen solids that appear contained within the ‘cracked’ residual region.

In contrast, the substrates cleaned with the commercial cleaning solutions lacked traces of the cracking pattern, although a thin grainy layer is occasionally visible. This indicates that both were successful in weakening the adhesion of the soil to substrate. The residues mostly take the form of droplets of oil/fat adhered to the substrate surface. These are noticeably larger in the case of CCF1. Fats preferentially wet to stainless steel surfaces over than being suspended in water (Michalski and Briard, 2003). However, the relative difference in size of the droplets indicates a change in the surface energies of the substrate post-cleaning, or differences in the adsorption of the agents to the surface and/or into the oil/fat. This was not investigated further.

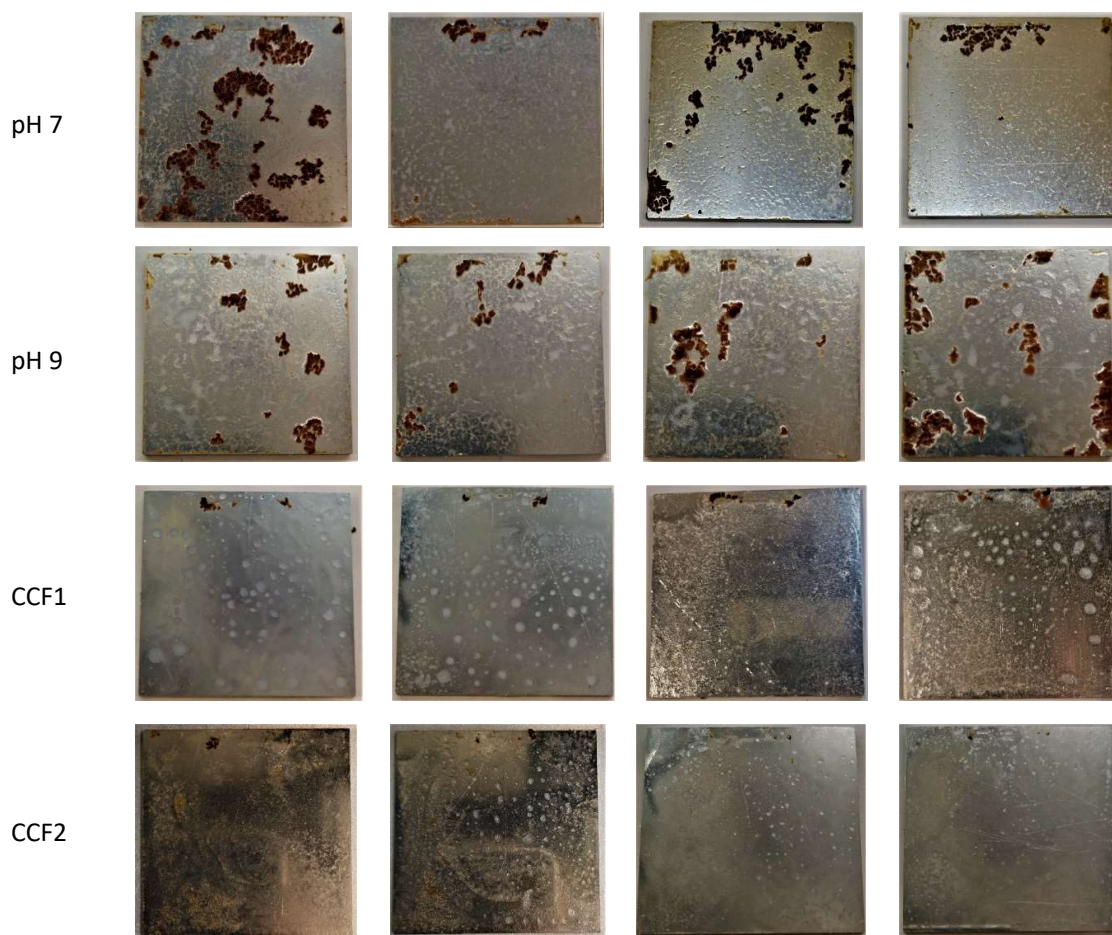


Figure 9.19: Colour enhanced photographs of sample plates after 2 hours immersion. Each plate is 50 x 50 mm.

9.3.3 Stage 3 conclusions

The role of detergent formulations on the mechanisms controlling cleaning of a complex fat, protein and carbohydrate soil mixture on stainless steel substrates was studied. CCF1 removed the most solubilised organic carbon after 2 hours of testing, followed by CCF2, pH 9 buffered solutions then deionised water. Gravimetric analysis of dried residual soil after 2 hours soaking placed CCF2 as being the most effective cleaning solution overall (1.1 wt.% remaining), followed by CCF1 (2.1 wt.%) with pH 9 and DI water both having approximately 10 wt.% of the soil remaining on the surface. Images of the soiled substrates taken after drying demonstrate a difference in cleaning mechanism. The commercial cleaning solution residuals took the form of small droplets of fat distributed across the surface (CCF1 droplets being larger and more widely dispersed than CCF2) whilst the residuals obtained with the simple cleaning liquids featured solids and the network of cracks present in the initial soil layer was still visible (implying that the burnt starch-protein network is still intact at the soil-substrate interface).

9.4 Applications conclusions

A bespoke testing rig was used to determine the applicability of the findings in this thesis to test methods conducted by the project sponsors. A significant discrepancy in the findings was a large induction time noted for CMS on the ADW rig before cleaning occurred, a factor of 5 times longer than that observed on the systems developed here. The longer delay was attributed to the periodic contact between the soil and solution; when the periodicity is taken into account the findings of the ADW were consistent with the work at Cambridge. Surfactants reduced the induction time of CMS cleaning, as did alkaline pH. The combination of the two had a synergistic impact on cleaning rate, similar to that observed in Chapters 5 and 7.

Three techniques were used to monitor the impact of commercial formulations on the cleaning of CMS. The impact of bleach and MGDA, both alone in as part of CCF1 was investigated on glass and stainless steel substrates. MM3 and SiDG testing both showed that MGDA and bleach interact antagonistically, inhibiting the reduction of $\langle F_w \rangle$ as well as the extent of swelling. This is also shown in testing with commercial cleaning formulations, which have slower kinetics after cleaning onset for removing CMS layers than surfactant solutions alone. The CCF however exhibited faster and more complete cleaning overall and to a greater extent.

Staged release of individual components offer a route to maximise the effectiveness of each component. Glass substrates exhibited reduced cleanability in full formulation systems, despite exhibiting a weaker soil-substrate interactions of the dry soil with the substrate.

An adapted form of the solution analysis, altered to use with enzymes, was developed to run a comparison between two commercial formulations. One formulation (CCF1) removed the majority of solubilised organic carbon after 2 hours of testing, while the other (CCF2) was significantly less effective, and pH 9 buffered solutions and pH 7 water less so again.

Gravimetric analysis of dried residual soil after 2 hours soaking placed CCF2 as being the most effective cleaning solution overall, followed by CCF1. This reversal of cleaning effectiveness indicates a difference in cleaning mechanisms; whilst both solutions remove the soil from the substrate, the cleaning occurring with CCF1 breaks the soil down into smaller fragments, allowing TOC analysis. This work highlights the range of techniques that need to be used to elucidate differences in cleaning mechanisms and therefore effectiveness, the understanding of which is vital to improving upon current formulations.

10. Project conclusions and looking forward

Prior to this study, little was known about the cleaning of baked heterogeneous food soiling layers and the mechanisms involved in removing them from substrates in cleaning operations such as stainless steel.

10.1 Simple food soils

The approach taken built on the work of Ali (2015(a)) on polymerised greasy food soils. The first task was to generate and characterise burnt lard soils. Thinner samples, of $\delta \approx 0.3$ mm, were identified as being more suitable. The repeatability of sample generation by this protocol was then established.

Confocal fluorescence microscopy was used to investigate the impact of baking time, pH and surfactancy on the mechanism of solution motion into the soil layer, i.e. via ingress or penetration. Two techniques were established, the first to monitor the movement of surfactant into the soil layer and the second to monitor the movement of the soil layer into the solution. These techniques showed that in neutral pH solutions the surfactant ingressed into the soil layer from the solution-soil interface, but under alkaline conditions solution penetrated at the soil-substrate interface. Surfactants were shown to either swell (CTAB) or erode (SDBS) the soil layer.

Further work in this area could include the use of two-photon pulsed laser microscopy with Coherent Anti-Stokes Raman Scattering (CARS), which was the intention of the work placement in China. This technique would allow the simultaneous monitoring of the thickness of the soiling layer as well as the movement of the fluorescent surfactants. Additionally, the CARS functionality allows specific functional groups (such as those in starch) to be targeted to trace their interaction with the cleaning solution over time.

10.2 Complex food soils

A method of developing a complex model food soil (CMS) layers was developed in order to study the impact of including burnt starches and proteins in the hydrophobic soil on its resistance to cleaning. A requirement of these soils was that they (I) were representative of household baked deposits, (II) could be reproduced within acceptable repeatability limits, and (III) were suitable for testing with the available research techniques. The protocol was based on a sponsor formulation. Cracks could not be eliminated, the size and distribution of which were shown to have a significant impact on both the adhesive and swelling characteristics of the soil when exposed to cleaning solutions. Over the course of this project the technique of generating these layers was refined to minimise the crack size in order to generate reproducible uniform crack distributions and improve repeatability.

10.2.1 Microscale imaging

Confocal fluorescence microscopy was demonstrated to be unsuitable for monitoring the cleaning of CMS, due to the swelling of the soil on submersion in solution. Alternative techniques could be used to monitor whether the surfactant solution enters the layer via solution penetration at the soil-substrate interface or via ingress at the solution-soil interface. One such method includes baking CMS onto a glass substrate and using a dyed solution and image analysis to visually track the ingress or penetration of solution into the soil.

10.2.2 Soil swelling

A number of techniques were used in this work to monitor the cleaning of complex soils. Fluid dynamic gauging was used to measure changes in soil thickness as a function of time immersed in cleaning solutions. Initial testing employed on the zFDG device developed by Wang (2017). The protocol required >60 s to locate the sample and determine the initial thickness, so that initial hydration could not be measured.

All subsequent testing was conducted on the SiDG, developed in this project, allowing data point to be collected within 6 s of soil immersion. Hydration of CMS could then be measured and was shown to increase linearly with pH between pH 7 and pH 10. After hydration the soil swelled to a maximum extent dependent upon the chemistry of the solution; higher pH solutions gave a larger $\Delta\delta_{max}$, as did surfactants such as SDBS. A synergistic response between high pH and the use of surfactants was observed for SDBS at pH 9.

Further work in the area of swelling includes investigating the impact of substrate surface energy via testing with alternative substrates, such as glass or copper, as well as investigating the effect of different deposit thermal history.

10.2.3 Solution analysis

Two techniques were established to monitor the transfer of soil into the solution. The first was solution analysis via TOC testing. Testing was conducted with both static and flowing solutions at temperatures up to 50 °C. Enhanced transfer of organic material was observed above 35 °C, associated with the melting of some of the fat components present. Raising the pH, adding surfactants and using bleach similarly caused an increase in the release of carbon-based material into the solution. Of all static solutions tested, the bleach solution was most effective, closely followed by the use of cationic surfactants.

Image analysis of CMS layers submerged in static solutions cleaning corroborated these findings, with 0.1 % CTAB solution at 50 °C proving to be the most effective at promoting the formation and

detachment of oily droplets from the surface of the CMS layer into the cleaning solution. Two simple models for droplet formation were presented, which provided some insight into the likely mechanism controlling the rate of oil displacement. A model relating the interfacial conditions that promote droplet detachment from the soil was developed, and corroborated the experimental findings.

Flowing solutions released lower amounts of the soil into the solution than static ones. An optimal flow rate was observed at 10 ml min^{-1} , although this was due to experimental set-up and was not a function of the soil or solution composition. At this flow rate the anionic surfactant SDBS was shown to be the most effective cleaning solution tested, and was the only solution to promote the cleaning of CMS above its static solution equivalent.

Further work in this area could include the use the dot samples generated for the P&G ADW testing rig in order to control the volume of available oil to form each droplet. Additionally, further work is required to refine the models used to investigate the mechanisms of penetration and ingress, specifically the impact of surfactants on the contact angle of droplets requires significant further investigation.

10.2.4 Millimanipulation

The MM3 technique described by Magens *et al.* (2017) was modified to include a solution flow system, allowing for the *in situ* monitoring of adhesive and cohesive soil strength after exposure to cleaning solutions. CMS layers exhibited cohesive and/or adhesive failure during removal, depending on the cleaning solution chemistry. Temperature had a uniformly beneficial effect on soil weakening, with water at pH 7 at 50°C exhibiting a transition between cohesive and adhesive failure after an initial soaking period. The length of this initial soaking period was reduced when TX-100 or SDBS was present. This behaviour was attributed to the fat in the soil being mobilised at 50°C . CTAB, the cationic surfactant, promoted adhesive failure at 20°C and 50°C , indicating that it promoted a different removal mechanism. Solution pH had little effect on its own. When combined with surfactants high pH promoted weakening of the soil-substrate bonds as well as breakdown of the soils cohesive strength. This work provided quantitative evidence on how different cleaning mechanisms are promoted by cleaning agents, and the timescales over which these mechanisms occur.

Further work in this area could include an investigation into the impact of substrate type and surface energy on the adhesive strength of soil-substrate interactions as a function of submersion time.

10.2.5 Data Fusion

The timescales at which swelling, removal forces, and soil solubilisation occur after submersion of CMS into a cleaning solution were compared and the step-wise nature of the cleaning investigated.

In the reference case, 50 °C pH 7 water demonstrated a simultaneous drop in adhesive strength of the soil and swelling of the soil layer for 500 s. After this time droplets of oil started to form on the CMS surface, growing and detaching for a further 1000 s, after which all metrics measured reached an asymptote. The rate constants associated with each stage were tabulated, with both swelling and droplet growth having first order rate constants on the order of 10^{-3} s^{-1} , whilst oil recovery testing occurred on the order of 10^{-6} s^{-1} , indicating that the transfer of oily soil material to the soil-solution interface was much faster than solubilisation of the oil from the surface into the solution. This transfer of oil did however occur after a time delay, the length of which was dependant on solution formulation and temperature, as well as the soils swelling.

Addition of pH and/or surfactants influenced the cleaning stages in different ways. Higher pH accelerated soil swelling, and slightly enhanced the onset of droplet growth, whilst surfactants significantly enhanced the weakening of adhesive and/or cohesive strength of the soil, as well as causing droplets to form earlier after submersion, whilst the soil was still swelling. These differences were attributed to whether the cleaning agent acted on the solid soil matrix or on the mobile oily material.

This investigation has provided improved knowledge of the stages in cleaning which can be used to enhance the cleaning effectiveness of commercial cleaning formulations. Further exploration into the stepwise nature of swelling followed by oil loss in simple cleaning solutions will elucidate information on the mechanism of action in softening the CMS layer to the point at which cleaning takes place. This could be achieved through the combination of current techniques, e.g. running image analysis and solution composition analysis of the SiDG solution as it completes a test.

Furthermore, combinations of surfactants at a range of pH and temperatures, including staged release, requires further investigation to better inform upon the complex interactions that occur between the soil and cleaning solution in a dishwashing environment.

10.2.6 Application of findings to commercial formulations

Two packages of work were undertaken to translate the learnings to industrial practice; the first investigated the use of simple cleaning additives on an existing P&G® testing apparatus. The second investigated P&G® cleaning formulations with the methods developed in this thesis.

The general trends of cleaning with simple systems (varying temperature, pH and surfactancy) were consistent between the Cambridge studies and the P&G equipment. The onset of cleaning on the rig was significantly longer, due to it using a cycling water jet which reduced the contact time between the soil and the cleaning solution. The chelant MGDA was required to be used in order for soil drop off to occur on their test, above which component effects could be observed.

The commercial detergent systems reduced the time of onset cleaning but had little impact on the rate of cleaning thereafter. Components such as MGDA and the bleach were found to be antagonistic, causing reduced swelling and inhibiting the breakdown of the adhesive and cohesive strength of the soil layer. Staging the release of these components to target their respective functions could be the subject of further study. CMS fixed to glass substrates was tested with the commercial cleaning solutions and was shown to have a lower cleaning rate and effectiveness than the equivalent stainless steel substrates.

Other avenues of research in this area could include (I) the impact of a continuous water jet on the ADW rig, (II) the investigation of the impact of oscillatory flow on the MM3, (III) further work into the impact of MGDA on the cleaning rate of CMS and (IV) investigating the impact of each commercial cleaning component on the adhesive strength of CMS to glass substrates over time.

10.3 Achievements

This work has provided several new insights into the cleaning behaviour of complex heterogeneous burnt food soils. The millimanipulation device has been developed to include a flowing solution system allowing for in situ monitoring of soil adhesion and cohesion. Advances in the current state of fluid dynamic gauging apparatus through this work have enabled access to hydration data as well as swelling data, information that is essential in recording accurate swelling measurements of heterogeneous soils. This thesis has highlighted the inherent difficulty of cleaning complex burnt food soils, and has developed a slate of techniques that allows several aspects of cleaning to be accurately monitored and evaluated in terms of their impact on the timescales of cleaning. These timescales should be taken into account when developing new, improved cleaning formulations that target burnt food soils and related fouling deposits.

References

- Abele, C., *Needed: A reliable field determinant of cleanliness*, J. Milk Food Technol., **28**, 257, 1965
- Acmite, *Global Surfactant Market* (4th edition), 605 pages, Acmite Market Intelligence, 2016
- Akhtar, N., Bowen, J., Asteriadou, K., Robbins, P. T., Zhang, Z., Fryer P. J. *Matching the nano- to the meso-scale: Measuring deposit–surface interactions with atomic force microscopy and micromanipulation*, Food and Bioproducts Processing, **88**, 341–348, 2010
- Airey P, Verran J., *Potential use of copper as a hygienic surface; problems associated with cumulative soiling and cleaning*. J Hosp Infect, **67**, 271–277, 2007
- Ali, A.: *Understanding the cleaning of greasy polymerised food soils*. [PhD thesis] University of Cambridge, 2015(a)
- Ali, A., Alam, Z., Ward, G., Wilson, D. I., *Using the fluid dynamic gauging device to understand the cleaning of baked lard soiling layers* . J. Surfact. Deterg., **18**, 933-947. 2015(b)
- Ali, A., de’Ath, D., Gibson, D., Parkin, J., Ward, G., Alam, Z. and Wilson, D.I. *Development of a millimanipulation device to quantify the strength of food fouling deposits*, Food Bioproducts Proc., **93**, 265-258, 2015 (c)
- Alvarez, N., Daufin, G., Gésan-Guiziou, G., *Recommendations for rationalizing cleaning-in-place in the dairy industry: Case study of an ultra-high temperature heat exchanger*, Journal of Dairy Science, **93**, (2), 808-821, 2010
- Armbruster, E. H., *Field test procedure for cleanliness measurement of multiple use eating utensils.*, The Sanitarian, 1960
- Armbruster, E. H., *Evaluation of surface contamination*, The Santiarian, 1962
- Ashokkumar, S., Adler-Nissen, J., *Evaluating non-stick properties of different surface materials for contact frying*. J. Food Eng. **105**, 537–544. 2011
- Asteriadou, K., Othman, A. M., Goode, K., Fryer, P. J., *Improving cleaning of industrial heat induced food and beverages deposits: A scientific approach to practice*. Heating Exchanger and Fouling Conference, 158-164, 2009
- Atherton, T. J., Kerbyson, D. J., *Using phase to represent radius in the coherent circle Hough transform*, Proc, IEE Colloquium on the Hough Transform, IEE, 1993
- Augustin, W., Chew, Y.M.J., Gordon, P.W., Lister, V.Y., Mayer, M., Paterson, W.R., Peralta, J.M., Scholl, S., Wilson, D.I., *Dynamic gauging of soft fouling layers on solid and porous surfaces*, Chem. Ing. Tech., **84**, 46-53, 2012
- Aziz, N. S., *Factors that affect cleaning process efficiency*. [PhD thesis]. School of Chemical Engineering, University of Birmingham, 2008
- Babadagli, T. *Analysis of oil recovery by spontaneous imbibitions of surfactant solution*, Paper presented at the SPE international improved oil recovery conference in Asia Pacific, Kuala Lumpur, Malaysia, 20–21 Oct 2003

- Bäck, G., Singh, P., *Susceptibility of stainless steel alloys to crevice corrosion in ClO₂ bleach plants*, Corrosion Science, **46**, 2159-2182, 2004
- Ball, D.W., Hill, J.W., Scott, R.J., *The basics of general organic and biological chemistry*, Chapter 16.4, Saylor Foundation, 2011
- Barish, J. A., Goddard, J. M., *Anti-fouling surface modified stainless steel for food processing*, Food and Bioproducts Processing, **91**, (4), 352-361, 2013
- BASF, *Trilon M types: Technical Information*, Save on Citric, BASF, 2007
- Beck, W. J., *The antiquity of modern methodology*, Ass. of Food and Drug Officials of the U. S., 1962
- Belinato, G., Canale, L., Totten, G., Canale, L. W., Dean, S., *Effect of Antioxidants on Oxidative Stability and Quenching Performance of Soybean Oil and Palm Oil Quenchants*, Journal of ASTM International, **8**, 121-130, 2011
- Benzing-Purdie, L. M., Ripmeester, J. A., Ratcliffe, C. I., *Effects of Temperature on Maillard Reaction Products* J. Agric. Food Chem., **33**, (1), 198, 1985
- Berman, H.M., Westbrook, J., Feng, Z., Gilliland, G., Bhat, T.N., Weissig, H., Shindyalov, I.N., Bourne, P.E., *The Protein Data Bank*, Nucleic Acids Research, **28**, (1), 235–242, 2000.
- Beuf, M., Rizzo, G., Leuliet, J. C., Müller-Steinhagen, H., Yiantsios, S., Karabelas, A., Benezech, T., *Heat Exchanger Fouling and Cleaning: Fundamentals and Applications, Engineering Conferences International Year 2003*, Fouling and Cleaning of Modified, Stainless Steel Plate Heat Exchangers, Processing Milk Products, 1-8, 2003
- Bhagat, R.K., Perera, A.M., Wilson, D.I., *Cleaning vessel walls by moving water jets: simple models and supporting experiments*, Food and Bioproducts Processing, **102**, 31 – 54, 2017
- Biresaw, G., Adhvaryu, A., Erhan, S.Z., *Friction and adsorption properties of normal and high-oleic soybean oils*, J. Amer. Oil. Chem. Soc. **79**, 53, 2002
- Biresaw, G., Mittal, K., *Surfactants in Tribology – Chapter 13*, CRC Press, 2013
- Bishop, A. *Cleaning in the food industry*, Reprinted by permission of Wesmar Company Inc. from Basic Principles of Sanitation, 1997
- Bobbe, U., Hofmann, J., Sommer, K., Beck, U., Reiners, G., *Adhesion - where cleaning starts*. Trends Food Sci. Technol., **18**, 36-39. 2007
- Borghetty, H.C., Bergman, C.A., *Synthetic detergents in the soap industry*, J. Am. Oil. Chem. Soc., **27**, 88, 1950
- Bouman, S., Lund, D. B., Driessen, F. M., Schmidt, D. G., *Growth of thermoresistant streptococci and deposition of milk constituents on plates of heat exchangers during long operating times*, J. Food Prot., **45**, 806–812, 1982
- Bourne, M.C., Jennings, W.G., *Kinetic studies of detergency. II. Effect of age, temperature and cleaning time on rates of soil removal*, J. Amer. Oil Chem. Soc., **40**, 523, 1963

- Bowen, W. R., Doneva, T., Hilal, N., Wright, C. J., *Atomic force microscopy: images and interactions*, *Microsc. Anal.*, **81**, 5–7, 2001
- Boxler, C., Augustin, W., Scholl, S., *Influence of surface modification on the composition of a calcium phosphate-rich whey protein deposit in a plate heat exchanger*, *Dairy Science & Technology*, **94**, (1), 17–31, 2014
- Brambilla, E., Ugel, M., *Dishwasher and method for detecting the water level within a dishwasher*, US9451868B2, 2013
- Brennan, C.S., Blake, D.E., Ellis, P.R., Schofield, J. D. *Effects of guar galactomannan on wheat bread microstructure and on the in vitro and in vivo digestibility of starch in bread*. *J. Cereal Sci.*, **24**, 151–160, 1996.
- British Nutrition Foundation, *Dietary Fibre*, Retrieved 26 July 2018.
- Brudzynski, K., Miotto, D., *The recognition of high molecular weight melanoidins as the main components responsible for radical-scavenging capacity of unheated and heat-treated Canadian honeys*, *Journal of Food Chemistry*, **125**, (2), 570-575, 2011,
- Calhoun, G., Hewett, W. A., US3041284A, *Shell company*, 1958
- Cambridge Water Company, <https://www.cambridge-water.co.uk/household/my-water-supply/water-quality/water-hardness>, accessed 14/03/2019.
- Castner, D. G., Ratner, B. D. *Biomedical surface science: foundations to frontiers*. *Surf. Sci.*, **500**, 28-60, 2002
- Capuano, E., *The behaviour of dietary fibre in the gastrointestinal tract determines its physiological effect*, *Crit. Rev. Food Sci. Nutr.*, **57**, (16), 3543-3564, 2017
- Ceresana®, *Market Study: Surfactants* (3rd edition), Market Research Study, 2017
- Challa, R., Johnston, D., Singh, V., Tumbleson, M., Rausch, K., *Fouling characteristics of model carbohydrate mixtures and their interaction effects*, *Food and Bioproducts Processing*, **93**, 197–204, 2015
- Chee, M. Ahuja, T., Bhagat, R., Taesopapong, N., Wan, S., Wigmore, R., Wilson, D.I., *Impinging jet cleaning of tank walls: Effect of jet length, wall curvature and related phenomena*. *Food and Bioproducts Processing*, **113**, 142-153, 2019
- Chen, X., Fickak, A., Hatfield, E. *Influence of run time and aging on fouling and cleaning of whey protein deposits on heat exchanger surface*, *J. Food Res.*, **1**, 212-224, 2012
- Cheraghian, G., Hendraningrat, L. *A review on applications of nanotechnology in the enhanced oil recovery part A: effects of nanoparticles on interfacial tension*, *Int. Nano. Lett.*, **6**, 129–138, 2016
- Chew, J.Y.M., Paterson, W.R., Wilson, D.I., *Dynamic gauging for measuring the strength of soft deposits*, *J. Food Eng*, **65**, (2), 175-187, 2004
- Christian, G. K., Fryer, P. J. *The effect of pulsing cleaning chemicals on the cleaning of whey protein deposits*, *Food Bioproducts Proc.*, **84**, 320-328, 2006

- Cleine, J.H., Dixon, K.E., *The effect of egg rotation on the differentiation of primordial germ cells in Xenopus laevis*, J. Embryol. Exp. Morphol., **90**, 79–99, 1985
- Cluett, J.D., *Cleanability of certain stainless steel surface finishes in the brewing process*. [MPhil Thesis]. South Africa: Faculty of Mechanical Engineering, Rand Afrikaans University, 2001
- Codex Alimentarius Commission, *Procedural Manual*, 21st Edition, World Health Organisation, 2014
- Collins English Dictionary, Fibre, Definition – Noun, 2019
- Conforti, F. D., *Cake Manufacture: Chapter 32*, Bakery Products Science and Technology, 558, 2014
- Cooper, M.S., Hardin, W.R., Petersen, T.W., Cattolico, R.A., *Visualizing “green oil” in live algal cells*, J. Biosci. Bioeng., **109**, 198–201, 2010
- Corless, R. M., Gonnet, G.H., Hare, D.E.G., Jeffrey, D.J., Knuth, D.E., *On the Lambert W function*. Advances in Computational Mathematics, **5**, 329-359, 1996
- Cox, G., *Biological confocal microscopy*, Materials Today, **5**, (3), 34-41, 2002
- Crank, J. *The Mathematics of Diffusion*, Oxford: Clarendon Press, 1975.
- Cucci, M., *The use of radioactive phosphorus to measure the amounts of milkstone deposited on rubber, pyrex glass and tygon tubings.*, J. Milk Food Technol., **17**, 332, 1954
- Cuckston, G.L., Alam, Z., Goodwin, J., Ward, G., Wilson, D.I., Quantifying the effect of solution formulation on the removal of soft solid food deposits from stainless steel substrates, Journal of Food Engineering, **243**, 22-32, 2019
- D’Alessio, S. J. D., Pascal, J. P. Jasmine, H. A., *Instability in gravity-driven flow over uneven surfaces*, Physics of Fluids, **21**, (6), 62105–11, 2009
- Daerr, A., Eggers, J., Limat, L., Valade, N., *General mechanism for the meandering instability of rivulets of Newtonian fluids*, Phys. Rev. Lett., **106**, 184501, 2011
- DePalma, A., *Viral Safety Methods for Manufacturing*, Genetic Engineering & Biotechnology News, **30** (8), 2010
- Deshpande, A., Mohamed, M., Daftardar, S.B., Patel, M., Boddur, S.H.S., Nesamony, J., *Emerging nanotechnologies for diagnostics, drug delivery and medical devices*, Chapter 12 - Solid Lipid Nanoparticles in Drug Delivery: Opportunities and Challenges, Micro and Nano Technologies, 291-330, 2017
- Detry J. G., Rouxhet, P. G., Boulange-Petermann, L., Deroanne, C., Sindic, M., *Cleanability assessment of model solid surfaces with a radial-flow cell*. Colloids Surf. A: Physicochem. Eng. Aspects, **302**, 540-548, 2007
- Detry, J.G., Deroanne, C., Sindic, M. *Hydrodynamic systems for assessing surface fouling, soil adherence and cleaning in laboratory installations*, Biotechnol. Agron. Soc. Environ., **13**, 427-439, 2009
- Detry, J.G., Sindic, M., Deroanne, C., *Hygiene and cleanability: a focus on surfaces*, Crit. Rev. Food Sci. Nutr., **50**, 583– 604, 2010

- Dhadwar, S.S., Bemman, T., Anderson, W.A., Chen, P., *Yeast cell adhesion on oligopeptide modified surfaces*, *Biotechnol. Adv.*, **21**, 395–406, 2003
- Digman, M.A., Brown, C.M., Horwitz, A.R., Mantulin, W.W., Gratton, E., *Paxillin dynamics measured during adhesion assembly and disassembly by correlation spectroscopy*, *Biophys. J.* **94**, 2819–2831, 2008
- Din, R. A., Bird, M. R., *Removal Characteristics of Baked Wheat Starch Deposits Treated with Aqueous Cleaning Agents*, *Proceedings of the Second European Conference for Young Researchers in Chemical Engineering*, Leeds, UK, **1**, 187–189, 1996
- Domingo, E., *Fluorochromatic method for organic matter on dishware*, *Proc. 37th Ann. Meeting, Chem. Specialties Mfg. Ass., Inc.*, 1950
- Dong, L., Xu, Z., Qiao, W., Li, Z., Cheng, L., *Synthesis and Properties of a Novel Fluorescent Surfactant*, *Energy Sources, Part A*, **29**, (15), 1407-1413, 2007
- Duda, R.O., Hart, P. E., *Use of the Hough Transformation to Detect Lines and Curves in Pictures*. *Comm. ACM*, **15**, 11-15, 1972
- Dunstan, T. S., Fletcher, P. D. I., *The removal of thermally aged films of triacylglycerides by surfactant solutions*. *J. Surfact. Deterg.*, **17**, 899-910, 2014
- Dürr, H., *Influence of Surface Roughness and Wettability of Stainless Steel on Soil Adhesion, Cleanability and Microbial Inactivation*, *Food and Bioproducts Processing*, **85**, (1), 49-56, 2007
- Eginton, P. J., Gibson, H., Holah, J., Handley, P. S., Gilbert, P., *Quantification of the ease of removal of bacteria from surfaces*, *J. Ind. Microbiol.*, **15**, 305–310, 1995
- Fellers, T.J., Davidson, M.W., *Introduction to confocal microscopy*, *Microscopy Primer*, 2019
- Flitsch, S.L., Ulijh, R. V., *Sugars tied to the spit*, *Nature*, 421, 219-20, 2003
- Friedman, M., *Food Browning and Its Prevention: An Overview*, *J. Agric. Food Chem* **44**, (3) 631-653, 1996
- Fryer, P.J., Asteriadou, K., *A classification of industrial cleaning processes*. *Trends in Food and Science Technology*, **20**, (6), 255-262, 2009
- Gallardo-Moreno, A.M., Gonzalez-Martina, M.L., Bruque, J.M., Pérez-Giraldo, C., *The adhesion strength of Candida parapsilosis to glass and silicone as a function of hydrophobicity, roughness and cell morphology*, *Colloids Surf. A.*, **249**, 99–103, 2004
- Ghauharali, R. I., Brakenhoff, G. J., *Fluorescence photobleaching-based image standardization for fluorescence microscopy*, *Journal of Microscopy*, **198**, 88-100, 2001
- Gilbert, D., *A new look at important issues in the food industries - introduction to CIP*. *Vista 2 Diversay COT*. **2**, 1-52, 1994.
- Gilcreas, F.O.J., *Laboratory studies of methods for cleansing of eating utensils and evaluating detergents.*, *Amer. J. Public Health*, **31**, (2), 143-150, 1941

- Gillham, C.R., Fryer, P.J., Hasting, A.P.M. and Wilson, D.I., *Enhanced cleaning of whey protein fouling deposits using pulsed flows*, J. Food Engineering, **46**, (3), 199-209, 2000
- Girod, B., *Template Matching 1*, Digital Image Processing, Stanford University, 2013
- Glover, H.W., Brass, T., Bhagat, R.K., Davidson, J.F., Pratt, L., Wilson, D.I., *Cleaning of complex soil layers on vertical walls by fixed and moving impinging liquid jets*, Journal of Food Engineering, **178**, 95-109, 2016
- Goode, K.R., Asteriadou, K., Fryer, P.J., Picksley, M., Robbins, P.T., *Characterising the cleaning mechanisms of yeast and the implications for cleaning in place (CIP)*. Food Bioprod. Process, **88**, 365 – 74, 2010
- Gordon, P. W., Brooker, A. D. M, Chew, Y. M. J., Wilson, D. I., York, D. W., *A scanning fluid dynamic gauging technique for probing surface layers*. Meas. Sci Technol., **21**, 85-103, 2010
- Gordon P., *Development of a Scanning Fluid Dynamic Gauge for Cleaning Studies*. Ph.D. Thesis, Department of Chemical Engineering and Biotechnology, University of Cambridge, UK, 2012
- Gorenje, GV66260UK, *Fully Integrated A+++ Dishwasher*, Available at: <https://www.gorenje.co.uk/products/3390/gv66260uk/728248>, Accessed: 22/02/2019
- Greenspan, P., Fowler, S.D., *Spectrofluorometric studies of the lipid probe, Nile red*, J. Lipid Res., **26**, 781–9, 1985
- Griffith, C. J., Davidson, C. A., Peters, A. C., Fielding, L. M., *Towards a strategic cleaning assessment programme: hygienic monitoring and ATP luminometry, an options appraisal*, Food Sci. Technol. Today., **11**, 15–24, 1997
- Gropper, S. S., Smith, J. L., Groff, J. L., *Advanced nutrition and human metabolism (5th ed.)*. Cengage Learning, 114, 2008
- Gu. T., Chew, Y.M.J., Paterson, W.R., Wilson, D.I., *Experimental and CFD studies of fluid dynamic gauging in annular flows*. AIChE Journal., **55**, (8), 1937-1947, 2006
- Gu. T., Chew, Y.M.J., Paterson, W.R., Wilson, D.I., *Experimental and CFD studies of fluid dynamic gauging in duct flows*. Chem Eng Sci., **64**, (2), 219-227, 2009
- Hagsten, C., *Cleaning of ultra-high temperature milk fouling -Structural and compositional changes*. Department of Chemistry, Lund University, 160-166, 2016
- Hammond, J., *Microbiological techniques to confirm CIP effectiveness*, Brewer, **82**, 332-338, 1996
- Heinz, J. M. R. A. M., *Determining cleanliness of milk contact surfaces by analysing for calcium residual: Preliminary studies.*, J. Milk Food Technol., **30**, 337-356, 1967.
- Hepler, P. K., Gunning, B. E. S., *Confocal fluorescence microscopy of plant cells Review article 1*, Protoplasma, **201**, 121-157, 1998
- Hocking, L. M., *Spreading and instability of a viscous fluid sheet*, J. Fluid Mech, **211**, 373–392, 1990
- Hodge, J. E, *Dehydrated food chemistry of browning reactions in model systems*, J. Agric. Food. Chem., **1**, (15), 923-943, 1953

- Holland, R. S. J. T. D. W. H., *Cleaning stainless lines in place.*, Food Eng., **25**, (5), 75, 1953
- Hooper, R.J., Liu, W., Fryer, P.J., Paterson, W.R., Wilson, D.I., Zhang, Z., *Comparative studies of fluid dynamic gauging and a micromanipulation probe for strength measurements*, Food and Bioproducts Processing, **84**, 353-358, 2006
- Hornof, V., Morrow, N.R., *Gravity effects in the displacement of oil by surfactant solution*, SPE Paper No. 13573, SPE Reserv. Eng., **2**, 627–633, 1987
- Hough, P. V. C., *Method and means for recognizing complex patterns*. U.S. Patent 3069654, 1962
- Huang, K., Goddard, J.M., *Influence of fluid milk product composition on fouling and cleaning of Ni-PTFE modified stainless steel heat exchanger surfaces*, Journal of Food Engineering, **158**, 22-29, 2015
- Innovation Centre for U.S. Dairy, *Dairy's environmental footprint: A summary of findings (2008-2012)*, 2012
- Israelachvili, J. N., *Intermolecular and Surface Forces*, Elsevier. 3rd Edition, 2011
- Jadhunandan, P.P., Morrow, N.R., *Effect of wettability on waterflood recovery for crude-oil/brine/rock systems*. SPERE., **10**, (1), 40–46, 1995
- Jamaloei, B.Y., Kharrat, R. *Analysis of Microscopic Displacement Mechanisms of Dilute Surfactant Flooding in Oil-wet and Water-wet Porous Media*, Transp. Porous. Med., **81**, 1, 2010
- James, K.E., *Laboratory research on fluid flowing through porous media—Surfactants in an oil–water–sand system*, Paper presented at the Fall meeting of the Los Angeles basin section, Los Angeles, CA, 16–17 Oct 1958
- Javadi, K., Moezzi-Rafie, H., Goodarzi-Ardakani, V., Javadi, A., Miller, R., *Flow physics exploration of surface tension driven flows*, Colloids and Surfaces A: Physicochemical and Engineering Aspects, **518**, 30-45, 2017
- Jennings. W. G., *Theory and practice of hard-surface cleaning*, Adv. Food Res., **14**, 325-458, 1965
- Jensen, J., *Measuring detergency functions as affected by various detergents and procedures against milk films by application of a mechanical washing apparatus.*, J. Dairy Sci., **29**, 453-463, 1946
- Jensen, B., Stenby, M., Nielsen, D.F., *Improving the cleaning effect by changing average velocity*, Trends Food Sci. Technol. **18**, 52– 63, 2007
- Johnson, P.E., Waller, G.R., Feather, M.S., *The Maillard Reaction in Foods and Nutrition: The effect of browned and unbrowned corn products on absorption of zinc, iron and copper in humans*, American Chemical Society, Washington, DC, 349-360, 1983
- Jones, J. M., *CODEX-aligned dietary fibre definitions help to bridge the 'fibre gap'*. Nutrition Journal, **13**, (34), 1-10, 2014
- Jonhed, A., Andersson, C., Jarnstrom, L., *Effects of film forming and hydrophobic properties of starches on surface sized packaging paper*. Pack. Technol. Sci., **21**, 123-135. 2008

- Jonkman, J., Brown, C.M., *Any Way You Slice It-A Comparison of Confocal Microscopy Techniques*, J. Biomol. Tech., **26**, (2), 54–65, 2015
- Joscelyne, S., Göransson, A., Tragardh, C., *Particle transport in turbulent boundary layers*, Fouling & cleaning in food processing, 201-211, 1994
- Jurado-Alameda, E., Rodriguez, V.B., Moreno, R.B., Olea, J.N., Vaz, D.A., *Fatty soils removal from hard surfaces in a clean-in-place system*, Journal of Food Process Engineering, **34**, (4), 1053-1070, 2011
- Jurado-Alameda, E., Garcia-Roman, M., Altmajer, V.D., Jimenez-Perez, J.L., *Assessment of the use of ozone for cleaning fatty soils in the food industry*, Journal of Food Engineering, **110**, (1), 44-52, 2012.
- Jurado-Alameda, E., Herrera-Márquez, O., Martínez-Gallegos, J. F., Vicaria, J. M., *Starch-soiled stainless steel cleaning using surfactants and α -amylase*, J. Food Eng. **160**, 56-64, 2015
- Kälviäinen, H., Hirvonen, P., Xu, L., Oja, E., *Probabilistic and nonprobabilistic Hough transforms: overview and comparisons*, Image Vis. Comput., **13**, 239-252, 1995
- Karel, M., *Protein-lipid interactions*, J. Food Sci., **38**, (5), 756-763, 1973
- Karlsson, C.A.C., Tragardh, A.C., *Cleaning of stainless steel surfaces fouled by protein*. In: Wilson, D.I., Fryer, P.J., Hastings, A.P.M., (eds) *Fouling and Cleanability in Food Processing '98*. Office for Official Publications, European Community, Luxembourg, 246–253, 1999
- Kemp, I., *The surface analysis of particles of certain wheat flours*, Proc. Roy. Soc., 837-843, 1936
- Kim, H. S., Kweon, J. H., *Cleaning of lubricating products from machinery parts using supercritical water*, KSCE Journal of Civil Engineering, **14**, (1), 1-6, 2009
- Kimme, C., Ballard, D., Sklansky, J., *Finding circles by an array of accumulators*, Proc. ACM, **18**, 120-122, 1975
- Köhler, H., Stoye, H., Mauermann, M., Weyrauch, T., Majschak, J.-P., *How to assess cleaning? Evaluating the cleaning performance of moving impinging jets*, Food and Bioproducts Processing, **93**, 327-332, 2015
- Komatsu, D., Souza, E. C., Carvalho de Souza, E., Canale, L. C. F., Totten, G. E., *Effect of Antioxidants and Corrosion Inhibitor Additives on the Quenching Performance of Soybean Oil*, Journal of Mechanical Engineering, **56**, (2), 121–130, 2010
- Koutsoukos, P.G., Kofina, A.N., Kanellopoulou, D.G., *Solubility of salts in water: key issue for crystal growth and dissolution processes*, Pure Appl. Chem., **79**, (5), 825–850, 2007
- Kovrizhnykh, A.M., *Determining the shear angle, forces, and sizes of shearing elements during metal cutting*, J. Appl. Mech. Tech. Phy., **50**, 147-154, 2009
- Kramer, D.N., Guilbault, G.G., *A Substrate for the Fluorometric Determination of Lipase Activity*, Anal. Chem., **35**, (4), 588-589, 1963

- Król, P., Król, B., *Determination of free surface energy values for ceramic materials and polyurethane surface-modifying aqueous emulsions*, Journal of the European Ceramic Society, **26**, (12), 2241-2248, 2006
- Kulkarni, S.M., Maxcy, R.B., Arnold, R.G., *Evaluation of Soil Deposition and Removal Processes: An Interpretive Review*, Journal of Dairy Science, **58**, (12), 1922-1936, 1975
- Kumar, A., Staedler, T., Jiang, X., *Role of relative size of asperities and adhering particles on the adhesion force*. J. Colloid Interface Sci., **409**, 211-218, 2013
- LaMarche, C. Q., Leadley, S., Liu, P., Kellogg, K. M., Hrenya, C. M., *Method of quantifying surface roughness for accurate adhesive force predictions*, Chemical Engineering Science, **158**, 140-153, 2017
- Lavis, L. D., *Teaching Old Dyes New Tricks: Biological Probes Built from Fluoresceins and Rhodamines*, Annual Review of Biochemistry, **86**, (1), 825-843, 2017
- Lee, W.P., Routh, A.F., *Why do drying films crack?* Langmuir, **20**, (23), 9885-9888, 2004
- Leenerts, L. O., *Soil removal by dishwashing detergents*, J. Amer. Oil Chem. Soc., **33**, 110-122, 1956
- Lefèvre, G., Čerović, L., Milonjić, S., Fédoroff, M., Finne, J., Jaubertie, A., *Determination of isoelectric points of metals and metallic alloys by adhesion of latex particles*, Journal of Colloid and Interface Science, **337**, (2), 449-455, 2009
- Lelievre, C., Faille, F., Benezech, T., *Removal kinetics of bacillus cereus spores from stainless steel pipes under cip procedure: Influence of soiling and cleaning conditions*, Journal of Food Process Engineering, **24**, 359-379, 2001
- Lelièvre, C., Legentilhomme, P., Gaucher, C., Legrand, J., Faille, C., and B'énézech, T., *Cleaning in Place: Effect of Local Shear Stress Variation on Bacterial Removal from Stainless Steel Equipment*, Chem. Eng. Sci., **57**, 1287-1287, 2002
- Lenz, E., *Ueber die Bestimmung der Richtung der durch elektodynamische Vertheilung erregten galvanischen Ströme*", Annalen der Physik und Chemie, 107 (31), pp. 483-494. A partial translation of the paper is available in Magie, W. M. (1963), A Source Book in Physics, Harvard: Cambridge MA, 511-513, 1834
- Linderer, M., Wildbrett, G., *Starch residues in the cleaning process*, Fouling & cleaning in food processing, 146-155, 1994
- Lindner, M., Höflsauer, F., Heider, J., Reinelt, M., Langowski, H-C, *Comparison of thickness determination methods for physical-vapor-deposited aluminum coatings in packaging applications*, Thin Solid Films, **666**, 6-14, 2018
- Liu, W., Christian, G. K., Zhang, Z., Fryer, P. J., *Development and use of a micromanipulation technique for measuring the force required to disrupt and remove fouling deposits*. Food and Bioproducts Processing. **80**, 286-291, 2002
- Liu, W., Christian, G. K., Zhang, Z., Fryer, P. J., *Direct measurement of the force required to disrupt and remove fouling deposits of whey protein concentrate*, International Dairy Journal, **16**, 164-172, 2006

- Liu, W., Fryer, P. J., Zhang, Z., Zhao, Q., Liu, Y., *Identification of cohesive and adhesive effects in the cleaning of food fouling deposits*. Innovative Food Science and Emerging Technologies, **7**, 263-269, 2006(a)
- Liu, W., Zhang, Z., Fryer, P. J., *Identification and modelling of different removal modes in the cleaning of a model food deposit*, Chemical Engineering Science, **61**, 7528-7534, 2006(b)
- Liu, W., Aziz, N.A., Zhang, Z., Fryer, P. J., *Quantification of the cleaning of egg albumin deposits using micromanipulation and direct observation techniques*, Journal of Food Engineering, **78**, 217-224, 2007
- Liu, Y., Kitts, D.D., *Confirmation that the Maillard reaction is the principle contributor to the antioxidant capacity of coffee brews*, Food Research International, **44**, (8), 2418-2424, 2011
- Lubarda, V.A., Talke, K.A., *Analysis of the Equilibrium Droplet Shape Based on an Ellipsoidal Droplet Model*, Langmuir, **27**, (17), 10705-10713, 2011
- Macleod, N., Cox, M. D., Todd, R. B., *A profilometric technique for determining local mass-transfer rates: Application to the estimation of local heat-transfer coefficients in a nuclear reactor*, Chemical Engineering Science, **17**, (11), 923-935, 1962
- Maillard, L.C., *Action of amino acids on sugars – in French*, Compt. Rend., **154**, 66-68, 1912
- Magens, O. M., Liu, Y., Hofmans, J. F. A., Nelissen, J. A., Wilson, D. I., *Adhesion and cleaning of foods with complex structure: Effect of oil content and fluoropolymer coating characteristics on the detachment of cake from baking surfaces*, J. Food Eng., **197**, 48-59, 2017
- Magens, O., Hofmans, J., Adriaenssens, Y., Wilson, D.I., *Comparison of fouling of raw milk and whey protein solution on stainless steel and fluorocarbon coated surfaces: effects on fouling performance, deposit structure and composition*. Chemical Engineering Science, **195**, 423-432, 2019
- Magens, O. M., *Mitigating fouling of heat exchangers with fluoropolymer coatings* (Doctoral thesis), 2019
- Martins, S.I.F.S., Jongen, W.M.F., van Boekel, M.A.J.S., *A review of Maillard reaction in food and implications to kinetic modelling*, Trends in Food Science and Technology, **11**, 264-373, 2001
- Martins, S.I.F.S., Van Boekel, M.A.J.S., *Kinetics of the glucose/glycine Maillard reaction pathways: influences of pH and reactant initial concentrations*, J. Food Chemistry, **92**, 437-448, 2005
- Master, B.I., Chunangad, K.S., Pushpanathan, V., *Fouling mitigation using helixchanger heat exchangers*, Heat Exchanger Fouling and Cleaning: Fundamentals and Applications Engineering Conferences International, 2003
- Mauermann, M., Eschenhagen, U., Bley T.H., Majschak, J.-P., *Surface modifications - Application potential for the reduction of cleaning costs in the food processing industry*, Trends in Food Science & Technology, **20**, 8-15, 2009
- Maxcy, R., *The relationship between residual soil and microbial growth after circulation cleaning*, Food Technol, **20**, 123, 1966

- Mercadé-Prieto, R., X.D. Chen, *Dissolution of whey protein concentrate gels in alkali*, Bioengineering, Food and Natural Products, **52**, 792-803, 2006
- Mercier-Bonin, M., Ouazzani, K., Schmitz, P., Lorthois, S., *Study of bioadhesion on a flat plate with a yeast/glass model system*, J. Colloid Interface, Sci., **271**, 342–50, 2004
- Meyers, M. A., Chen, P-Y, Lin, A.Y-M., Seki, Y., *Biological materials: structure and mechanical properties*, Progress in Materials Science, **53**, (1), 1–206, 2008
- Michalski, M.C., Desobry, S., Babak, V., Hardy, J., *Adhesion of food emulsions to packaging and equipment surfaces*, Colloids and Surfaces A: Physicochemical and Engineering Aspects, **149**, (1–3), 107-121, 1999
- Michalski, M.C., Briard, V., *Fat-Related surface tension and wetting properties of milk*, Milchwissenschaft, **58**, 26-29, 2003
- Minor, L. G., Sklansky, J., *Detection and segmentation of blobs in infrared images*. IEEE Trans. SMC, **11**, 194-201, 1981
- Moeller, R. S., Nirschl, H., *Adhesion and cleanability of surfaces in the baker's trade*, J. Food Eng., **194**, 99-108, 2017
- Moody, L. F., *Friction factors for pipe flow*, Transactions of the ASME, **66**, (8), 671–684, 1944
- Morison, K. R., Thorpe, R. J., *Spinning disc cleaning of skimmed milk and whey protein deposits*. Trans IChemE, **80**, 319-325, 2002
- Mueller-Steinhagen, H., Malayeri, M.R., Watkinson, A.P., *Fouling of heat exchanger-new approaches to solve old problem*. Heat Transfer Engineering, **26**, (2), 1-4, 2005
- Muzychka, Y.S., Yovanovich, M.M., *Modelling friction factors in non-circular ducts for developing laminar flow*, American Institute of Aeronautics and Astronautics, **98**, 1-12, 1998
- Nikami, M., *Chemistry of maillard reactions: recent studies on the browning reaction mechanism and the development of antioxidants and mutagens*, PhD Thesis, 1988.
- Onaizi, S., He, L., Middleberg, A.P., *Rapid screening of surfactant and biosurfactant surface cleaning performance*, Colloids and Surfaces B: Biointerfaces, **72**, (1), 68-74, 2009
- Otto, C., Zahn, S., Hauschild, M., Babick, F., Rohm, H., *Comparative cleaning tests with modified protein and starch residues*, J. Food Eng., **178**, 145-150, 2016
- Palmisano, P., Hernandez, S. P., Hussaina, M., Finoa, D., Russoa, N., *A new concept for a self-cleaning household oven*, Chemical Engineering Journal, **170**, 253–259, 2011
- Papp, Z.F., Demel, U., Titz, G.P., *Laser scanning confocal fluorescence microscopy: an overview*, International Immunopharmacology, **3**, (13–14), 1715-1729, 2003
- Pawley, J.B., *Fundamental limits in confocal microscopy*. In: Handbook of biological confocal microscopy, 2nd edn. Plenum, New York, 19-38, 1995
- Peck, O.P.W Chew, Y.M.J., Bird, M.R., Bolhuis, A., *Application of fluid dynamic gauging in the characterization and removal of biofouling deposits*, Heat Trans. Eng., **36**, 685-694, 2015

- Pellegrino, L., Van Boekel, M.A.J.S., Gruppen, H., Resmini, P. and Pagani, M.A., *Heat-induced Aggregation and Covalent Linkages in b-casein Model System*, Int. Dairy J. **9**, 255–260, 1999
- Percival, S., Verran, J., Boyd, R. D., Walker, J. T., *Microscopy methods to investigate the structure of potable water biofilms*, Methods Enzymol., **337**, 243–255, 2001
- Pérez-Mohedano, R., Letzelter, N., Amador, C., VanderRoest, C.T., Bakalis, S., *Positron Emission Particle Tracking (PEPT) for the analysis of water motion in a domestic dishwasher*, Chemical Engineering Journal, **259**, 724-736, 2015
- Pérez-Mohedano, R., Letzelter, N., Bakalis, S., *Swelling and hydration studies on egg yolk samples via scanning fluid dynamic gauge and gravimetric tests*. J. Food Eng., **169**, 101-113, 2016
- PerkinElmer, *An Introduction to Fluorescence Spectroscopy*, PerkinElmer Ltd, 1-34, 2000
- Piegari, A., Masetti, E., *Thin film thickness measurement: A comparison of various techniques*, Thin Solid Films, **124**, (3–4), 249-257, 1985
- Piepiorka-Stepuk, J., Tandecka, K., Jakubowski, M., *An analysis of milk fouling formed during heat treatment on a stainless steel surface with different degrees of roughness*, Czech J. Food Sci., **34**, 271-279, 2016
- Pongsawasdi, P., Murakami, S., *Carbohydrases in detergents*, Nova Science Publishers, 71-95, 2010
- Poredoš, P., Povsic, K., Novak, B., Jezeršek, M., *Three-Dimensional Measurements of Bodies in Motion Based on Multiple- Laser-Plane Triangulation*, Revista Tecnica de la Facultad de Ingenieria Universidad del Zulia, **38**, 53-61, 2015
- Poullis, J.A., de Pijper, M., Mossel, D.A.A., Dekkers, P.Ph.A., *Assessment of cleaning and disinfection in the food industry with the rapid ATP-bioluminescence technique combined with the tissue fluid contamination test and a conventional microbiological method*, International Journal of Food Microbiology, **20**, (2), 109-116, 1993
- Prendergast, F.G., Mann, K.G., *Chemical and physical properties of aequorin and the green fluorescent protein isolated from Aequorea forskålea*, Biochemistry, **17**, (17), 3448–53, 1978
- Previdello B.A.F., Carvalho F.R.D., Tessaro A.L., Souza V.R.D., Hioka N., *The pKa of acid-base indicators and the influence of colloidal systems*. Química Nova, **29**, (3), 600–606, 2006
- Rabe, M., Verdes, D., Seeger, S., *Understanding protein adsorption phenomena at solid surfaces*, Adv. Colloid Interface Sci., **162**, (1-2), 87-106, 2011
- Rao, S.R., *Chapter 3 - Physical and Physico-Chemical Processes*, Waste Management Series, 7, 35-69, 2006
- Rask, C., *Thermal properties of dough and bakery products: a review of published data*, Journal of Food Engineering, **9**, 167-193, 1989
- Ravoisin, N., *Development and Validation of an Experimental Set-up and Image Analysis Method for Quantification of Oil Mobility from Fatty Soils*. Master's Thesis, Chemical Engineering and Biotechnology, University of Cambridge, 2018
- Regtien, P.P.L., *Chapter 5 - Capacitive Sensors*, Sensors for Mechatronics, 101-124, 2012

- Rennie, P.R., Chen, X.D., Mackereth, A.R., *Adhesion characteristics of whole milk powder to a stainless steel surface*, Powder Technology, **97**, (3), 191-199, 1998
- Resch-Genger, U., Grabolle, M., Cavaliere-Jaricot, S., Nitschke, R., Nann, T., *Quantum dots versus organic dyes as fluorescent labels*, Nat. Methods 5, 763–775, 2008
- Reynolds, O., *An experimental investigation of the circumstances which determine whether the motion of water shall be direct or sinuous, and of the law of resistance in parallel channels*, Philosophical Transactions of the Royal Society of London, **174**, 935-982, 1883
- Robertson, T. A., Bunel, F., Roberts, M.S., *Fluorescein derivatives in intravital fluorescence imaging*, Cells, **2**, (3), 591–606, 2013
- Rosa, F., Rovida, E., Graziosi, S., Giudici, P., Guarnaschelli, C., and Bongini, D., *Dishwasher history and its role in modern design*, Third IEEE History of Electro-technology conference 'The Origins of Electrotechnologies', Pavia, Italy, 2012
- Rosen, M.J., Kunjappu, J.T., *Surfactants and Interfacial Phenomena*, New Jersey: John Wiley & Sons Inc., 2012
- Ruiz C.C., Molina-Bolivar J.A., Aguiar J., MacIsaac G., Moroze S., Palepu R., *Thermodynamic and structural studies of Triton X-100 micelles in ethylene glycol-water mixed solvents*, Langmuir, **17**,(22), 6831–6840, 2001
- Salley, B., Gordon, P.W., McCormick, A.J., Fisher, A.C., and Wilson, D.I., *Characterising the structure of photosynthetic biofilms using fluid dynamic gauging*. Biofouling, **28**, (2), 159–173, 2012
- Sandison, D.R., Williams, R.M., Wells, K.S., Strickler, J., Webb, W.W., *Quantitative fluorescence confocal laser scanning microscopy (CLSM)*. In: Handbook of biological confocal microscopy, 2nd edn. Plenum, New York, 39-54, 1995
- Sanz J., Lombraña J. I., Luís A., *Ultraviolet-H2O2 oxidation of surfactants*. Environmental Chemistry Letters, **1**, (1), 32–37, 2003
- Sargent, M.J., *The extrusion processing of instant coffee for the purposes of creating a pressurised microstructure*, PhD Thesis, University of Cambridge, 2018
- Schramm. L.L., Stasiuk, E.N., Marangoni, G.D., *Surfactants and their applications*, Annu. Rep. Prog. Chem., Sect. C, **99**, 3–48, 2003
- Seiberling, D.H.W., *Evaluation of the cleanability of CIP Automatic valves.*, J. Dairy Sci., **39**, 919, 1956
- Sengupta, P., *Potential health impacts of hard water*, Int. J. Prev. Med., **4**,(8), 866–875, 2013
- Shoulders, M.D., Raines, R.T., *Collagen Structure and Stability*, Annual Review of Biochemistry, **78**, 929-958, 2009
- Showell, M., *Part D: Formulation, Handbook of Detergents*, Boca Raton, Florida, CRC Press, 158-163, 2005
- Sigma Aldrich, “Fluorescein dilaurate,” Sigma-Aldrich Co. LLC, 2016. [Online]. Available: <https://www.sigmaaldrich.com/catalog/product/sigma/46943?lang=en®ion=GB> [Accessed 19 12 2019]

- Silvi, N., Dussan V.E.B., *On the rewetting of an inclined solid surface by a liquid*. Phys. Fluids, **28**, 5–7, 1985
- Sinner, H., *The Sinner Circle "TACT."* Sinner's Cleaning Philosophy, Henkel, 1959
- Slade, D.R.J., Gravity-driven thin liquid films: Rivulets and flow dynamics, PhD Thesis, University of Leeds, 2013
- Smith, J.L., *On the simultaneous staining of neutral fat and fatty acid by oxazine dyes*, J. Pathol. Bacteriol., **12**, 1–4, 1908
- Sparks, J., *The Basics of Alkaline In-Process Cleaning for Metal Substrates*, Oakite Products, Inc, New Jersey, 1999
- Srilakshmi, B., *Food Science*, New Age International Limited Publishers, New Delhi, 105-110, 2003
- Stanga, M., *Sanitation: Cleaning and Disinfection in the Food Industry*. Wiley VCH, Weinheim, 2010
- Strokina, N., Matas, J., Eerola, T., *Detection of bubbles as concentric circular arrangements*. Mach. Vis. Appl., **27**, 387-396, 2016
- Thompson, J. L., Scheetz, B. E., Schock, M. R., Lytle, D. A., Delaney, P. J., *Sodium Silicate Corrosion Inhibitors: Issues of Effectiveness and Mechanism*. Presented at the Denver Water Quality Technology Conference, November 9-12, 1997.
- Truong, T.H., Kirkpatrick, K., Anema, S.G., *Role of beta-lactoglobulin in the fouling of stainless steel surfaces by heated milk*, Int. Dairy J., **197**, 48-59, 2017
- Tsai, J-H., Cuckston, G.L., Hallmark, B. and Wilson, D.I., *Fluid-dynamic gauging for studying the initial swelling of soft solid layers*, AIChE Journal, **65**, (9), 1-13, 2019
- Tsien, R.Y., Waggoner, A., *Fluorophores for confocal microscopy*. In: Pawley JB (ed) Handbook of biological confocal microscopy, 2nd edn. Plenum, New York, 267-280, 1995
- Tuladhar, T.R., Paterson, W.R., Macleod, N., Wilson, D.I., *Development of a novel non-contact proximity gauge for thickness measurement of soft deposits and its application in fouling studies*, The Canadian Journal of Chemical Engineering. **78**, (5), 935-947, 2000
- Tuladhar, T.R., Paterson, W.R., Wilson, D.I., *Investigation of alkaline cleaning-in-place of whey protein deposits using dynamic gauging*. Food Bioprod Process., **80**, (3), 199-214, 2002
- VDMA Information sheet, *Process plant and equipment association: Riboflavin test for low-germ or sterile process technologies*, Food, aseptic, pharmacy and chemistry, 2007
- Verran, J., Boyd, R. D., Hall, K., West, R. H., *Microbiological and chemical analysis of stainless steel and ceramic subjected to repeated soiling and cleaning treatments*, J. Food Prot., **64**, 1377–1387, 2001
- Verran, J., Boyd, R.D., Hall, K.E., West, R., *The Detection of Microorganisms and Organic Material on Stainless Steel Food Contact Surfaces*, Biofouling, **18**, (3), 167-176, 2002
- Wagner, I., Musso, H., *New Naturally Occurring Amino Acids*. Angewandte Chemie International Edition in English. **22**, (11), 816–828, 1983.

- Wang, H-Y., Qian, H., Yao, W-R., *Melanoidins produced by the Maillard reaction: Structure and biological activity*, J. Food Chemistry, **128**, (3), 573-584, 2011
- Wang, S., Wilson, D.I., *Zero-discharge fluid-dynamic gauging for studying the swelling of soft solid layers*, Ind. Eng. Chem. Res., **54**, 7859-787, 2015
- Wang, S., Schlüter, F., Gottschalk, N., Augustin, W., *Aseptic Zero Discharge Fluid Dynamic Gauging for Measuring the Thickness of Soft Layers on Surfaces*. Chemie Ingenieur Technik, **88**, (10), 1530-1538, 2016
- Wang, S., *The development of automated zero-discharge fluid dynamic gauging for studying soft solid surface layers*, PhD Thesis, University of Cambridge, 2017
- Wawerla, M., Stolle, A., Schalch, B., Eisgruber, H., *Impedance microbiology: applications in food hygiene*, J. Food Prot., **62**, 1488–1496, 1999
- Weiss, M., Denger, K., Huhn, T., Schleheck, D., *Two enzymes of a complete degradation pathway for linear alkylbenzenesulfonate (LAS) surfactants: 4-sulfoacetophenone Baeyer-Villiger monooxygenase and 4-sulfophenylacetate esterase in Comamonas testosteroni KF-1*, Appl. Environ. Microbiol., **78**, (23), 8254-63, 2012
- Westgate, *The cost of recalling products in the food industry, data from 2016*, published 21/09/2018.
- Wildbrett, G., Sauer, V., *Cleanability of PMMA and PP compared with stainless steel*. In: Kessler H. G., Lund D. B. (eds) Proc. 3rd Int. Conf. Fouling and Cleaning in Food Processing, 163–177, 1989
- Williams, J.J., *Handbook for Cleaning/Decontamination of Surfaces, B.1.II - Formulation of Carpet Cleaners*, **1**, 103-123, 2007
- Williams J.K., Dawe R.A., *Photographic observations of unusual flow phenomena in porous media at interfacial tensions below 0.1 mN m⁻¹*, J. Colloid Interface Sci., **124**, (2), 691–696, 1988
- Wilson, D. I., Atkinson, P., Kohler, H., Mauremann, M., Stoye, H., Suddaby, K., Wang, T., Davidson, J.F., Majschak, J.P., *Cleaning of soft-solid soil layers on vertical and horizontal surfaces by stationary coherent impinging jets*, Chemical Engineering Science, **109**, 183-196, 2014
- Wilson, D. I., Kohler, H., Cai, L., Majschak, J. P., Davidson, J. F., *Cleaning of a model food soil from horizontal plates by a moving vertical water jet*, Chemical Engineering Science, **123**, 450-459, 2015
- Wilson, D.I., *Fouling during food processing – progress in tackling this inconvenient truth*, Current Opinion in Food Science, **23**, 105-112, 2018
- Wongsirichot, P., *MPhil ACE Report: Millimanipulation*, University of Cambridge, Cambridge, 2014
- Yang, Q., Wilson, D.I., Chang, S., Shi, L., *A New Approach for Mitigating Biofouling by Promoting Online Cleaning Using a Sacrificial Paraffin Coating*, Heat Transfer Engineering, **36**, (7-8), 695-705, 2015
- Yazawa. M., Hsueh, B., Jia, X., Pasca, A.M., Bernstein, J.A., Hallmayer, J., Dolmetsch, R.E., *Using induced pluripotent stem cells to investigate cardiac phenotypes in Timothy syndrome*, Nature, 471, 230–234, 2011

- Zabulis, X., Papara, M., Chatziargyriou, A., Karapantsios, T.D., *Detection of densely dispersed spherical bubbles in digital images based on a template matching technique: Application to wet foams*, Colloids Surf. A Physicochem. Eng. Asp., **309**, 96-106, 2007
- Zhang, S. and Vardhanabhuti, B. *Intragastric gelation of whey protein–pectin alters the digestibility of whey protein during in vitro pepsin digestion*, Food Funct., **5**, 102–110, 2014
- Zhang Z., Ferenczi M. A., Lush A. C., and Thomas C. R., *A novel micromanipulation technique for measuring the bursting strength of single mammalian cells*, Applied Microbiology and Biotechnology, **36**, (2), 208–210, 1991
- Zhang Z., Al-Rubeai M., and Thomas C. R., *Mechanical properties of hybridoma cells in batch culture*, Biotechnology Letters, **14**, (1), 11–16, 1992
- Zhao Q., Liu Y., Müller-Steinhagen, H. and Liu G., *Graded Ni-P-PTFE Coatings and Their Potential Applications*, Surface & Coatings Technology, **155**, 279-284, 2002
- Zhongye, X., Yan, T., Yi, Z., Qinyuan, D., *Surface and thickness measurement of transparent thin-film layers utilizing modulation-based structured-illumination microscopy*, Optics Expressed, **26**, (3), 2944 – 2953, 2018
- Zhou, K.X., Li, N., Christie, G., Wilson, D.I., *Assessing the Impact of Germination Sporulation Conditions on the Adhesion of Bacillus Spores to Glass and Stainless Steel by Fluid Dynamic Gauging*, J. Food Sci., **82**, 2614-2625, 2017
- Zorita, S. , Niquet, C. , Bonhoure, J. , Robert, N., Tessier, F. J., *Optimisation of a model food mixture using response surface methodology to evaluate the anti-adhesive properties of cooking materials*. International Journal of Food Science & Technology, **45**, 2494-2501, 2010

12. Appendix

12.1 The Lambert Function

The Lambert W function is defined as the reciprocal of the product:

$$f(z) = ze^z \quad (\text{Equation 12.1})$$

Where z is generally a complex variable. Hence:

$$z = W(f(z)) \quad (\text{Equation 12.2})$$

Equation 6.52 can be rearranged to give:

$$\frac{(r^*)^2}{2} \left(\ln(r^*) - \frac{1}{2} \right) + \frac{1}{4} = \frac{\Delta P_c}{\alpha a^2} t \quad (\text{Equation 12.3})$$

$$\rightarrow e^{2 \ln(r^*)} (2 \ln(r^*) - 1) = \frac{4 \Delta P_c}{\alpha a^2} t - 1 \quad (\text{Equation 12.3a})$$

$$\rightarrow e^{(2 \ln(r^*) - 1) + 1} (2 \ln(r^*) - 1) = \frac{4 \Delta P_c}{\alpha a^2} t - 1 \quad (\text{Equation 12.3b})$$

$$\rightarrow e^{(2 \ln(r^*) - 1)} (2 \ln(r^*) - 1) = \frac{\frac{4 \Delta P_c}{\alpha a^2} t - 1}{e} \quad (\text{Equation 12.3c})$$

Applying the above definition to Equation 12.2 then gives:

$$2 \ln(r^*) - 1 = W \left(\frac{\frac{4 \Delta P_c}{\alpha a^2} t - 1}{e} \right) \quad (\text{Equation 12.4})$$

$$\Rightarrow r^*(t) = e^{\frac{1}{2} \left(W \left(\frac{\frac{4 \Delta P_c}{\alpha a^2} t - 1}{e} \right) + 1 \right)} \quad (\text{Equation 12.5})$$

The time at which the water penetration front reaches the centre of the control volume (that is, the characteristic time of the system for the mechanism considered), t' , is thus given by:

$$t' = \frac{\alpha a^2}{4 \Delta P_c} \quad (\text{Equation 12.6})$$

Letting $t^* = \frac{t}{t'}$, Equation 12.5 thus becomes:

$$r^*(t^*) = e^{\frac{1}{2} \left(W \left(\frac{t^* - 1}{e} \right) + 1 \right)} \quad (\text{Equation 12.7})$$

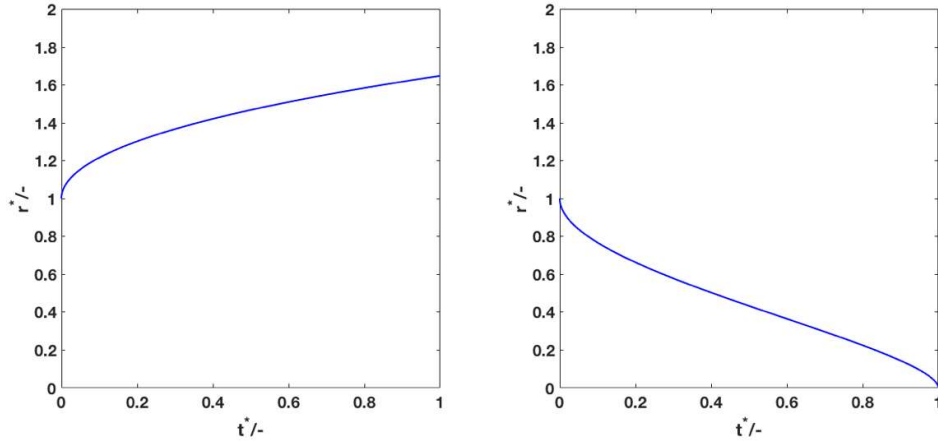


Figure 12.1: Profiles of r^* computed from Equation 12.7 using (a): W_0 , and (b): W_{-1} .

The Lambert W function is multivalued over its domain and is therefore divided into two branches: W_0 and W_{-1} . The choice of which branch to use depends on the required behaviour of r^* . As explained above, r^* should initially adopt a value of one and progressively decrease towards zero. Comparing the profiles of r^* obtained using either W or W_{-1} (Figure 12.1) indicates that W_{-1} gives the desired behaviour. Taking the natural logarithm of Equation 12.7 gives:

$$\ln(r^*(t^*)) = \frac{1}{2} \left(W_{-1} \left(\frac{t^*-1}{e} \right) + 1 \right) \quad (\text{Equation 12.8})$$

Substituting Equation 12.8 into 12.5 then yields:

$$\frac{dr}{dt} = \begin{cases} \frac{\Delta P_c}{2\alpha r (W_{-1}(\frac{t^*-1}{e}) + 1)}, & 0 < t^* \leq 1 \\ 0, & t^* > 1 \end{cases} \quad (\text{Equation 12.9})$$

Inserting the above result into [8], and substituting $t = \frac{\alpha a^2}{4\Delta P_c} t^*$:

$$\frac{dV}{dt^*} \approx -\pi \delta a^2 \phi_{oil} \frac{1}{(W_{-1}(\frac{t^*-1}{e}) + 1)} \quad (\text{Equation 12.10})$$

Letting $\tau = \frac{t^*-1}{e}$, where τ is a dummy variable, allows the above equation to be integrated through a change of variables:

$$\frac{d\tau}{dt^*} = \frac{1}{e} \quad (\text{Equation 12.11})$$

$$\Rightarrow dt^* = e d\tau \quad (\text{Equation 12.11a})$$

$$\rightarrow \int_0^V dV \approx -\pi a^2 \delta \phi_{oil} e \int_{-\frac{1}{e}}^{\frac{t^*-1}{e}} \frac{d\tau}{W_{-1}(\tau) + 1} \quad (\text{Equation 12.11b})$$

Since $\int_a^b \frac{dx}{W(x)+1} = \left[\frac{x}{W(x)} \right]_a^b$, Equation 12.11b reduces to:

$$V(\tau) \approx -\pi a^2 \delta \phi_{oil} e \left[\frac{\tau}{W_{-1}(\tau)} \right]_{\frac{-1}{e}}^{\frac{t^*-1}{e}} \quad (\text{Equation 12.12})$$

$$\rightarrow V(t^*) \approx -\pi a^2 \delta \phi_{oil} e \left[\frac{\frac{t^*-1}{e}}{W_{-1}\left(\frac{t^*-1}{e}\right)} - \frac{\frac{-1}{e}}{W_{-1}\left(\frac{-1}{e}\right)} \right] \quad (\text{Equation 12.12b})$$

Noting that $W_{-1}\left(-\frac{1}{e}\right) = -1$, and cancelling out the e term yields:

$$V(t^*) \approx \begin{cases} \pi a^2 \delta \phi_{oil} \left(1 - \frac{t^*-1}{W_{-1}\left(\frac{t^*-1}{e}\right)} \right), & 0 \leq t^* < 1 \\ \pi a^2 \delta \phi_{oil}, & t^* \geq 1 \end{cases} \quad (\text{Equation 12.13})$$

12.2: CTAB Oil droplet formation

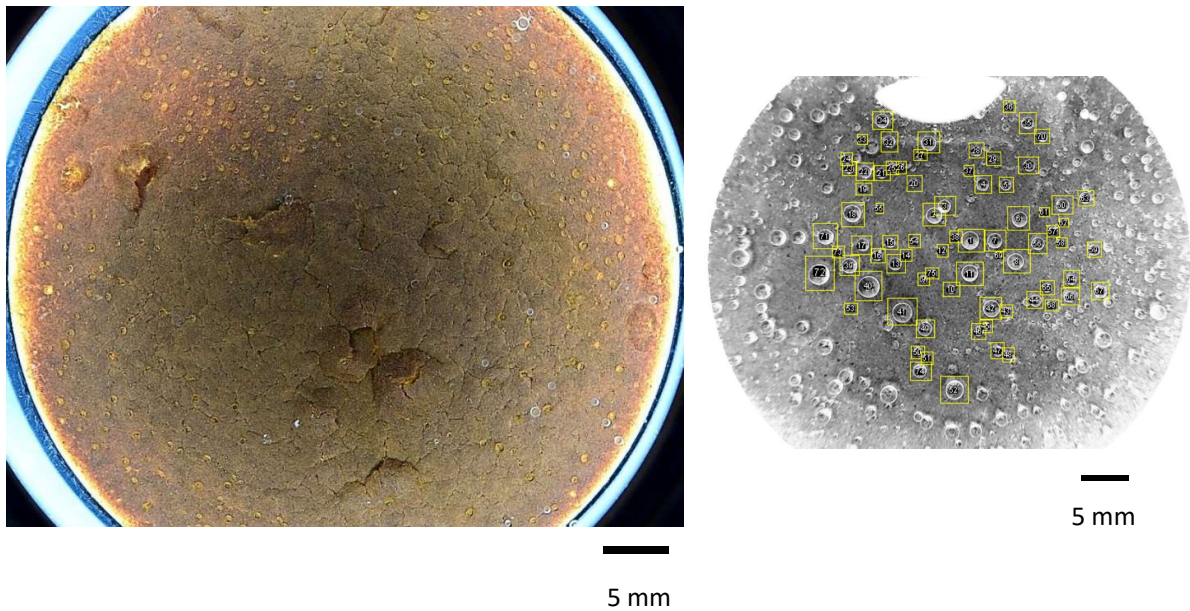


Figure 12.2: Example of droplet formation on CMS submerged in (a) 0.01% CTAB solution and (b) pH 7, water at 50 °C.